

STRUCTURAL DYNAMICS

RECENT ADVANCES

DTIC QUALITY INSPECTED 4

20000908 139

PROCEEDINGS OF THE
7TH INTERNATIONAL
CONFERENCE

EDITED BY:
N. S. FERGUSON
H. F. WOLFE
M. A. FERMAN
S. A. RIZZI

REPORT DOCUMENTATION PAGE

Form Approved OMB No. 0704-0188

Public reporting burden for this collection of information is estimated to average 1 hour per response, including the time for reviewing instructions, searching existing data sources, gathering and maintaining the data needed, and completing and reviewing the collection of information. Send comments regarding this burden estimate or any other aspect of this collection of information, including suggestions for reducing this burden to Washington Headquarters Services, Directorate for Information Operations and Reports, 1215 Jefferson Davis Highway, Suite 1204, Arlington, VA 22202-4302, and to the Office of Management and Budget, Paperwork Reduction Project (0704-0188), Washington, DC 20503.

1. AGENCY USE ONLY (Leave blank)		2. REPORT DATE 27 July 2000	3. REPORT TYPE AND DATES COVERED Conference Proceedings	
4. TITLE AND SUBTITLE Seventh International Conference on Recent Advances in Structural Dynamics			5. FUNDING NUMBERS F61775-00-WF065	
6. AUTHOR(S) Conference Committee				
7. PERFORMING ORGANIZATION NAME(S) AND ADDRESS(ES) University of Southampton Highfield Southampton SO17 1BJ United Kingdom			8. PERFORMING ORGANIZATION REPORT NUMBER N/A	
9. SPONSORING/MONITORING AGENCY NAME(S) AND ADDRESS(ES) EOARD PSC 802 BOX 14 FPO 09499-0200			10. SPONSORING/MONITORING AGENCY REPORT NUMBER CSP 00-5065	
11. SUPPLEMENTARY NOTES Two volumes.				
12a. DISTRIBUTION/AVAILABILITY STATEMENT Approved for public release; distribution is unlimited.			12b. DISTRIBUTION CODE A	
13. ABSTRACT (Maximum 200 words) The Final Proceedings for Seventh International Conference on Recent Advances in Structural Dynamics, 24 July 2000 - 27 July 2000 Aeronautics and Flutter; Analytical Developments; Numerical Methods; Finite Element Methods; Nonlinear Vibration; Experimental techniques; Rotating Machines; Control; System Identification; Acoustic Fatigue and Thermal Effects; Power Flow Approaches and Impact Dynamics				
14. SUBJECT TERMS EOARD, Aerodynamics, Fatigue, Aeroelasticity			15. NUMBER OF PAGES 1048	
			16. PRICE CODE N/A	
17. SECURITY CLASSIFICATION OF REPORT UNCLASSIFIED	18. SECURITY CLASSIFICATION OF THIS PAGE UNCLASSIFIED	19. SECURITY CLASSIFICATION OF ABSTRACT UNCLASSIFIED	20. LIMITATION OF ABSTRACT UL	

NSN 7540-01-280-5500

Standard Form 298 (Rev. 2-89)
Prescribed by ANSI Std. Z39-18
298-102

STRUCTURAL DYNAMICS: RECENT ADVANCES

Proceedings of the 7th International Conference

Volume II

Proceedings of the Seventh International Conference on Recent Advances in Structural Dynamics, held at the Institute of Sound and Vibration Research, University of Southampton, England, from 24th to 27th July, 2000, co-sponsored by the US Airforce European Office of Aerospace Research and Development, the Air Force Research Laboratory, Wright Patterson Air Force Base, Parks College of Engineering and Aviation, St. Louis University, and the Structural Acoustics Branch at NASA Langley Research Center.

Edited by

N.S. FERGUSON

*Institute of Sound and Vibration Research,
University of Southampton, Southampton, UK.*

H.F. WOLFE

*Air Force Research Laboratory
Wright Patterson Air Force Base, Ohio, USA.*

M.A. FERMAN

*Parks College of Engineering and Aviation
St Louis University, St Louis, USA*

and

S.A. RIZZI

*NASA Langley Research Center
Hampton, Virginia, USA*

AQF00-11-3745

PREFACE

The International Conference series on Recent Advances in Structural Dynamics enters its third decade of existence since its inception in 1980. This is the seventh conference to be held at the Institute of Sound and Vibration Research (ISVR) and it is through the continued support and sponsorship, in time and resources, of the ISVR, the Air Force Research Laboratory (Wright Patterson Air Force Base), Parks College of Engineering and Aviation (St Louis University) and NASA Langley Research Center that we have succeeded in organising the event. On this occasion there are two new co-organisers, Prof. M.A. Ferman and Dr S.A. Rizzi, who have been excellent replacements for Prof. C. Mei, who previously contributed so much. The new co-organisers have been instrumental in the organisation of new sessions, one namely Aerodynamics and Flutter, and have also continued the long standing tradition, topics and interests of the Structural Dynamics community, such as Acoustic Fatigue.

The conference has maintained its high standards by continuing to review submitted papers and thanks are directed towards the authors, Invited Speakers, paper reviewers and session chairmen for their contribution and support. Likewise the conference has a strong international participation, allowing for good technical discussion, dissemination and interchange of ideas. It is also anticipated that the published proceedings will provide a good source of material for future research activities and be a true record of the papers presented. The arrangement of the papers, in two volumes, is to accompany the programme of presentations and likewise the papers are grouped into the most appropriate sessions.

The organisers would like to thank the following for their contribution to the success of the conference: the United States Air Force European Office of Aerospace Research and Development. Personally I would like to acknowledge and thank all of the other conference organisers of the event:

Dr. H.F. Wolfe	Air Force Research Laboratory, Wright Patterson Air Force Base, USA
Prof. M.A. Ferman	Parks College of Engineering and Aviation, St Louis University, USA
Dr. S.A. Rizzi	Structural Acoustics Branch, NASA Langley Research Center, USA

Last, but not least, also tremendous thanks to Mrs. M.Z. Strickland, Conference Secretary and general assistant for all things technical and administrative.

N.S. Ferguson

**Seventh International Conference on
Recent Advances in Structural Dynamics**

Volume II

Contents

Page No.

INVITED PAPERS

K.K.TAMMA, R.KANAPADY, X.ZHOU and D.SHA
Recent Advances in Computational Structural Dynamics
Algorithms

731

ACOUSTIC FATIGUE

R.UDRESCU
Nonlinear Vibrations of thermally Buckled Panels

757

J-M.DHAINAUT, BIN DUAN, C.MEI, S.M.SPOTTSWOOD
and H.F.WOLFE
Non-Linear response of composite panels to random excitations
at elevated temperatures

769

S.M.SPOTTSWOOD, H.F.WOLFE and D.L.BROWN
The effects of record length on determining the cumulative damage
of a ceramic matrix composite beam

785

P.R.CUNNINGHAM, D.M.A.MILLAR and R.G.WHITE
High intensity acoustic testing of doubly curved composite honeycomb
sandwich panels

801

N.W.M.BISHOP, N.DAVIS, A.CASERIO and S.KERR
Fatigue Analysis of an F16 Navigation Pod

815

S.A.RIZZI and A.A.MURAVYOV
Comparison of non-linear random response using equivalent
linearization and numerical simulation

833

J.LEE
Effects of temperature dependent physical properties on the
responses of thermally buckled plates

847

FE and APPLICATIONS

K.DEDOUCH, J.HORACEK and J.SVEC Frequency modal analysis of supraglottal vocal tract	863
G.CATANIA Combined influence of cutouts and initial stresses on the free vibration response of general, double curvature shell structures	875
S.E.HIRDARIS S.E.and A.W.LEES On the identification of natural frequencies of thick portal frames	887
C.REMILLAT, G.R.TOMLINSON and R. LEWIN A new multiple-layer finite element shell incorporating very thin damping layers: application to a multilayered cylindrical shell	901
D.K.L.TSANG, S.O.OYADJI and A.Y.T.LEUNG Predicting the dynamic stress intensity factor for a circumferential crack in a hollow cylinder using fractal finite element method	913

SYSTEM IDENTIFICATION

S.D.GARVEY, M.I. FRISWELL and J.E.T. PENNY A Geometric-Algebraic Approach to Identifying Second Order Continuous Systems	925
A.RIVOLA Comparison between second and higher order spectral analysis in detecting structural damages	937
N.JAKSIC, M.BOLTEZAR and A.KUHELJ Parameter identification of a single degree of freedom dynamical system based on phase space variables	951
K.WORDEN, G.W.MANSON and C.REMILLAT Damage Localisation Using Novelty Indices	965
HOON SOHN, M.L.FUGATE and C.R.FARRAR Damage Diagnosis Using Statistical Process Control	979
C.K.MECHEFSKE, Y.WU and B.K.RUTT MRI Gradient Coil Cylinder Sound Field Simulation and Measurement	995
Z.CHEN, C.K.MECHEFSKE Application of the Prony Method in Machine Condition Monitoring	1003
K.T.FEROZ, S.O.OYADJI, J.R.WRIGHT and A.Y.T.LEUNG Finite element analysis of rubber mounts under shock loading	1015

- HUANG YU, TANG YIQUN, YE WEIMIN and CHEN ZHUCHANG
A dynamic calculation model of Shanghai saturated soft soil 1027
- C.J.C.JONES, D.J.THOMPSON and M.G.R.TOWARD
The dynamic stiffness of the ballast layer in railway track 1037

INVITED PAPERS

Recent Advances in Computational Structural Dynamics Algorithms

K. K. Tamma*, R. Kanapady†, X. Zhou‡ and D. Sha§

Dept. of Mechanical Engineering, University of Minnesota, Minneapolis, MN 55455 U. S. A

Abstract

Recent advances describing a generalized unified framework for the generic design of time discretized operators for structural dynamics applications is described. Emanating from a generalized time weighted philosophy for performing the time discretization process, the burden of weight carried by the so-called and resulting discrete numerically assigned [DNA] algorithmic markers serves as a prelude to providing a basis for the classification, characterization and design of computational algorithms for structural dynamic computations. An overview of recent advances encompassing time discretized operators which we have recently classified as Type 1, 2 and 3 is briefly highlighted and subsequently, for illustration, emphasis is primarily placed on applicability of Type3 classification to general non-linear/linear problems, practical issues, and implementation aspects.

1 Introduction

For the solution of the semi-discretized system of equations of structural dynamic problems, the so-called time integration algorithms are widely used. Especially for non-linear structural dynamic problems, time integration algorithms are the major tools, which leads to the primary motivation for a precise understanding of computational algorithms for time dependent problems. Due to the cumbersome issues associated with nonlinear situations, most of the time integration algorithms are customarily developed starting from the linear semi-discretized system or modal equations. The extension of time integration algorithms to non-linear problems is then conducted. In contrast, we focus our attention here on recent advances in the design and application of computational algorithms under the umbrella of a generalized unified framework for the simulation of structural dynamics problems.

Emanating from and explained via a generalized time weighted residual philosophy, Tamma et al. [1, 2] have recently described the resulting time discretized operators for the semi-discretized single field or two field equations of motion of structural dynamic problems as pertaining to three major classifications, namely, Type 1 classification, Type 2 classification, and Type 3 classification (see [1, 2] for details). Type 1 classification are an outcome of selecting the weighted time fields (which are matrix representations) as the homogeneous solution of the linear semi-discretized system of equations with or without the notion of

*Professor, to receive correspondence, ktamma@tc.umn.edu

†Doctoral student, ramdev@me.umn.edu

‡Doctoral student, xiangmin@me.umn.edu

§Visiting Professor, Dalian University of Technology, P. R. China, sha@msi.umn.edu

transforming the semi-discretized system of equations into modal basis. The Type 1 classifications lead to explicit time integral representations of the exact solution of the linear semi-discretized system of equations of the structural dynamic problems. Here, the approximations for the dependent field variables are not pertinent. The Type 2 classification of time discretized operators are a result of introducing further approximations to the theoretical weighted time fields pertaining to Type 1 which still preserve the matrix representation for the weighted time fields and without considering the notion of transforming modal basis merely for convenience in the theoretical design developments. Again, for time discretized operators of Type 2 classification, approximations for the dependent field variables are not pertinent. In contrast, Type 3 classification of time discretized operators are a result of further introducing approximations to the theoretical weighted time fields, thereby leading to a degenerated vector or a degenerated scalar representation which does not preserve the original theoretical representations. As a consequence, the approximations for the dependent field variables is now necessary for designing the time integrators and the associated updates. This Type 3 classification leads to a wide variety of generalized integration operators in time which not only provide new avenues [3] but also recover the existing and so-called time integration algorithms (both dissipative and non-dissipative) we are mostly familiar with. Characterization as employed here, pertains to that which not only permits the classification of the time discretized operators to be undertaken but also provides the underlying theoretical basis towards their subsequent theoretical design via discrete numerically assigned [DNA] algorithmic markers which essentially comprise of: (i) weighted time fields utilized for enacting the time discretization process, and (ii) the corresponding conditions invoked (if any) and dictated by these weighted time fields for approximating the dependent field variable(s) in the design of time integrators and the associated updates.

2 Semi-Discretized Equations of Motion

2.1 Single-Field Form

Firstly, we consider the semi-discretized system of equations of linear structural dynamic problems after space discretization (say in a finite element sense) of the single field form of representation resulting in

$$\mathbf{M}\ddot{\mathbf{u}}(t) + \mathbf{C}\dot{\mathbf{u}}(t) + \mathbf{K}\mathbf{u}(t) = \mathbf{f}(t), \quad \mathbf{u}(0) = \mathbf{u}_0, \dot{\mathbf{u}}(0) = \dot{\mathbf{u}}_0 \quad (1)$$

where \mathbf{M} is the mass matrix, \mathbf{C} is the damping matrix, and \mathbf{K} is the stiffness matrix. Under the framework of a time weighted residual approach with an arbitrary weighted time field, $\mathbf{W}(t)$, we have the representation after integrating by parts twice

$$\begin{aligned} & \int_0^{\Delta t} \left(\ddot{\mathbf{W}}^\top \mathbf{M} - \dot{\mathbf{W}}^\top \mathbf{C} + \mathbf{W}^\top \mathbf{K} \right) \mathbf{u} dt \\ &= -\mathbf{W}^\top \mathbf{M} \dot{\mathbf{u}} \Big|_0^{\Delta t} + \dot{\mathbf{W}}^\top \mathbf{M} \mathbf{u} \Big|_0^{\Delta t} + \mathbf{W}^\top \mathbf{C} \mathbf{u} \Big|_0^{\Delta t} + \int_0^{\Delta t} \mathbf{W}^\top \mathbf{f} dt \end{aligned} \quad (2)$$

2.2 Two-Field Form

Alternatively, equation (1) can be cast into a two field representation by letting $\dot{\mathbf{u}} = \mathbf{v}$ and $\ddot{\mathbf{u}} = \dot{\mathbf{v}}$, resulting in

$$\dot{\mathbf{d}} + \mathbf{A}\mathbf{d} = \mathbf{F} \quad (3)$$

where

$$\mathbf{A} = \begin{bmatrix} \mathbf{0} & -\mathbf{I} \\ \mathbf{M}^{-1}\mathbf{K} & \mathbf{M}^{-1}\mathbf{C} \end{bmatrix}, \quad \mathbf{d} = \begin{bmatrix} \mathbf{u} \\ \mathbf{v} \end{bmatrix}, \quad \mathbf{F} = \begin{bmatrix} \mathbf{0} \\ \mathbf{M}^{-1}\mathbf{f} \end{bmatrix}$$

Again considering the weighted residual satisfaction with an arbitrary weighted time field $\mathbf{W}(t)$, after integrating by parts once, leads to

$$\mathbf{W}^T \mathbf{d} \Big|_0^{\Delta t} + \int_0^{\Delta t} [(\mathbf{W}^T \mathbf{A} - \dot{\mathbf{W}}^T) \mathbf{d} - \mathbf{W}^T \mathbf{F}] dt = 0 \quad (4)$$

3 Time Discretized Operators of Type 1 Classification

3.1 Single Field Form

Consider the weighted time fields \mathbf{W} as the solution of the adjoint operator in Eq. 2, and substituting the obtained theoretical weighted time field $\mathbf{W} = \mathbf{W}_{Exact}(t)$ into equation (2) and transforming the resulting equation into modal basis by using the eigenvector matrix \mathbf{X} obtained from

$$\mathbf{K}\mathbf{X} = \mathbf{M}\mathbf{X}\Omega^2 \quad (5)$$

The resulting exact time integral representations (equivalent to the Duhamel representations) are explicit in nature and are obtained as

$$\begin{pmatrix} q_i(t_{n+1}) \\ \dot{q}_i(t_{n+1}) \end{pmatrix} = \mathbf{A}_{amp} \begin{pmatrix} q_i(t_n) \\ \dot{q}_i(t_n) \end{pmatrix} + \tilde{\mathbf{L}} \quad (6)$$

where the details are given in [2]. An approximate integral operator is readily constructed by approximating the load term. The applicability of such Type 1 representations to linear/nonlinear problems is addressed in Refs. [1, 4]. Alternatively, without considering transformation to modal basis, although a theoretical representation can be derived, no practically useful time discretized representations result.

3.2 Two Field Form

Next consider the weighted time fields, \mathbf{W} , as the solution of the adjoint operator in Eq. 3, and substituting the fundamental solution, into equation (4), we have the closed form time integral representation of the equation (3) as

$$\exp[\mathbf{A}\Delta t]\mathbf{d}_{n+1} = \mathbf{d}_n + \int_0^{\Delta t} \exp[\mathbf{A}t']\mathbf{F}(t' + t_n)dt' \quad (7)$$

A key idea towards the generic theoretical design and development of a new generation of a generalized family of time discretized operators pertaining to Type 2 classification is that the matrix \mathbf{A} is first decomposed into a symmetric and unsymmetric part as

$$\mathbf{A} = \mathbf{A}_D + \beta \mathbf{A}_\Omega + (1 - \beta) \mathbf{A}_\Omega \quad (8)$$

where

$$\mathbf{A}_D = \alpha \begin{bmatrix} \mathbf{M}^{-1}\mathbf{C} & \mathbf{0} \\ \mathbf{0} & \mathbf{M}^{-1}\mathbf{C} \end{bmatrix}, \quad \mathbf{A}_\Omega = \begin{bmatrix} -\alpha \mathbf{M}^{-1}\mathbf{C} & -\mathbf{I} \\ \mathbf{M}^{-1}\mathbf{K} & (1 - \alpha) \mathbf{M}^{-1}\mathbf{C} \end{bmatrix} \quad (9)$$

$\alpha \in [0, 1]$ and $\beta \in [0, 1]$ are typical control parameters introduced for convenience in the theoretical design and are subsequently addressed. After some algebra we have the closed form explicit time integral representation as

$$\begin{aligned} \exp[\mathbf{A}_D \Delta t] \exp[\beta \mathbf{A}_\Omega \Delta t] \mathbf{d}_{n+1} &= \exp[(\beta - 1) \mathbf{A}_\Omega \Delta t] \mathbf{d}_n \\ &+ \exp[\mathbf{A}_D (1 - \beta) \Delta t] \int_0^{\Delta t} \exp[\mathbf{A} \{(\beta - 1) \Delta t + t'\}] \mathbf{F}(t' + t_n) dt' \end{aligned} \quad (10)$$

However, the above Type 1 classification is not practical and is computationally unattractive.

4 Time Discretized Operators of Type 2 Classification

Considering the decomposition of matrix \mathbf{A} with parameters α and β , the design leading to Type 2 classifications of time discretized operators follows.

4.1 Case of $\alpha = \beta = 0$: On the design of some new and existing variants of Type 2 classification of time discretized operators

When $\alpha = 0$ and $\beta = 0$, the exact solution of the linear dynamic two-field form yields the representation:

$$\mathbf{d}_{n+1} = \exp[-\mathbf{A} \Delta t] \mathbf{d}_n + \exp[-\mathbf{A} \Delta t] \int_0^{\Delta t} \exp[\mathbf{A} t'] \mathbf{F}(t' + t_n) dt' \quad (11)$$

The design of some existing variants which pertain to and are subsets of Type 2 classification of time discretized operators, namely, existing approaches towards approximating the theoretical solution exist in the literature with attempts to introduce approximations to the exponential matrix $e^{-\mathbf{A} \Delta t}$. Various approaches are highlighted here for the approximation of the exponential matrix term. Of the various approaches, those which encompass a wide variety of existing algorithms includes: i) Taylor series expansion and its equivalent approximation [5, 6], ii) rational, Padé approximation [7, 8], and sub-stepping which includes serial (multiplicative decomposition) and parallel (additive decomposition) sub-stepping [9, 6]. Rational and Padé approximation and sub-stepping can be shown to be inherently *matrix identical* (in the sense of the amplification matrix). See Refs. [1, 10] where we describe further details.

4.2 Case of $\alpha \in [0, 1]$ and $\beta \in [0, 1]$: On the Design of a New Generation of a Generalized Family of Nth-Order Accurate Representations of Type 2 Classification of time discretized operators

We next simply highlight a new generation of a generalized family of time discretized operators with excellent algorithmic attributes and which pertain to Type 2 classification where $\mathbf{W} = \mathbf{W}_{Approx}$ is employed and is still a matrix representation and again with no approximations whatsoever for the displacement, velocity, and acceleration. Associated with the symmetric part we employ m_D terms and associated with the unsymmetric part we employ m_Ω terms, and for the load we employ m_P terms. We also introduce the notion of local truncation error terms.

Algorithm 1 : Find vector \mathbf{d}_{n+1} for given vector \mathbf{d}_n for a generalized family of time discretized operators emanating from approximations associated with the exact weighted time fields which indeed preserve the original theoretical form, but do not involve the notion of approximations for the dependent field variables or state vectors:

$$\mathbf{K}_{m_D}^D \mathbf{K}_{m_L}^L \mathbf{d}_{n+1} = \mathbf{K}_{m_R}^R \mathbf{d}_n + \mathbf{P}_{m_P} \quad (12)$$

where

$$\mathbf{K}_{m_D}^D = \sum_{p=0}^{m_D} \frac{1}{p!} (\mathbf{A}_D \Delta t)^p + \frac{\Gamma^D}{(m_D + 1)!} [\Theta(\gamma^D, \theta^D) (\mathbf{A}_D \Delta t)^{m_D+1}] \quad (13)$$

$$\mathbf{K}_m^L = \sum_{p=0}^m \frac{1}{p!} (\beta \mathbf{A}_\Omega \Delta t)^p + \frac{\Gamma^\Omega}{(m + 1)!} \Theta(\gamma^\Omega, \theta^\Omega) (\mathbf{A}_\Omega \Delta t)^{m+1} \quad (14)$$

$$\mathbf{K}_m^R = \sum_{p=0}^m \frac{1}{p!} [(\beta - 1) \mathbf{A}_\Omega \Delta t]^p - \frac{\Gamma^\Omega}{(m + 1)!} \Theta^*(\gamma^\Omega, \theta^\Omega) (\mathbf{A}_\Omega \Delta t)^{m+1} \quad (15)$$

$$\begin{aligned} \mathbf{P}_{m_P} = & \sum_{r=0}^{m_P} \frac{1}{r!} [(1 - \beta) \mathbf{A}_D \Delta t]^r \left\{ \sum_{p=0}^{m_P} \sum_{q=0}^{m_P-p-1} \frac{(-1)^q}{(p + q + 1)!} \mathbf{A}^p [(\beta \Delta t)^{p+q+1}] \mathbf{F}_{n+1}^{(q)} - \right. \\ & (\beta \Delta t - \Delta t)^{p+q+1} \mathbf{F}_n^{(q)} + \sum_{q=0}^{m_P} \frac{(-1)^{m_P-q} \Gamma^f}{m_P!} [\Theta^*(\gamma^f, \theta^f) \mathbf{A}^q (\beta - 1)^{m_P} \Delta t^{m_P+1} \mathbf{F}_n^{(m_P-q)} \\ & \left. + \Theta(\gamma^f, \theta^f) \mathbf{A}^q \beta^{m_P} \Delta t^{m_P+1} \mathbf{F}_{n+1}^{(m_P-q)}] \right\} \end{aligned} \quad (16)$$

Note that in the above equation (12-16) for **Algorithm 1**, m_D are the finite number of terms in the series associated with the symmetric part, $m_L = m_R = m_\Omega = m$ and m_P are the finite number of terms associated with the unsymmetric part and the load term respectively. γ^f, θ^f are the parameters associated with the load terms associated with Γ^f . Also, the 'local truncations error correcting terms' of the Taylor expansion approximation of

the approximate solution given by equations (12-16): $\Gamma^D \Theta(\gamma^D, \theta^D)(\mathbf{A}_\Omega \Delta t)^{m_D+1}/(m_D+1)!$, $\Gamma^\Omega \Theta^*(\gamma^\Omega, \theta^\Omega)(\mathbf{A}_\Omega \Delta t)^{m+1}/(m+1)!$ and $\Gamma^\Omega \Theta(\gamma^\Omega, \theta^\Omega)(\mathbf{A}_\Omega \Delta t)^{m+1}/(m+1)!$ may be used to improve the accuracy and stability in several special cases. $\Gamma^I \Theta(\gamma^I, \theta^I)$ and $\Gamma^I \Theta^*(\gamma^I, \theta^I)$ associated with the load affect the accuracy but not the stability. The above encompasses a generalized family of implicit and explicit representations, where: (i) The resulting N th order integration operators inherit features which are energy conserving for undamped systems and L-stable for damped systems [E/LNInO], and (ii) The resulting N th order accurate integration operators also yield time discretized operators which are explicit and L-stable for nonlinear structural dynamics [E-LNInO]. Detailed developments and applicability to structural dynamics problems are discussed elsewhere in Refs. [2, 10].

5 Time Discretized Operators of Type 3 Classification

The class of time discretized operators of Type 3 classification encompass: (i) single-field form, and (ii) Two-field form. These follow next.

5.1 Type 3-[GInO]_{Single-Field}: Single-Field Form

The developments leading to bridging of the relationships between integral operators in time pertaining to Type 1 classification described previously and the so-called time integration operators which we are mostly familiar with of Type 3 classification follows.

Consider the theoretical premise (approximation in a mean sense) of approximating all the system values pertaining to the dynamic problems as:

$$\omega_{d_m} = \frac{1}{n} (\omega_{d_1} + \dots + \omega_{d_n}); \quad \omega_m = \frac{1}{n} (\omega_1 + \dots + \omega_n); \quad \xi_m = \frac{1}{n} (\xi_1 + \dots + \xi_n) \quad (17)$$

where ω_{d_m} , ω_m and ξ_m are the quantities of all the system values. Thus, \mathbf{W}_{Exact} , described previously pertaining to Type 1 classification yields

$$W(t) = \frac{1}{\omega_{d_m}} e^{\xi_m \omega_m (t-\tau)} \sin(\omega_{d_m} (t-\tau)) H(t-\tau) \quad (18)$$

Consider now employing an asymptotic type series expansion for the above up to order (p+1) as:

$$W_{Asymp}(t) = [w_0 + w_1 ((t-\tau)/\Delta t) + \dots + w_{p+1} ((t-\tau)/\Delta t)^{p+1}] H(t-\tau) \quad (19)$$

Design of Time Integrator: Nth-Order Accurate Representations: Setting $\tau = t_n$ and letting $t - t_n = \bar{\tau}$, and denoting $\Gamma = \frac{t-t_n}{\Delta t}$, yields

$$W_{Asymp}(t) = w_0 + w_1 \Gamma + w_2 \Gamma^2 + \dots + w_p \Gamma^p + w_{p+1} \Gamma^{p+1} \quad (20)$$

where w_0, w_1, \dots, w_{p+1} are constant coefficients. An asymptotic type series expansion is consistently selected for the dependent field variables as:

$$\begin{aligned} \mathbf{u}_{Asymp} &= \mathbf{u}_n + \Lambda_1 \dot{\mathbf{u}}_n \bar{\tau} + \Lambda_2 \ddot{\mathbf{u}}_n \bar{\tau}^2 + \dots + \Lambda_p \mathbf{u}_n^{(p)} \bar{\tau}^p + \Lambda_{p+1} \bar{\tau}^{p+1} \Delta \mathbf{u}_{n+1}^{(p)} / \Delta t \\ \dot{\mathbf{u}}_{Asymp} &= \dot{\mathbf{u}}_n + \Lambda_{p+2} \ddot{\mathbf{u}}_n \bar{\tau} + \dots + \Lambda_{2p} \mathbf{u}_n^{(p)} \bar{\tau}^{p-1} + \Lambda_{2p+1} \bar{\tau}^p \Delta \mathbf{u}_{n+1}^{(p)} / \Delta t \\ \ddot{\mathbf{u}}_{Asymp} &= \ddot{\mathbf{u}}_n + \Lambda_{2p+2} \ddot{\mathbf{u}}_n \bar{\tau} + \dots + \Lambda_{3p-1} \mathbf{u}_n^{(p)} \bar{\tau}^{p-2} + \Lambda_{3p} \bar{\tau}^{p-1} \Delta \mathbf{u}_{n+1}^{(p)} / \Delta t \end{aligned} \quad (21)$$

where $\Lambda_i, i = 1, 2, \dots, 3p$ are arbitrary parameters and the load is approximated as

$$\mathbf{f} = \mathbf{f}_n + \dot{\mathbf{f}}_n \bar{\tau} + \dots + \mathbf{f}_n^{(p-1)} \bar{\tau}^{p-1} \quad (22)$$

Now, substituting both the above approximations for $W_{Asymp}(t)$ and $\mathbf{u}_{Asymp}, \dot{\mathbf{u}}_{Asymp}$, and $\ddot{\mathbf{u}}_{Asymp}$ into the time weighted residual semi-discretized dynamic field problem, yields:

Generalized Integration Operators [GInO]_{Single-Field}: Nth-Order Accurate Representations

$$\begin{aligned} & \mathbf{M} \left[\ddot{\mathbf{u}}_n + \Lambda_{2p+2} \frac{W_{p+1,1}}{W_{p+1,0}} \ddot{\mathbf{u}}_n + \dots + \Lambda_{3p-1} \frac{W_{p+1,p-2}}{W_{p+1,0}} \mathbf{u}_n^{(p)} + \Lambda_{3p} \frac{W_{p+1,p-1}}{W_{p+1,0}} \Delta \mathbf{u}_{n+1}^{(p)} \right] \\ & + \mathbf{C} \left[\dot{\mathbf{u}}_n + \Lambda_{p+2} \frac{W_{p+1,1}}{W_{p+1,0}} \dot{\mathbf{u}}_n + \dots + \Lambda_{2p} \frac{W_{p+1,p-1}}{W_{p+1,0}} \mathbf{u}_n^{(p)} + \Lambda_{2p+1} \frac{W_{p+1,p}}{W_{p+1,0}} \Delta \mathbf{u}_{n+1}^{(p)} \right] \\ & + \mathbf{K} \left[\mathbf{u}_n + \Lambda_1 \frac{W_{p+1,1}}{W_{p+1,0}} \mathbf{u}_n + \dots + \Lambda_p \frac{W_{p+1,p}}{W_{p+1,0}} \mathbf{u}_n^{(p)} + \Lambda_{p+1} \frac{W_{p+1,p+1}}{W_{p+1,0}} \Delta \mathbf{u}_{n+1}^{(p)} \right] \\ & = \mathbf{f}_n + \frac{W_{p+1,1}}{W_{p+1,0}} \dot{\mathbf{f}}_n + \dots + \frac{W_{p+1,p-1}}{W_{p+1,0}} \mathbf{f}_n^{(p-1)} \end{aligned} \quad (23)$$

where $W_{p,j} = \int_0^{\Delta t} W \bar{\tau}^j d\bar{\tau} = \Delta t^{j+1} \sum_{i=0}^p \frac{w_i}{1+i+j}$. Once $\mathbf{u}_{n+1}^{(p)}$ is found, the displacement, velocity and the associated higher-order derivatives can, in general, be obtained from the following proposed design for the updates:

$$\begin{aligned} \mathbf{u}_{n+1} &= \mathbf{u}_n + \lambda_1 \dot{\mathbf{u}}_n \Delta t + \lambda_2 \ddot{\mathbf{u}}_n \Delta t^2 + \dots + \lambda_p \mathbf{u}_n^{(p)} \Delta t^p + \lambda_{p+1} \Delta t^p \Delta \mathbf{u}_{n+1}^{(p)} \\ \dot{\mathbf{u}}_{n+1} &= \dot{\mathbf{u}}_n + \lambda_{p+2} \ddot{\mathbf{u}}_n \Delta t + \dots + \lambda_{2p} \mathbf{u}_n^{(p)} \Delta t^{p-1} + \lambda_{2p+1} \Delta t^{p-1} \Delta \mathbf{u}_{n+1}^{(p)} \\ &\vdots \\ \mathbf{u}_{n+1}^{(p-1)} &= \mathbf{u}_n^{(p-1)} + \lambda_{\frac{p(p+3)}{2}-1} \mathbf{u}_n^{(p)} \Delta t + \lambda_{\frac{p(p+3)}{2}} \Delta t \Delta \mathbf{u}_{n+1}^{(p)} \end{aligned} \quad (24)$$

Equation (23) with w_i and Λ_i and equation (24) with $\lambda_i, i = 1, 2, \dots, \frac{p(p+3)}{2}$, are termed as the family of generalized integration operators [GInO]_{Single-Field}, since they represent the generalized form of time discretized operators by appropriate selection of the DNA markers ($w_i, \Lambda_i, \lambda_i$) for both domain collocation types and point collocation types of time discretized operators and pertain to Type 3 classification. For illustration, of interest here and shown are second-order time accurate representations of [GInO] which readily yield:

$$\mathbf{M} [\ddot{\mathbf{u}}_n + \Lambda_6 W_1 (\ddot{\mathbf{u}}_{n+1} - \ddot{\mathbf{u}}_n)] + \mathbf{C} [\dot{\mathbf{u}}_n + \Lambda_4 W_1 \dot{\mathbf{u}}_n \Delta t + \Lambda_5 W_2 (\dot{\mathbf{u}}_{n+1} - \dot{\mathbf{u}}_n) \Delta t] + \mathbf{K} [\mathbf{u}_n + \Lambda_1 W_1 \mathbf{u}_n \Delta t + \Lambda_2 W_2 \ddot{\mathbf{u}}_n \Delta t^2 + \Lambda_3 W_3 (\ddot{\mathbf{u}}_{n+1} - \ddot{\mathbf{u}}_n) \Delta t^2] = \mathbf{F}_n + W_1 \dot{\mathbf{F}}_n \Delta t \quad (25)$$

$$\mathbf{u}_{n+1} = \mathbf{u}_n + \lambda_1 \dot{\mathbf{u}}_n \Delta t + \lambda_2 \ddot{\mathbf{u}}_n \Delta t^2 + \lambda_3 (\ddot{\mathbf{u}}_{n+1} - \ddot{\mathbf{u}}_n) \Delta t^2 \quad (26)$$

$$\dot{\mathbf{u}}_{n+1} = \dot{\mathbf{u}}_n + \lambda_4 \ddot{\mathbf{u}}_n \Delta t + \lambda_5 (\ddot{\mathbf{u}}_{n+1} - \ddot{\mathbf{u}}_n) \Delta t \quad (27)$$

where $W_i = \frac{W_{3,i}}{\Delta t^i W_{3,0}}$; $i = 1, 2, 3$ is defined for convenience. For convenience in presentation, the family of [GInO]_{Single-Field} which fall under the Type 3 classification of time discretized operators can be sub-categorized into different sub-types and further characterized as described next.

5.1.1 Dynamic Algorithms: Theoretical Design and Further Characterization of a Wide Variety of Algorithms Via Discrete Numerically Assigned [DNA] Markers: Type 3-[GInO]_{Single-Field}

A wide variety of computational algorithms pertaining to Type 3 classification and described previously under the framework of [GInO]_{Single-Field} and a formally standardized procedure leading to the theoretical design and for further providing avenues for characterizing a wide variety of new and unexplored (see Ref. [3] for details) and/or existing dynamic algorithms (as presented here) follows. Although the Type 3 classification of time discretized operators pertain to only a specific class, simply to illustrate and identify the comparative relationships based on the development of computational algorithms from historical perspectives as evident chronologically in the literature, we purposely further subcategorize these as follows:

[GInO]_{Single-Field} Sub-type 1: This class of representations for time discretized operators provide new avenues which have not been explored and/or exploited to-date leading to zero order displacement and velocity overshoot with controllable numerical dissipative features as discussed elsewhere [3] and/or recover the existing original algorithmic developments with dissipative features which exhibit linear velocity overshoot due to initial displacement for a wide variety of direct time integration approaches in structural dynamics and thus represent **true identity**. Definition: **True identity** is defined as those representations which yield identical time discretized operators as in the original methods of algorithmic development. In summary, the Type 3-[GInO]_{Single-Field} Sub-type 1 [DNA] markers are represented in the Table 1

[GInO]_{Single-Field} Sub-type 2: This class of representations of time discretized operators readily yield the so-called Newmark family of methods which also represent **true identity** as related to the original developments. The resulting time integrator and updates (note truncated Taylor series) are obtained as:

$$\mathbf{M} [\ddot{\mathbf{u}}_n + \Lambda_6 \Delta \ddot{\mathbf{u}}_{n+1}] + \mathbf{C} [\dot{\mathbf{u}}_n + \ddot{\mathbf{u}}_n \Delta t + \Lambda_5 \Delta \ddot{\mathbf{u}}_{n+1} \Delta t] + \mathbf{K} [\mathbf{u}_n + \dot{\mathbf{u}}_n \Delta t + \frac{1}{2} \ddot{\mathbf{u}}_n \Delta t^2 + \Lambda_3 \Delta \ddot{\mathbf{u}}_{n+1} \Delta t^2] = \mathbf{F}_n + \dot{\mathbf{F}}_n \Delta t \quad (28)$$

$$\mathbf{u}_{n+1} = \mathbf{u}_n + \dot{\mathbf{u}}_n \Delta t + \frac{1}{2} \ddot{\mathbf{u}}_n \Delta t^2 + \lambda_3 (\ddot{\mathbf{u}}_{n+1} - \ddot{\mathbf{u}}_n) \Delta t^2 \quad (29)$$

$$\dot{\mathbf{u}}_{n+1} = \dot{\mathbf{u}}_n + \ddot{\mathbf{u}}_n \Delta t + \lambda_5 (\ddot{\mathbf{u}}_{n+1} - \ddot{\mathbf{u}}_n) \Delta t \quad (30)$$

The generalized integration operators [GInO]_{Single-Field} of sub-type 2, equations (28-30), readily yield the above Newmark based time discretized operators described elsewhere as the [GNpj] type in Zienkiewicz and Taylor [11]. Sub-type 2 with respect to [DNA] markers are represented in the Table 1.

[GInO]_{Single-Field} Sub-type 3: [SSInO] This class of representations, on the other hand, readily yield a wide sub-class of other related so-called single-step integration operators [SSInO] of which a variety of algorithms and known methods are subsets of [GInO]. And, the representations only inherit either **matrix identity** or **spectral identity** (in the sense of the amplification matrix) to the original methods of development. These time discretized operators may not yield **true identity** representations to the original developments. The resulting integrator and updates are (note no truncated error terms):

$$\begin{aligned} & \mathbf{M} \left[\ddot{\mathbf{u}}_n + \dots + \frac{\mathbf{u}_n^{(p)}}{(p-2)!} \frac{W_{p+1,p-2}}{W_{p+1,0}} \right] + \mathbf{C} \left[\dot{\mathbf{u}}_n + \dots + \frac{\mathbf{u}_n^{(p)}}{(p-1)!} \frac{W_{p+1,p-1}}{W_{p+1,0}} \right] \\ & + \mathbf{K} \left[\mathbf{u}_n + \dots + \frac{\mathbf{u}_n^{(p)}}{p!} \frac{W_{p+1,p}}{W_{p+1,0}} \right] = \sum_{i=0}^{p+1} w_i \int_0^{\Delta t} \tau^i \mathbf{F} d\tau \end{aligned} \quad (31)$$

$$\begin{aligned} \mathbf{u}_{n+1} &= \mathbf{u}_n + \dot{\mathbf{u}}_n \Delta t + \ddot{\mathbf{u}}_n \frac{\Delta t^2}{2!} + \dots + \mathbf{u}_n^{(p)} \frac{\Delta t^p}{p!} \\ & \vdots \\ \mathbf{u}_{n+1}^{(p-1)} &= \mathbf{u}_n^{(p-1)} + \mathbf{u}_n^{(p)} \Delta t \end{aligned} \quad (32)$$

Equations (31-32) are the so-called family of single-step integration operators [SSInO] (see Table 1) in time described by Tamma et al. [4]. Elsewhere, analogous representations termed as the [SSpj] type appear in the literature [12, 13, 11].

5.2 On the Design of Generalized Integration Operators [GInO] for Non-linear Structural Dynamics

We next extend the previous developments to nonlinear situations (elasto-plastic, large deformation and total Lagrangian formulations are employed subsequently), where the equations of motion are expressed as (strong form) as:

$$\mathbf{M} \ddot{\mathbf{u}} + \mathbf{C} \dot{\mathbf{u}} + \mathbf{p}(\mathbf{u}) = \mathbf{f} \quad (33)$$

A concise implementation becomes a crucial aspect of the developments. Concise representation should include: i) consistent and systematic derivation of the weak form of the integrator for non-linear systems which truly represents the strong form at any time level t , ii) systematic and consistent treatment of linearization of the non-linear operator (*ad hoc* linearizations are avoided as the consequences for non-linear dynamic systems are not known and not predictable), iii) predictor multi-corrector representation which allows very simple explicit time-stepping schemes and sophisticated implicit time-stepping schemes using Newton-Raphson or "Newton-like" methods, iv) a convergence criterion within the non-linear iterations such that computations are robust and reliable as to preserving the accuracy and completion of the computation. To this end, first, it is necessary to identify different treatments in developing the weak form of the time discretized operators. In contrast to the linear case, the non-linear problem offers the two possibilities of putting the parameters of the integrator either inside or outside the non-linear operator $\mathbf{p}(\mathbf{u})$. It should be pointed out that putting the parameters inside the operator is more natural for a generalized unified framework of the time discretized operator as described in the sections to follow. In addition it overcomes most of the disadvantages of the methods with parameters outside the nonlinear operator. Some of the cited disadvantages of putting the parameters outside the nonlinear operators are: i) firstly no concise representation exists from the context of a generalized unified framework of the time discretized operators, though, a concise representation exists for the individual integrators, ii) unlike the more accurate evaluation of $\mathbf{p}(\mathbf{u})$ at some interior point $\hat{t} \in [t_n, t_{n+1}]$ using parameters inside the operator, employing parameters outside the operator such as: 1) $\mathbf{p}(\mathbf{u}_{n+\alpha}) \approx \alpha \mathbf{p}(\mathbf{u}_n) + (1-\alpha) \mathbf{p}(\mathbf{u}_{n+1})$ [14, 15] for α -methods and 2) $\mathbf{p}(\mathbf{u}_n + \theta_1 \dot{\mathbf{u}} \Delta t + \frac{1}{2} \theta_2 \mathbf{a}_n \Delta t^2) \approx \mathbf{p}(\mathbf{u}_n) + (\theta_1 \dot{\mathbf{u}} \Delta t + \frac{1}{2} \theta_2 \mathbf{a}_n \Delta t^2) \mathbf{p}'(\dot{\mathbf{u}}_n)$ [16] for SS22 methods,

and the like, are only first order accurate in $O(\Delta \mathbf{u})$ compared to the parameters inside the operator $\mathbf{p}(\mathbf{u})$, iii) other approximations may lead to costly computations such as multiple evaluations of $\mathbf{p}(\mathbf{u})$ in contrast to one evaluation of $\mathbf{p}(\mathbf{u})$, or additional matrix-vector multiplications in contrast to none for the concise representations in the computation of dynamical out-of-balance forces for every non-linear iteration at each time step leading to more memory requirements for large scale applications, and the like.

Due to the presence of non-linear term $\mathbf{p}(\mathbf{u})$ in Eq. 33, further simplifications need to be made. Let $\mathbf{p}(\mathbf{u}) = \mathbf{K}(\mathbf{u})\mathbf{u}$ where \mathbf{K} is the total stiffness matrix. Evaluating the stiffness matrix at $\bar{\mathbf{u}}$, assuming an arbitrary virtual field or weighted time field, $\mathbf{W}(t)$, for enacting the time discretization process, the above semi-discretized equation can be cast in the weighted residual form:

$$\int_{t_n}^{t_{n+1}} \mathbf{W}^T (\mathbf{M} \ddot{\mathbf{u}} + \mathbf{C} \dot{\mathbf{u}} + \mathbf{K}(\bar{\mathbf{u}})\mathbf{u} - \mathbf{f}) dt = 0 \quad (34)$$

where $\bar{\mathbf{u}}$ is a time weighted average of the displacement field. For the family of Generalized Integration Operator [GInO], we naturally have a scalar weighted time field, $W(t)$ as $W_{Asymp}(t)$, Eq. 20 (of interest here are second-order accuracy) and consistently approximate the dependent field variables \mathbf{u} , $\dot{\mathbf{u}}$ and $\ddot{\mathbf{u}}$ by employing an asymptotic series type expansion as, Eqs. 21 and the load is linearly interpolated. Substituting Eqs. 21 into Eq. 34 and for convenience, defining $W_i = \frac{W_{3,i}}{\Delta t W_{3,0}}$; $i = 1, 2, 3$ leads to a family of generalized integration operators [GInO] up to second-order accurate in time for the single-field form of the non-linear dynamic equations of motion and represented as:

$$\mathbf{M} \ddot{\mathbf{u}}_{n+1} + \mathbf{C} \dot{\mathbf{u}}_{n+1} + \mathbf{p}(\dot{\mathbf{u}}_{n+1}) = \hat{\mathbf{F}}_{n+1} \quad (35)$$

$$\text{where } \mathbf{u}_{n+1} = \mathbf{u}_n + \Lambda_1 W_1 \dot{\mathbf{u}}_n \Delta t + \Lambda_2 W_2 \ddot{\mathbf{u}}_n \Delta t^2 + \Lambda_3 W_3 \Delta \ddot{\mathbf{u}} \Delta t^2 \quad (36)$$

$$\dot{\mathbf{u}}_{n+1} = \dot{\mathbf{u}}_n + \Lambda_4 W_1 \ddot{\mathbf{u}}_n \Delta t + \Lambda_5 W_2 \Delta \ddot{\mathbf{u}} \Delta t \quad (37)$$

$$\ddot{\mathbf{u}}_{n+1} = \ddot{\mathbf{u}}_n + \Lambda_6 W_1 \Delta \ddot{\mathbf{u}} \quad (38)$$

$$\hat{\mathbf{F}}_{n+1} = (1 - W_1) \mathbf{f}_n + W_1 \mathbf{f}_{n+1} \quad (39)$$

Once $\ddot{\mathbf{u}}_{n+1}$ is found using the integrator Eq. 35, the displacement \mathbf{u}_{n+1} , velocity $\dot{\mathbf{u}}_{n+1}$ can be obtained from the proposed design for the updates Eqs. 26 – 27. Eqs. 35 – 39 and 26 – 27 encompass a unified family of [GInO] a -form representations for non-linear structural dynamics. The predictor multi-corrector formulations for the family of [GInO] for non-linear systems in incremental a -form, v -form, and d -form are developed and are obtained as shown in Tables 2 and 3 (all are equivalent but the number of iterations to convergence will vary).

5.2.1 Stability and accuracy analysis of [GInO] representations

The stability and accuracy of the existing developments is not hampered for the various forms. In addition, we also wish to show that all the predictor multi-corrector representations ([GInO]_{ALGO:A1}, [GInO]_{ALGO:V1}, [GInO]_{ALGO:V2}, [GInO]_{ALGO:D1} and [GInO]_{ALGO:D2}) are equivalent in terms of the order of accuracy in time and stability as illustrated in the examples to follow.

Bilinear softening spring: This example is used to investigate the stability of the algorithms using energy bounds. It is chosen here to investigate the stability of algorithms when

stiffness jumps occur and causes the accumulation of strain energy. The free vibration with an initial velocity $\dot{u}_0 = 25$ and the nodal internal force $p(u, t)$ is described by Fig. 1a. The results are shown in Fig. 1. For $\rho_\infty = 0.9466$ (\approx close to 1) for the $\text{GInO}_{\text{Generalized-}\alpha}$, it closely tends to the $\text{GInO}_{\text{midpoint}}$ rule a -form and the $\text{GInO}_{\text{SS22}}$ $\theta_1 = 1/2, \theta_2 = 1/2$ which is also spectrally similar and hence it is not surprising that they almost conserve energy ($E_n/E_0 \approx 1$) over the time for this selection of parameters.

Hardening spring: This example is used to investigate the accuracy of the [GInO] family of representations. The hardening spring problem is described in Fig. 1a. which is an undamped free vibration with an initial displacement $u_0 = 0.2$. Employing the predictor multi-corrector [GInO] representations with the respective [DNA] markers corresponding to the above mentioned methods and with one and two multi-corrector non-linear iterations within each time step, the relative error is plotted against the $\Delta t/T$ as shown in Fig. 1 for $[\text{GInO}]_{\text{ALGO:A1}}$, $[\text{GInO}]_{\text{ALGO:V1}}$, $[\text{GInO}]_{\text{ALGO:V2}}$, $[\text{GInO}]_{\text{ALGO:D1}}$ and $[\text{GInO}]_{\text{ALGO:D2}}$ respectively. Also it is clear that incremental a -form, incremental v -form and incremental d -form are identical.

5.2.2 Single d.o.f numerical results

Analysis of non-linear dynamic systems are illustrated by comparing results of the non-linear implementation as described in the literature of a fairly simple non-linear equation of motion, namely, the so-called Duffing equation. We take the initial conditions $\dot{u}_0 = 0$ with $u_0 = 0.1 (T = 0.61)$ and $u_0 = 1.5 (T = 0.15)$ to yield two cases of increasing degree of non-linearities. From the literature we consider two implementations, namely one due to Wood and Oduor [16] and another due to Kuhl and Crisfield [15]. From the former we compare the results of SS22 ($\theta_1 = 1/2, \theta_2 = 1/2$) with $\hat{u}_n = u_n, (u_n + u_{n+1})/2$ and $\hat{u}_n = u_{n+1}$ linearization approximations with the results obtained employing the present $\text{GInO}_{\text{SS22}}$ predictor multi-corrector representations. From the latter, results of the Generalized- α methods with parameters outside the non-linear operator $p(u)$ for $\rho_\infty = 1$ and 0.9 are compared with the results obtained employing the present $\text{GInO}_{\text{Generalized-}\alpha}$ predictor multi-corrector representations. Note that the Generalized- α methods with $\rho_\infty = 1$ is the a -form of Mid-point rule ($\alpha_m = \alpha_f = 2\beta = \gamma = 1/2$) [15]. It should also be noted that for linear situations, this a -form of the mid-point rule and the classical d -form mid-point rule are different, and are spectrally identical to each other under only certain conditions. Note that unlike the results of SS22 in Ref. [16], the present results of $\text{GInO}_{\text{SS22}}$ are stable (bounded) and are undamped for both $u_0 = 0.1$ and $u_0 = 1.5$ initial conditions (Fig. 1a and 1b). For both $u_0 = 0.1$ and $u_0 = 1.5$ initial condition problems, it can be shown that for the entire range of time steps size $0 < \Delta t/T \leq 1$ the $\text{GInO}_{\text{SS22}}$ predictor multi-corrector representations gives stable and undamped results.

The displacements plots Figs. 3a– 3b indicate that the Generalized- α representation due to [15] has period contraction. Energy plots Figs. 3c– 3d indicates that the Generalized- α representation due to [15] slightly over estimates the energy ($E_n/E_0 \geq 1$) compared to the Energy estimation ($E_n/E_0 \leq 1$) of the present GInO predictor multi-corrector representations pertaining to the $[\text{GInO}]_{\text{Generalized-}\alpha}$ representations. Again, it can be shown that all the present three incremental predictor multi-corrector representations (a -form, v -form and d -form) give identical results with parameters inside which is natural to the present developments and is recommended here.

5.2.3 Illustrative examples

From considerations of a unified framework, the predictor multi-corrector [GInO] representations for non-linear systems described in the previous sections which encompass a wide variety of algorithms have been implemented in a single analysis code termed DINOSAURUS [Dynamic INtegration Operators for Structural Analysis Using Robust Unified Schemes]. In this section, the results are presented using a single analysis code for an example problem to verify the unified family of [GInO] formulations as applied to non-linear structural dynamics problems. Also, we investigate the effect of dissipative properties of typical dissipative time integration schemes such as the θ_1 -method, the H-H-T- α , the Newmark-Bossak method and the Generalized- α emanating from the [GInO] representations on the dynamic response. Results of these methods are compared with the traditional Newmark integration method ($\gamma = 1/2, \beta = 1/4$) which does not inherit dissipative properties. In the results presented for the dissipative schemes, the dissipative parameters are chosen such that the $\rho_\infty = 0.9466$ as described before. The cylindrical panel described in Fig. 4a and Fig. 4b, is a somewhat involved example taken from [17], and the calculated predictions employing a four-noded degenerated shell element formulation are compared with available experimental results. For details of material properties, refer [17]. Figure 4 shows the comparative results and Table 4 shows the percentage decrease in the number of non-linear iterations for various methods for given predictor multi-corrector [GInO] representations.

5.3 Type 3-[GInO]_{Two-Field}: Two-Field Form

The family of Type 3-[GInO]_{Two-Field} encompassing the premise of both double and single time weighted philosophy and representations are highlighted in this section.

Double Weighted Time Fields Representation of Type 3-[GInO]_{Two-Field}

In the double weighted time field formulation, two different weighted time fields are chosen for the two equations in the two-field form, which are represented as

$$\tilde{W} = \begin{pmatrix} W \\ \hat{W} \end{pmatrix} = \begin{pmatrix} 1 + w_1\Gamma + \dots + w_{p+1}\Gamma^{p+1} \\ 1 + \hat{w}_1\Gamma + \dots + \hat{w}_{p+1}\Gamma^{p+1} \end{pmatrix} \quad (40)$$

and the dependent variable fields are now consistently approximated as

$$\begin{aligned} \mathbf{u}_{Asymp} &= \mathbf{u}_n + \Lambda_1 \dot{\mathbf{u}}_n \bar{\tau} + \Lambda_2 \ddot{\mathbf{u}}_n \bar{\tau}^2 + \dots + \Lambda_p \mathbf{u}_n^{(p)} \bar{\tau}^p + \Lambda_{p+1} \bar{\tau}^{p+1} \Delta \mathbf{u}_{n+1}^{(p)} / \Delta t \\ \dot{\mathbf{u}}_{Asymp} &= \dot{\mathbf{u}}_n + \Lambda_{p+2} \ddot{\mathbf{u}}_n \bar{\tau} + \dots + \Lambda_{2p} \mathbf{u}_n^{(p)} \bar{\tau}^{p-1} + \Lambda_{2p+1} \bar{\tau}^p \Delta \mathbf{u}_{n+1}^{(p)} / \Delta t \end{aligned} \quad (41)$$

$$\begin{aligned} \mathbf{v}_{Asymp} &= \mathbf{v}_n + \Psi_1 \dot{\mathbf{v}}_n \bar{\tau} + \Psi_2 \ddot{\mathbf{v}}_n \bar{\tau}^2 + \dots + \Psi_p \mathbf{v}_n^{(p)} \bar{\tau}^p + \Psi_{p+1} \bar{\tau}^{p+1} \Delta \mathbf{v}_{n+1}^{(p)} / \Delta t \\ \dot{\mathbf{v}}_{Asymp} &= \dot{\mathbf{v}}_n + \Psi_{p+2} \ddot{\mathbf{v}}_n \bar{\tau} + \dots + \Psi_{2p} \mathbf{v}_n^{(p)} \bar{\tau}^{p-1} + \Psi_{2p+1} \bar{\tau}^p \Delta \mathbf{v}_{n+1}^{(p)} / \Delta t \end{aligned} \quad (42)$$

We also impose the relation between displacement and velocity back to the two-field form as

$$\dot{\mathbf{u}}_n = \mathbf{v}_n, \ddot{\mathbf{u}}_n = \dot{\mathbf{v}}_n = \mathbf{M}^{-1} (\mathbf{F}_n - \mathbf{C}\mathbf{v}_n - \mathbf{K}\mathbf{u}_n), \ddot{\mathbf{u}}_n = \dot{\mathbf{v}}_n, \dots, \mathbf{u}_n^{(p)} = \mathbf{v}_n^{(p-1)} \quad (43)$$

to yield the resulting [GInO]_{Two-Field} for the double time weighted field representations as:

$$\Lambda_{p+2}W_1\ddot{\mathbf{u}}_n + \dots + \Lambda_{2p+1}W_p\Delta\mathbf{u}_{n+1}^{(p)}\Delta t^{p-2} = \Psi_1W_1\dot{\mathbf{v}}_n + \dots + \Psi_{p+1}W_{p+1}\Delta\mathbf{v}_{n+1}^{(p)}\Delta t^{p-1} \quad (44)$$

$$\mathbf{M} \left[\dot{\mathbf{v}}_n + \dots + \Psi_{2p+1}\dot{W}_p\Delta\mathbf{v}_{n+1}^{(p)}\Delta t^{p-1} \right] + \mathbf{C} \left[\mathbf{v}_n + \dots + \Psi_{p+1}\dot{W}_{p+1}\Delta\mathbf{v}_{n+1}^{(p)}\Delta t^p \right] + \mathbf{K} \left[\mathbf{u}_n + \dots + \Lambda_{p+1}\dot{W}_{p+1}\Delta\mathbf{u}_{n+1}^{(p)}\Delta t^p \right] = \mathbf{F}_n + \dots + \dot{W}_{p-1}\mathbf{F}_n^{(p-1)}\Delta t^{p-1} \quad (45)$$

$$\mathbf{u}_{n+1} = \mathbf{u}_n + \lambda_1\dot{\mathbf{u}}_n\Delta t + \lambda_2\ddot{\mathbf{u}}_n\Delta t^2 + \dots + \lambda_p\mathbf{u}_n^{(p)}\Delta t^p + \lambda_{p+1}\Delta t^p\Delta\mathbf{u}_{n+1}^{(p)} \quad (46)$$

$$\dot{\mathbf{u}}_{n+1} = \mathbf{v}_{n+1} = \mathbf{v}_n = \dot{\mathbf{v}}_n\Delta t + \psi_2\ddot{\mathbf{v}}_n\Delta t^2 + \dots + \psi_p\mathbf{v}_n^{(p)}\Delta t^p + \psi_{p+1}\Delta t^p\Delta\mathbf{v}_{n+1}^{(p)} \quad (47)$$

$$\ddot{\mathbf{u}}_{n+1} = \dot{\mathbf{v}}_{n+1} = \mathbf{M}^{-1}(\mathbf{F}_{n+1} - \mathbf{C}\mathbf{v}_{n+1} - \mathbf{K}\mathbf{u}_{n+1}) \quad (48)$$

$$\vdots \quad (49)$$

$$\mathbf{u}_{n+1}^{(p)} = \mathbf{v}_{n+1}^{(p-1)} = \mathbf{v}_n^{(p-1)} + \psi_{\frac{p(p+3)}{2}-1}\mathbf{v}_n^{(p)}\Delta t + \psi_{\frac{p(p+3)}{2}}\Delta t\Delta\mathbf{v}_{n+1}^{(p)} \quad (50)$$

For illustration, the recovery of a variety of explicit methods is highlighted in Table 5 via [DNA] markers.

Single Weighted Time Field Representation of [GInO]_{Two-Field}: In contrast, employing a single time weighted philosophy, we have:

$$W = 1 + w_1\Gamma + \dots + w_p\Gamma^p + w_{p+1}\Gamma^{p+1} \quad (51)$$

$$\mathbf{d} = \mathbf{d}_n + \Lambda_1\dot{\mathbf{d}}_n\bar{\tau} + \dots + \Lambda_p\mathbf{d}_n^{(p)}\bar{\tau}^p + \Lambda_{p+1}\Delta\mathbf{d}_{n+1}^{(p)}\bar{\tau}^{p+1}/\Delta t \quad (52)$$

$$\dot{\mathbf{d}} = \dot{\mathbf{d}}_n + \Lambda_{p+2}\ddot{\mathbf{d}}_n\bar{\tau} + \dots + \Lambda_{2p}\mathbf{d}_n^{(p)}\bar{\tau}^{p-1} + \Lambda_{2p+1}\Delta\mathbf{d}_{n+1}^{(p)}\bar{\tau}^p/\Delta t \quad (53)$$

This leads to the family of time integrators [GInO]_{Two-Field} for the single time weighted representation of the two-field form as:

$$\dot{\mathbf{d}}_n + \Lambda_{p+2}W_1\ddot{\mathbf{d}}_n\Delta t + \dots + \Lambda_{2p+1}W_p\Delta\mathbf{d}_{n+1}^{(p)}\Delta t^{p-1} \quad (54)$$

$$\mathbf{A} \left[\mathbf{d}_n + \dots + \Lambda_{p+1}W_{p+1}\Delta\mathbf{d}_{n+1}^{(p)}\Delta t^p \right] = \mathbf{F}_n + \dots + W_{p-1}\mathbf{F}_n^{(p-1)}\Delta t^{p-1} \quad (55)$$

$$\mathbf{d}_{n+1} = \mathbf{d}_n + \lambda_1\dot{\mathbf{d}}_n\Delta t + \dots + \lambda_p\mathbf{d}_n^{(p)}\Delta t^p + \lambda_{p+1}\Delta\mathbf{d}_{n+1}^{(p)}\Delta t^p \quad (56)$$

$$\vdots$$

$$\mathbf{d}_{n+1}^{(p-1)} = \mathbf{d}_n^{(p-1)} + \lambda_{\frac{p(p+1)}{2}-1}\mathbf{d}_n^{(p)}\Delta t + \lambda_{\frac{p(p+1)}{2}}\Delta\mathbf{d}_{n+1}^{(p)}\Delta t \quad (57)$$

Equations (55-57) represent a family of [GInO]_{Two-Field} single time weighted philosophy of development. For illustration, the second-order accurate, unconditionally stable, implicit Park's method [20] with $p = 3$ pertains to this category (see Table 6). Also see Table 7 for general implementation aspects for illustration.

6 Concluding Remarks

Recent advances highlighting design of time discretized operators for structural dynamics with respect to computational algorithms and their DNA markers emanating from a generalized time weighted philosophy were described via a unified framework. For illustration, of the various Type 1, 2 and 3 classifications, emphasis was placed on applicability of a specific

Type 3 classification for general non-linear /linear dynamic problems. Under the umbrella of a unified framework, the generalized integration operators [GInO] not only provide new avenues which have to date not been exploited and/or explored (see Ref. [3] for details), but also recover a wide variety of existing dissipative/non-dissipative algorithms whose design and implementation aspects were fully detailed. Based on a summary of the overall developments presented here and more recent developments described elsewhere [3] as related to Type 3 classification of time discretized operators, a desirable algorithm pertaining to this classification for structural dynamics must inherit the following characteristic features: **Stability:** Unconditional stability required, **Accuracy:** At least second-order in time accuracy, **Algorithmic properties:** No more than zero-order displacement and velocity overshoot behavior with minimal dissipation and dispersion, and with controllable algorithmic dissipative features, **Computational performance:** Self starting features with no more than one set of single-field system of implicit equations to be solved at each time step to include ease of implementation and computational simplicity. Other design and applicability guidelines for the various classifications are currently being investigated. We hope to disseminate these and other new developments of our ongoing quest for general design of computational algorithms for structural dynamics in the near future.

Acknowledgments

The authors are very pleased to acknowledge support in part by Battelle/U. S. Army Research Office (ARO) Research Triangle Park, North Carolina, under grant number DAAH04-96-C-0086, and by the Army High Performance Computing Research Center (AHPCRC) under the auspices of the Department of the Army, Army Research Laboratory (ARL) cooperative agreement number DAAH04-95-2-0003/contract number DAAH04-95-C-0008. The content does not necessarily reflect the position or the policy of the government, and no official endorsement should be inferred. Support in part by Dr. Andrew Mark of the Integrated Modeling and Testing (IMT) Computational Technical Activity and the ARL/MSRC facilities is also gratefully acknowledged. Special thanks are due to the CIC Directorate at the U.S. Army Research Laboratory (ARL), Aberdeen Proving Ground, Maryland. Other related support in form of computer grants from the Minnesota Supercomputer Institute (MSI), Minneapolis, Minnesota is also gratefully acknowledged.

References

- [1] K. K. Tamma, X. Zhou, and D. Sha. A Theory of Development and Design of Generalized Integration Operators for Computational Structural Dynamics. *International Journal for Numerical Methods in Engineering (to appear)*, 2000.
- [2] K. K. Tamma, X. Zhou, and D. Sha. The Time Dimension: A Theory of Development/Evolution, Classification, Characterization and Design of Computational Algorithms for Transient/Dynamic Applications. *Archives Comput. Methods Engr.*, June 2000.
- [3] X. Zhou, K. Tamma, R. Kanapady, and D. Sha. The Time Dimension: New and Recent Advances and a Unified Framework Towards Design of Time Discretized Operators for Structural Dynamics. In *7th European Congress on Computational Methods in Applied Sciences and Engineering, ECCOMAS 2000*, Barcelona, Spain, 11-14 September 2000.

-
- [4] K. K. Tamma, X. Zhou, and R. Valasutean. Computational Algorithms for Transient Analysis: The Burden of Weight and Consequences Towards Formalizing Discrete Numerically Assigned [DNA] Algorithmic Markers: Wp-Family. *Computer Methods in Applied Mechanics and Engineering*, 149:153, 1997.
- [5] T. C. Fung. A Precise Time-Step Integration Method by Step-Response and Impulsive-Response Matrices for Dynamic Problems. *International Journal for Numerical Methods in Engineering*, 40:4501, 1997.
- [6] T. C. Fung. Complex-Time-Step Newmark Methods with Controllable Numerical Dissipation. *International Journal for Numerical Methods in Engineering*, 41:65, 1998.
- [7] G. M. Hulbert. A Unified Set of Single-Step Asymptotic Annihilation Algorithms for Structural Dynamics. *Comput. Methods Appl. Mech. Engrg.*, 113:1–9, 1994.
- [8] M. Gellert. A New Algorithm for Integration of Dynamic System. *Comput. Struct.*, 9:401–408, 1978.
- [9] N. Tarnow and J. C. Simo. How to Render Second-Order Accurate Time Stepping Algorithms Fourth-Order Accurate While Remaining the Stability and Conservation Properties. *Computer Methods in Applied Mechanics and Engineering*, 115:233, 1994.
- [10] D. Sha, K. K. Tamma, and X. Zhou. Time Discretized Operators: Towards the Theoretical Design of a New Generation of Implicit and Explicit Representations of Time Operators for Structural Dynamics: Part 2. *Computer Methods in Applied Mechanics and Engineering (to appear)*, 2000.
- [11] O. C. Zienkiewicz and R. L. Taylor. *The Finite Element Method*, volume 1. McGraw-Hill, New York, 1994.
- [12] O. C. Zienkiewicz. A New Look at Newmark, Houbolt and Other Time Stepping Formulas: A Weighted Residual Approach. *Earthquake Engineering and Structural Dynamics*, 5:283, 1977.
- [13] O. C. Zienkiewicz, W. L. Wood, N. W. Hine, and R. L. Taylor. A Unified Set of Single-Step Algorithms, Part 1: General Formulations and Applications. *International Journal for Numerical Methods in Engineering*, 20:1529, 1984.
- [14] C. Hoff, T.J.R. Hughes, G. Hulbert, and P.J. Phal. Extended Comparison of the Hilber-Hughes-Taylor α -Method and the Θ_1 -method. *Comput. Methods Appl. Mech. Engrg.*, 76:87–93, 1989.
- [15] D. Kuhl and M. A. Crisfield. Energy-Conserving and Decaying Algorithms in Non-linear Structural Dynamics. *Int. J. Numer. Methods Engrg.*, 45:569–599, 1999.
- [16] W. L. Wood and M. E. Oduor. Stability Properties of Some Algorithms for The Solution of Nonlinear Dynamic Vibration Equations. *Commun. Numer. Methods Engrg.*, 4:205–212, 1988.
- [17] L. Mornio, J. W. Leech., and E. A. Witmer. An Improved Numerical Calculation Technique for Large Elastic-Plastic Transient Deformations of Thin Shells Part 2–Evaluation and Applications. *J. Applied Mechanics*, pages 429–436, June 1971.
- [18] J. Kujawski and R. H. Gallagher. A Family of Higher-Order Explicit Algorithms for the Transient Dynamic Analysis. *Trans. Soc. Comp. Simulation*, 1:155, 1984.

-
- [19] C. Hoff and R. L. Taylor. Higher Derivative Explicit One Step Methods For Non-Linear Dynamic Problems. Part I: Design and Theory. *International Journal for Numerical Methods in Engineering*, 29:275, 1990.
- [20] K. C. Park. An Improved Stiffly Stable Method for Direct Integration of Nonlinear Structural Dynamic Equations. *Transactions of the American Society of Mechanical Engineers*, 1:464, 1975.

Algo	w_1	w_2	w_3	Λ_1, λ_1	Λ_2, λ_2	Λ_3, λ_3	Λ_4, λ_4	Λ_5, λ_5	Λ_6
Type 3 [GlnO] _{single-field} sub-type 1 time discretized operators									
1	$-\frac{15(2p-1)}{4p-1}$	$\frac{15(4p-3)}{4p-1}$	$-\frac{35(p-1)}{4p-1}$	1	$\frac{p}{2(1+p)}$	$\frac{1}{(1+p)(1+p^2)}$	$\frac{p}{2(1+p)}$	$\frac{1}{1+p^2}$	$\frac{2}{1+p^2}$
2	$-\frac{15(-2+20p-45p^2+28p^3)}{-4+30p-60p^2+35p^3}$	$-\frac{15(-4+45p-108p^2+70p^3)}{-4+30p-60p^2+35p^3}$	$-\frac{35(-1+12p-30p^2+20p^3)}{-4+30p-60p^2+35p^3}$	1	$\frac{1}{2}$	$\frac{1}{6}$	1	$\frac{1}{2}$	1
3	$-\frac{15(1+3\alpha)}{1+5\alpha}$	$\frac{15(3+7\alpha)}{1+5\alpha}$	$-\frac{35(1+2\alpha)}{1+5\alpha}$	1	$\frac{1}{2}$	$\frac{1}{4}(1-\alpha)^2$	1	$\frac{1}{2}-\alpha$	$\frac{1}{1+\alpha}$
4	-15	45	-35	1	$\frac{1}{2}$	$\frac{1}{4}(1-\alpha\beta)^2$	1	$\frac{1}{2}-\alpha\beta$	$1-\alpha\beta$
5	$\frac{15(-20+\frac{19}{\Theta_1})}{(-30+\frac{19}{\Theta_1})}$	$\frac{45(-15+\frac{14}{\Theta_1})}{(-30+\frac{14}{\Theta_1})}$	$\frac{35(-12+\frac{11}{\Theta_1})}{(-30+\frac{11}{\Theta_1})}$	1	$\frac{1}{2}$	$\frac{1}{4\Theta_1^2}$	1	$\frac{3}{2}-\Theta_1$	$\frac{1}{\Theta_1}$
6	$-\frac{15(1-3\alpha f)}{(1-5\alpha f)}$	$\frac{15(3-7\alpha f)}{(1-5\alpha f)}$	$-\frac{35(1-2\alpha f)}{(1-5\alpha f)}$	1	$\frac{1}{2}$	$\frac{(1-\alpha_m+\alpha f)^2}{4}$	1	$\frac{1}{2}-\alpha_m+\alpha f$	$\frac{1-\alpha_m}{1-\alpha f}$
Type 3 [GlnO] _{single-field} sub-type 2 time discretized operators									
7	-15	45	-35	1	$\frac{1}{2}$	$\frac{1}{12}$	1	$\frac{1}{2}$	1
8	-15	45	-35	1	$\frac{1}{2}$	0	1	$\frac{1}{2}$	1
9	-15	45	-35	1	$\frac{1}{2}$	$\frac{1}{4}$	1	$\frac{1}{2}$	1
10	-15	45	-35	1	$\frac{1}{2}$	$\frac{1}{6}$	1	$\frac{1}{2}$	1
Type 3 [GlnO] _{single-field} sub-type 3 time discretized operators $W_p, p=2$									
11	-6	7.5			1	$\frac{1}{2}$	1		
12	-5	5			1	$\frac{1}{2}$	1		
13	0	0			1	$\frac{1}{2}$	1		
14	$-\frac{15}{2}$	$\frac{15}{2}$			1	$\frac{1}{2}$	1		
15	$-\frac{20}{3}$	$\frac{20}{3}$			1	$\frac{1}{2}$	1		
Type 3 [GlnO] _{single-field} sub-type 3 time discretized operators $W_p, p=3$									
16	$-\frac{615}{4629}$	$\frac{825}{4925}$	$-\frac{1155}{4465}$	1	$\frac{1}{2}$	$\frac{1}{6}$	1	$\frac{1}{2}$	1
17	$-\frac{137}{180}$	$\frac{137}{180}$	$-\frac{437}{350}$	1	$\frac{1}{2}$	$\frac{1}{6}$	1	$\frac{1}{2}$	1
18	$-\frac{4478}{3229}$	$\frac{126830}{3229}$	$-\frac{85530}{3229}$	1	$\frac{1}{2}$	$\frac{1}{6}$	1	$\frac{1}{2}$	1
19	$-\frac{3729}{103}$	$\frac{3229}{103}$	$-\frac{3229}{103}$	1	$\frac{1}{2}$	$\frac{1}{6}$	1	$\frac{1}{2}$	1
20	$-\frac{103}{103}$	$\frac{103}{103}$	$-\frac{103}{103}$	1	$\frac{1}{2}$	$\frac{1}{6}$	1	$\frac{1}{2}$	1

Table 1: [DNA] markers: weighted time fields for family of Type 3 [GlnO]_{single-field} sub-type 1, sub-type 2 and sub-type 3 time discretized operators. Algorithms are 1) ρ -method, 2) Wilson- θ , 3) HHT- α , 4) WBZ, 5) θ_1 -method 6) Generalized- α 7),14 Fox-Goodwin, 8),15) Central difference, 9),12) Newmark (average acceleration), 10),13) Linear acceleration, 11) SS22 $\Theta_1 = 3/4, \Theta_2 = 2/3$, 16) Houbolt, 17) Wilson- θ $\theta = 1.14$, 18) WBZ $\alpha_B = 0.5$, 19) HHT $\alpha_H = -0.1$, $\beta_H = 0.3025$, 20) SS32, $\Theta_1 = 2/3, \Theta_2 = 3/2$. Note: $w_0 = 1$ for all the above methods.

α -form [GlnO] _{ALGO-A1}	v -form [GlnO] _{ALGO-V1}	d -form [GlnO] _{ALGO-D1}
<i>At the start of time step</i>		
$\hat{u}_{n+1}^j = u_n + \Lambda_1 W_1 \dot{u}_n \Delta t + \Lambda_2 W_2 \ddot{u}_n \Delta t^2$	<i>Predict the state vectors employing</i>	
$\hat{u}_{n+1}^j = \dot{u}_n + \Lambda_4 W_1 \ddot{u}_n \Delta t$	$\hat{u}_{n+1}^j = u_n + \Lambda_1 W_1 \dot{u}_n \Delta t + (\Lambda_2 W_2 - \frac{\Lambda_3 \Lambda_1 W_3}{\lambda_3}) \ddot{u}_n \Delta t^2$	$\hat{u}_{n+1}^j = u_n + (\Lambda_1 W_1 - \frac{\Lambda_3 \Lambda_1 W_3}{\lambda_3}) \dot{u}_n \Delta t + (\Lambda_2 W_2 - \frac{\Lambda_3 W_2 \Delta_2}{\lambda_3}) \ddot{u}_n \Delta t^2$
$\hat{u}_{n+1}^j = \ddot{u}_n$	$\hat{u}_{n+1}^j = \dot{u}_n + (\Lambda_4 W_1 - \frac{\Lambda_5 W_2 \Delta_4}{\lambda_5}) \ddot{u}_n \Delta t$	$\hat{u}_{n+1}^j = (1 - \frac{\Lambda_5 \Delta_4 W_1}{\lambda_5}) \ddot{u}_n$
<i>Satisfy equilibrium in a loop over multi-corrector iterations</i>		
Solve $\overline{M} \Delta \hat{u}_{n+1}^{j+1} = \overline{F}$	Solve $\overline{C} \Delta \hat{u}_{n+1}^{j+1} = \overline{F}$	Solve $\overline{K} \Delta \hat{u}_{n+1}^{j+1} = \overline{F}$
where		
$\overline{M} = [\Lambda_6 W_1 M + \Lambda_5 W_2 \Delta t C + \Lambda_3 W_3 \Delta t^2 K_t]$	$\overline{C} = [\frac{\Lambda_6 W_1}{\lambda_5 \Delta t} M + \frac{\Lambda_5 W_2}{\lambda_5} C + \frac{\Lambda_3 W_3 \Delta t}{\lambda_5} K_t]$	$\overline{K} = [\frac{\Lambda_6 W_1}{\lambda_3 \Delta t^2} M + \frac{\Lambda_5 W_2}{\lambda_3 \Delta t} C + \frac{\Lambda_3 W_3}{\lambda_3} K_t]$
$\overline{F} = \hat{F}_{n+1} - M \ddot{u}_{n+1}^j - C \dot{u}_{n+1}^j - p(\hat{u}_{n+1}^j)$	$\overline{F} = \hat{F}_{n+1} - M \ddot{u}_{n+1}^j - C \dot{u}_{n+1}^j - p(\hat{u}_{n+1}^j)$	$\overline{F} = \hat{F}_{n+1} - M \ddot{u}_{n+1}^j - C \dot{u}_{n+1}^j - p(\hat{u}_{n+1}^j)$
$\hat{u}_{n+1}^{j+1} = \hat{u}_{n+1}^j + \Lambda_3 W_3 \Delta \hat{u}_{n+1}^{j+1} \Delta t^2$	$\hat{u}_{n+1}^{j+1} = \hat{u}_{n+1}^j + \Lambda_3 W_3 \Delta \hat{u}_{n+1}^{j+1} \Delta t$	$\hat{u}_{n+1}^{j+1} = \hat{u}_{n+1}^j + \Lambda_3 W_3 \Delta \hat{u}_{n+1}^{j+1}$
$\hat{u}_{n+1}^{j+1} = \dot{u}_{n+1}^j + \Lambda_5 W_2 \Delta \hat{u}_{n+1}^{j+1} \Delta t$	$\hat{u}_{n+1}^{j+1} = \dot{u}_{n+1}^j + \Lambda_5 W_2 \Delta \hat{u}_{n+1}^{j+1}$	$\hat{u}_{n+1}^{j+1} = \dot{u}_{n+1}^j + \Lambda_5 W_2 \Delta \hat{u}_{n+1}^{j+1}$
$\hat{u}_{n+1}^{j+1} = \ddot{u}_{n+1}^j + \Lambda_6 W_1 \Delta \hat{u}_{n+1}^{j+1}$	$\hat{u}_{n+1}^{j+1} = \ddot{u}_{n+1}^j + \Lambda_6 W_1 \Delta \hat{u}_{n+1}^{j+1}$	$\hat{u}_{n+1}^{j+1} = \ddot{u}_{n+1}^j + \Lambda_6 W_1 \Delta \hat{u}_{n+1}^{j+1}$
$\ \Delta \ddot{u}\ _2 / \ \hat{u}_{n+1}\ _2 \leq \epsilon$ or $\ \overline{F}_{n+1}\ _2 / \ \hat{u}_{n+1}\ _2 \leq \epsilon$	$\ \Delta \dot{u}\ _2 / \ \hat{u}_{n+1}\ _2 \leq \epsilon$ or $\ \overline{F}_{n+1}\ _2 / \ \hat{u}_{n+1}\ _2 \leq \epsilon$	$\ \Delta u\ _2 / \ \hat{u}_{n+1}\ _2 \leq \epsilon$ or $\ \overline{F}_{n+1}\ _2 / \ \hat{u}_{n+1}\ _2 \leq \epsilon$
<i>Design updates at end of time step</i>		
	$\hat{u}_{n+1} = \hat{u}_n + (\hat{u}_{n+1} - \hat{u}_n) / \Lambda_6 W_1$	
	$\dot{u}_{n+1} = \dot{u}_n + \lambda_4 \ddot{u}_n \Delta t + \lambda_5 (\ddot{u}_{n+1} - \ddot{u}_n) \Delta t$	
	$u_{n+1} = u_n + \lambda_1 \dot{u}_n \Delta t + \lambda_2 \ddot{u}_n \Delta t^2 + \lambda_3 (\ddot{u}_{n+1} - \ddot{u}_n) \Delta t^2$	

Table 2: Predictor multi-corrector true incremental α -form, v -form and d -form of [GlnO]_{Single-Field} representations for non-linear dynamic systems.

a -form: $[\text{GInO}]_{\text{ALGO:A1}}$	v -form $[\text{GInO}]_{\text{ALGO:V2}}$	d -form $[\text{GInO}]_{\text{ALGO:D2}}$
<i>At the start of time step</i>		
$\hat{u}_{n+1}^j = u_n + \Lambda_1 W_1 \dot{u}_n \Delta t + \Lambda_2 W_2 \ddot{u}_n \Delta t^2$	<i>Predict the state vectors employing</i>	
$\hat{u}_{n+1}^j = \dot{u}_n + \Lambda_4 W_1 \ddot{u}_n \Delta t$	$\hat{u}_{n+1}^j = u_n + \Lambda_1 W_1 \dot{u}_n \Delta t + (\Lambda_2 W_2 - \frac{\Lambda_3 \Lambda_4 W_1 W_3}{\Lambda_5 W_2}) \ddot{u}_n \Delta t^2$	$\hat{u}_{n+1}^j = u_n$
$\hat{u}_{n+1}^j = \ddot{u}_n$	$\hat{u}_{n+1}^j = \dot{u}_n$	$\hat{u}_{n+1}^j = \left(1 - \frac{\Lambda_3 \Lambda_4 W_1 W_2}{\Lambda_5 W_3}\right) \ddot{u}_n + \left(\Lambda_4 W_1 - \frac{\Lambda_3 \Lambda_4 W_1 W_2}{\Lambda_5 W_3}\right) \ddot{u}_n \Delta t$
<i>Satisfy equilibrium in a loop over multi-corrector iterations</i>		
Solve $\bar{M} \Delta \hat{u}_{n+1}^{j+1} = \bar{F}$ where	Solve $\bar{C} \Delta \hat{u}_{n+1}^{j+1} = \bar{F}$	Solve $\bar{K} \Delta \hat{u}_{n+1}^{j+1} = \bar{F}$
$\bar{M} = [\Lambda_6 W_1 M + \Lambda_5 W_2 \Delta t C + \Lambda_3 W_3 \Delta t^2 K_t]$	$\bar{C} = [\frac{\Lambda_6 W_1}{\Lambda_3 W_2 \Delta t} M + C + \frac{\Lambda_3 W_3 \Delta t}{\Lambda_5 W_2} K_t]$	$\bar{K} = [\frac{\Lambda_6 W_1}{\Lambda_3 W_3 \Delta t^2} M + \frac{\Lambda_3 W_3}{\Lambda_5 W_2 \Delta t} C + K_t]$
$\bar{F} = \hat{F}_{n+1} - M \ddot{u}_{n+1}^j - C \hat{u}_{n+1}^j - p(\hat{u}_{n+1}^j)$	$\bar{F} = \hat{F}_{n+1} - M \ddot{u}_{n+1}^j - C \hat{u}_{n+1}^j - p(\hat{u}_{n+1}^j)$	$\bar{F} = \hat{F}_{n+1} - M \ddot{u}_{n+1}^j - C \hat{u}_{n+1}^j - p(\hat{u}_{n+1}^j)$
$\hat{u}_{n+1}^{j+1} = \hat{u}_{n+1}^j + \Lambda_3 W_3 \Delta \hat{u}_{n+1}^{j+1} \Delta t^2$	$\hat{u}_{n+1}^{j+1} = \hat{u}_{n+1}^j + \frac{\Lambda_3 W_3}{\Lambda_5 W_2} \Delta \hat{u}_{n+1}^{j+1} \Delta t$	$\hat{u}_{n+1}^{j+1} = \hat{u}_{n+1}^j + \Delta \hat{u}_{n+1}^{j+1}$
$\hat{u}_{n+1}^{j+1} = \dot{u}_{n+1}^j + \Lambda_5 W_2 \Delta \hat{u}_{n+1}^{j+1} \Delta t$	$\hat{u}_{n+1}^{j+1} = \dot{u}_{n+1}^j \Delta \hat{u}_{n+1}^{j+1}$	$\hat{u}_{n+1}^{j+1} = \dot{u}_{n+1}^j + \frac{\Lambda_5 W_2}{\Lambda_3 W_3 \Delta t} \Delta \hat{u}_{n+1}^{j+1}$
$\hat{u}_{n+1}^{j+1} = \ddot{u}_{n+1}^j + \Lambda_6 W_1 \Delta \hat{u}_{n+1}^{j+1}$	$\hat{u}_{n+1}^{j+1} = \ddot{u}_{n+1}^j + \frac{\Lambda_6 W_1}{\Lambda_3 W_3 \Delta t^2} \Delta \hat{u}_{n+1}^{j+1}$	$\hat{u}_{n+1}^{j+1} = \ddot{u}_{n+1}^j + \frac{\Lambda_6 W_1}{\Lambda_3 W_3 \Delta t^2} \Delta \hat{u}_{n+1}^{j+1}$
$\ \Delta \hat{u}\ _2 / \ \hat{u}_{n+1}\ _2 \leq \epsilon$ or $\ \bar{F}_{n+1}\ _2 / \ \hat{f}_{n+1}\ _2 \leq \epsilon$	$\ \Delta \hat{u}\ _2 / \ \hat{u}_{n+1}\ _2 \leq \epsilon$ or $\ \bar{F}_{n+1}\ _2 / \ \hat{f}_{n+1}\ _2 \leq \epsilon$	$\ \Delta \hat{u}\ _2 / \ \hat{u}_{n+1}\ _2 \leq \epsilon$ or $\ \bar{F}_{n+1}\ _2 / \ \hat{f}_{n+1}\ _2 \leq \epsilon$
<i>Design updates at end of time step</i>		
$\ddot{u}_{n+1} = \ddot{u}_n + (\hat{u}_{n+1}^{j+1} - \ddot{u}_n) / \Lambda_6 W_1$		
$\dot{u}_{n+1} = \dot{u}_n + \lambda_4 \dot{u}_n \Delta t + \lambda_5 (\hat{u}_{n+1} - \dot{u}_n) \Delta t$		
$u_{n+1} = u_n + \lambda_1 \dot{u}_n \Delta t + \lambda_2 \ddot{u}_n \Delta t^2 + \lambda_3 (\ddot{u}_{n+1} - \ddot{u}_n) \Delta t^2$		

Table 3: Predictor multi-corrector pseudo incremental a -form, v -form and d -form of $[\text{GInO}]_{\text{Single-Field}}$ representations for non-linear dynamic systems.

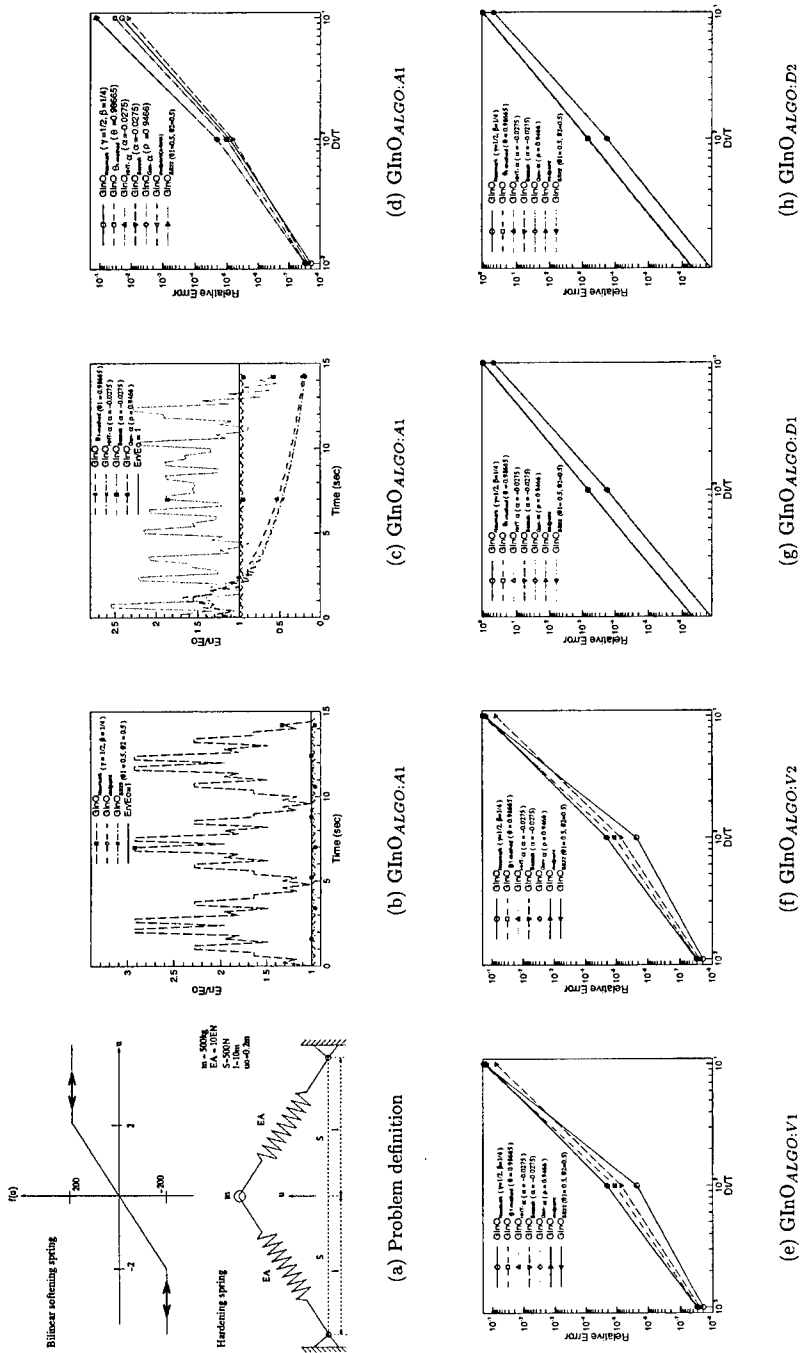
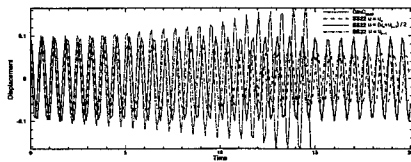
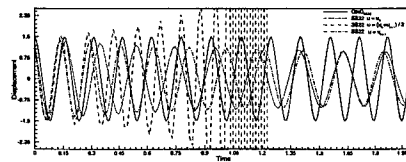


Figure 1: Stability and accuracy analysis for [GlnO] representations: a) Bilinear softening spring and hardening spring problem, b) E_n/E_o over time for non-dissipative schemes c) E_n/E_o over time for dissipative schemes d),e),f),g) and h) are accuracy for predictor multi-corrector incremental α , v and d -form of [GlnO] representations with multi-corrector non-linear iteration.

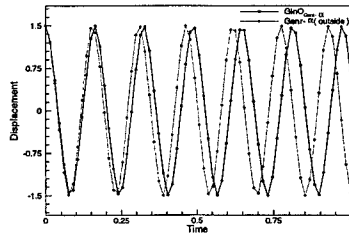


(a) $u_0 = .1, \dot{u}_0 = 0, \Delta t/T = 0.15$

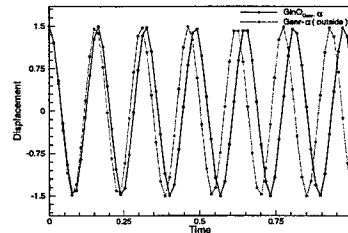


(b) $u_0 = 1.5, \dot{u}_0 = 0, \Delta t/T = 0.06$

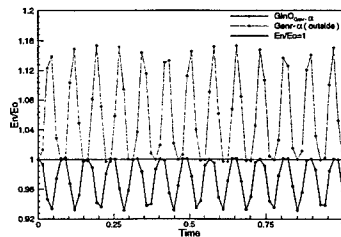
Figure 2: $\ddot{u} + 100u(1 + 10u^2) = 0$. $\text{GInO}_{SS22, \theta_1=1/2, \theta_2=1/2}$ and $\text{SS22 } \theta_1 = 1/2, \theta_2 = 1/2$ with (a) $\hat{u}_n = u_n$, (b) $\hat{u}_n = \frac{1}{2}(u_n + u_{n+1})$ and (c) $\hat{u}_n = u_{n+1}$ due to [16].



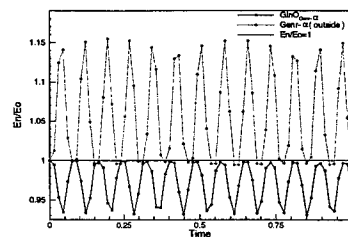
(a) $u_0 = 1.5, \dot{u}_0 = 0, \rho_\infty = 1.$



(b) $u_0 = 1.5, \dot{u}_0 = 0., \rho_\infty = 0.9$

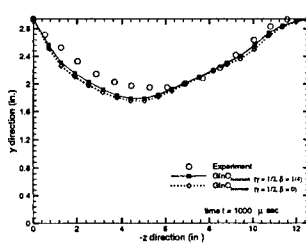
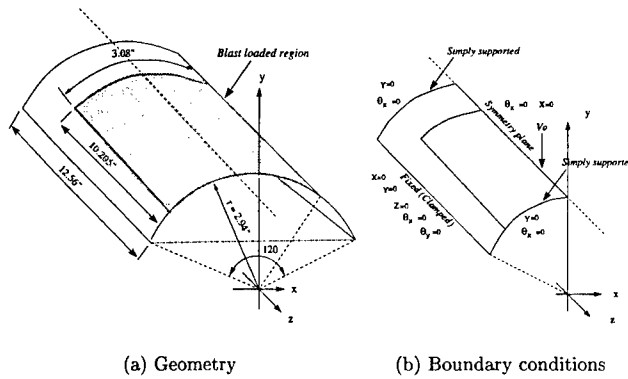


(c) $u_0 = 1.5, \dot{u}_0 = 0, \rho_\infty = 1.$

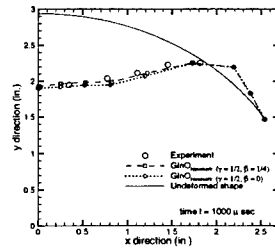


(d) $u_0 = 1.5, \dot{u}_0 = 0., \rho_\infty = 0.9$

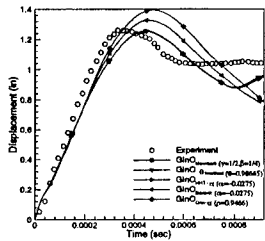
Figure 3: Displacement response and E_n/E_o for $\ddot{u} + 100u(1 + 10u^2) = 0, \Delta t/T = 0.1$. $\text{GInO}_{\text{Generalized-}\alpha}$ and Generalized- α due to [15].



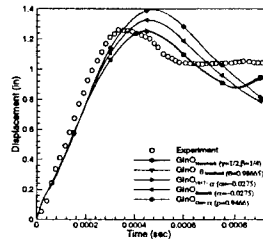
(c) Deformed shape of the cylindrical panel crown-line



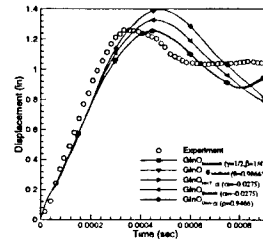
(d) Deformed shape of the cylindrical panel cross section at $z = 0.0$



(e) incremental a -form



(f) incremental v -form



(g) incremental d -form

Figure 4: Cylindrical panel subjected to blast loading: geometry, boundary conditions and large, elastic, elasto-plastic dynamic response employing predictor multi-corrector [GInO] representations.

Percentage change in number of non-linear iterations with respect to incremental α -form $[\text{GlnO}]_{\text{ALGO:A1}}$									
Algorithm	ALGO:V1	Algorithm	ALGO:D1	Algorithm	ALGO:V2	Algorithm	ALGO:D2		
GlnONM	0.5	GlnOWBZ	34.8	GlnONM	0.4	GlnOWBZ	31.9		
GlnOG- α	3.1	GlnOG- α	35.2	GlnOWBZ	7.1	GlnOMP	37.6		
GlnOWBZ	3.8	GlnOMP	37.1	GlnOG- α	11.8	GlnOSS22	37.6		
GlnOMP	8.9	GlnOSS22	37.1	GlnOHTT	16.9	GlnOG- α	41.0		
GlnOSS22	8.9	GlnONM	48.9	GlnOMP	17.3	GlnONM	48.9		
GlnOHTT	16.6	GlnOHTT	49.6	GlnOSS22	17.3	GlnOHTT	50.0		
GlnO θ_1	17.3	GlnO θ_1	50.8	GlnO θ_1	17.4	GlnOMP	50.8		
Percentage increase in number of non-linear iterations of different methods									
Algo	ALGO:A1	Algo	ALGO:V1	Algo	ALGO:V2	Algo	ALGO:D1	Algo	ALGO:D2
GlnOWBZ	0.0	GlnOWBZ	0.0	GlnOWBZ	0.0	GlnOWBZ	0.0	GlnOWBZ	0.0
GlnOG- α	24.8	GlnOG- α	25.7	GlnOMP	18.3	GlnO θ_1	19.1	GlnOG- α	16.4
GlnOMP	32.7	GlnOMP	25.8	GlnOSS22	18.3	GlnOHTT	19.4	GlnOHTT	22.3
GlnOSS22	32.7	GlnOSS22	25.8	GlnOG- α	18.5	GlnONM	19.6	GlnO θ_1	22.7
GlnONM	52.6	GlnOHTT	33.9	GlnOHTT	38.3	GlnOG- α	24.1	GlnONM	23.3
GlnOHTT	54.5	GlnO θ_1	35.4	GlnO θ_1	40.1	GlnOMP	28.1	GlnOMP	31.0
GlnO θ_1	57.6	GlnONM	59.4	GlnONM	65.1	GlnOSS22	28.1	GlnOSS22	31.0

Table 4: Percentage increase in number of non-linear iterations of different methods.

Table 5: [DNA] markers: Selected Type 3-[GInO] $_{Two-Field}$ Algorithms - Double weighted time fields.

[DNA] markers	Kujawski and Gallagher [18]	Hoff and Taylor [19]	Hoff and Taylor [19]
w_0	1	1	1
w_1	$-\frac{15(\Lambda_3+27\Psi_3)}{\Lambda_3+34\Psi_3}$	$-\frac{90}{7}$	$-\frac{15(24-645\Psi_3+28\Psi_3^2)}{24-806\Psi_3+35\Psi_3^2}$
w_2	$\frac{15(3\Lambda_3+67\Psi_3)}{\Lambda_3+34\Psi_3}$	$\frac{465}{14}$	$\frac{15(72-1613\Psi_3+70\Psi_3^2)}{24-806\Psi_3+35\Psi_3^2}$
w_3	$-\frac{35(\Lambda_3+19\Psi_3)}{\Lambda_3+34\Psi_3}$	$-\frac{45}{2}$	$-\frac{35(24-461\Psi_3+20\Psi_3^2)}{24-806\Psi_3+35\Psi_3^2}$
\hat{w}_0	1	1	1
\hat{w}_1	$-\frac{135(3+2\Psi_3)}{2(17+13\Psi_3)}$	-36	$-\frac{135(3+7\Psi_3)}{2(17+43\Psi_3)}$
\hat{w}_2	$\frac{15(67+41\Psi_3)}{2(17+13\Psi_3)}$	150	$\frac{15(67+149\Psi_3)}{2(17+43\Psi_3)}$
\hat{w}_3	$-\frac{35(19+11\Psi_3)}{2(17+13\Psi_3)}$	-140	$-\frac{35(19+41\Psi_3)}{2(17+43\Psi_3)}$
Λ_1	1	1	1
Λ_2	$\frac{1}{2}$	1	1
Λ_3	Λ_3	$\frac{341}{630}$	$\frac{2}{\Psi_3} \left(\frac{1}{24} - \Psi_3^2 \right)$
Λ_4	1	1	1
Λ_5	1	1	1
Ψ_1	1	1	1
Ψ_2	$\sqrt{1 + \frac{4}{\Lambda_3}} - 1$	$\frac{7}{30}$	Ψ_3
Ψ_3	$\frac{\Lambda_3}{2} \left(\sqrt{1 + \frac{4}{\Lambda_3}} - 1 \right)$	$\frac{1}{4}$	Ψ_3
Ψ_4	1	1	1
Ψ_5	$1 - \left(\sqrt{1 + \frac{4}{\Lambda_3}} - 1 \right)$	$\frac{3}{2}$	$\frac{1-\Psi_3}{1+\Psi_3}$
λ_1	1	1	1
λ_2	$\frac{1}{2}$	1	1
λ_3	Λ_3	$\frac{341}{630}$	$\frac{2}{\Psi_3} \left(\frac{1}{24} - \Psi_3^2 \right)$
ψ_1	1	1	1
ψ_2	$\sqrt{1 + \frac{4}{\Lambda_3}} - 1$	$\frac{7}{30}$	Ψ_3
ψ_3	$\frac{\Lambda_3}{2} \left(\sqrt{1 + \frac{4}{\Lambda_3}} - 1 \right)$	$\frac{1}{4}$	Ψ_3

Table 6: [DNA] markers: Selected Type 3-[GInO] $_{Two-Field}$ Algorithm-Single weighted time field.

[DNA] markers	Park [20]	[DNA] markers	Park [20]	[DNA] markers	Park [20]
w_0	1	w_1	$\frac{315}{16}$	w_2	$\frac{975}{16}$
w_3	$\frac{235}{16}$	w_4	0	Λ_1	1
Λ_2	$\frac{1}{2}$	Λ_3	$\frac{1}{6}$	Λ_4	0
Λ_5	1	Λ_6	$\frac{5}{11}$	Λ_7	0
λ_1	1	λ_2	$\frac{1}{2}$	λ_3	$\frac{1}{6}$
λ_4	0	λ_5	1	λ_6	$\frac{1}{2}$
λ_7	0	λ_8	1	λ_9	0

At the start of time step

Predict the state vectors employing (Predictors)

$$\hat{\mathbf{d}}_{n+1}^j = \mathbf{d}_n + \Lambda_1 W_1 \dot{\mathbf{d}}_n \Delta t + \dots + \Lambda_p W_p \mathbf{d}_n^{(p)} \Delta t^p$$

$$\dot{\hat{\mathbf{d}}}_{n+1}^j = \dot{\mathbf{d}}_n + \Lambda_{p+2} W_1 \ddot{\mathbf{d}}_n \Delta t + \dots + \Lambda_{2p} W_{p-1} \mathbf{d}_n^{(p)} \Delta t^{p-1}$$

Satisfy equilibrium in a loop over multi-corrector iterations

$$\text{Solve } \bar{\mathbf{A}} \Delta \mathbf{d}_{n+1}^{(p)j+1} = \mathbf{R}$$

$$\text{where } \bar{\mathbf{A}} = [\Lambda_{2p+1} W_p \Delta t^{p-1} \mathbf{I} + \Lambda_{p+1} W_{p+1} \Delta t^p \mathbf{A}_t], \quad \mathbf{R} = \hat{\mathbf{F}} - \mathbf{g}(\hat{\mathbf{d}}_{n+1}^j) - \dot{\mathbf{d}}_{n+1}^j$$

Update or correct the state vectors (Correctors)

$$\hat{\mathbf{d}}_{n+1}^{j+1} = \hat{\mathbf{d}}_{n+1}^j + \Lambda_{p+1} W_{p+1} \Delta \mathbf{d}_{n+1}^{(p)j+1} \Delta t^p$$

$$\dot{\hat{\mathbf{d}}}_{n+1}^{j+1} = \dot{\hat{\mathbf{d}}}_{n+1}^j + \Lambda_{2p+1} W_p \Delta \mathbf{d}_{n+1}^{(p)j+1} \Delta t^{p-1}$$

$$\text{Till convergence } \frac{\|\mathbf{R}\|_2}{\|\mathbf{F}\|_2} \leq \epsilon$$

Design updates at end of time step

$$\mathbf{d}_{n+1}^{(p)} = \mathbf{d}_n^{(p)} + (\hat{\mathbf{d}}_{n+1}^{j+1} - \dot{\mathbf{d}}_n - \Lambda_{p+2} W_1 \ddot{\mathbf{d}}_n \Delta t - \dots - \Lambda_{2p} W_{p-1} \mathbf{d}_n^{(p)} \Delta t^{p-1}) / (\Lambda_{2p+1} W_p \Delta t^{p-1})$$

$$\mathbf{d}_{n+1}^{(p-1)} = \mathbf{d}_n^{(p-1)} + \lambda_{\frac{p(p+1)}{2}-1} \mathbf{d}_n^{(p)} \Delta t + \lambda_{\frac{p(p+1)}{2}} (\mathbf{d}_{n+1}^{(p)} - \mathbf{d}_n^{(p)}) \Delta t$$

\vdots

$$\dot{\mathbf{d}}_{n+1} = \dot{\mathbf{d}}_n + \lambda_{p+2} \ddot{\mathbf{d}}_n \Delta t + \dots + \lambda_{2p} p \mathbf{d}_n^{(p)} \Delta t^{p-1} + \lambda_{2p+1} (\mathbf{d}_{n+1}^{(p)} - \mathbf{d}_n^{(p)}) \Delta t^{p-1}$$

$$\mathbf{d}_{n+1} = \mathbf{d}_n + \lambda_1 \dot{\mathbf{d}}_n \Delta t + \dots + \lambda_p \mathbf{d}_n^{(p)} \Delta t^p + \lambda_{p+1} (\mathbf{d}_{n+1}^{(p)} - \mathbf{d}_n^{(p)}) \Delta t^p$$

where

$$\mathbf{g}(\hat{\mathbf{d}}) = \begin{Bmatrix} -\mathbf{v} \\ \mathbf{p}(\dot{\mathbf{u}}, \mathbf{u}) \end{Bmatrix}, \quad \mathbf{A}_t = \begin{bmatrix} \mathbf{0} & -\mathbf{I} \\ -\mathbf{M}^{-1} \mathbf{K}_t & -\mathbf{M}^{-1} \mathbf{C}_t \end{bmatrix}, \quad \hat{\mathbf{F}} = \mathbf{F}_n + \dots + W_{p-1} \mathbf{F}_n^{(p-1)} \Delta t^{p-1}$$

Table 7: Illustrative predictor multi-corrector incremental $\Delta \mathbf{d}^{(p)}$ form of the single weighted time field of $[\text{GInO}]_{\text{Two-Field}}$ representations for non-linear dynamics systems.

ACOUSTIC FATIGUE

NONLINEAR VIBRATIONS OF THERMALLY BUCKLED PANELS

Radu UDRESCU

INAS SA –Institute for Analysis of Systems
Iancu de Hunedoara 29, 71202 Bucharest, ROMANIA

This paper investigates the nonlinear dynamic behaviour of panels subjected to supercritical thermal stresses due to temperature difference between their edges and support. Free and forced vibrations under harmonic out-of-plane pressure excitations are studied by using a finite element model extended to large deflection theory. The snap-through phenomenon is identified as intermittent or persistent oscillations about, and between, the multiple equilibria.

I. INTRODUCTION

The dynamic behaviour of thermally buckled panels has received resurgent interest due to the development of structures working in conditions of noise and high temperatures. These structural systems are known as exhibiting intermittent or persistent oscillations about, and between, various equilibrium positions. For example, this unpredictable phenomenon (termed snap-through) can be induced by the kinetic heating of the supersonic flow combined with aeroacoustic excitations (of noise, turbulent boundary layer, or oscillating shock waves) acting on the panel substructure of a high speed vehicle (Fig.1).

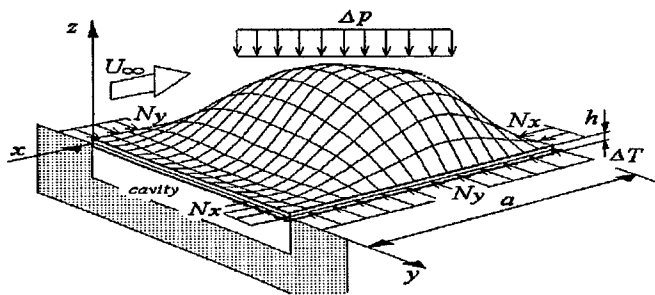


Fig.1 Skew of panel under thermal forces

In a static context, buckling is usually accompanied by the appearance of multiple equilibria. The underlying potential energy function has a number of locally distinct minima, and large perturbations may cause the system to “snap” to an alternate equilibrium configuration.

From a practical point of view, these large amplitudes, nonlinear oscillations are detrimental to the integrity of the structure. Snap-through

produces large changes in curvature over short time intervals, which increases wear and greatly reduces fatigue life. In extreme cases, catastrophic, failure may result.

Recent experimental investigations of panels under combination of axial and lateral loading have already confirmed [1] a significant loss of predictability due to the possibility of snap-through resulting from disturbances and transient dynamics.

The purpose of this paper is to give a general model for the nonlinear vibrations of the slender panels subjected to thermal in-plane loading and also externally excited. A high-order finite-element model extended to large deflection theory (which takes into account the in-plane stresses induced by the large amplitudes of the out-of-plane motion) is used for the identification of dynamic pattern of the responses with and without applied excitations of various amplitudes and frequencies.

II. GENERAL CONSIDERATIONS

The general theory of elastic instability phenomena [2] states that the location and stability of the system's equilibria are dictated by the strain energy function. Assuming the deflection of a system given by a single generalized coordinate, q , the (strain) potential energy function for an axially loaded, slender structure in the initial postbuckling range can be written in a suitable nondimensionalization form as:

$$U(q) \equiv q^4 - \lambda q^2 \quad (1)$$

where λ represents a control parameter, e.g., the axial load or, in this case, the temperature rise. The first derivative of the potential:

$$\frac{dU}{dq} \equiv V'(q) = 4q^3 - 2\lambda q = 0 \quad (2)$$

defines equilibria resulting in:

$$q_{eq} = 0, \pm \sqrt{\frac{\lambda}{2}} \quad (3)$$

The sign of the second derivative of the potential evaluated at each q_{ef} determines the stability of these configurations. The trivial solution is unstable, and the two symmetric solutions are stable.

$$\frac{d^2U}{dq^2} \equiv V''(q) = 12q^2 - 2\lambda \quad (4)$$

The generic case is considered by including an imperfection parameter:

$$U(q) = q^4 - \lambda q^2 + \varepsilon q \quad (5)$$

where ε might represent an initial geometric imperfection, a small transverse load or an axial load eccentricity. In this case, the symmetry is broken and all three equilibria are nonzero and have certain physical meaning:

- one stable configuration represented by the dominant, primary solution q_1 (which would be followed by a natural quasistatic loading path)
- the other stable position representing a secondary solution q_3 which requires a large perturbation or a special loading history in order to be realized.
- one unstable position, solution q_2 between the two equilibria (as in Fig.2 showing schematically the case of a "double well" unsymmetric potential).

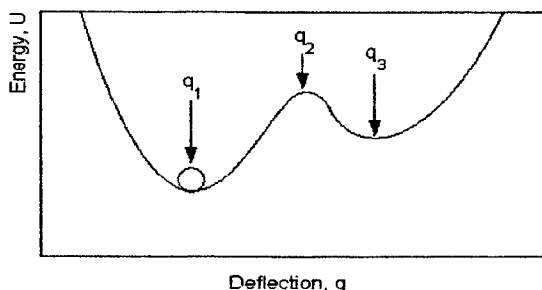


Fig.2 Sketch of a two-well potential energy function

In the static case, the equilibrium configurations and their stability are readily evident. In the dynamic case, the displacement of the plate may be conceptually viewed as a ball moving on this potential energy surface under external forcing (shaking horizontally the potential surface). For small amplitude excitations, the ball will undergo small periodic oscillations about the primary equilibrium (in the normal course of events). Under greater excitation, the ball may escape the local confines of the potential well and undergo intermittent oscillations as the ball traverses both wells in an unpredictable manner. This motion is analogous to dynamic snap-through of the plate.

III. MODEL OF THERMALLY BUCKLED PANEL

The theoretical model of thermally buckled panels is built by using the known expression of the strain energy arisen in an isotropic Hookean plate (having bending rigidity D and Poisson's coefficient ν). The strain energy is written as the sum of a stretching and pure bending components:

$$U = \frac{1}{2} \iiint [\sigma_{xx} \varepsilon_{xx} + \sigma_{yy} \varepsilon_{yy} + \sigma_{xy} \varepsilon_{xy}] dx dy dz = U_s + U_B \quad (6)$$

where the two terms have been identified as having the following expressions:

$$U_s = \frac{1}{2} \iint [N_x \varepsilon_{xx0} + N_y \varepsilon_{yy0} + N_{xy} \varepsilon_{xy0}] dx dy \quad (7)$$

$$U_B = \frac{D}{2} \iint \left[\left(\frac{\partial^2 w}{\partial x^2} \right)^2 + \left(\frac{\partial^2 w}{\partial y^2} \right)^2 \right] dx dy + \frac{D}{2} \iint \left[2\nu \frac{\partial^2 w}{\partial x^2} \frac{\partial^2 w}{\partial y^2} + 2(1-\nu) \left(\frac{\partial^2 w}{\partial x \partial y} \right)^2 \right] dx dy$$

The above relations are obtained by using the von Karman nonlinear strain-displacement expressions. For the plate element undergoing both extension and bending at any point z the strain state is a sum of membrane and change of curvature strain components:

$$\begin{aligned} \varepsilon_{xx} &= \frac{\partial u}{\partial x} + \frac{1}{2} \left(\frac{\partial w}{\partial x} \right)^2 - z \frac{\partial^2 w}{\partial x^2} = \varepsilon_{xx0} - z \frac{\partial^2 w}{\partial x^2} \\ \varepsilon_{yy} &= \frac{\partial v}{\partial y} + \frac{1}{2} \left(\frac{\partial w}{\partial y} \right)^2 - z \frac{\partial^2 w}{\partial y^2} = \varepsilon_{yy0} - z \frac{\partial^2 w}{\partial y^2} \\ \varepsilon_{xy} &= \frac{\partial v}{\partial x} + \frac{\partial u}{\partial y} + \frac{\partial w}{\partial x} \frac{\partial w}{\partial y} - 2z \frac{\partial^2 w}{\partial x \partial y} = \varepsilon_{xy0} - 2z \frac{\partial^2 w}{\partial x \partial y} \end{aligned} \quad (8)$$

The tensions N_x, N_y, N_{xy} in equation (7) correspond to the normal and shear elastic and thermal stress components (when applying a uniform temperature difference ΔT over the plate having coefficient of thermal expansion α):

$$\begin{aligned} N_x &= \frac{hE}{(1-\nu^2)} [\varepsilon_{yy} + \nu \varepsilon_{xx}] - \frac{hE}{(1-\nu)} \alpha \Delta T \\ N_y &= \frac{hE}{(1-\nu^2)} [\varepsilon_{xx} + \nu \varepsilon_{yy}] - \frac{hE}{(1-\nu)} \alpha \Delta T \\ N_{xy} &= \frac{hE}{2(1+\nu)} \varepsilon_{xy} \end{aligned} \quad (9)$$

The governing equation of the general thermoelastic model is obtained through the applications of Hamilton's principle:

$$\int (\delta T - \delta U + \delta W) dt = 0 \quad (10)$$

and has the known expression [3]:

$$D\Delta^2 w - N_x \frac{\partial^2 w}{\partial x^2} - N_y \frac{\partial^2 w}{\partial y^2} + m \frac{\partial^2 w}{\partial t^2} = \Delta p_s \quad (11)$$

where Δp_s is the transversal pressure. The finite element formulation of this equation has a classical nondimensional form [4] (denoted by superscript "o"):

$$\begin{aligned} & \begin{bmatrix} \mathbf{M}_{bb}^o & \mathbf{O} \\ \mathbf{O}^t & \mathbf{M}_{mm}^o \end{bmatrix} \begin{bmatrix} \ddot{\mathbf{r}}_b^o \\ \ddot{\mathbf{r}}_m^o \end{bmatrix} + \left(\begin{bmatrix} \mathbf{K}_{bb}^o + \sigma_x \mathbf{K}_g^o & \mathbf{O} \\ \mathbf{O}^t & \mathbf{K}_{mm}^o \end{bmatrix} \right. \\ & \left. + \begin{bmatrix} \mathbf{K}_{1bb}^o & \mathbf{K}_{1bm}^o \\ \mathbf{K}_{1mb}^o & \mathbf{O} \end{bmatrix} + \begin{bmatrix} \mathbf{K}_{2bb}^o & \mathbf{O} \\ \mathbf{O}^t & \mathbf{O} \end{bmatrix} \right) \begin{bmatrix} \mathbf{r}_b^o \\ \mathbf{r}_m^o \end{bmatrix} = \begin{bmatrix} p \mathbf{P}_s^o \\ \sigma_x \mathbf{P}_x^o \end{bmatrix} \end{aligned} \quad (12)$$

obtained by using a dimensionless time parameter:

$$\tau = t \sqrt{\frac{D}{ma^2}} \quad (13)$$

Subscripts "b" and "m" denote separately the bending and membrane components, m is the panel mass/area, \mathbf{M} and \mathbf{K} are the global mass and linear stiffness matrices, respectively; \mathbf{K}_g is the geometric stiffness due to thermal forces; \mathbf{K}_1 , \mathbf{K}_2 are the nonlinear stiffness matrices that depend linearly and quadratically on element plate " \mathbf{r}_b " and membrane " \mathbf{r}_m " displacements, respectively; \mathbf{P}_s , \mathbf{P}_x are the externally applied out-of-plane pressure and in-plane load, respectively. Also σ_x and p are dimensionless parameters for in-plane load and transversal pressure, respectively:

$$\begin{aligned} \sigma_x &= \frac{N_{x0} a^2}{D} \\ p &= \frac{\Delta p_s a^4}{Dh} \end{aligned} \quad (14)$$

Thermal buckling tension $N_x^{\Delta T}$ arises when the kinetic heating of the panel surface yields a temperature difference ΔT between the fixed edges (completely restrained against in-plane motions) and their supports. The thermal in-plane stress resultants equal:

$$N_x^{\Delta T} = N_y^{\Delta T} = - \frac{Eh\alpha\Delta T(t)}{1-\nu} \quad (15)$$

Knowing the critical buckling load for a simply supported square plate:

$$\sigma_x = \frac{N_{cr} a^2}{D} = 2\pi^2 \quad (16)$$

the compressive load parameter σ_x can be related to the critical buckling conditions:

$$\frac{\sigma_x(t)}{2\pi^2} = \frac{\Delta T(t)}{\Delta T_{cr}} \quad (17)$$

IV. RESULTS

An original computational program has been used for the study of the dynamic behaviour of a simply supported isotropic square panel ($a/b=1$, $h/a=0.01$) under uniform temperature change ΔT . The FE mesh (shown in Fig.3) consists of eight complex plate-membrane triangular elements with a reduced number of active degrees of freedom: 54 DOFs for a simply supported isotropic square panel. This FE idealisation (presented in detail in [5]) has already provided its capabilities in solving nonlinear panel flutter problems [6].

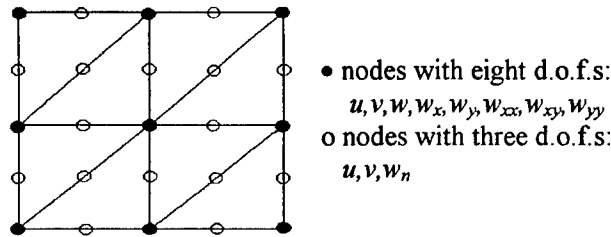


Fig.3 Finite-element mesh

An important aspect of thermal effect may be seen in terms of the three amplitude response diagrams of Fig.4.

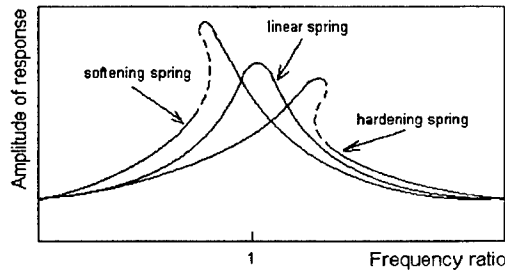


Fig.4 Sketch of amplitude diagram for motion about a single equilibrium

The nonlinear softening spring and the linear and nonlinear hardening springs cases corresponds to the curves bending to the left, straight up and bending to the right, respectively.

For a fixed temperature change $\Delta T < \Delta T_{cr}$, periodic plate motions are of the hardening type (bending right) due to the additional membrane stiffness. However, in this prebuckled regime the bending stiffness decreases as the thermal load is increased from ambient to ΔT_{cr} . For a fixed $\Delta T > \Delta T_{cr}$, the system is of the softening spring type (bending left) due to the presence of the unstable equilibrium (the hilltop on the potential surface) separating two stable equilibria. This theory is verified numerically by the free vibrations of a panel subjected to increasing thermal buckling loads. The graphics shown in Fig.5 are drawn in dimensionless units: displacement (at the mid-point of panel) scaled to panel thickness $W=w/h$ (above) and nondimensional temperature parameter $\Delta T/\Delta T_{cr}$ (below, crossing the sub/supercritical domain) versus nondimensional time τ . The dynamic response is obtained by step-by-step integration of equation system (12) starting from the perturbation solution of a small deformed shape due to a constant distribution pressure. The in-plane inertia M_{mm}^0 is neglected.

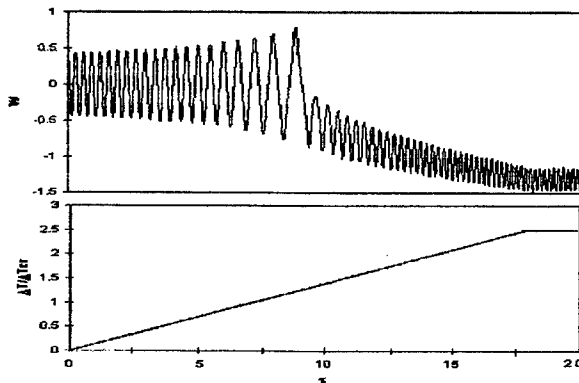


Fig 5. Free vibrations of panel under increasing thermal forces

Investigating the pattern of this diagram in terms of amplitude and frequency related to the levels of compressive load, it can be observed that the frequency of vibration decreases (equivalent to decreasing of the bending stiffness) in the prebuckled regime as the temperature difference is increased from ambient to ΔT_{cr} . After crossing the critical regime into the postbuckled region $\Delta T/\Delta T_{cr} > 1$, the frequency of vibration becomes higher (the bending stiffness increases with increased thermal load). The system oscillates now around a buckled state of the panel. These observations are consistent with the above considerations related to Fig.4.

It is important to point out that the diagram from Fig.4 pertain to motion about one equilibrium position (one potential well). They do not correspond to amplitudes of snap-through phenomenon as it was defined in the section of general considerations. There it was mentioned that the external excitation becomes essential in forcing the system to undergo periodic oscillations about two alternate equilibrium positions. This behaviour has already been confirmed by experiments in dynamics of thermally buckled panels acoustically excited [1]. That is why the next analysis considers additional excitations over the panel in terms of harmonic uniformly distributed out-of-plane pressures (expressed in nondimensional form p defined by Eq.14).

The numerical investigations start around the critical buckling point and then are focused on the postbuckled regime. The graphics show simultaneously the nondimensional dynamic response W and excitation p versus time τ . The patterns of external loading include time-delayed functions of increasing amplitudes and various frequencies in order to compare the free and forced vibrations. When applying excitation of nonzero mean value in subcritical regime $\Delta T/\Delta T_{cr}=0.9$ it can observed a beating phenomenon which is suppressed at increasing pressures (Fig.6).

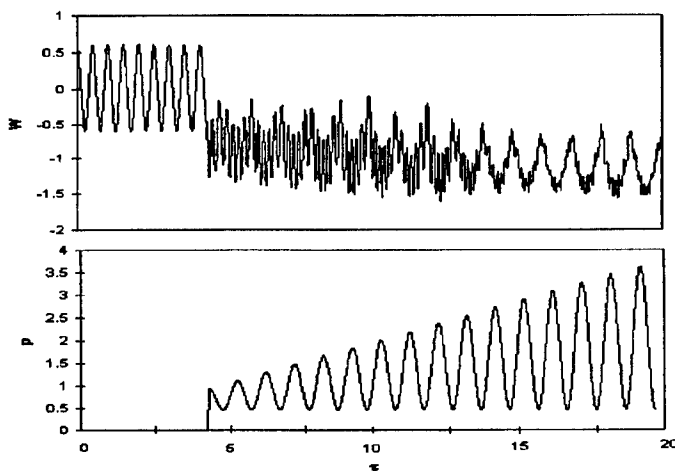


Fig.6 Dynamic response and excitation ($\Delta T/\Delta T_{cr}=0.9$)

The postbuckling regime $\Delta T/\Delta T_{cr}=1.1$ is studied in two cases of harmonic excitations having the same pattern of amplitude, but different frequencies. By forcing at moderate excitation (Fig.7) the beating behaviour is maintained as well as the dominant frequency of excitation. When exciting at lower frequency (Fig.8) the response is disturbed into a pattern which suggests a snap-through phenomenon with intermittent oscillations about, and between, the multiple equilibria.

This dynamic behaviour becomes obvious at higher thermal compressive load ($\Delta T/\Delta T_{cr}=1.9$) and moderate frequency excitation (Fig.9). Indeed the forced motion began around the secondary equilibrium, then settled around the primary equilibrium and alternated between both positions. Various numerical tests confirm that the transient dynamics of excitation play a more significant role in likelihood of snap-through.

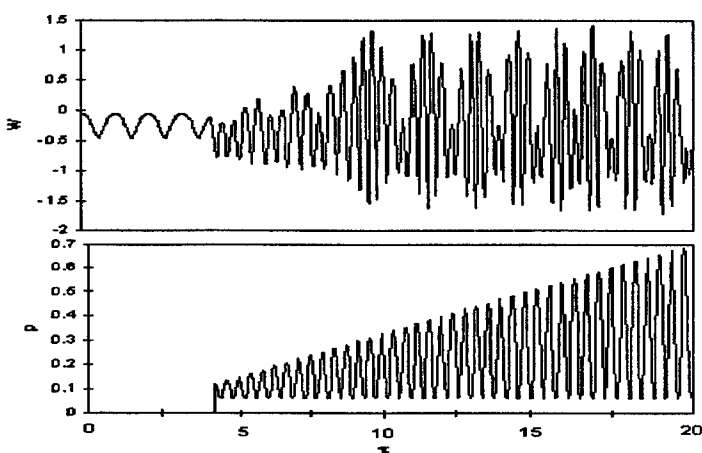


Fig.7 Dynamic response and excitation - Case 1 ($\Delta T/\Delta T_{cr}=1.1$)

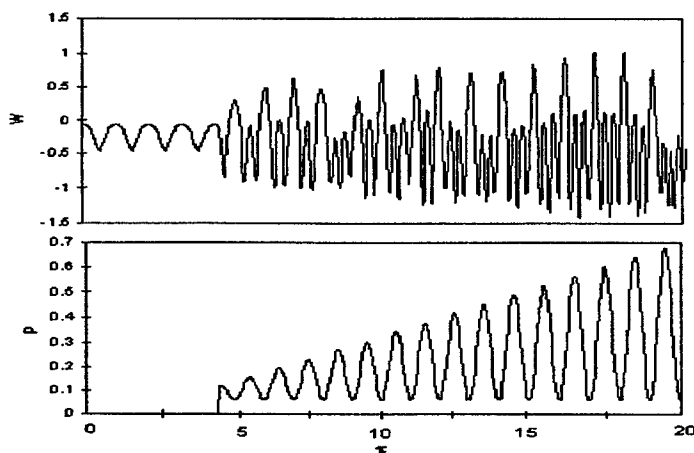


Fig.8 Dynamic response and excitation - Case 2 ($\Delta T/\Delta T_{cr}=1.1$)

Thus, the behaviour becomes unpredictable at lower frequency excitations (Fig.10) when the oscillations become irregular around one equilibrium position and decrease in amplitude in spite of a forcing level higher than the previous case.

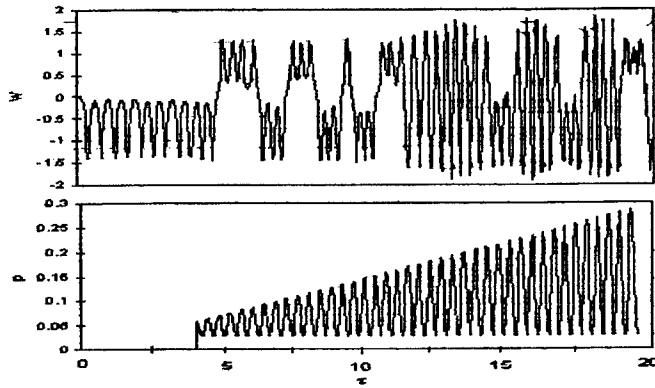


Fig.9 Dynamic response and excitation - Case 1 ($\Delta T/\Delta T_{cr}=1.9$)

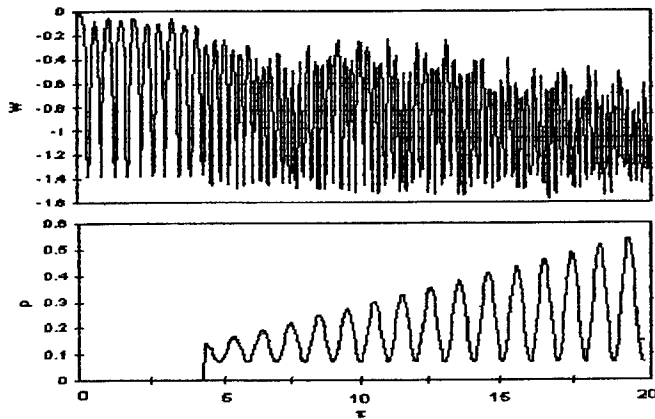


Fig.10 Dynamic response and excitation - Case 2 ($\Delta T/\Delta T_{cr}=1.9$)

The beating and snap-through phenomena (confirmed again at higher postbuckling regime -Figs.11 and 12, respectively, at $\Delta T/\Delta T_{cr}=2.0$) seem to be governed by the excitation amplitude. Lower amplitudes forced the system into a steady-state beating behaviour (Fig.11), but harmonic excitations of larger amplitudes disturbed this initial pattern into the irregularly oscillation of snap-through motion (Fig.12). Usually the beating phenomenon may be connected to a saddle node bifurcation [7], i.e., the jump in amplitude. It has already been confirmed by experiments on thermally buckled panels excited by sound pressures [1].

The above dimensionless analysis has the advantage of expressing the various results in a most compact form, establishing scaling laws to extrapolate results for certain physical situations. Regarding the amplitude of the response, the graphical results showed out-of-plane displacements of the

same magnitude as panel thickness (which is characteristic to large amplitudes domain).

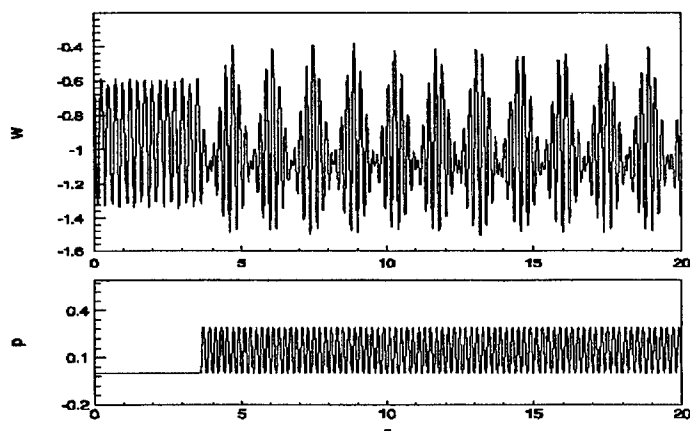


Fig.11 Dynamic response and excitation - Case 1 ($\Delta T/\Delta T_{cr}=2.0$)

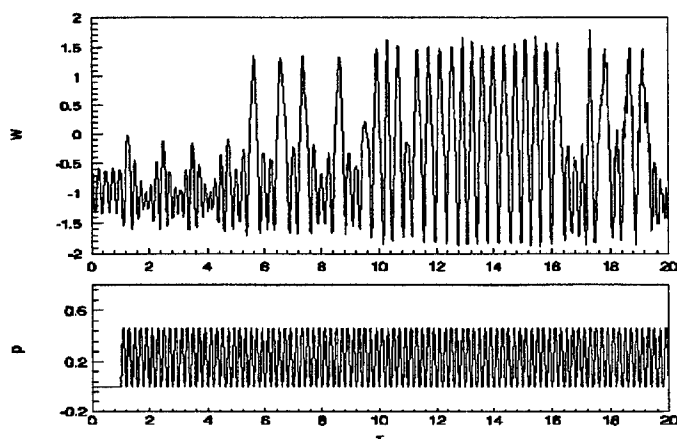


Fig.12 Dynamic response and excitation - Case 2 ($\Delta T/\Delta T_{cr}=2.0$)

In order to have quantitative information about the real time t and pressure Δp_s , it is necessary to perform the dimensional analysis by correlating the dimensionless parameters -time τ and pressure p from Eqs.(13), and (14), respectively- with data of panel geometry and material, as following:

$$t[\text{sec}] = \frac{a^2}{h} \sqrt{\frac{12(1-\nu^2)}{E} \rho} \tau \quad (18)$$

$$\Delta p_s [Pa] = \frac{E}{12(1-\nu^2)} \left(\frac{h}{a}\right)^4 p \quad (19)$$

V. CONCLUSIONS

This paper investigated the nonlinear dynamic behaviour of panels with fixed edges (simply supported) subjected to thermal stresses and also excited harmonically by uniformly distributed pressures. The analysis was performed on a high-order finite element model extended to nonlinear elastic theory which took into account the in-plane stretching stresses induced by the large amplitudes of the out-of-plane motion..

Examples of free and forced nonlinear vibrations of panels in postbuckled regime were presented in nondimensional time domain diagrams. The patterns of dynamic behaviour confirmed the sensitivity of the response to transient dynamic excitation which play a significant role in forcing the system to oscillate about, and between, the multiple equilibria.

The proposed model has the capabilities to extend the analysis to other perturbations, nonstationary or random effects in order to obtain the reliable information about the snap-through as detrimental phenomenon to the structural integrity.

REFERENCES

1. Murphy, K.,D., Virgin, L.,N., Rizzi, S.,A., Experimental Snap-through Boundaries for Acoustically Excited, Thermally Buckled Plates, *Experimental Mechanics*, 1996, **36** (4), 312-317.
2. Thompson, J.,M.,T., Hunt, G.,W., *Elastic Instability Phenomena*, John Wiley & Sons, Chichester, England, 1984.
3. Dowell, E.,H., *Aeroelasticity of plates and shells*, Dordrecht: Kluwer Academic Publishers, 1974.
4. Surace, G., Udrescu, R., Finite-Element Analysis of the Fluttering Panels Excited by External Forces, *Journal of Sound and Vibration* (1999) **224**(5), 917-935.
5. Udrescu, R., A Higher Finite Element Model in Nonlinear Panel Flutter Analysis, AIAA paper no. 98-1843, *A collection of technical papers of the 39th AIAA/ASME/ASCE/AHS/ACS Structures, Structural Dynamics and Materials Conference*, Part 2, 1252-1262.
6. Udrescu, R., Surace, G., An Enhanced Aeroelastic Analysis of Panels Under Transitory Hypersonic Flow Conditions, AIAA paper no 99-1432, *A collection of technical papers of the 40th AIAA/ASME/ASCE/ AHS/ASC Structures, Structural Dynamics, and Materials Conference*, Part 3, 1953-1962.
7. Thompson, J.,M.,T., Virgin, L.,N., Predicting a Jump to Resonance Using Transient Maps and Beats, *Int. J. Non-linear Mech.*, 1986, **21**(3), 205-211.

NON-LINEAR RESPONSE OF COMPOSITE PANELS TO RANDOM EXCITATIONS AT ELEVATED TEMPERATURES

Jean-Michel Dhainaut, Bin Duan and Chuh Mei
Department of Aerospace Engineering, Old Dominion University, Norfolk, VA 23529
and
S. Michael Spottswood and Howard F. Wolfe
Structural Dynamic Branch, AFRL/VASS, Wright-Patterson AFB, OH 45433

ABSTRACT

Sonic fatigue is being considered as one of the major design parameters for the new generation of high-speed flight vehicles. Efficient analysis methods for predicting nonlinear random response and fatigue life are urgently needed. This paper presents a finite element formulation for the prediction of non-linear random response of thin composite panels subjected to high acoustic loads and elevated temperatures. Laminated plate theory and von Karman large displacement relations are used to derive the non-linear equations of motion for an arbitrarily laminated composite panel subjected to combined acoustic and thermal loads. The non-linear equations of motion in structural node degrees of freedom are then transformed to a set of coupled nonlinear equations in truncated modal coordinates with rather small degrees of freedom. Numerical integration is employed to obtain the panel response with simulated Gaussian white noise. To validate the formulation, results are compared with the existing linear and nonlinear solutions to assess the accuracy of nonlinear modal stiffness matrices and simulated random loads. Examples are given for isotropic and composite panels at various combinations of sound pressure level and temperature. Numerical results include root mean square values of maximum deflection and strain, time histories of deflection and strain response, probability distribution functions, power spectrum densities and higher statistical moments.

1. INTRODUCTION

Resurgent interest in the high-speed flight vehicles necessitates the further development of sonic fatigue technology [1,2]. The surface thermal protection systems (TPS) of advanced high-speed aircraft and spacecraft, such as the X-33 Advanced Technology Demonstrator, the Reusable Launch Vehicle (RLV), the Joint Strike Fighter (JSF), and the High-Speed Civil Transport (HSCT), etc. will be constructed from high temperature resistant composite or superalloy materials. The major advantages that composite materials provide are the increased strength to weight ratio and the higher structural damping over superalloy structures. The larger damping would yield smaller dynamic response and strain, and thus enhancing fatigue life. The TPS would yield large displacements under high acoustic loads and buckling at elevated temperatures. Both of these effects are nonlinear in nature and make predicting fatigue life extremely difficult [1-3]. Because of

the high costs and difficulties with instrumentation at high acoustic intensity and elevated temperature, reliable experimental data is difficult to acquire. Thus, in the design process, greater emphasis will be placed on improved mathematical and computational prediction methods.

There are four major analysis methods, the perturbation, Fokker-Plank-Kolmogorov (FPK), Monte Carlo methods, and the equivalent linearization (EL) for the prediction of nonlinear response of aircraft panels subjected to high sound pressure levels and temperatures. The perturbation technique [4] has been shown that it is limited to weak geometric nonlinearities, and the FPK approach [5] yields to exact solution but only to single one degree of freedom (DOF) systems. Monte Carlo simulation [6,7] is the most general method, but the use of partial differential equation (PDE) and Galerkin's approach limited its applicability to rather simple structures [8-10]. Equivalent linearization methods have been widely applied because of its ability to accurately capture the response statistics over a wide range of response while maintaining a relatively light computational burden [11,12]. The draw back of the equivalent linearization technique is the assumption that the response has to be Gaussian.

The application of the finite element method and EL was extended to structures subjected to thermal and acoustic loads [13-15]. The thermal post-buckling structural problem was solved first to obtain the deflection and thermal stresses, they were then treated as known preconditions for the subsequent random response analysis. The known preconditions dealt with only one of the two post-buckling positions, therefore the FE/EL approach does not give accurate predictions for oil canning and large non-linear random motions. This paper presents a new analytical method for the prediction of nonlinear random response of composite panels at elevated temperatures. The system equations of motion are first derived in the structural node DOF using the finite element approach, then they are reduced to a set of coupled nonlinear modal equations. Numerical integration is used to obtain the panel response. All the three motions: (i) linear random vibration about one of the buckled position, (ii) snap-through between the two buckled positions, and (iii) non-linear random vibration over the two thermally buckled positions, can be predicted. Examples are given for an isotropic plate and a composite plate.

2. FINITE ELEMENT FORMULATION

The governing nonlinear equations of motion are derived for an arbitrarily laminated composite plate subjected to a set of simultaneously applied thermal and acoustic loads. The thermal load is taken to be an arbitrary distribution and steady state, i.e., $\Delta T(x,y,z)$. The acoustic excitation is assumed to be a band-limited Gaussian random noise and uniformly distributed over the structural surface.

2.1 Equations of Motion in Structural Node DOF

The displacement functions are:

$$\begin{aligned} u_x &= u(x, y, t) - zw_{,x}(x, y, t) \\ u_y &= v(x, y, t) - zw_{,y}(x, y, t) \\ u_z &= w(x, y, t) \end{aligned} \quad (1)$$

where u_x , u_y , u_z are the three displacement components at any point in the element, and u , v , w are the displacements of the middle surface. The von Karman strain displacement relations for large deflection are given by

$$\{\varepsilon\} = \{\varepsilon^0\} + z\{\kappa\} \quad (2)$$

and

$$\{\varepsilon^0\} = \begin{Bmatrix} u_{,x} \\ v_{,y} \\ u_{,y} + v_{,x} \end{Bmatrix} + \frac{1}{2} \begin{Bmatrix} w_{,x}^2 \\ w_{,y}^2 \\ 2w_{,x}w_{,y} \end{Bmatrix} = \{\varepsilon_m^0\} + \{\varepsilon_b^0\} \quad (3)$$

$$\{\kappa\} = \begin{Bmatrix} -w_{,xx} \\ -w_{,yy} \\ -2w_{,xy} \end{Bmatrix} \quad (4)$$

where $\{\varepsilon^0\}$ and $\{\kappa\}$ denote the in-plane strain and curvature vectors, respectively, and the subscripts "m" and "b" denote that the in-plane strain components are due to membrane and bending, respectively. The comma denotes the derivative.

For the k^{th} layer of a thin laminate with an orientation of θ , the stress-strain relations are

$$\{\sigma\}_k = \begin{Bmatrix} \sigma_x \\ \sigma_y \\ \tau_{xy} \end{Bmatrix}_k = \begin{bmatrix} \bar{Q}_{11} & \bar{Q}_{12} & \bar{Q}_{16} \\ \bar{Q}_{21} & \bar{Q}_{22} & \bar{Q}_{26} \\ \bar{Q}_{61} & \bar{Q}_{62} & \bar{Q}_{66} \end{bmatrix}_k \begin{Bmatrix} \varepsilon_x \\ \varepsilon_y \\ \gamma_{xy} \end{Bmatrix}_k - \Delta T \begin{Bmatrix} \alpha_x \\ \alpha_y \\ \alpha_{xy} \end{Bmatrix}_k \quad (5)$$

or

$$\{\sigma\}_k = [\bar{Q}]_k (\{\varepsilon\} - \Delta T \{\alpha\}_k) \quad (6)$$

where $[\bar{Q}]_k$ and $\{\alpha\}_k$ are the transformed reduced stiffness matrix and the coefficient of thermal expansion, respectively.

The resultant forces and moments per unit length are

$$\left\{ \begin{matrix} N \\ M \end{matrix} \right\} = \int_{-h/2}^{h/2} \left\{ \sigma \right\}_k (1, z) dz \quad (7)$$

and the constitutive equations for a laminate can be written as

$$\left\{ \begin{matrix} N \\ M \end{matrix} \right\} = \begin{bmatrix} A & B \\ B & D \end{bmatrix} \left\{ \begin{matrix} \epsilon^o \\ \kappa \end{matrix} \right\} - \left\{ \begin{matrix} N_{\Delta T} \\ M_{\Delta T} \end{matrix} \right\} \quad (8)$$

where [A], [B] and [D] are the laminate extensional, extension-bending and bending stiffness matrices, respectively. The vectors $\{N_{\Delta T}\}$ and $\{M_{\Delta T}\}$ are the in-plane force and moment due to thermal expansion

$$\left\{ \begin{matrix} N_{\Delta T} \\ M_{\Delta T} \end{matrix} \right\} = \int_{-h/2}^{h/2} [\bar{Q}]_k \Delta T \left\{ \alpha \right\}_k (1, z) dz \quad (9)$$

Using the principle of virtual work, the nonlinear element equations of motion are derived with the internal and external virtual work as

$$\begin{aligned} \delta W_{int} &= \int_A \left(\left\{ \delta \epsilon^o \right\}^T \left\{ N \right\} + \left\{ \delta \kappa \right\}^T \left\{ M \right\} \right) dA \\ \delta W_{ext} &= \int_A \left\{ \delta w \left(p(x, y, t) - \rho h w_{,tt} \right) - \delta u \left(\rho h u_{,tt} \right) - \delta v \left(\rho h v_{,tt} \right) \right\} dA \end{aligned} \quad (10)$$

and the element equations of motion can be expressed as

$$\begin{aligned} & \begin{bmatrix} m_b & 0 \\ 0 & m_m \end{bmatrix} \left\{ \begin{matrix} \ddot{w}_b \\ \ddot{w}_m \end{matrix} \right\} + \left(\begin{bmatrix} k_b & k_B \\ k_B^T & k_m \end{bmatrix} - \begin{bmatrix} k_{N\Delta T} & 0 \\ 0 & 0 \end{bmatrix} \right) \left\{ \begin{matrix} w_b \\ w_m \end{matrix} \right\} \\ & + \left(\begin{bmatrix} k_{1Nm} + k_{1NB} & k_{1bm} \\ k_{1mb} & 0 \end{bmatrix} + \begin{bmatrix} k_{2b} & 0 \\ 0 & 0 \end{bmatrix} \right) \left\{ \begin{matrix} w_b \\ w_m \end{matrix} \right\} = \left\{ \begin{matrix} p_{b\Delta T} \\ p_{m\Delta T} \end{matrix} \right\} + \left\{ \begin{matrix} p_b(t) \\ 0 \end{matrix} \right\} \end{aligned} \quad (11)$$

Assembling all the elements and taking into account the kinematic boundary conditions, the system equations of motion in structural node DOF can be expressed as

$$[M] \{\ddot{W}\} + ([K] - [K_{N\Delta T}] + [K_1] + [K_2]) \{W\} = \{P_{\Delta T}\} + \{P(t)\} \quad (12)$$

where [M], [K] and {P} denote the system mass, linear stiffness matrices and load vector, respectively, and [K₁], [K₂] denote the first and second order nonlinear stiffness matrices which depend linearly and quadratically on displacement {W}. The subscripts B, NΔT, Nm and NB denote that the

corresponding stiffness matrix is due to the laminate extension-bending [B], in-plane force components $\{N_{\Delta T}\}, \{N_m\} = [A]\{\epsilon_m^0\}$ and $\{N_B\} = [B]\{k\}$, respectively.

2.2 Equations of Motion in Modal Coordinates

For a given temperature rise ΔT , Eq.(12) can be solved by numerical integration in the structural node DOF with simulated random loads. This approach has been carried out for random response analysis with simulated random loads [16,17]. It turned out to be computationally costly because of (i) the large number of DOF of the system, (ii) the nonlinear stiffness matrices $[K_1]$ and $[K_2]$ are to be assembled and updated from the element nonlinear stiffness matrices at each time step, and (iii) the time step of integration has to be extremely small. Consequently, Eq.(12) is transformed into a set of truncated modal coordinates with rather small DOF. For symmetrically laminated composite and isotropic panels, the laminate coupling stiffness [B] is null, the two submatrices in Eq.(12) are

$$[K_B] = [K_{1NB}] = 0 \quad (13)$$

By neglecting the membrane inertia term, the membrane displacement vector can be expressed in terms of the bending displacement vector as

$$\{W_m\} = [K_m]^{-1} (\{P_{m\Delta T}\} - [K_{1mb}]\{W_b\}) \quad (14)$$

Then Eq.(12) can be written in terms of the bending displacement as

$$\begin{aligned} [M_b]\{\ddot{W}_b\} + ([K_b] - [K_{N\Delta T}])\{W_b\} + [K_{1bm}][K_m]^{-1}\{P_{m\Delta T}\} \\ + [K_{1Nm}]\{W_b\} + ([K_2] - [K_{1bm}][K_m]^{-1}[K_{1mb}])\{W_b\} = \{P_{b\Delta T}\} + \{P_b(t)\} \end{aligned} \quad (15)$$

In the above system, the nonlinear stiffness matrices can be expressed in terms of modal coordinates. This is accomplished by expressing the panel deflection as a linear combination of some base functions (modal transformation)

$$\{W_b\} = \sum_{r=1}^n q_r(t)\{\phi_r\} = [\phi]\{q\} \quad (16)$$

where $\{\phi_r\}$ corresponds to the normal modes of the linear vibration problem

$$\omega_r^2 [M_b]\{\phi_r\} = ([K_b] - [K_{N\Delta T}])\{\phi_r\} \quad (17)$$

Matrices $[K_{1bm}]$ and $[K_2]$ are both in function of $\{W_b\}$, they can be expressed as the sum of products of modal coordinates and nonlinear modal stiffnesses matrices as

$$\begin{aligned} [K_{1bm}] &= [K_{1mb}]^T = \sum_{r=1}^n q_r(t) [K_{1bm}]^{(r)} \\ [K_2] &= \sum_r \sum_s q_r(t) q_s(t) [K_{2b}]^{(rs)} \end{aligned} \quad (18)$$

where the super indexes of those non-linear modal stiffness matrices denote that they are assembled from the corresponding element non-linear stiffness matrices. Those non-linear stiffness matrices are evaluated with the corresponding element components $\{w_b\}^{(t)}$ obtained from the known system mode $\{\phi_r\}$.

The nonlinear stiffness matrix $[K_{1Nm}]$ is linearly dependent on the displacement $\{W_m\}$. Recalling the membrane displacement vector of Eq.(14)

$$\begin{aligned} \{W_m\} &= [K_m]^{-1} (\{P_{m\Delta T}\} - [K_{1mb}] \{W_b\}) \\ &= [K_m]^{-1} \{P_{m\Delta T}\} - \sum_{r=1}^n \sum_{s=1}^n q_r(t) q_s(t) [K_{1mb}]^{(rs)} \{\phi_s\} \\ &= \{\phi_{m0}\} - \sum_{r=1}^n \sum_{s=1}^n q_r(t) q_s(t) \{\phi_{mrs}\} \end{aligned} \quad (19)$$

It is observed that $[K_{1Nm}]$ is the sum of two matrices, the first $[K_{Nm}]$ is evaluated with $\{\phi_{m0}\}$ and the second $[K_{2Nm}]$ is evaluated with $\{\phi_{mrs}\}$, as

$$[K_{1Nm}] = [K_{Nm}] - \sum_{r=1}^n \sum_{s=1}^n q_r(t) q_s(t) [K_{2Nm}]^{(rs)} \quad (20)$$

Introducing a structural modal damping $2\xi_r \omega_r \bar{M}_r [I]$, where the modal damping, ξ_r , can be determined experimentally or pre-selected from a similar structure. The equations of motion (15) reduce to a set of coupled modal equations as

$$[\bar{M}] \{\ddot{q}\} + 2\xi_r \omega_r \bar{M}_r [I] \{\dot{q}\} + ([\bar{K}_L] + [\bar{K}_{qq}]) \{q\} = \{\bar{P}\} \quad (21)$$

where the diagonal modal mass is

$$[\bar{M}] = [\phi]^T [M_b] [\phi] = \bar{M}_r [I] \quad (22)$$

the linear and cubic terms are

$$\begin{aligned} [\bar{K}_L] \{q\} &= [\phi]^T ([K_b] - [K_{N\Delta T}] + [K_{Nm}]) [\phi] \{q\} \\ &+ [\phi]^T \left(\sum_{r=1}^n q_r(t) [K_{lbm}]^{(r)} \{\phi_{m0}\} \right) \end{aligned} \quad (23)$$

$$\begin{aligned} [\bar{K}_{qq}] \{q\} &= [\phi]^T \sum_{r=1}^n \sum_{s=1}^n q_r(t) q_s(t) ([K_{2b}]^{(rs)} - [K_{2Nm}]^{(rs)} \\ &- [K_{lbm}]^{(r)} [K_m]^{-1} [K_{lbm}]^{(s)}) [\phi] \{q\} \end{aligned} \quad (24)$$

and the modal thermal and random load vector is

$$\{\bar{P}\} = [\phi]^T (\{P_{b\Delta T}\} + \{P_b(t)\}) \quad (25)$$

The nonlinear random response for a given symmetric composite or isotropic panel at certain temperature can thus be determined from Eq.(21). The advantages of using this modal equation are: (i) the number of modal equations is small (DOF of $\{q\} \ll \text{DOF of } \{W_b\}$), (ii) there is no need to assemble and update the nonlinear cubic terms since all the nonlinear modal stiffness matrices are constant matrices, and (iii) the time step of integration could be larger. For asymmetric composite panels ($[B] \neq 0$), the derivation of the governing modal equation is simpler and the readers are referred to reference [18].

2.3 Strain Calculations

After the modal displacement $\{q\}$ for a given combination of acoustic load and elevated temperature case is known, $\{W_b\}$ and $\{W_m\}$ can be evaluated with Eq.(16) and Eq.(19). The element in-plane and bending ($\pm h\{\kappa\}/2$) strain components can be calculated using Eq.(3) and Eq.(4), respectively.

2.4 Uniform Distribution Random Pressure

Consider a random pressure $p(x,y,t)$ acting on the surface of a high-speed flight vehicle. The pressure acting normal to the panel surface varies randomly in time and space along the surface coordinates x and y . The pressure $p(x,y,t)$ is characterized by a cross-spectral density function $S_p(\xi, \eta, \omega)$, where $\xi = x_1 - x_2$ and $\eta = y_1 - y_2$ are the spatial separations and ω is the frequency. The simplest form of the cross-spectral density is the truncated Gaussian white noise pressure uniformly distributed with spatial coordinates x and y

$$S_p(\xi, \eta, f) = \begin{cases} S_0 & \text{if } 0 \leq f \leq f_u \\ 0 & \text{if } f < 0 \text{ or } f > f_u \end{cases} \quad (26)$$

where S_0 is constant and f_u is the upper cut-off frequency. The expression for S_0 can be written as [8],

$$S_0 = p_0^2 10^{SPL/10} \quad (27)$$

where p_0 is the reference pressure, $p_0 = 2.90075 \cdot 10^{-9}$ psi (20 μ Pa) and SPL is the sound pressure level expressed in decibels. A typical simulated random load for the composite plate is shown in Fig 1. The band-limited white noise is simulated by a Fortran code that generates a random pressure using complex numbers with independent random phase angles uniformly distributed between 0 and 2π . The power spectrum density (PSD) value of the random process is obtained by taking the ensemble average of the Fourier transform of the random load, the PSD value is then compare to the exact one given by Eq.(27). The analyses presented are obtained for a cut-off frequency of 512 Hz for the isotropic plate and 1024 Hz for the composite plate. The selected frequency bandwidth is $\Delta\omega=0$ rad/sec (1 cycle/sec) with the random load prescribed in decibels (dB). For instance, for a uniformly Gaussian random load of 100 dB over a frequency range of 0-512 Hz corresponds to an overall SPL of 127 dB.

3. RESULTS AND DISCUSSIONS

3.1 Validation

Accurate nonlinear analytical multimode results and test data is not available in the literature. Validation of the present nonlinear modal formulation will thus consists of two parts: (i) nonlinear free vibrations to assess the accuracy of the left-side of Eq.(21) with zero damping, and (ii) linear random vibrations to validate the simulated random load $\{\bar{P}\}$ at the right-side of Eq.(21). The accuracy of the nonlinear stiffness matrices in modal coordinates has been verified in reference [19] for nonlinear free vibration of fundamental and higher modes of plates and beams. The validation of simulated random loads is by comparison of the linear displacements with linear analytical results shown in Table 1. The FPK method is an exact solution [5] to the single DOF forced Duffing equation, the present time domain numerical simulation results are also shown in Table 1.

Table 1. Comparison of RMS W_{\max}/h for a Simply Supported 15 \times 12 \times 0.040 in. Isotropic Plate

SPL (dB)	Linear Analytical		FE Lin. Num. Sim.		FPK [5]	Present
	4 modes	7 modes	4 modes	Err.%	1 mode	4 modes
90	0.2759	0.2759	0.2760	0.0362	0.249	0.266
100	0.8725	0.8725	0.8728	0.0362	0.592	0.578
110	2.7590	2.7590	2.7600	0.0362	1.187	1.432
120	8.7248	8.7250	8.7281	0.0362	2.200	2.572

3.2 Simply Supported Isotropic Plate

An isotropic rectangular plate with simply supported and immovable in-plane edge conditions $u(0,y)=u(a,y)=v(x,0)=v(x,b)=0$ subjected to random excitation is studied first. The plate is 15x12x0.040 in. (38.1x30.5x0.1 cm.) and the material properties are $E=10.5$ Msi (72.33 GPa) and $\nu=0.3$. A damping ratio $\xi=0.01$ is used for all the examples. The plate is modeled with a 6x6 mesh or 36 Bogner-Fox-Schmit (BFS) elements in a quarter plate. The number of structure node DOF $\{W_b\}$ is 144 for the system equations in Eq.(15). The number of modal equations is four and the lowest symmetric modes (1,1), (3,1), (1,3), (3,3) are included for numerical integration. The Root Mean Square (RMS) maximum deflection/h and the RMS maximum strain versus the SPL are shown in Fig.2. The maximum strain is the ϵ_y located at the plate center. Both linear small deflection and non-linear large deflection structural theories are employed, and the nonlinear theory gives lower RMS deflection and strain results. The maximum deflection and the maximum strain response time histories, probability distribution functions (PDF) and power spectrum densities (PSD) in psi^2/Hz at SPL=90 and 120 dB are shown in Figs.3 and 4, respectively. Table 2 presents the maximum deflection and maximum strain response statistical moments for the four SPL.

Table 2. Moments of the W_{\max}/h and Maximum Strain for the 15x12x0.040 Isotropic Plate

SPL dB	Rms	mean in./in.	variance in^2/in^2	skewness in^3/in^3	kurtosis in^4/in^4
W_{\max}/h					
90	0.266	0.00037	0.0706	0.00530	0.156
100	0.578	-0.00217	0.3340	-0.01210	-0.313
110	1.432	-0.00325	2.0516	-0.00679	-0.436
120	2.572	0.00615	6.6149	-0.00810	-0.529
Strain					
		$\mu\text{in./in.}$	$\mu\text{in}^2/\text{in}^2$	in^3/in^3	in^4/in^4
90	1.551×10^{-5}	-0.3396	0.00024	-0.1238	0.3296
100	3.258×10^{-5}	-1.3259	0.00106	-1.7415	-0.0232
110	1.065×10^{-4}	-0.934	0.01126	-0.2375	-0.6599
120	3.916×10^{-4}	38.76	0.01518	1.6028	4.1865

The skewness and kurtosis coefficients are defined as

$$\text{Skewness}=\mu_3/\sigma^3, \text{ Kurtosis}=\mu_4/\sigma^4-3 \quad (28)$$

where μ_k and σ are the k^{th} central moment and standard deviation, respectively. At the low 90 dB SPL, the plate behaviors basically a small deflection ($W_{\max}/h = 0.266$) random vibration dominated by the fundamental (1,1) mode as indicated in the PSD plot. The time-history response at the high 120 dB SPL is clearly a large deflection ($W_{\max}/h > 1.0$) non-linear random

vibration. This is demonstrated by the peaks in PSD plots that they are broadening and shifting to the higher frequency and by the presence of the nonzero mean in-plane strain shown in the strain plots. The large deviation from the Gaussian distribution is shown by the strain probability of Fig.4 as well as the large skewness and kurtosis values of 1.6028 and 4.1865, respectively, for strain response in Table 2.

3.3 Clamped Composite Plate

Nonlinear response of a composite plate subjected to combined acoustic and thermal loads can be determined using the present modal formulation. Three types of panel behavior: (i) small deflection random vibration about one of the two thermally buckled equilibrium positions, (ii) snap-through or oil canning phenomenon between the two buckled positions, and (iii) large nonlinear random vibration covering both thermally buckled positions, can be predicted. As the second example, a clamped rectangular Graphite-Epoxy plate of eight layers $[0/45/-45/90]_s$ is investigated. The plate is of 15x12x0.048 in. (38.1x30.5x0.12 cm.) and the material properties are: $E_1=22.5$ Msi (155 GPa), $E_2=1.17$ (8.07), $G_{12}=0.66$ (4.55), $\rho=0.1468 \times 10^{-3}$ lb-sec²/in.⁴ (1550 kg/m³), $\nu_{12}=0.22$, and $\alpha_1=-0.04 \times 10^{-6}/^{\circ}\text{F}$ ($-0.07 \times 10^{-6}/^{\circ}\text{C}$), $\alpha_2=16.7 \times 10^{-6}$ (30.1x10⁻⁶). The in-plane edges are immovable and the plate is modeled with a quarter plate 6x6 mesh. The number of system equations in structure node DOF $\{W_b\}$ is 121. The system equations are reduced to the modal coordinates using the lowest four symmetric modes.

The maximum deflection and the maximum strain response time histories, PDF and PSD at $\Delta T/\Delta T_{cr}=2.0$ and SPL=90, 100 and 120 dB are shown in Figs.5-7, respectively. The time history, PDF and PSD plots clearly show the three distinctive motions of linear vibration about one of the buckled position at low 90 dB SPL, oil canning jump behavior at moderate 100 dB, and large deflection nonlinear random vibration at high SPL of 120 dB. It is also interesting to note that the maximum thermal deflection $(W_{max}/h)_{\Delta T}$ of the plate at $\Delta T/\Delta T_{cr}=2.0$ can be also obtained from the deflection time histories in Figs.5 and 6. The maximum thermal deflection from the time history plots is $W_{max}/h=\pm 1.15$ at $\Delta T/\Delta T_{cr}=2.0$, and the thermal postbuckling analyses are $\Delta T_{cr}=36.52$ °F and $(W_{max}/h)=\pm 1.134$ from reference [20]. The deflection PDF shown in Figs. 6 and 7 demonstrate the large deviation from Gaussian distribution. The statistical moments for the maximum deflection and maximum strain response are presented in Table 3.

Table 3. Moments of the W_{\max}/h and Maximum Strain for the Clamped [0/45/-45/90]_s Plate at $\Delta T/\Delta T_{cr}=2.0$

SPL dB	Rms	mean in./in.	variance in ² /in ² .	skewness in ³ /in ³ .	kurtosis in ⁴ /in ⁴ .
			W_{\max}/h		
90	1.1502	-1.1446	0.0128	1.9214	12.127
100	1.0683	0.3667	1.0070	-0.6616	-1.2339
120	1.4475	0.0080	2.0955	-0.0149	-0.7977
			Strain		
		$\mu\text{in./in.}$	$\mu\text{in}^2/\text{in}^2.$	$\text{in}^3/\text{in}^3.$	$\text{in}^4/\text{in}^4.$
90	2.567×10^{-4}	251.636	0.002558	-1.2716	4.965
100	2.397×10^{-4}	161.351	0.003142	-1.1297	0.4679
120	5.219×10^{-4}	46.799	27.0207	-0.0422	-0.3237

4. CONCLUSION

A finite element time domain modal formulation is presented for the prediction of non-linear random response of composite panels subjected to acoustic pressure at elevated temperature. The modal formulation is computationally efficient that (i) the number of modal equations is small, (ii) the non-linear modal stiffness matrices are constant matrices, and (iii) the time step of integration could be reasonably large. It is demonstrated that all three types of panel motions: (i) linear random vibration about one of the buckled equilibrium position, (ii) snap-through motions between the two buckled positions, and (iii) non-linear random response over both buckled positions can be predicted. Results of deflection PDF at the high SPL also show that the assumption of Gaussian distribution by the equivalent linearization technique is inappropriate

ACKNOWLEDGEMENT

The first three authors would like to acknowledge the support by AFRL contract F33615-98-D-3210 No.5.

REFERENCES

1. Clarkson, B.L., Review of sonic fatigue technology. *NASA CR-4587*, 1994.
2. Wolfe, H.F., Shroger, C.A., Brown, D.L. and Simmons, L.W., An experimental investigation of nonlinear behavior of beams and plates excited to high levels of dynamic response. *WL-TR-96-3057*, Wright-Patterson AFB, OH, 1995.
3. Istenes, R.R. Jr, Rizzi, S.A. and Wolfe, H.F., Experimental nonlinear random vibration results of thermally buckled composite panels, *AIAA-95-1345*, 1995.

4. Iwan, W.D. and Yang, M.I., Application of statistical linearization techniques to nonlinear multi-degree of freedom systems. *J. Applied Mechanics*, 1972, Vol.39, 545-550.
5. Bolotin, V.V., *Random Vibration of Elastic Systems*, Martinus Nijhoff Publishers, pp:290-292, 1984.
6. Shinozuka, M. and Jan, D.M., Digital simulation of random processes and its applications. *J. Sound Vibration*, 1972, Vol.25,111-128.
7. Shinozuka, M. and Wen, Y.K., Monte Carlo solution of nonlinear vibrations. *AIAA J.*, Vol.10, No.1, 1972, 37-40.
8. Arnold, R.R. and Vaicaitis, R., Nonlinear response and fatigue of surface panels by the time domain Monte Carlo approach, *WRDC-TR-90-3081*, Wright-Patterson AFB, OH, 1990.
9. Vaicaitis, R. and Kavallieratos, P.A., Nonlinear response of composite panels to random excitation. *Proceedings 34th Structures, Structures Structural Dynamics and Materials Conference*, La Jolla, CA, 1993, 1041-1049.
10. Vaicaitis, R., Recent advances of time domain approach for nonlinear response and sonic fatigue. *Proceedings 4th International Conference on Structural Dynamics, ISVR*, 1991, 84-103.
11. Elishakoff I. and Zhang, X., An appraisal of different stochastic linearization techniques. *J. Sound Vibration*, 1992, Vol.153, 370-375.
12. Roberts, J.B. and Spanos, P.D., *Random Vibration of Statistical Linearization*, John Wiley & Sons, NY, 1990.
13. Locke J.E, Mei C., A finite element formulation for the large deflection random response of thermally buckled beams, *AIAA J.*, 1990, Vol. 28, 2125-2131.
14. Locke, J.E., A finite element formulation for the large deflection random response of thermally buckled structures. *Ph.D. Dissertation*, Old Dominion University, 1988.
15. Mei, C. and Chen, R.R., Finite element nonlinear random response of composite panels of arbitrary shape to acoustic and thermal loads applied simultaneously. *WL-TR-97-3085*, Wright-Patterson AFB, OH, 1997.
16. Green, P.D. and Killey, A., Time domain dynamic finite element modeling in acoustic fatigue design, *Proceedings 6th International Conference on Structural Dynamics, ISVR*, 1997, 1007-1026.
17. Robinson, J.H., Finite element formulation and numerical simulation of the large deflection random vibration of laminated composite plates. *MS Thesis*, Old Dominion University, 1990.
18. Zhou R.C., Xue D.Y. and Mei C., Finite element time domain modal formulation for nonlinear flutter of composite panels, *AIAA J.*, 1994, Vol.32, 2044-2052.
19. Shi, Y., Lee, R. and Mei, C., A Finite element multimode method to nonlinear free vibrations of composite plates, *AIAA J.*, 1997, Vol.35, 159-166.

20. Mei, C., Duan, B., Zhang, Z. and Wolfe, H.F. Large thermal deflections of composite plates with temperature dependent properties", *AFRL-VA-WP-TR-1999-3036*, Wright-Patterson AFB, OH, 1999.

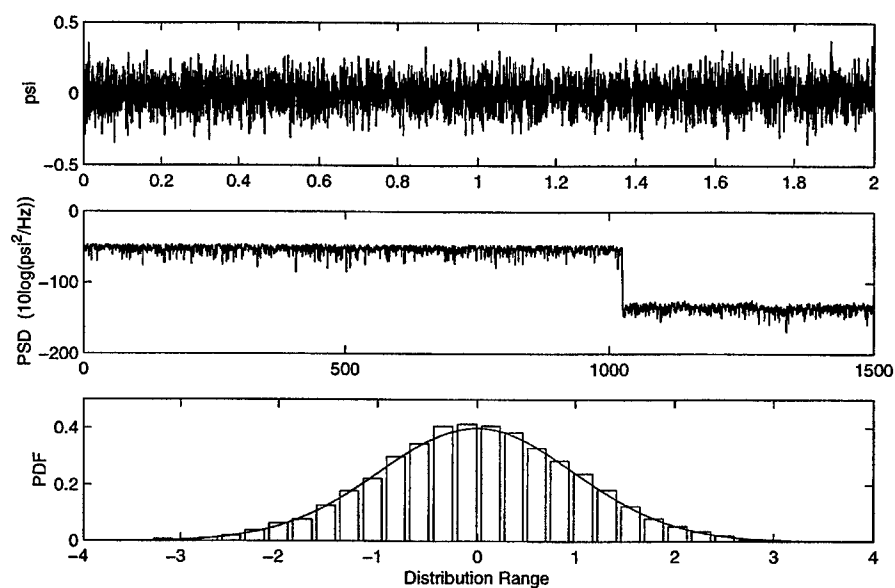


Figure 1. Random Noise Generation

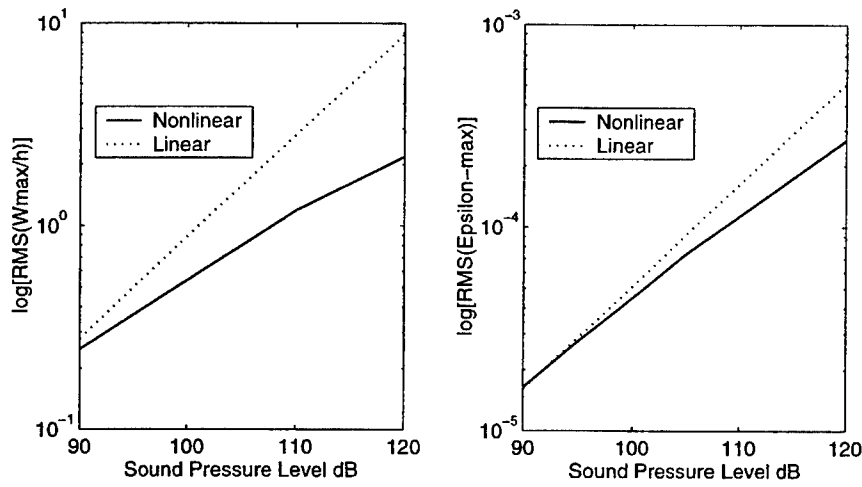


Figure 2. RMS Displacement and Strain versus SPL of an Isotropic Simply Supported Plate

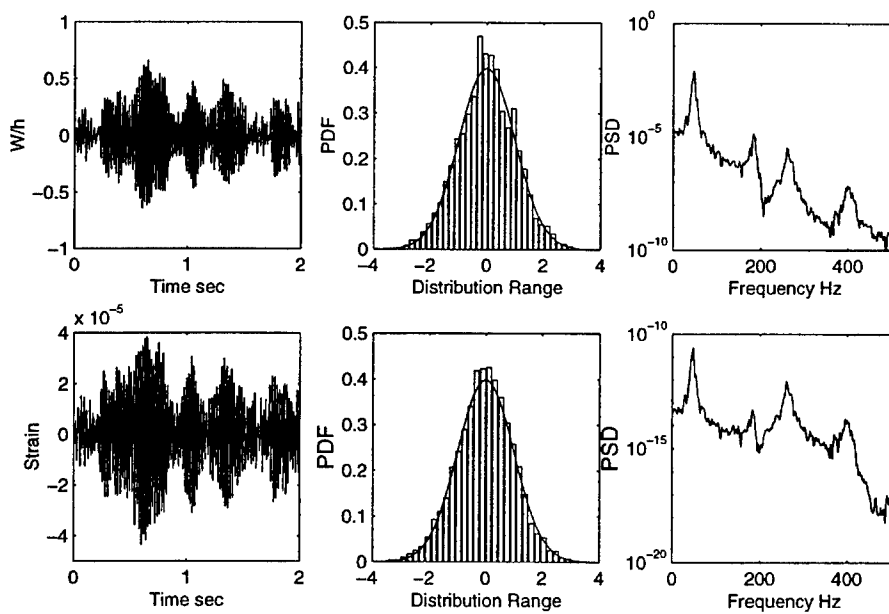


Figure 3. Random Response of an Isotropic Simply Supported Plate at $\text{SPL}=90$ dB

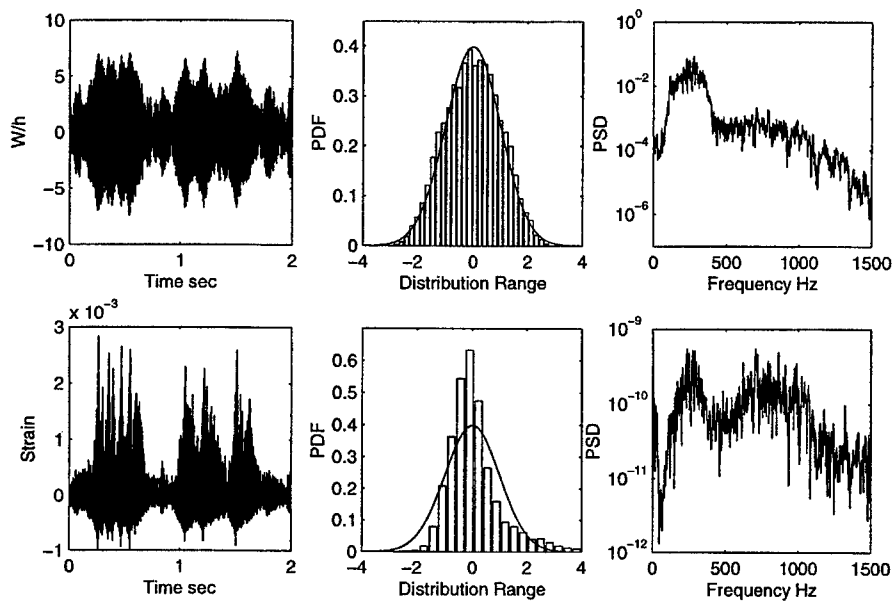


Figure 4. Random Response of an Isotropic Simply Supported Plate at SPL= 120 dB

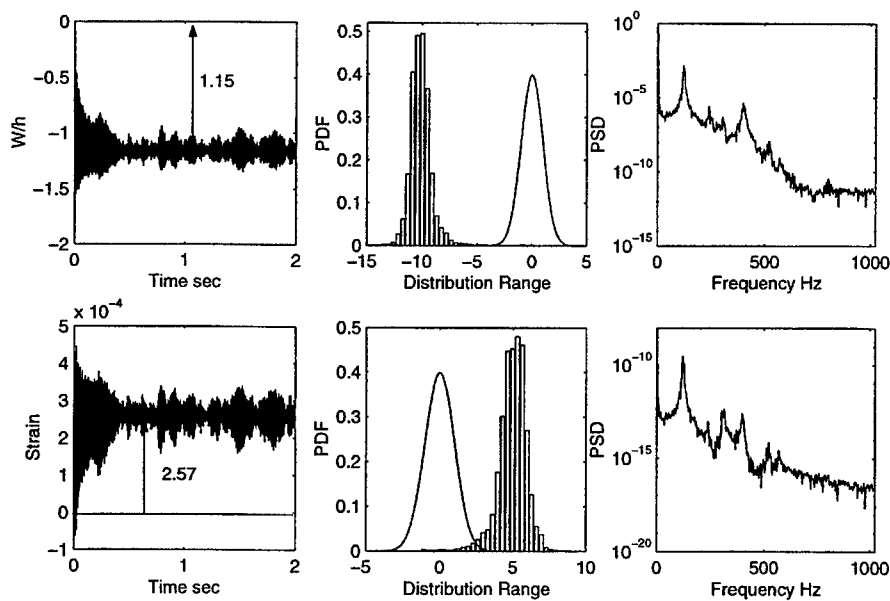


Figure 5. Random Response of a $[0/45/-45/90]_s$ Composite Plate at SPL=90 dB and $\Delta T/\Delta T_{cr}=2.0$

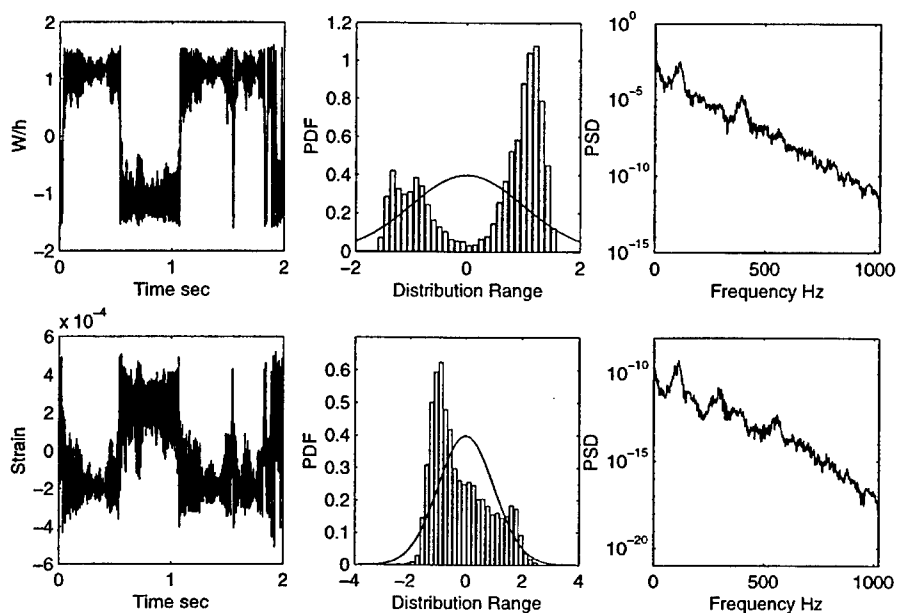


Figure 6. Random Response of a $[0/45/-45/90]_s$ Composite Plate at $SPL=100$ dB and $\Delta T/\Delta T_{cr}=2.0$

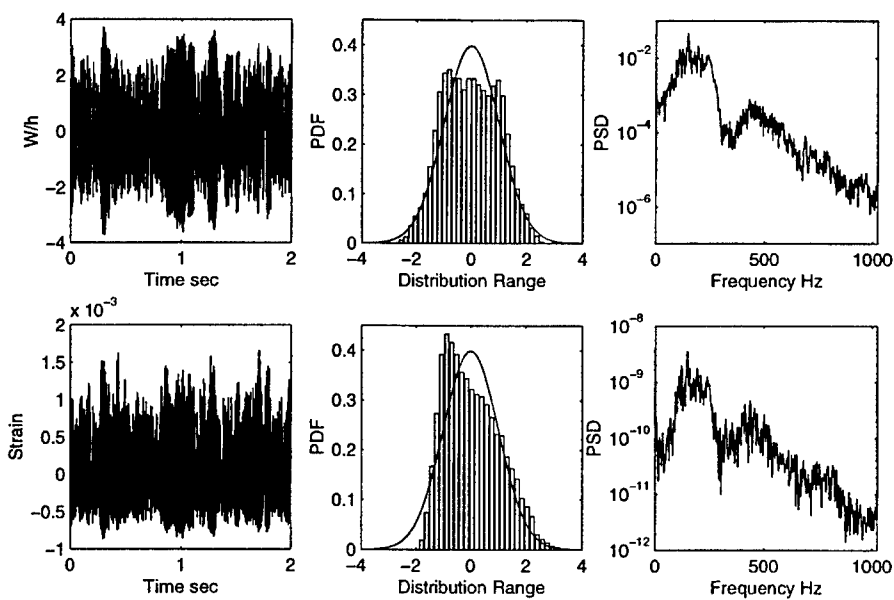


Figure 7. Random Response of a $[0/45/-45/90]_s$ Composite Plate at $SPL=120$ dB and $\Delta T/\Delta T_{cr}=2.0$

THE EFFECTS OF RECORD LENGTH ON DETERMINING THE CUMULATIVE DAMAGE OF A CERAMIC MATRIX COMPOSITE BEAM

S. Michael Spottswood

Howard F. Wolfe

Dansen L. Brown

Structures Division, Flight Dynamics Directorate, Air Force Research
Laboratory, 2145 Fifth St. Ste 2, Wright-Patterson AFB, OH, 45433-7006, USA.

ABSTRACT

The effect of record length on the calculated fatigue life was determined for ceramic matrix composite (CMC) Blackglas™ beams. The root mean square (RMS) strain and peak probability density functions (PPDFs) are critical variables in the estimation of fatigue life. Therefore, accurate estimation of fatigue life requires the convergence of the previously mentioned variables. In this analysis, the statistical moments, including the mean, variance, skewness and kurtosis for the input/output signals of various time segments of a 70-minute time history were determined. The time history was divided into cumulative segments, allowing the properties to reach convergence as the duration of the respective cumulative record increased. Results indicate convergence of the RMS values for both the input and output signals was achieved within the first 60 seconds. In addition, PPDFs for the same cumulative data segments were determined for the input and output signals. Results indicate convergence of the PPDFs within the first 60 seconds. Fatigue life calculations and cumulative damage plots also indicate convergence in approximately 60 seconds. Fatigue life and cumulative damage comparisons made with a modified Rayleigh distribution, yielded significantly more conservative results.

INTRODUCTION

With the increasing use of composite materials in the design of critical aircraft structural components, developing accurate life prediction techniques is crucial. Recent developments in the field of ceramic matrix composites require the understanding of their behavior in extreme thermal and acoustic environments. Accurate characterization is essential, as minor variances in life prediction can result in significant differences in structural design. An overly conservative design can result in undesirable weight penalties, while under conservative designs can result in premature failures.

High sigma events were previously studied for the narrow band random response of a CMC Blackglas™ cantilevered beam excited by a 4,000 lb_f electrodynamic shaker using a half-sine clamp [1-3], shown in Fig. 1. The testing examined the effects of clipping the input signal to the shaker. Tests were conducted without shaker sigma limiting, sigma limited to 3.5 and sigma limited to 2.5. For the purposes of this investigation, sigma is defined as the ratio of the amplitudes or peaks of the appropriate probability density functions to the respective standard deviation. Long duration time histories of the high sigma strain responses were required in order to capture 6 sigma extreme events. Long time records as well as high sampling rates are needed when examining the effects of time sampling on the statistical properties of the signals, as the length of the data record affects the statistical properties. The record length of most dynamic tests is rather short in duration and is usually truncated after 5-30 seconds. This is typically the case for well established sinusoidal and stationary random data. The record length is minimized for practical purposes, i.e., reducing the record storage space and required processing hardware. The record lengths involved in the aforementioned testing, required approximately 8 gigabytes of storage space for one four-channel record in addition to the required capability of processing and presenting the results.

The purpose of this investigation was to examine the effect of record length on the peak probability density functions (PPDFs), RMS values, and the statistical moments. Essentially, what record length is sufficient for the test data to be assumed stationary. Typically, the statistical properties of random data are taken to be stationary or consistent over time, provided that the time history is of significant duration and damage has not occurred within the specimen. Truly random data is non-stationary, however, stationarity is often assumed if the statistical properties do not change significantly with time. Previous studies investigated the effect that the time record had on the PPDF of a clamped plate [4]. However, as the time records only include 20 second and 3.5-hour segments, a more detailed analysis was required.

FATIGUE MODEL DEVELOPMENT

The Miner single modal fatigue model was selected to characterize the fatigue life of the CMC Blackglas™ cantilevered beam specimens and is expressed in the following equation:

$$N_t = \left[\sum \frac{P(\epsilon)}{N} \right]^{-1} \quad (1)$$

where N_t is the total number of cycles to failure, $P(\epsilon)$ is the peak strain probability density, and N is the total number of cycles to failure at incremental constant amplitude strain levels [5-8]. Expressing Eq. (1) in terms of hours results in the following:

$$t(\text{hours}) = \left\{ \left[\sum \frac{P(\text{sd})}{N_c} \right] 3600 \cdot f_c \right\}^{-1} \quad (2)$$

where $P_p(\text{sd})$ is the peak standard deviation probability density, N_c is the total number of cycles to failure at a specified strain level, and f_c is the cyclic frequency. For a single mode case, the cyclic frequency is taken to be the natural frequency. The minor peak counting method was used to determine the PPDF, which is consistent with previous fatigue studies [8]. This method accounts for all stress reversals or a positive slope followed by a negative slope in the time record. Typically, ϵ -N or S-N reverse bending curves on a log-log plot are characterized using the following expression:

$$\epsilon = \left[\frac{K}{N_c} \right]^{\alpha} \quad (3)$$

where K and α are constants dependent upon the material properties. Finally, incorporating Eq. (3) into Eq. (2) yields the following relation:

$$t(\text{hours}) = \left\{ \left[\sum \frac{P(\text{sd})}{K/(\epsilon)^{1/\alpha}} \right] 3600 \cdot f_c \right\}^{-1} \quad (4)$$

where the fatigue life in hours is defined in terms of the strain, ϵ , and the material properties K and α .

RECORD LENGTH EFFECTS

The data used in this investigation was collected during previously accomplished testing on CMC Blackglas™ beams [3]. Tests were conducted with a 4,000 lb_i electrodynamic shaker; with sigma limiting turned off, limited to 2.5 and limited to 3.5. The sampling rate for all test scenarios was 32,000 cycles/sec. Input excitation was monitored using an accelerometer on the shaker, while strain measurements were made with gauges at the beam-clamp interface. The beam displacement was monitored using a vibrometer. Displacement measurements were made slightly removed from the beam-clamp interface, shown in Fig. 1 as the light-colored patch on the

beam surface. The strain gauge results used in this investigation were gathered using a gauge positioned at the beam-clamp interface, aligned along the beam axis of symmetry. Shown in Fig. 2 is the excitation or accelerometer spectral density. Similarly, Fig. 3 displays the response or vibrometer spectral density. Notice that the frequency bandwidth, 174-258 Hz, only included the first modal frequency, 222 Hz.

In order to capture the high sigma events in question, many hours of testing was required. The amount of data recording lent itself to further investigation on the effects of truncation after minimal testing. Typically, testing of this nature is truncated after 5-30 seconds. The time history for this test was divided into successively larger cumulative time segments. The first minute of testing was separated into 5, 15, 30, 45 and 60 second records. After the first minute, 100, 300, 600, 1800 and 4200 second cumulative time histories were investigated. Under consideration, were the effects of the cumulative time records on the respective statistical moments, PPDFs, and ultimately the fatigue life of the specimen.

Convergence of statistical moments

The statistical moments, or the mean, standard deviation, variance, skewness and kurtosis, for the amplitude probability density functions (APDFs) were determined for the input and output cumulative time records. The mean (\bar{x}), or expected value, of a discrete distribution is defined for a set of N values of x_n in the following expression:

$$\bar{x} = \frac{1}{N} \sum_{n=1}^N x_n \quad (5)$$

The mean-square value ($\overline{x^2}$), defined by the second moment, is shown in the following expression:

$$\overline{x^2} = \frac{1}{N} \sum_{n=1}^N x_n^2 \quad (6)$$

The variance (sd^2), defined as the mean-square value about the mean, is shown in the proceeding expression:

$$sd^2 = \frac{1}{N} \sum_{n=1}^N (x_n - \bar{x})^2 \quad (7)$$

or:

$$sd^2 = \overline{x^2} - (\bar{x})^2 \quad (8)$$

where the variance, (sd^2) , is defined as a function of the mean (\bar{x}) and the mean-square $(\overline{x^2})$. For a distribution with a mean equal to zero, the RMS is directly equal to the standard deviation, where the standard deviation (sd) is the positive square root of the variance. Together, the standard deviation and variance measure the spread of a distribution about the mean value [9].

The skewness (γ_1) , or the third moment shown in the following equation, is a measure of the degree to which a distribution is asymmetrical:

$$\gamma_1 = \frac{1}{N} \sum_{n=1}^N (x_n - \bar{x})^3 \quad (9)$$

where \bar{x} is the mean. For example, if the distribution is shifted to the right, this denotes a positive skewness. The kurtosis (γ_2) , or the fourth moment, is a measure of the peakedness of the distribution and is defined in the following expression [10]:

$$\gamma_2 = \frac{1}{N} \sum_{n=1}^N (x_n - \bar{x})^4 \quad (10)$$

For a Gaussian distribution, the mean and skewness are zero, and the kurtosis is three. Note in Table I, that the kurtosis of the center strain gauge, or response data, converges to a value of 3.214. This indicates a sharper distribution as compared to a Gaussian distribution. APDFs for the response data are displayed in Fig. 4 for several cumulative time records.

As expected, longer experimental time records resulted in convergence of the respective statistical moments. Included in the analysis of the statistical properties are 95% confidence intervals of the mean value of each statistic, shown in Figs. 5-8 by the "bars" surrounding each data point. Each cumulative record length was divided into 10 even segments. The statistical property being examined was calculated for each of the 10 segments, and the 95% confidence intervals were then estimated from the mean and standard deviation of those 10 values using a Student t distribution [11]. Notice that the confidence intervals themselves are narrowing as the cumulative time record lengthens, indicating convergence of the statistical properties themselves.

Estimates of the statistical properties are shown in Tables I and II. Considering the entire 4200 second output time record, the mean was $-1.460 \mu\epsilon$, the skewness was 0.229 and the kurtosis was 3.214. The output signal mean value of $-1.460 \mu\epsilon$ resulted in the RMS strain essentially equating to the standard deviation as shown in Table I. For the data records discussed in this report, the RMS values were

approximately equal to the standard deviation values for all time records.

Considering Tables I and II, note that convergence of both the center strain gauge and accelerometer data was realized within approximately 60 seconds. Since the ultimate goal of this investigation was to determine the effects of cumulative time records on fatigue life, the RMS values and PPDFs, to be discussed subsequently, were used to define convergence. For example, within 60 seconds, the RMS input and output values represent less than a 1% difference as compared to the 4200 second time record. Specifically, the rate of convergence, or the rate that the RMS values were changing with respect to the 4200 second time record, was negligible after 60 seconds. This convergence trend continued for the variance, skewness and kurtosis, although, as shown in Tables I and II, not all of the statistical properties represent less than a 1% difference in the first 60 seconds. In an effort to further characterize convergence, comparisons will be made between the 5, 60 and 4200 second time records for both the input and output signals. Therefore, examining Tables I and II, the 5, 60 and 4200 second time records reveal RMS values of 164.8, 192.6 and 193.7 $\mu\epsilon$ for the output signal or center strain gauge. Comparing the 5 and 60 second records to the 4200 second record, represent 14.92% and 0.567% differences respectively. Similarly, the 5, 60 and 4200 second time records reveal RMS values of 3.748, 3.886 and 3.919 g's for the input signal, resulting in 4.363% and 0.842% differences in the 5 and 60 second input time records, as compared to the 4200 second record. Examining Fig. 5, the 95% confidence intervals for the 5, 60 and 4200 second time records represent ± 18.50 , ± 9.833 and ± 1.474 $\mu\epsilon$ for the center strain gauge and ± 0.166 , ± 0.069 and ± 0.007 g's for the accelerometer.

Examining the 5, 60 and 4200 second time records in Table I, reveal variance (sd^2) values of 27160, 37070 and 37520 ($\mu\epsilon$)² for the output signal. Comparing the 5 and 60 second records to the 4200 second record, resulted in 27.61% and 1.199% differences. Similarly, the 5, 60 and 4200 second time records reveal values of 14.05, 15.10 and 15.36 (g)² for the input signal, resulting in 8.523% and 1.693% differences in the 5 and 60 second input time records, as compared to the 4200 second record. Examining Fig. 6, the 95% confidence intervals for the 5, 60 and 4200 second time records represent ± 6090 , ± 3735 and ± 568.8 ($\mu\epsilon$)² for the center strain gauge and ± 1.253 , ± 0.542 and ± 0.054 (g)² for the accelerometer.

The convergence of the skewness (γ_1) is likewise displayed in Tables I and II. Values for the 5, 60 and 4200 second APDFs for the center strain gauge signal were 0.2185, 0.2291 and 0.2287 respectively.

This represents a 4.459% and 0.175% difference when comparing the 5 and 60 second records to the 4200 second time record. The skewness of the 5, 60 and 4200 second APDFs for the accelerometer was 1.92E-3, 8.39E-4 and 8.99E-4 respectively. This equates to a 113.5% and 6.692% difference when comparing the 5 and 60 second records to the 4200 second time record. Examining Fig. 7, the 95% confidence intervals for the 5, 60 and 4200 second time records represent a spread of ± 0.012 , ± 0.002 and $\pm 3E-4$ for the center strain gauge and ± 0.003 , $\pm 6.0E-4$ and $\pm 7.0E-5$ for the accelerometer.

Finally, examining the 5, 60 and 4200 second time records APDFs, reveal a kurtosis (γ_2) of 2.696, 3.286 and 3.214 for the output signal shown in Table I. Comparing the kurtosis of the 5 and 60 second APDFs to the 4200 second APDF, revealed 16.12% and 2.240% differences. Similarly, the 5, 60 and 4200 second time records in Table II, reveal values of 2.916, 2.969 and 2.919 for the input signal, resulting in 0.103% and 1.713% differences in the 5 and 60 second input time records as compared with the 4200 second record. Examining Fig. 8, the 95% confidence intervals for the 5, 60 and 4200 second time records represent a spread of ± 0.279 , ± 0.220 and ± 0.038 for the center strain gauge and ± 0.212 , ± 0.064 and ± 0.012 for the accelerometer.

Convergence of the peak probability density functions

Normalized PPDFs were determined for the output signal and are shown for selected cumulative time records in Fig. 9. The PPDF for each time record was normalized with its respective standard deviation value. Note the difference in distribution between the experimental strain gauge or output signal PPDFs and the modified Rayleigh PDF, displayed for comparison purposes. The difference in the distributions result in significant variations in the estimated fatigue life, as will be discussed subsequently.

Minimal differences in the experimental PPDFs can be determined visually for time records greater than 30 seconds in length. A measure of discrepancy was used in order to quantify convergence in the PPDFs. The mean integrated square error (MISE) shown in the following expression quantified the error or difference in PPDFs, assuming the 4200-second time record was the true density:

$$MISE(\hat{f}(x)) = E \int \{\hat{f}(x) - f(x)\}^2 dx \quad (11)$$

where $f(x)$ is the true density and $\hat{f}(x)$ is the estimator [12]. As the PPDFs of the cumulative records approach the distribution seen in the 4200-second record, MISE approaches zero. The results of Eq. (11) are

shown in Fig. 10, where again, differences in the PPDFs were negligible within approximately 60 seconds.

Convergence of the estimated fatigue life

For each of the cumulative time records, the estimated fatigue life was calculated using Eq. (4). The CMC Blackglas™ 3% S-N curve displayed in Fig. 11, resulted in a K and slope α of $1.06 \times 10^{30} (\mu\epsilon)^{1/\alpha}$ and -0.108 respectively. Note that the value of K is dependent upon the form of Eq. (3). In the absence of an appropriate CMC Blackglas™ correction factor, a 7075-T6 Aluminum correction factor (C_f) of 1.38 was used to convert the random ϵ -N curve to the approximate sinusoidal model [13]. In addition to the CMC Blackglas™ S-N curves, 7075-T6 Aluminum was included for comparison purposes. Note the relative shallow slope of the Blackglas™ specimen, resulting in greater sensitivity to the fatigue calculations, i.e., a small change in RMS strain resulted in a significant change in estimated fatigue life. The cyclic frequency, f_c , was taken to be the experimentally measured beam resonant frequency, or 222 Hz. The estimated fatigue life for the cumulative time segments is displayed in Fig. 12. Note again, that the lifetime has stabilized within the first 60 seconds. The 45 and 60 second time records resulted in fatigue life estimates of 13.9 and 13.1 hours compared with a fatigue lifetime of 13.2 hours for the 4200-second time record. Note the wide variation in fatigue life within the first 60 seconds. After recording only 5, 15 and 30 seconds of data, the estimated life was 143, 41.0 and 32.2 hours respectively. The wide variability of results underscores the importance of realizing the convergence of both the RMS strains and PPDFs.

For a narrow-band, random scenario, as experienced in the test effort, the peak probability density distribution approaches a Rayleigh distribution. Therefore, for comparison purposes, the fatigue life was also calculated for a modified Rayleigh PDF. A general Rayleigh distribution is given by the following equation:

$$p(x_p) = x_p e^{(-1/2)x_p^2} \quad (12)$$

where x_p in this case represents the independent variable, or sigma [9]. A standard deviation value of $200\mu\epsilon$ was utilized for the modified Rayleigh fatigue calculation. Taking the absolute value of Eq. (12) in order to represent both positive and negative sigma events, modified the Rayleigh distribution, shown in Fig. 9. Note that the results using the modified Rayleigh PDF are extremely conservative, with an estimated fatigue life of only 0.47 hours. The conservative result can

be attributed to the relatively significant occurrence of high sigma events, i.e., the regions at the extreme ends or "tails" of the modified Rayleigh distribution. Since the extreme events, or high sigma values, equate to high strain and therefore relatively few cycles to failure, the occurrence of these events significantly reduces the overall estimated life of the specimen. In addition, due to the nonlinear response exhibited by the beam, the modified Rayleigh distribution may not be appropriate as a fatigue life estimator.

The cumulative damage for each of the PPDFs was determined, by considering the associated damage attributed to each sigma event throughout the distributions. The cumulative damage results are shown in Fig. 13. Immediately noticeable, is the greater occurrence of failure in the positive sigma region for all time records. In other words, while the modified Rayleigh distribution shows an equal distribution of damage for both the positive and negative sigma regions, the experimental time records reveal a significantly greater occurrence of damage in the positive sigma region. As an example, consider the 5-second time record in Fig. 13, where nearly 80% of the total damage occurred in the positive sigma region. This was due to the peak asymmetry of the experimental PPDF distributions, shown in Fig. 9. In other words, the relative spread in the positive and negative sigma regions is significantly different. The peak elevation in the positive sigma region differs from that in the negative sigma region. The lower peaks, shown in Fig. 9, in the positive sigma region resulted in a greater occurrence of extreme events or events within the positive sigma "tails" and therefore significantly more damage. By 45 seconds of recording, the cumulative damage trend displayed in Fig. 13 had stabilized, with approximately 65% of the total damage occurring within the positive sigma region.

CONCLUSION

Ultimately, the results of this study will be used as a benchmark for future random vibration testing of CMC coupons. The goal of this work was to determine the minimum amount of recording time required to generate accurate fatigue estimation results. Typically, between 5 and 30 seconds of data is collected for experimental random vibration testing. Results of this investigation demonstrate the wide variability of results within the first 60 seconds of testing. However, it is important to note that the 60 second convergence result is applicable to this geometry only, and that the results presented in this report should be used to establish general trends. Results indicate that a

minimum of 60 seconds of data was required for convergence of the estimated fatigue life for the CMC beam. This conclusion is based upon the analysis of successive cumulative time records from previously accomplished random vibration testing. First, a study of the statistical properties of both the input and output signal was accomplished. Results in the form of RMS strain/acceleration, variance, skewness and kurtosis were determined. Next, the respective PPDFs for the various time records were computed and the convergence was verified using the mean integrated square error technique. Finally, the estimated fatigue life of the specimen was calculated for the cumulative time record PPDFs as well as for a modified Rayleigh PDF. All experimental results indicate reasonable convergence within the first 60 seconds of recording, while the modified Rayleigh distribution is inappropriate as a fatigue life estimate due to the nonlinear nature of the beam response.

REFERENCES

- [1] H. F. Wolfe, M. P. Camden, D. L. Brown, L. W. Simmons. "Six sigma effects on the response of a cantilevered beam with random excitation," *67th Shock and Vibration Symposium*, Monterey, CA, November 18-22, 1996.
- [2] M. P. Camden, Donald B. Paul, L. W. Simmons, H. F. Wolfe, Larry W. Byrd. "High cycle fatigue testing of BLACKGLAS™ composite coupons using a half sine clamp," *68th Shock and Vibration Symposium*, Hunt Valley, MD, November 4-7, 1997.
- [3] H. F. Wolfe, M. P. Camden, D. L. Brown, L. W. Simmons. "Sigma limiting effects on the response of a ceramic matrix beam," *AIAA 40th Structures, Structural Dynamics and Materials Conference (SDM)*, St. Louis, Missouri, April 12-15, 1999.
- [4] H. F. Wolfe, M. P. Camden, K. R. Wentz, L. W. Simmons. "Determining the peak probability distribution function of the nonlinear random response of a clamped plate," *Second International Conference on Non-linear Problems in Aviation and Aerospace*, Daytona Beach, FL, April 29-May 1, 1998.
- [5] Miner, M.A., Cumulative damage in Fatigue, *Trans. ASME, J. Applied Mechanics*, 67, A159-A182, 1945.

[6] M. M. Bennouna and R. G. White, "The effects of large vibration amplitudes on the dynamic strain response of a clamped-clamped beam with consideration on fatigue life," *Journal of Sound and Vibration*, 96 (3): 281-308, 1984.

[7] J. R. Ballentine, F. F. Rudder, J. T. Mathis and H. E. Plumblee, "Refinement of sonic fatigue structural design criteria," AFFDL TR 67-156, D831118, Wright-Patterson AFB, Ohio, 1968.

[8] H. F. Wolfe and R. G. White, "The development and evaluation of a new multimodal acoustic fatigue damage model," *Sixth International Conference on Recent Advances in Structural Dynamics*, University of Southampton, UK, 14-17 July 1997.

[9] W. T. Thomson. *Vibration theory and applications*. Englewood Cliffs, N.J., Prentice-Hall Inc., 1965.

[10] R. G. DeJong, (editor), "Compendium of methods for applying measured data to vibration and acoustic problems", AFWAL-TR-85-3080, Wright-Patterson AFB, OH, 1985.

[11] Bendat, J. S., and Piersol, A. G, *Measurement and analysis of random data*. New York: John Wiley & Sons, Inc., 1966.

[12] B. W. Silverman. *Density Estimation for Statistics and Data Analysis*. New York: Chapman and Hall Ltd, 1986.

[13] H. F. Wolfe, K. R. Wentz, M. P. Camden and L. W. Simmons. "The development and evaluation of a new multimodal acoustic fatigue damage model: effects of multimodal frequency," *39th SDM Conference*, Long Beach, CA, 20-23 April, 1998.

Table I – Statistical properties for center strain gauge					
Time (sec)	RMS ($\mu\epsilon$)/% Diff	sd ($\mu\epsilon$)/% Diff	sd ² ($\mu\epsilon$) ² / % Diff	γ_1 / % Diff	γ_2 / % Diff
5	164.8/14.92	164.8/14.92	27160/27.61	0.2185/4.459	2.696/16.12
15	186.3/3.820	186.3/3.820	34690/7.543	0.2279/0.349	2.911/9.423
30	185.6/4.182	185.6/4.182	34430/8.235	0.2279/0.349	2.989/7.0
45	190.3/1.756	190.3/1.756	36200/3.518	0.2296/0.393	3.299/2.645
60	192.6/0.568	192.5/0.619	37070/1.199	0.2291/0.175	3.286/2.240
100	196.4/1.394	196.4/1.394	38560/2.772	0.2284/0.131	3.181/1.027
300	193.8/0.052	193.8/0.052	37540/0.053	0.2291/0.175	3.242/0.871
600	194.7/0.516	194.6/0.465	37890/0.986	0.2287/0	3.278/1.991
1800	194.4/0.363	194.4/0.363	37790/0.719	0.2285/0.087	3.235/0.653
4200	193.7	193.7	37520	0.2287	3.214

Table II – Statistical properties for accelerometer					
Time (sec)	RMS (g)/% Diff	sd (g)/% Diff	sd ² (g) ² / % Diff	γ_1 / % Diff	γ_2 / % Diff
5	3.748/4.363	3.748/4.363	14.05/8.523	0.00192/113.5	2.916/0.103
15	3.818/2.577	3.818/2.577	14.58/5.078	0.00110/22.39	2.89/0.994
30	3.923/2.449	3.923/2.449	14.61/4.883	0.00086/4.824	2.919/0
45	3.85/1.761	3.85/1.761	14.82/3.516	0.00059/34.63	2.971/1.781
60	3.886/0.842	3.886/0.842	15.1/1.693	0.00084/6.692	2.969/1.713
100	3.946/0.689	3.946/0.689	15.57/1.367	0.00099/9.715	2.937/0.617
300	3.902/0.434	3.902/0.434	15.23/0.846	0.00099/10.85	2.932/0.445
600	3.911/0.204	3.911/0.204	15.3/0.391	0.00092/1.968	2.939/0.685
1800	3.918/0.026	3.918/0.026	15.35/0.065	0.00089/0.945	2.925/0.206
4200	3.919	3.919	15.36	0.00089	2.919

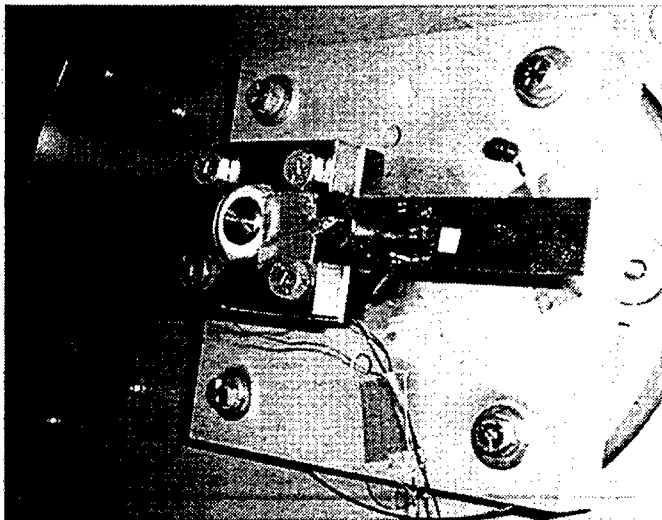


Figure 1: CMC Blackglas™ specimen in half-sine clamp

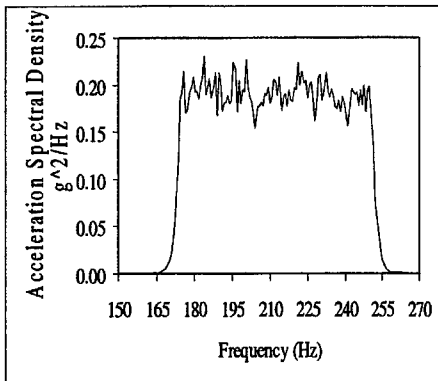


Figure 2: Excitation spectral density, 174-258 Hz

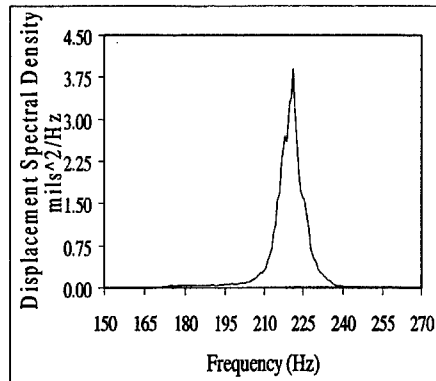


Figure 3: Response spectral density, 174-258 Hz

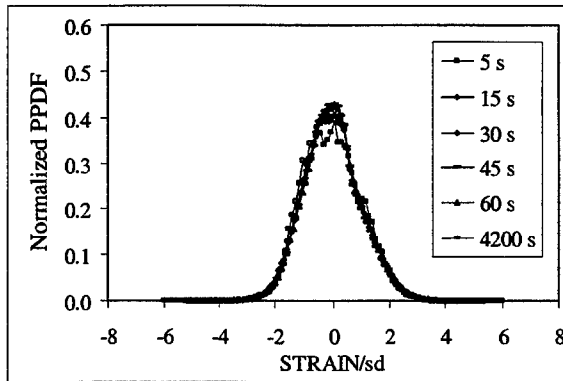


Figure 4: APDFs for center strain gauge cumulative time records

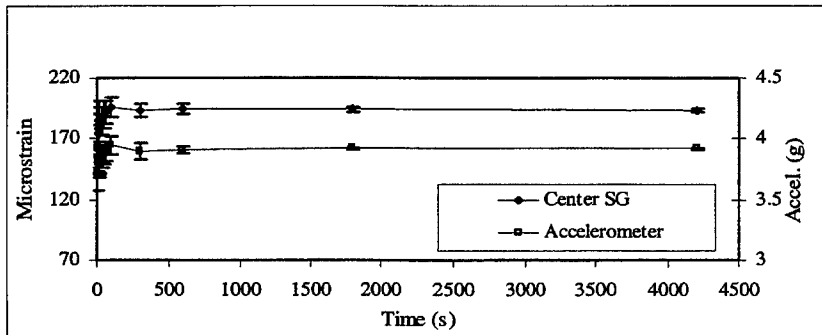


Figure 5: Input and output signal RMS

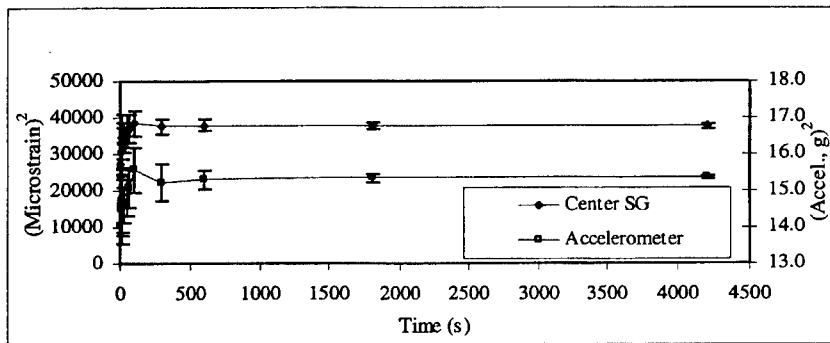


Figure 6: Variance of the input and output signals

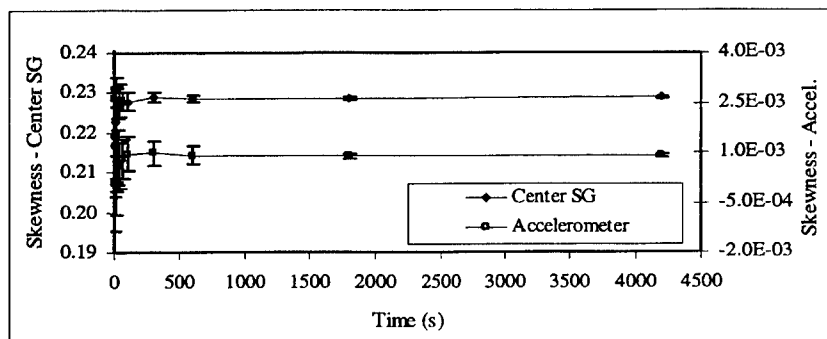


Figure 7: Input and output signal skewness

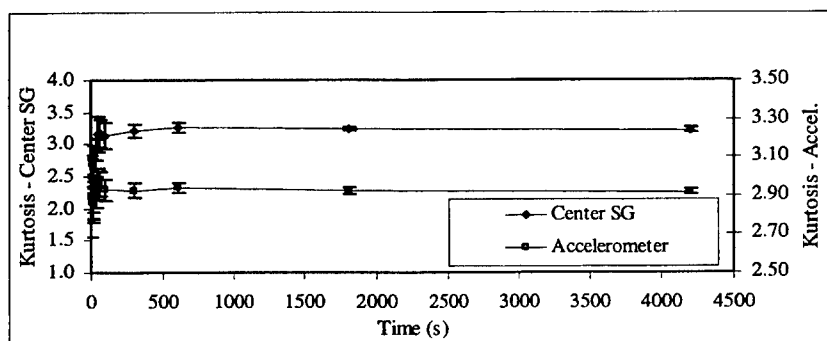


Figure 8: Input and output signal kurtosis

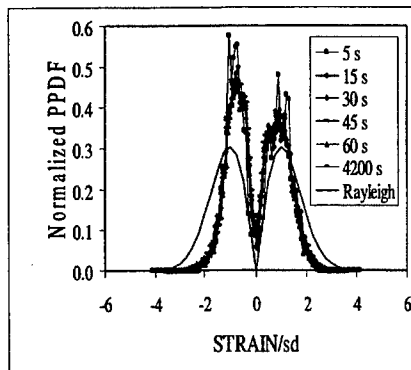


Figure 9: PPDFs for cumulative time records and Rayleigh distribution

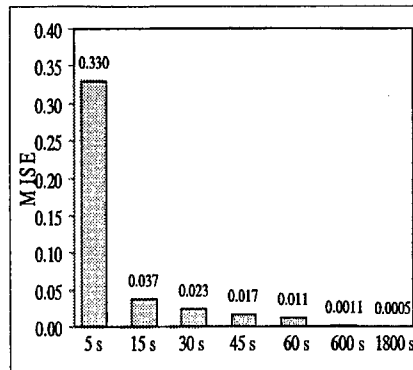


Figure 10: Mean integrated square error for cumulative time records

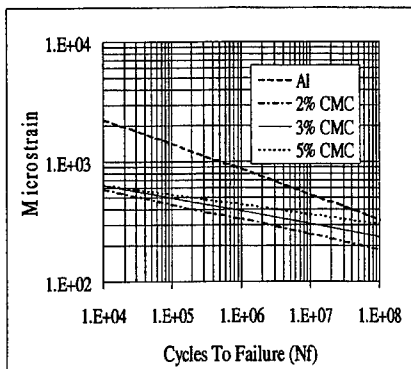


Figure 11: ϵ -N curves for CMC Blackglas™ and 7075-T6

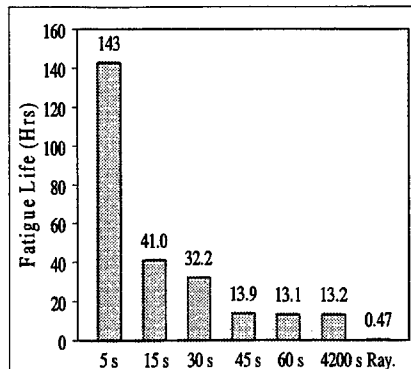


Figure 12: Estimated fatigue life for CMC Blackglas™ coupons

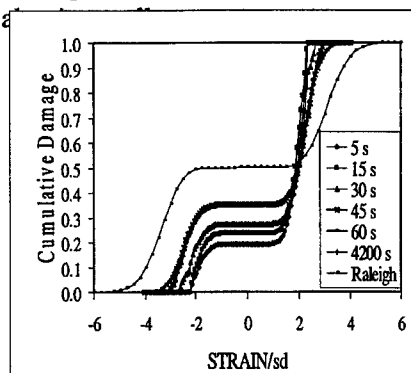


Figure 13: Damage accumulation for experimental/Rayleigh distributions

HIGH INTENSITY ACOUSTIC TESTING OF DOUBLY CURVED COMPOSITE HONEYCOMB SANDWICH PANELS

P.R. CUNNINGHAM[†], D.M.A. MILLAR[‡] AND R.G. WHITE[†]

ABSTRACT

The dynamic response of sandwich structures to random acoustic excitation has previously been investigated, but only for flat and singly curved panels. An investigation of the design data available has also revealed a lack of data for sandwich panels with a doubly curved geometry. To this end, a recent programme of experimental work was carried out at the University of Southampton concerned with the dynamic response of doubly curved composite honeycomb sandwich panels to random acoustic excitation. This paper gives details of the results from that programme of work. A set of three panels with various radii of curvature was tested in the ISVR Progressive Wave Tube facility at overall RMS Sound Pressure Levels from 142 dB to 164 dB with broad band random excitation from 80 Hz to 800 Hz.

To ensure that the highest possible strain was achieved for the purpose of investigating potential nonlinear effects, the panels were secured in the aperture of the PWT using circular steel springs. Results are presented for strain measurements taken at positions close to the centre of the panels on both the inner and outer faceplates. In addition, the panel response was compared with finite element predictions and the Blevins normal mode method was also used to predict the maximum strain at the predominant response frequency.

1. INTRODUCTION

Honeycomb sandwich panels have a very high stiffness-to-weight ratio and as such have found favour in the aircraft industry over the years. Panels employing a mixture of carbon fibre reinforced plastics and resin impregnated paper honeycomb can be found in applications such as fairing and floor panels, ailerons, helicopter blades, and engine intake barrel panels. The latter type of structure has a complicated geometry due to the shape of the engine intake, and as such can be considered doubly curved.

The dynamic response of sandwich structures to random acoustic excitation has previously been investigated [1-4], but only for flat and singly curved panels. An investigation of the design data available has also revealed a lack of data for sandwich panels with a doubly curved geometry [5]. To this end, a recent programme of experimental work was carried out at the University of Southampton concerned with the dynamic response of doubly curved composite honeycomb sandwich panels to random acoustic excitation.

[†] Department of Aeronautics and Astronautics, University of Southampton, Southampton SO17 1BJ, England

[‡] Research Student, Institute of Sound and Vibration Research, University of Southampton, Southampton, SO17 1BJ, England

The ISVR progressive wave tube facility was used to test the panels using broadband random acoustic excitation between 80 Hz and 800 Hz at OASPL's from 142 dB to 163 dB. The dynamic response was measured using strain gauges bonded to the inner and outer face-plates close to the centre of each panel, and comparisons have been made with theoretical predictions of the strain response. Finite element models of the panels were constructed and a modal analysis was carried out in order to predict the dynamic response in terms of the natural frequencies of vibration and the modal stress and strain for the predominant response mode identified from the experimental results. The predictions of modal stress and strain, along with the measured damping values, were used as inputs to the method of Blevins for approximating the response of structures to random acoustic excitation [6].

2. TEST PANEL DESIGN AND EXPERIMENTAL SET-UP

A set of three experimental test panels was designed and manufactured at the University of Southampton using epoxy pre-impregnated plain weave carbon cloth and over-expanded paper honeycomb core [7]. The panels were formed using fabricated aluminium alloy mould tools with a convex curvature to the specified radii, and were consolidated under vacuum pressure and cured in a conventional temperature controlled oven using a four stage pre-cure process.

TABLE 1. *Test panel geometry and ply lay-up*

Dimension [m]	Panel #1	Panel #2	Panel #3
a	0.912	0.912	0.912
b	0.525	0.525	0.525
R _a	3.5	1.2	3.5
R _b	1.0	1.0	0.5
Layer	Number of plies	Ply orientation	
Facing skin	4	[0/45] _s	
Doublers	2	[0/30]	
Spacers	2	[0 ₂]	
Edge pan	3	[0/45/0]	
Backing skin	4	[0/45] _s	

The panel design incorporates a panned-down, or bevelled edge, which is typical of in-service aircraft honeycomb sandwich panels. The honeycomb was chamfered along the four edges to form the pan, and the backing skin was laid up over the honeycomb to totally enclose the core. Doubler plies were incorporated in the lay-up in order to provide better load transfer in the bevelled edge region, and spacer plies were included in the edge pan to stiffen the attachment flange. The specifications for each panel are given in Tables 1 and 2, and a typical test panel drawing and the bevelled edge details are shown in Figures 1 and 2 respectively.

TABLE 2. Material specifications

Layer	t [m]	Elastic Modulus [Pa]		Shear Modulus [Pa]				ρ [kg/m ³]	ν
		E_{11}	E_{22}	E_{33}	G_{12}	G_{13}	G_{23}		
CFRP [*]	0.25e-3	57.93e9	57.93e9	-	3.7e9	-	-	1518	0.04
Core	19.0e-3	0	0	120e6	0	35e6	20e6	48	-

^{*}Properties obtained using cured test specimens with $[0_4]$ and $[45_4]$ ply lay-up and with 60% fibre volume fraction.

Each panel was secured in the test aperture of the PWT using four circular steel springs. This was done to ensure the highest possible strain was achieved in order to investigate potential non-linear effects. In addition, the panels and associated boundary conditions in the PWT can be modelled fairly easily using the finite element method with this configuration.

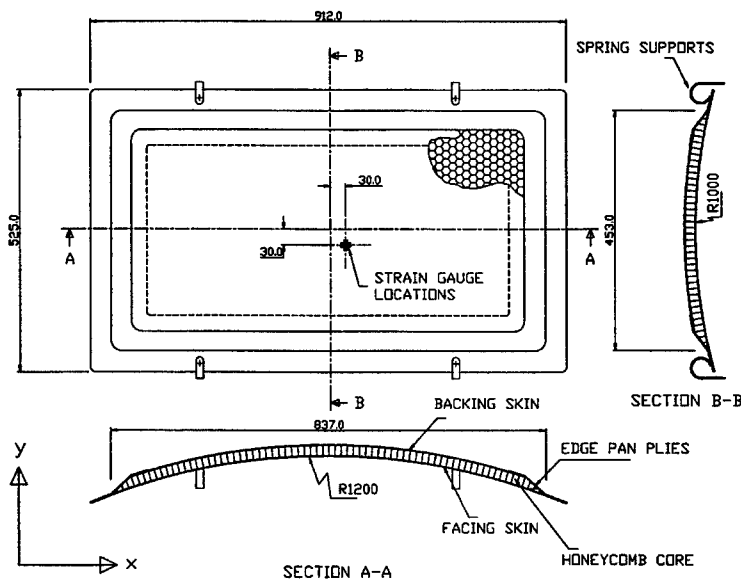


Figure 1. A typical test panel drawing.

The experimental set-up is shown in Figure 3. A B&K Type 1402 random noise generator was used to supply the drive signal, which was attenuated outside the 80 Hz to 800 Hz range using a spectrum shaper before being supplied to the WAS via a LDS PA 500L power amplifier. The SPL in the test section was monitored using a condenser microphone and a measuring amplifier which were calibrated to give the OASPL in dB (re 2×10^{-5} Pa) using a B&K pistonphone. Single element gauges, with a gauge length of 6mm, (TML FLA-6) and with a nominal resistance of $120\Omega \pm 0.5$ and a gauge factor of 2.1 were used to measure the dynamic response of the test panels.

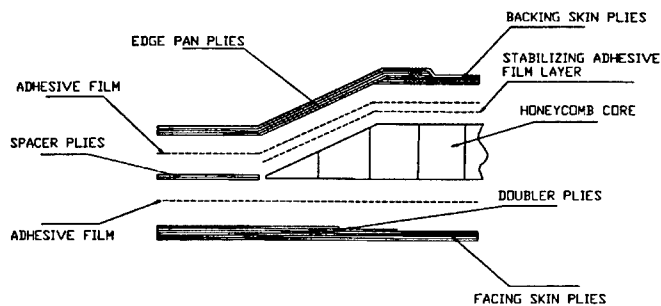


Figure 2. Bevelled edge details

These gauges, which were bonded to the inner and outer face-plates at positions close to the centre of the panel as shown in Figure 1, were wired into a quarter bridge circuit. A Measurements Group Model 2200 signal conditioning amplifier was used to calibrate and amplify the signals from the strain gauges, which were filtered at 1kHz using a 16 channel low pass filter set, and then digitally sampled using the National Instruments VXI data acquisition system.

Readings were taken at OASPL's of 140, 145, 150, 155, and 160dB, and the signals from the strain gauges were sampled at 6kHz for 10 seconds, giving 60,000 samples per excitation level. The digitised time histories were transformed to the frequency domain using the MATLAB spectrum function, which uses a radix-2 FFT algorithm. A Hanning window was applied over 8192 samples with an overlap of 50%, giving a frequency resolution of 0.73Hz, and Welch's method was used to average over the entire record.

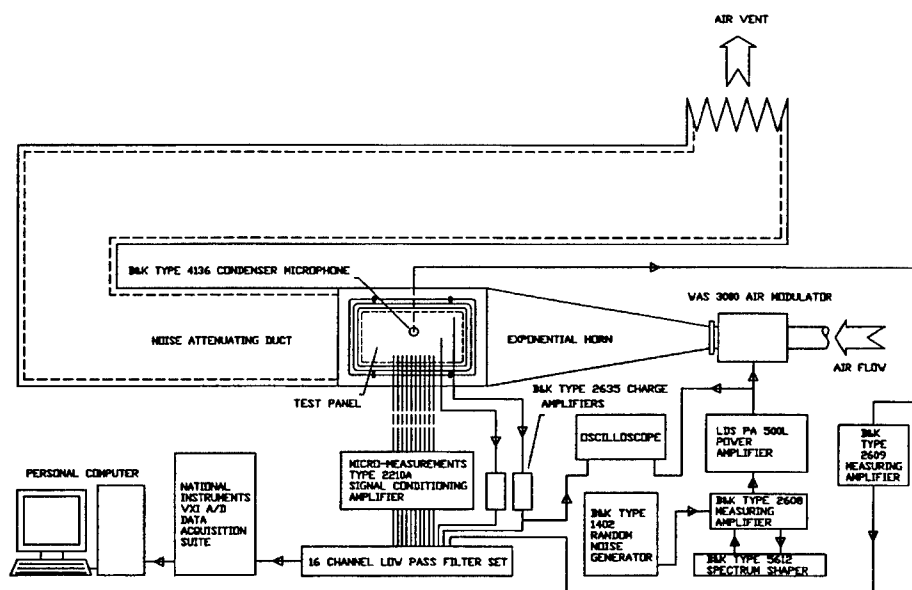


Figure 3. Experimental set-up.

3. EXPERIMENTAL RESULTS

Figure 4 shows the Sound Pressure Level spectrum for each of the five levels used in the tests. The OASPL in each case, for a 720Hz bandwidth, were 142dB, 149.6dB, 153.7dB, 158.7dB, and 163.7dB. The levels are fairly constant across the 80 to 800Hz band-width. Typical results for the response in terms of the strain Power Spectral Density (PSD), and a plot of the normalised integral across the PSD, for the inner gauge on panel #1 are shown in Figure 5. For all excitation levels, the modal contributions are evident, and in all cases the predominant response was at 210Hz, which corresponds to the second natural frequency of vibration of a freely supported panel [7].

A comparison of the measured resonance frequencies and the predicted natural frequencies of vibration, for the panels with freely supported and spring supported boundary conditions, is given in Table 3. It can be seen that from the PWT results, the predominant response corresponds with the first bending mode of vibration, whereas the first natural frequency of vibration (at 136Hz for panel #1) is associated with the first torsional mode shape. This was the case for all three panels. The torsional mode shape was not excited in the PWT due to the symmetrical pressure distribution acting on the surface of the panel. The lower plot in Figure 5 indicates that approximately 90% of the total response across the band was associated with the mode at 210Hz. Probability densities and cumulative probabilities for the inner gauge on panel #1 are also plotted in Figure 6. At all excitation levels, the probability densities are almost identical to the Gaussian distribution.

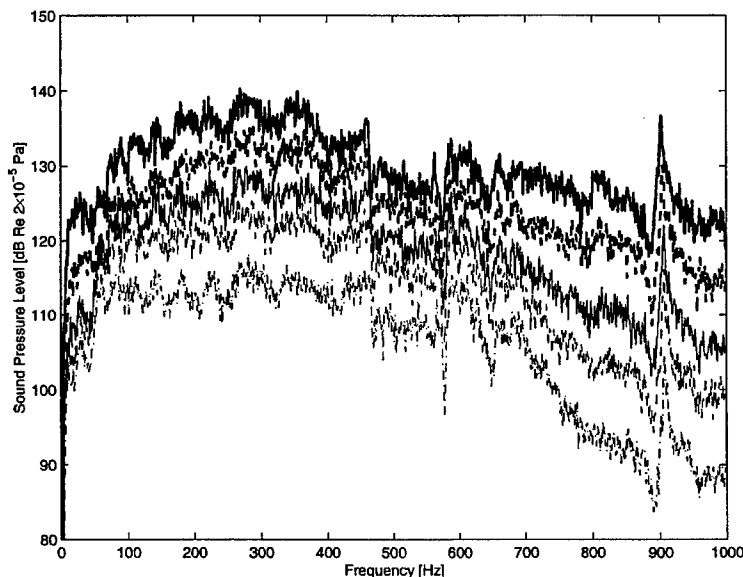


Figure 4. Sound Pressure Level spectrum for the five levels of excitation (-, 142dB, -- 149.6dB, - 153.7dB, -- 158.7dB, - 163.7dB).

The probability densities and cumulative probabilities for the other gauge measurements and for the other two panels showed similar distributions. The variation of overall RMS strain with OASPL is shown in Figures 7 to 9 for the three panels. For panels #1 and #2, where the short side (y-wise) radius of curvature is the same ($R_y=1.0\text{m}$), the highest measured overall RMS strain was found to be in the outer x-wise gauge. The inner x-wise gauge gave the lowest readings which indicates a large ratio between the outer and inner strains (of the order of 2.5 to 3.0). It has been reported that for singly curved sandwich panels, the ratio of strain measured on the outer and inner surfaces was of the order of 2.0 to 2.5 [1]. For the y-wise gauges, the ratio was considerably lower (of the order of 0.8 to 1.0), with the strain indicated by the inner gauge being consistently higher than that measured by the outer gauge.

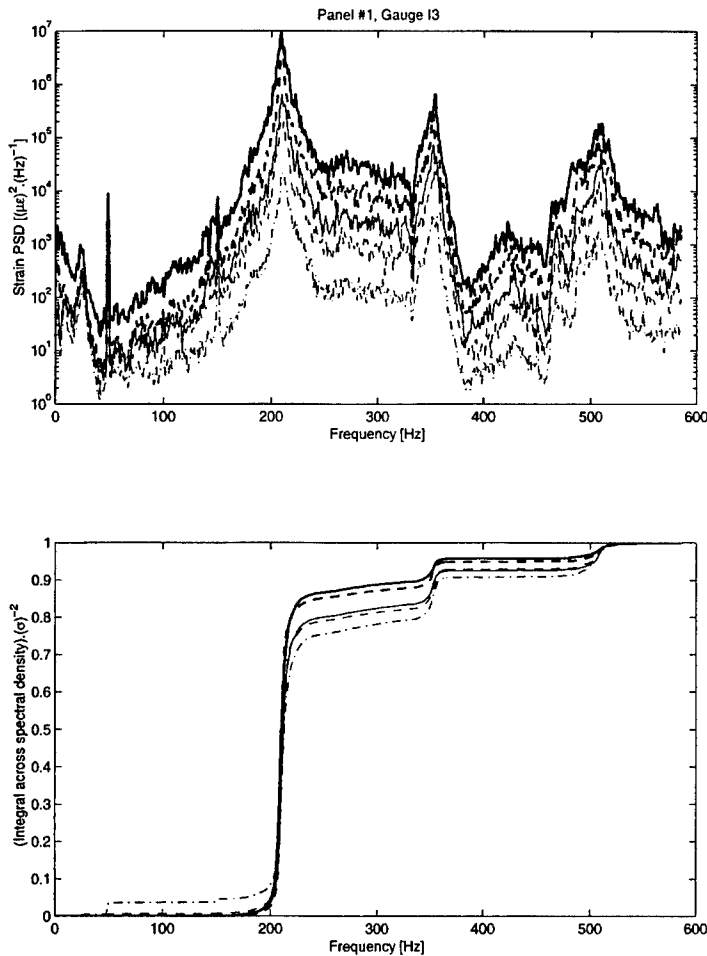


Figure 5. Strain spectral analysis for the inner gauge on panel #1.
(- 142dB, -- 149.6dB, - 153.7dB, -- 158.7dB, - 163.7dB).

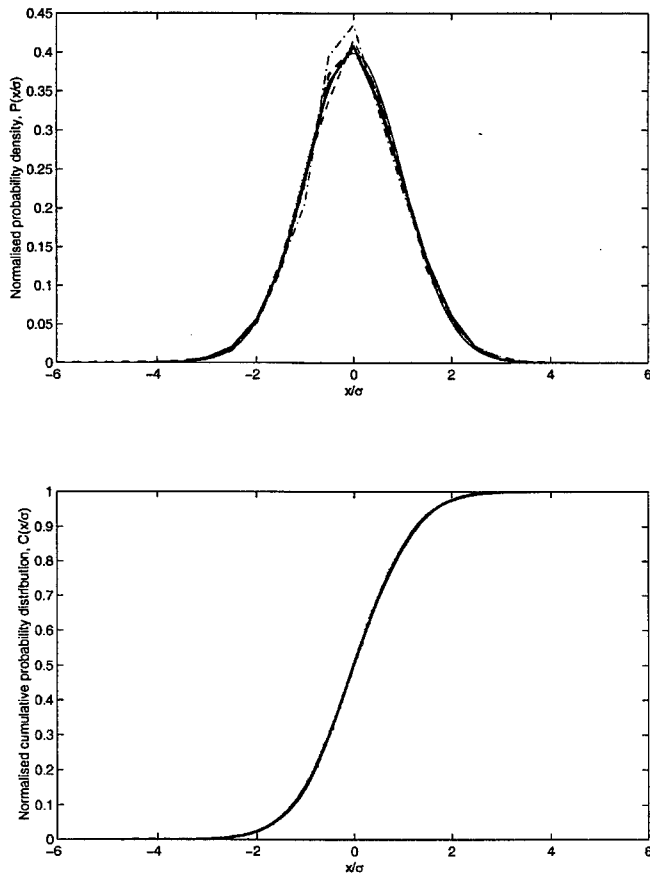


Figure 6. Probability analysis of strain signal for the inner gauge on panel #1.
 (-. 142dB, - 149.6dB, .. 153.7dB, -- 158.7dB, - 163.7dB, - gaussian distribution).

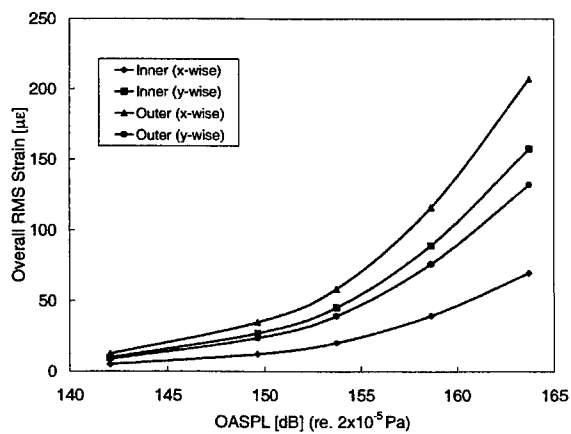


Figure 7. Overall RMS strain versus OASPL for panel #1

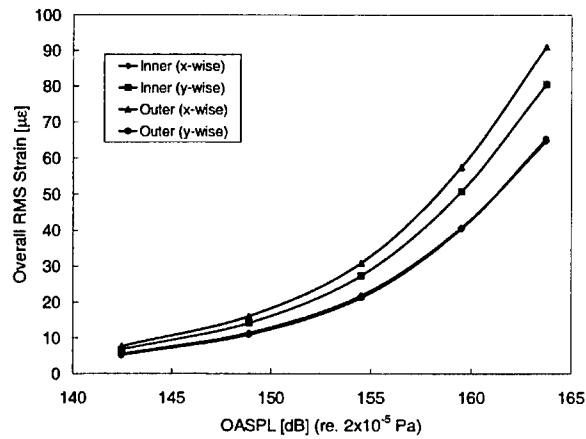


Figure 8. Overall RMS strain versus OASPL for panel #2

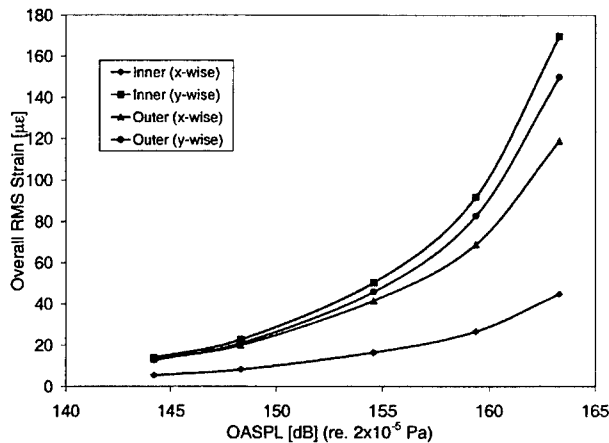


Figure 9. Overall RMS strain versus OASPL for panel #3

4. THEORETICAL MODEL

4.1 Finite Element model

The ANSYS finite element package was used to analyse the modal response of the doubly curved panels. Due to the geometry of the panels and the complex lay-up details, particularly around the bevelled edge, the model was built by constructing the doubly curved surface in the global cartesian coordinate system and meshing with SHELL91 elements [7]. This is a layered element which offers the choice of a “sandwich option”, whereby the middle layer is assumed to be thick (greater than 5/7 of the total thickness) and

orthotropic, and is assumed to carry all of the transverse shear. A modal analysis was carried out and the results for the first four non-rigid body modes of vibration were obtained. The natural frequencies of vibration, modal stress and strain, and modal displacement were recorded, and these results were used as the input in Blevins normal mode method [6], an explanation of which is given in the next section.

4.2 Response prediction using the Normal Mode Method of Blevins [6]

The traditional approach in estimating the response of a structure is based on the Miles equation [8]. This method assumes a uniform pressure, fully correlated over the surface of the structure. This approach can considerably over-estimate the joint acceptance and a modification of the Miles equation has been proposed by Blevins [6], which in its basic form uses a joint acceptance of unity. The basic form of the equation is:

$$S_{rms} = \sqrt{\frac{\pi f_n}{4\delta}} L_{ps}(f_n) \frac{S_o}{P_{ic}} \quad (1)$$

The main difference between the Miles equation and equation 1 is in the stress per unit pressure term. The form of the pressure distribution in Blevins' normal mode method is that of the mass weighted mode shape and involves matching a point on the surface (generally the point of maximum displacement) to the applied sound pressure level – as opposed to using a unit pressure over the entire surface. A crude estimation of the influence of the joint acceptance can be made by considering the acoustic wavelength in terms of the structural wavelength i.e. if the acoustic wavelength is greater than the structural wavelength then the joint acceptance of unity is valid. If the acoustic wavelength is very much greater than the structural wavelength, the loading approaches the Miles assumption of uniform pressure over the surface. As the acoustic wavelength becomes smaller than the structural wavelength, the joint acceptance becomes more important to correctly estimate the response. Blevins' normal mode method should theoretically work best when the acoustic and structural wavelengths match.

TABLE 3 – Comparison of structural and acoustic half wavelengths

Panel	Frequency (Hz)	Structural ½ Wavelength (m)	Acoustic ½ Wavelength (m)	Acoustic Wavelength as % of Structural
1	219.02	0.912	0.78	85.53
2	164.3	0.912	1.04	114.04
3	272.62	0.912	0.63	69.08

Table 3 shows the relationship between the structural half wavelength and the acoustic half wavelength for the predominant response frequency of

each of the three panels used in the test. As can be seen from Table 3, the structural and acoustic wavelengths (or half wavelengths) are of similar magnitude, and as such the joint acceptance of unity is acceptable.

Millar [9] showed the relationship between using a single mode (fundamental) and a joint acceptance of unity to that of estimating the joint acceptance and consequently the overall response for several modes of vibration within the bandwidth of excitation. The calculations were compared with test data and showed that the single mode and joint acceptance of unity approach overestimated the response while the attempt to calculate the overall response by calculating the joint acceptance for several modes actually underestimated the response. In that particular case good agreement with the test data was obtained by taking an average of the two calculations. The approach of using a single mode has been used extensively for some time [10] and is well founded. Experience has shown that in the majority of cases of in-service failures, the failure can be attributed to a single frequency. It is anticipated therefore that the single mode/J=1 approach will lead to an overestimate of the response in comparison with the test data.

The parameters obtained from the FE analysis which were required for the normal mode method calculations are presented in Table 4. The strain locations used for comparison with the test data were in the centre of the panel, parallel to both the long edge and the short edge, ϵ_x and ϵ_y respectively and on both the inner and outer skin, as shown in Figure 1. The outer skin was the convex surface and the inner skin was the "wetted" (concave) surface in the progressive wave tube. The spectrum level of acoustic pressure, $L_{ps}(f_n)$, was read from the sound pressure level (SPL) spectrum plot shown in Figure 4, and the damping used in these calculations was taken from the measured strain data. The mass per unit area for each of the panels was constant at 5.24 kg/m².

TABLE 4 – Data from FE model used in Blevins' Normal Mode Method calculations.

Panel	Panel surface	Frequency (Hz)	Modal displ. (m)	P_k (kN/m ²)	δ	$S_{nm}/(L_p \times S_d)$	Modal ϵ_x (I4) (m/m)	Modal ϵ_y (I3) (m/m)
1	INNER	219.02	1.376	13662.9	0.013	8.419E-06	8.80E-02	0.232
	OUTER	219.02	1.376	13662.9	0.013	8.419E-06	2.95E-01	0.176
2	INNER	164.3	1.211	6767.7	0.0155	1.472E-05	1.63E-01	0.168
	OUTER	164.3	1.211	6767.7	0.0155	1.472E-05	2.04E-01	0.131
3	INNER	272.62	1.405	21611.7	0.0113	5.938E-06	6.41E-02	0.349
	OUTER	272.62	1.405	21611.7	0.0113	5.938E-06	1.45E-01	0.279

The predicted RMS strains for the three panels are shown in Table 5, along with the measured strains for comparison.

TABLE 5- Comparison of calculated and measured strains for the three test panels

Panel	OASPL (dB)	Inner surface strains ($\mu\epsilon$)				Outer surface strains ($\mu\epsilon$)			
		ϵ_x (calc)	ϵ_x (meas)	ϵ_y (calc)	ϵ_y (meas)	ϵ_x (calc)	ϵ_x (meas)	ϵ_y (calc)	ϵ_y (meas)
1	142.00	6.89	4.91	18.17	9.79	23.12	12.47	13.76	8.68
	149.60	16.54	12.27	43.60	27.03	55.46	34.97	33.00	23.74
	153.70	32.54	20.37	85.79	45.48	109.14	58.68	64.95	39.43
	158.70	46.60	39.59	122.87	89.42	156.30	116.20	93.02	76.26
2	163.70	96.14	69.95	253.49	157.42	322.45	206.99	191.90	132.06
	142.50	19.71	5.57	20.21	6.77	24.65	7.66	15.79	5.22
	148.90	44.29	11.41	45.40	14.19	55.37	16.10	35.47	10.91
	154.50	72.99	21.93	74.83	27.45	91.25	30.97	58.46	21.33
3	159.50	129.80	40.76	133.06	50.87	162.28	57.64	103.97	40.52
	163.70	176.32	64.75	180.74	80.58	220.42	91.07	141.22	65.35
	144.20	6.52	5.35	35.57	13.87	14.75	13.22	28.36	12.71
	148.30	9.46	8.17	51.60	22.77	21.39	19.99	41.14	20.97
	154.60	18.44	16.49	100.61	50.27	41.70	41.56	80.21	45.74
	159.40	37.35	26.61	203.77	91.83	84.46	68.83	162.46	82.65
	163.30	52.15	44.78	284.53	169.65	117.94	118.92	226.86	149.85

The best results were obtained for panel 3 although no clear reason for the difference is apparent despite there being such good agreement between the measured and calculated natural frequencies for all three panels. In fact on the basis of the influence of the joint acceptance discussed above one would have anticipated that the best results would have been obtained for panels 1 and 2, where the acoustic wavelength more closely matched the structural wavelength. Despite the difference between the calculated and measured strain response, the Blevins approach did overestimate the response and as such can be confidently used as an acoustic fatigue design tool. The comparison of measured and calculated response for panel 3 has been presented in graphical form in Figure 10.

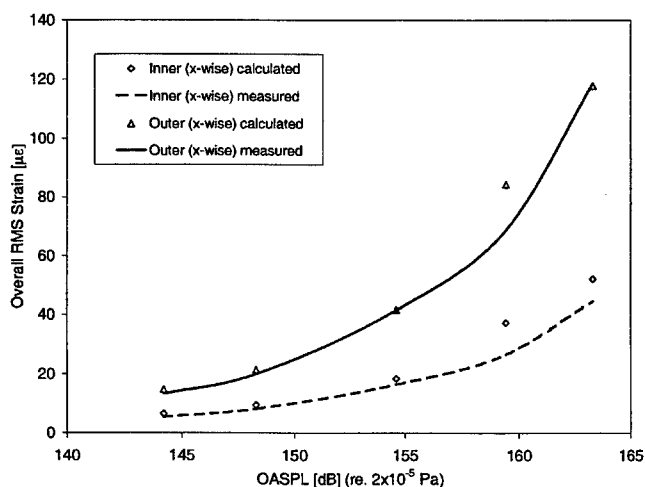


Figure 10. Comparison of measured and calculated RMS strain for panel 3

5. CONCLUSIONS

This paper has given details of a recent programme of work investigating the dynamic response of doubly curved composite honeycomb sandwich structures to random acoustic excitation. A set of three panels, which were designed and manufactured at the University of Southampton, has been tested in the ISVR progressive wave tube facility at overall sound pressure levels from 142 to 164 dB. Results have been presented for the overall RMS strain versus the OASPL, which has indicated a linear response at the excitation sound pressure levels used. In addition, probability analyses of the strain signals have shown that the probability density is almost identical to the Gaussian distribution at all excitation levels.

The measured RMS strain responses have been compared with theoretical predictions obtained using Blevins' normal mode method. The method gave reasonable results, where an overestimation of the overall RMS strain was observed for all three panels, therefore Blevins' normal mode method can be confidently used as an acoustic fatigue design tool for this type of structure.

ACKNOWLEDGEMENTS

This programme of research was supported by the Engineering and Physical Sciences Research Council, on EPSRC grant GR/K80600. The authors would also like to gratefully acknowledge the following for their support during this research programme: Professor Robin Langley at Cambridge University, Jim Baker and David Edwards at the University of Southampton, and Jacky Ridewood and Robin Phillips at Aerostructures (Hamble Group) Ltd.

REFERENCES

1. Sweers, J., Prediction of response and fatigue life of honeycomb sandwich panels. *Acoustical fatigue in aerospace structures*, Trapp, W.J., Forney, D.M. (Eds.), April 29-May 1, 1964, pp. 389-402.
2. Wallace, C., Stress response and fatigue life of acoustically excited sandwich panels. *Acoustical fatigue in aerospace structures*, Trapp, W.J., Forney, D.M. (Eds.), April 29-May 1, 1964, pp. 225-244.
3. Soovere, J., Random vibration analysis of stiffened honeycomb panels with bevelled edges. *AIAA Journal of Aircraft*, 1986, **23** (6), 537-544.
4. Holehouse, I., Sonic fatigue design techniques for advanced composite airplane structures. *PhD Thesis, University of Southampton*, 1984.
5. Engineering Sciences Data Unit. Vibration and acoustic fatigue. *ESDU Design Guide Series 1-6*.
6. Blevins, R.D., An approximate method for sonic fatigue analysis of plates and shells. *Journal of Sound and Vibration*, 1989, **129** (1), 51-71.
7. Cunningham, P.R., White, R.G., Aglietti, G.S., The effects of various design parameters on the free vibration of doubly curved composite

-
- sandwich structures. *Accepted for publication in the Journal of Sound and Vibration.*
8. Miles, J.W., On structural fatigue under random loading. *Journal of the Aeronautical Sciences*, 1954, **21**, 753-762.
 9. Millar, D.M.A., The behaviour of light weight honeycomb sandwich panels under acoustic loading. *Proceedings of the Sixth International Conference on Recent Advances in Structural Dynamics*, ISVR, University of Southampton, 1997, **2**, 995-1006.
 10. Clarkson, B.L., Stresses in skin panels subjected to random acoustic loading. *The Aeronautical Journal of the Royal Aeronautical Society*, 1968, **72**, 1000-1010.

APPENDIX: NOTATION

SPL	Sound Pressure Level
OASPL	Overall Sound Pressure Level
PWT	Progressive Wave Tube
RMS	Root Mean Square
S_{rms}	Overall RMS Strain
π	3.14159
f_n	predominant response frequency
$L_{ps}(f_n)$	Spectrum level of acoustic pressure (expressed as a fluctuating pressure in Pa in a 1 Hz band)
S_o	Modal strain
P_{ic}	Characteristic modal pressure
δ	Critical damping ratio

FATIGUE ANALYSIS OF AN F16 NAVIGATION POD

NWM Bishop¹, N Davies², A Caserio¹, S Kerr¹

¹MacNeal Schwendler Corporation, Lyon Way, Frimley, Camberley, Surrey,
UK, GU16 5ER.

²Marconi Naval Systems Ltd, Product Assurance Group, West Hanningfield
Road, Great Baddow, Essex, CM2 8HN.

ABSTRACT

An F16 POD containing optical equipment has been analysed using MSC.Fatigue. The purpose of the analysis was to show that current procedures could be improved in 3 ways. Firstly, a more accurate and widely applicable procedure based upon the Dirlik algorithm is used to compute fatigue damage from output PSD's of stress. Secondly, these calculations are performed on Principal stress axes (current FEA solvers such as NASTRAN, ABAQUS and ANSYS do not allow rotation of transfer functions onto Principal planes). Lastly, the calculations are automatically performed over the entire region of interest. Results for fatigue life are presented for a number of input loading conditions.

INTRODUCTION

The Marconi Electronic Systems (MES) Atlantic POD is designed to attach to the fuselage of the F16 aircraft, (see Figure 1). Its primary purpose is to provide night vision for the pilot via its forward looking infrared (FLIR) system. The infrared pictures can be seen by the pilot using his head-up display unit (HUD) in the cockpit.

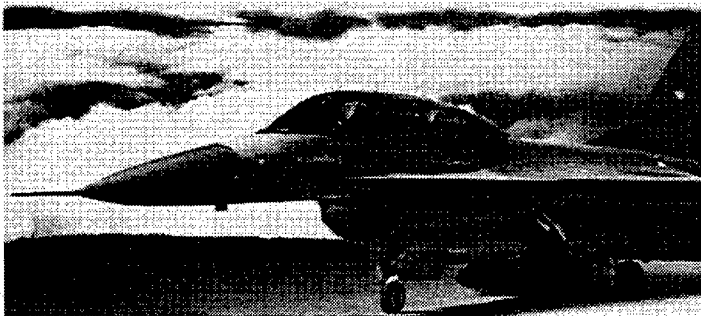


Figure 1. Atlantic Navigation POD attached to F16

The POD is basically a 10 inch diameter, 97 inch long, tube with a front and rear bulkhead containing three primary units; the electronics module, the environmental control unit and, most importantly, the sensor head assembly. The sensor head is mounted at the very front of the POD on two parallel longitudinal arms that attach primarily to the forward bulkhead. An early version of the Atlantic POD is shown in Figure 2. The sensor head houses the infra red cameras, lens assemblies and other sensors used for high speed, low level night time sorties.

During the conceptual design of the POD, the sensor head mounting arms were 'tuned' to give the right response so that boresight error resulting from vibration of the sensor could be minimised. The consequence, however, of this tuning was a weakening of the rear of the arms, as they were reduced from a thick solid section to a thinner cut-out one.

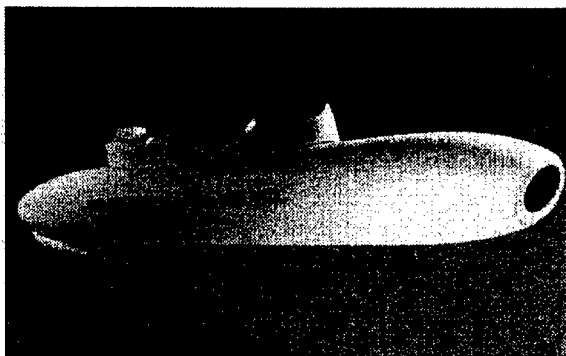


Figure 2. Concept Stage Atlantic Navigation POD

It was required to assess whether this weakening of the structure would cause problems under the severe random vibration loads applied to the POD. For this reason it was decided to perform a random vibration fatigue analysis on the POD structure to the levels and duration's defined in the POD test certification specification. An example of the types of input loads that might be used are shown in Figure 3. These were applied to the points on the POD which attach it to the F16.

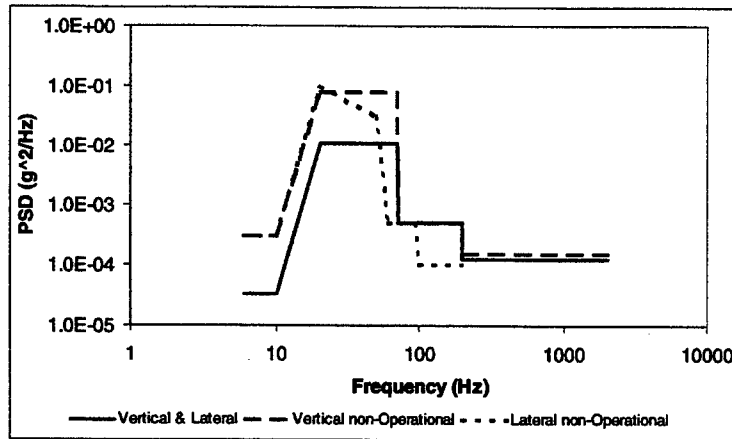


Figure 3. F16 POD vibration profiles

Typically, the POD is required to survive these vibration loadings for specified periods as shown in Table 1

F16 POD Vibration Profile	Duration
Lateral non-operational	5 minutes
Vertical non-operational	5 minutes
Lateral performance profile	30 minutes
Vertical performance profile	30 minutes

Table 1. Test duration's for each vibration profile

An FE model of the POD was created by Marconi Naval Systems Limited, Product Assurance Group (MNSL PAG). This was the model that was used for the analysis shown in this paper. The model was created using MSC.Patran and consists of TRI3 and QUAD4 shell elements for the tube and fairings, WEDGE6 and HEX8 solid elements for the bulkheads and sensor arms and lumped masses for the internal units mounted off RBE3s. The POD was constructed from various grades of Aluminium with the sensor head arms being machined from 2014 T6.

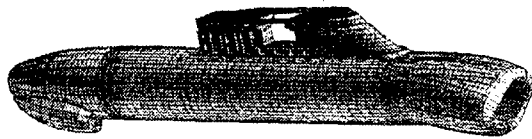


Figure 4. FE model of POD outer casing



Figure 5. FE modelling of POD internal components

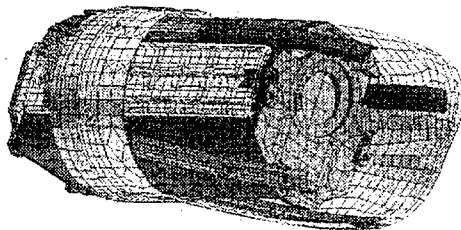


Figure 6. FE model of the sensor head assembly

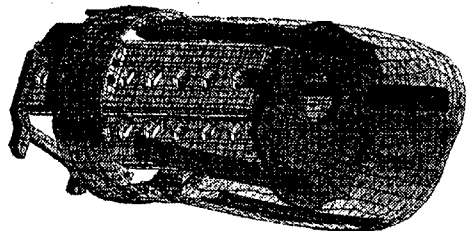


Figure 7. FE model of the sensor head assembly with the sensor head removed

Before the results are presented some technical background will be introduced.

TECHNICAL BACKGROUND – VIBRATIONS

What is the frequency domain?

Structural analysis can be carried out in either the time or frequency domains as shown in Figure 8. In the time domain the input takes the form of a time history of load (in this case wind speed). The structural response can be derived using a finite element representation coupled with a transient (convolution) solution approach. The output from this model is also expressed as a time history, in this case the stress at some particular location in the structure.

In the frequency domain the input is given in the form of a PSD of wind speed and the structure is modelled by a linear transfer function relating input wind speed to the output stress at a particular location in the structure. The output from the model is expressed as a PSD; in this case it is the PSD of stress.

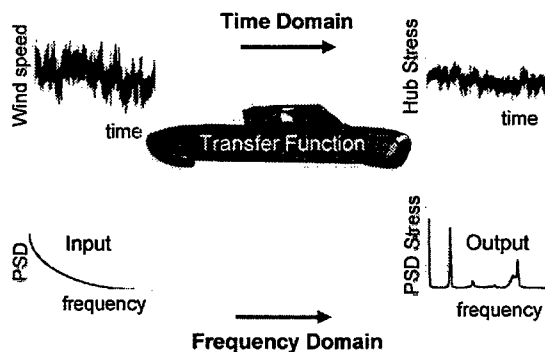


Figure 8. What is the frequency domain?

Most of the computational time is spent in solving the structural model. In the time domain, the structural model is solved for each time history of input; hence 20 load cases would take 20 times as long to calculate as 1. In contrast, for the frequency domain, once the linear transfer function has been calculated the response caused by additional input PSD's can be calculated without solving the structural model again.

Basically, the frequency domain is another way of representing a time history. Certain information about a random process becomes apparent

apparent in a frequency domain plot, which is difficult to see in the time domain. It is possible to flip back and forth between the two domains using the Fourier Transformation and Inverse Fourier Transformation respectively

Time histories & PSD's

Engineering processes can fall into a number of types and Figure 9 is useful as a means of characterising these different types of processes. In Figure 9(a), a *sinusoidal time history* appears as a single spike on the PSD plot. The spike is centred at the frequency of the sine wave and the area of the spike represents the mean square amplitude of the wave. In theory this spike should be infinitely tall and infinity narrow for a pure sine wave. However, if a practical FFT routine is applied to an arbitrarily truncated sine wave then, in general, the spike always has finite height and finite width. Remember, with PSD plots it is the area under the graph that is of interest and not the height of the graph.

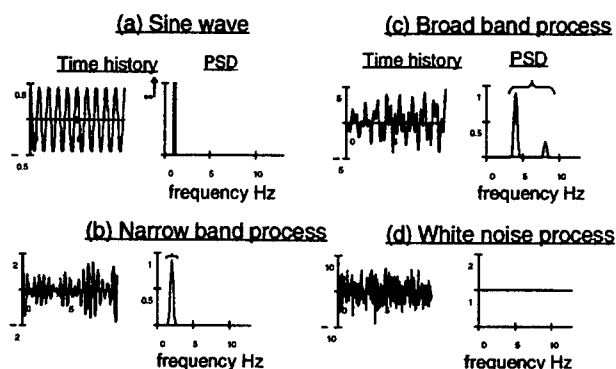


Figure 9. Equivalent time histories and PSD's

In Figure 9(b), a *narrow band process* is shown which is built up of sine waves covering only a narrow range of frequencies. A narrow band process is typically recognised in a time history by amplitude modulation, often referred to as a 'beat' envelope.

In Figure 9(c), a *broad band processes* is shown which is made up of sine waves over a broad range of frequencies. These are shown in the PSD plot as either a number of separate response peaks (as illustrated) or one wide peak covering many frequencies. This type of process is usually more difficult to identify from the time history but is typically

characterised by positive valleys (troughs in the signal above the mean level) and negative peaks.

In Figure 9(d), a *white noise process* is shown. This is a special time history, which is built up of sine waves over the whole frequency range.

Expected zeros, peaks and irregularity factor

Random stress or strain time histories can only properly be described using statistical parameters. This is because any sample time history can only be regarded as one sample from an infinite number of possible samples that could occur for the random process. Each time sample will be different. However, as long as the samples are reasonably long then the statistics of each sample should be constant. Two of the most important statistical parameters are the number of so-called *zero crossings* and *number of peaks* in the signal. Figure 10 shows a 1 second piece cut out from a typical wide band signal.

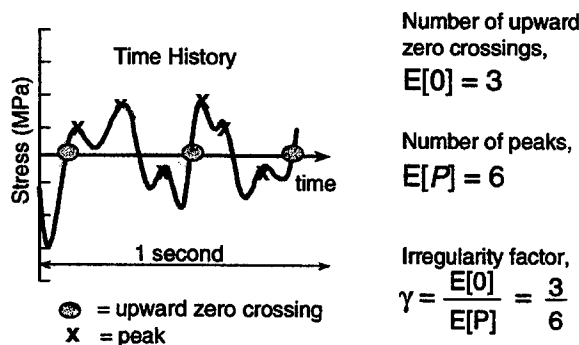


Figure 10. Zero and peak crossing rates

$E[0]$ represents the number of (upward) zero crossings, or mean level crossings for a signal with a non-zero mean. $E[P]$ represents the number of peaks in the same sample. These are both specified for a typical 1 second sample. The irregularity factor is defined as the number of upward zero crossings divided by the number of peaks.

In this particular case the number of zeros is 3, and the number of peaks is 6, so the irregularity factor is equal to 0.5. This number can theoretically only fall in the range 0 to 1. For a value of 1 the process must be narrow band as shown in Figure 9(b). As the divergence from

narrow band increases then the value for the irregularity factor tends towards 0.

Moments from a PSD

Since we are concerned with structural systems analysed in the frequency domain a method is required for extracting the pdf of rainflow ranges directly from the PSD of stress. The characteristics of the PSD that are used to obtain this information are the *nth moments* of the PSD function (Figure 11). The relevant spectral moments are easily computed from a one sided PSD $G(f)$ in units of Hertz using the following expression.

$$m_n = \int_0^{\infty} f^n \cdot G(f) df = \sum f_k^n \cdot G_k(f) \cdot \delta f$$

The n^{th} moment of area of the PSD (m_n) is calculated by dividing the curve into small strips as shown. The n^{th} moment of area of the strip is given by the area of the strip multiplied by the frequency raised to the power n . The n^{th} moment of area of the PSD is then found by summing the moments of all the strips.

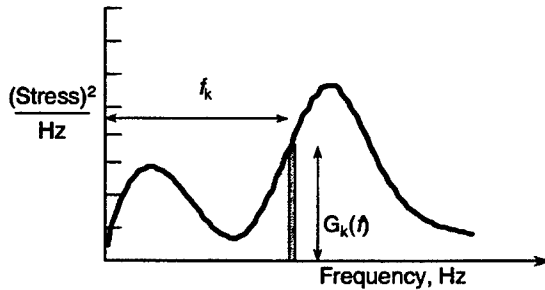


Figure 11. Calculating PSD moments

In theory, all possible moments are required to fully characterise the original process. However, in practice, we find that m_0 , m_1 , m_2 and m_4 are sufficient to compute all of the information required for the subsequent fatigue analysis.

Expected zeros, peaks and irregularity factor from a PSD.

The first serious effort at providing a solution for estimating fatigue damage from PSD's was undertaken by SO Rice in 1954 [1]. He developed the very important relationships for the number of upward mean crossings per second ($E[0]$) and peaks per second ($E[P]$) in a random signal expressed solely in terms of their spectral moments m_n .

$$E[0] = \sqrt{\frac{m_2}{m_0}} \quad E[P] = \sqrt{\frac{m_4}{m_2}}$$

$$\gamma = \frac{E[0]}{E[P]} = \sqrt{\frac{m_2^2}{m_0 m_4}}$$

TECHNICAL BACKGROUND - FATIGUE

Before introducing the concepts needed to estimate fatigue damage in the frequency domain it is useful to set out a parallel approach in the time domain. The approach highlighted is that of a traditional S-N (Stress-Life) approach (see Figure 12).

Time Domain S-N Fatigue Life Estimation

The starting point for any fatigue analysis is the response of the structure or component, which is usually expressed as a stress or strain time history. If the response time history was made up of constant amplitude stress or strain cycles then the fatigue design could be accomplished by referring to a typical S-N diagram. However, because real signals rarely conform to this ideal constant amplitude situation, an empirical approach is used for calculating the damage caused by stress signals of variable amplitude.

Despite its limitations, the Palmgren-Miner rule is generally used for this purpose. This linear relationship assumes that the damage caused by parts of a stress signal with a particular range can be calculated and accumulated to the total damage separately from that caused by other ranges. A ratio is calculated for each stress range, equal to the number of actual cycles at a particular stress range, n , divided by the allowable number of cycles to failure at that stress, N , (obtained from the S-N curve). Failure is assumed to occur when the sum of these ratios, for all stress ranges, equals 1.0.

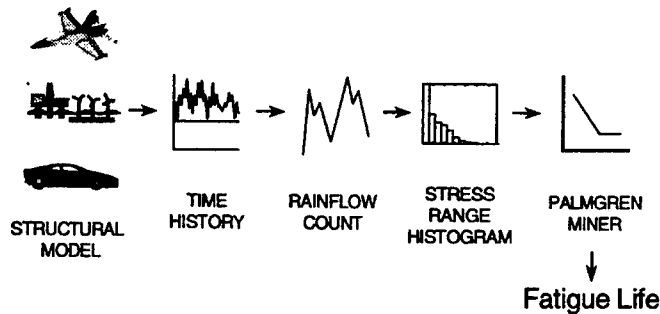


Figure 12. A standard S-N fatigue analysis

If the response time history is irregular with time, as shown in the Figure 12, then *rainflow* cycle counting is widely used to decompose the irregular time history into equivalent sets of block loading. The numbers of cycles in each block are usually recorded in a stress range histogram. This can then be used in the Palmgren Miner calculation. An example of the way rainflow ranges are extracted from a time signal is given in [2].

S-N Relationship

A traditional S-N curve as shown in Figure 13 is used to model the material properties of the components being analyzed. This simply shows that, under constant amplitude cyclic loading, a linear relationship exists between cycles to failure N and applied stress range S when plotted on log-log paper. There are two alternative ways of defining this relationship, as given below, where k and $SRI1$ are material constants.

$$NS^m = k \qquad N^{-b}S = SRI1$$

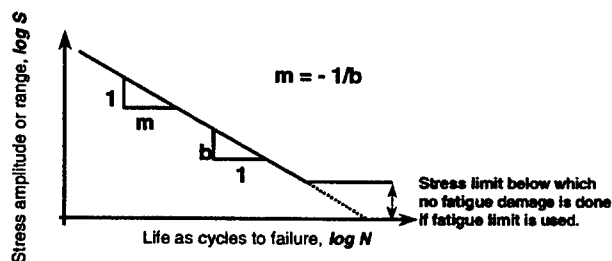


Figure 13. A typical S-N curve

Estimating fatigue life from a stress pdf

Once the stress range histogram has been converted into a stress range pdf then there is an elegant and efficient equation to describe the expected fatigue damage caused by this loading history. $E[\]$ has the usual meaning as "expectation operator" giving the mean or average value of a particular parameter.

$$E[D] = E[P] \frac{T}{k} \int_0^{\infty} S^m p(S) dS$$

In order to compute fatigue damage over the lifetime of the structure in seconds (T) the form of material (S-N) data must also be defined using the parameters k and m (or b and $SRI1$). In addition, the total number of cycles in time T must be determined from the number of peaks per second $E[P]$. If the damage caused in time T is greater than 1.0 then the structure is assumed to have failed. Or alternatively the fatigue life can be obtained by setting $E[D] = 1.0$ and then finding the fatigue life in seconds from the above equation.

The Frequency Domain Model

Figure 12 highlighted the overall process for fatigue life estimation in the time domain. The parallel approach in the frequency domain is shown in Figure 14. If we assume that the structural model shown is now an FEA model, this model would be identical for both the time domain and frequency domain approaches.

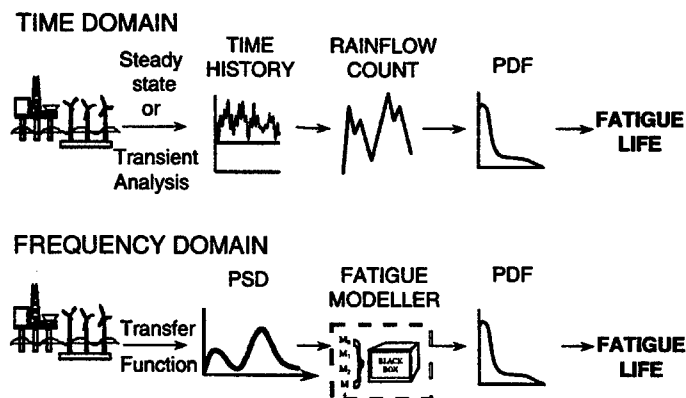


Figure 14. Time versus frequency domain calculations

In order to get structural response in the time domain a transient structural analysis would be required, before the fatigue analysis. In the frequency domain a transfer function would first be computed for the structural model. This is completely independent of the input loading and is a fundamental characteristic of the system, or model. The PSD response, caused by any PSD of input loading, is then obtained by multiplying the transfer function by the input loading PSD. Further response PSD's caused by additional PSD's of input loading can then be calculated with a trivial amount of computing time. Once the response PSD has been computed the remaining task is to estimate the fatigue damage using one of a number of fatigue models.

Narrow band solution

JS Bendat [3] presented the theoretical basis for the first of these frequency domain fatigue models, the so-called *Narrow Band* solution. This expression was defined solely in terms of the spectral moments up to m_4 . However, the fact that this solution was suitable only for a specific class of response conditions was an unhelpful limitation for the practical engineer. The narrow band formula is given below.

$$E[D] = \sum_i \frac{n_i}{N(S_i)} = \frac{S_t}{k} \int S^b p(S) dS$$

$$= \frac{E[P]T}{k} \int S^b \left[\frac{S}{4m_0} e^{\frac{-S^2}{8m_0}} \right] dS$$

This was the first frequency domain method for predicting fatigue damage from PSD's and it assumes that the pdf of peaks is equal to the pdf of stress amplitudes. The narrow band solution was then obtained by substituting the Rayleigh pdf of peaks with the pdf of stress ranges. The full equation is obtained by noting that S_t is equal to $E[P].T$, where T is the life of the structure in seconds (see Figure 15).

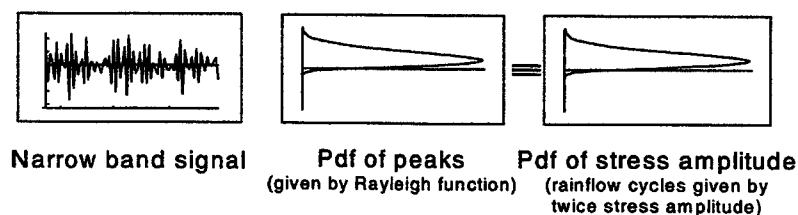


Figure 15. The basis of the narrow band solution

Figure 16 explains why the narrow band solution is so conservative for wide band cases. Two time histories are shown. The narrow band history (a) is made up by summing two independent sine waves at relatively close frequencies. The wide band history (b) uses two sine waves with relatively widely spaced frequencies.

Narrow banded time histories are characterised by frequency modulation known as a beat effect. Wide band processes are characterised by the presence of positive troughs and negative peaks and these are clearly seen in Figure 16 as a sinusoidal ripple superimposed on a larger, dominant sine wave.

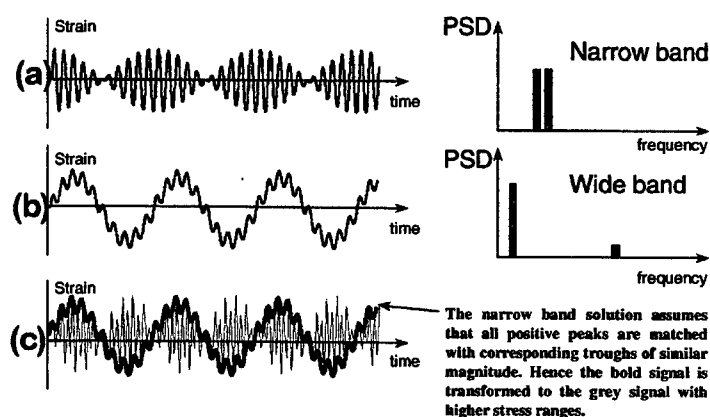


Figure 16. Why the narrow band solution is conservative

The problem with the narrow band solution is that positive troughs and negative peaks are ignored, and all positive peaks are matched with corresponding troughs of similar magnitude regardless of whether they actually form stress cycles. To illustrate this, take every

peak (and trough) and make a cycle with it by joining it to an imaginary trough (peak) at an equal distance the other side of the mean level. This is shown in Figure 16(c). It is easy to see that the resultant stress signal contains far more high stress range cycles than were present in the original signal. This is the reason why the narrow band solution is so conservative.

Dirlik's empirical solution for rainflow ranges

Dirlik [4] has produced an empirical closed form expression for the pdf of rainflow ranges, which was obtained using extensive computer simulations to model the signals using the Monte Carlo technique. Dirlik's solution is given below.

$$p(S) = \frac{\frac{D_1}{Q} e^{-\frac{Z}{Q}} + \frac{D_2 Z}{R^2} e^{-\frac{Z^2}{2R^2}} + D_3 Z e^{-\frac{Z^2}{2}}}{2(m_0)^{1/2}}$$

Where x_m , D_1 , D_2 , D_3 , Q and R are all functions of m_0 , m_1 , m_2 , and m_4 .

Z is a normalised variable equal to $\frac{S}{2(m_0)^{1/2}}$.

ANALYSIS OF NIGHT VISION MECHANISM

To understand the structural behaviour of the model it is worth considering Figure 7 and Figure 17. The sensor head assembly is basically a parallelogram supported at the bulkhead location half way down each rail. In order to resist lateral and vertical sway of the rails, and hence the sensor head, stresses are induced in the rails.

An MSC.Nastran frequency response analysis was performed on the whole FE model shown in Figure 5 using the Nastran solution routine SOL 111, which is used to generate transfer functions. The transfer function from this was then read in to MSC.Fatigue where they were resolved on to Principal planes. The vibration inputs defined in Figure 3 were then defined and applied inside the MSC.Fatigue program. Note that this was not done in NASTRAN. Since, in each case, only one vibration load was applied then the phase relationships between inputs did not have to be taken into account. Where necessary, MSC.Fatigue can also do this using the Cross PSD's between each input.

A separate group was created for the rails using MSC.Patran and only the results for this area were requested. PSD's of stress on Principal planes were produced at every node in this group and the Dirlik algorithm was then used to compute fatigue life. Figure 18 shows one of these rails connected between the forward and rear brackets.

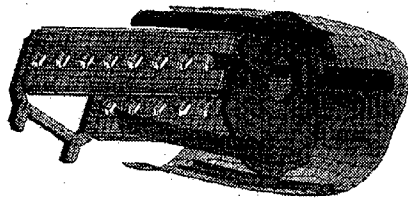


Figure 17. FE model showing 2 side rails attached to front and rear brackets

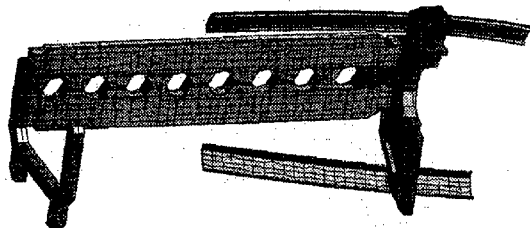


Figure 18. FE model showing side rail

RESULTS

Results were produced over the entire surface of the two rails using MSC.Fatigue. An example of the PSD response results for node 28214 (a critical location mid way along the rail) when subjected to the lateral performance profile is shown in Figure 19.

Using the fatigue life results computed over the entire surface, contour plots of fatigue life (in seconds) were produced. One example, for the lateral performance profile is shown in Figure 20. References [5] and [6] give full technical details of the adopted analysis procedure.

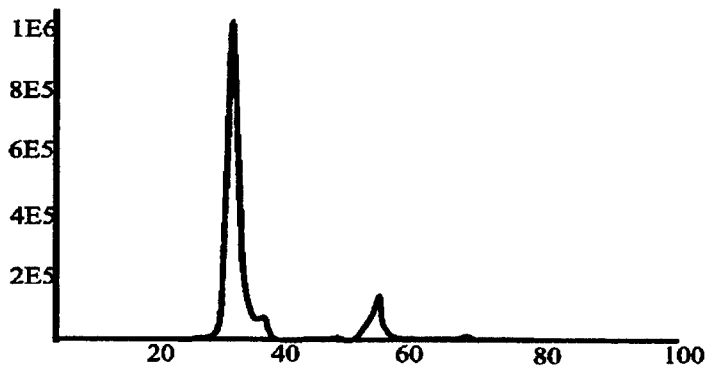


Figure 19. PSD result on Principal plane for node 28214 - lateral performance profile

In order to compute the derived (per mission) fatigue life the results processing tools of MSC.Patran were used. Firstly, all of the individual results were converted into fatigue damage per second. Then the derived result in Figure 21 was obtained by multiplying each subset by its duration in seconds. So, for example, the vertical performance profile damage result was multiplied by 1800 (30 minutes). The derived result was then obtained by summing the individual results and taking the reciprocal. This gave the fatigue life in minutes. The fatigue life of the critical location mid way along the rails is approximately 100 minutes, ie about 1.5 missions of 30, 30, 5 and 5 minutes. This result would suggest that the component would survive the 4 loading environments shown in Figure 3.

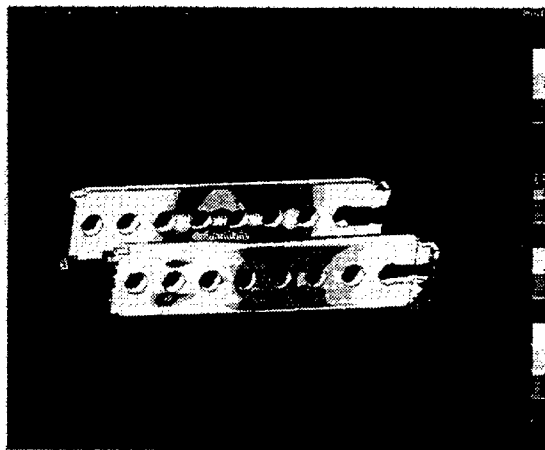


Figure 20. Fatigue life (secs) lat non-oper profile

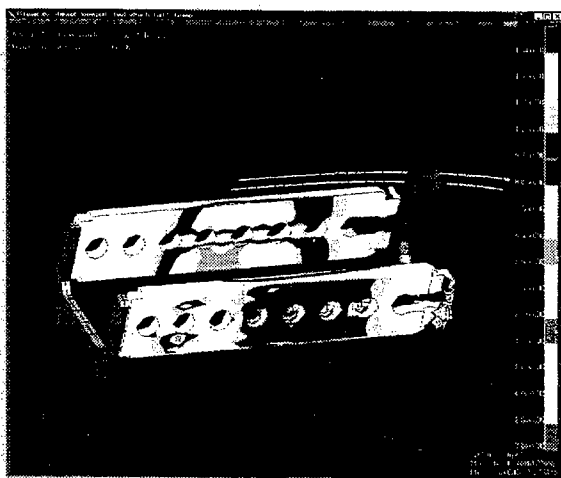


Figure 21. Derived fatigue life (mins) using all 4 profiles

CONCLUSIONS

MSC.Fatigue has been demonstrated as a powerful tool for undertaking full model fatigue calculations for bodies subject to random vibration. Several major improvements to current practice have been introduced. Firstly, a new solution for estimating fatigue life from PSD's is available which works for both narrow and broad band signals. Secondly, it is now possible to use Principal stress planes for fatigue calculations. And finally, it is possible to automatically obtain global results output.

REFERENCES.

1. Rice, SO. Mathematical analysis of random noise. Selected papers on noise and stochastic processes, Dover, New York, (1954).
2. Bishop, NWM and Sherratt, F. Fatigue life prediction from power spectral density data. Part 1, traditional approaches and Part 2, recent developments. Environmental Engineering, 2,(1989).
3. Bendat, JS. Probability functions for random responses. NASA report on contract NAS-5-4590, (1964).
4. Dirlik, T. Application of computers in Fatigue Analysis, University of Warwick Thesis, (1985).

-
5. MSC.Fatigue V8 QuickStart Guide, MSC Corporation, Los Angeles, CA, (1998).
 6. MSC.Fatigue V8 User Manual, MSC Corporation, Los Angeles, CA, (1998).
 7. Bishop, NWM. The use of frequency domain parameters to predict structural fatigue, PhD thesis, Warwick University, (1988).
 8. Bishop, NWM and Sherratt, F A theoretical solution for the estimation of rainflow ranges from power spectral density data. Fat. Fract. Engng. Mater. Struct., **13**, 311-326, (1990).

COMPARISON OF NONLINEAR RANDOM RESPONSE USING EQUIVALENT LINEARIZATION AND NUMERICAL SIMULATION

Stephen A. Rizzi[†] and Alexander A. Muravyov[‡]
NASA Langley Research Center
Structural Acoustics Branch
Hampton, VA 23681-2199

ABSTRACT

A recently developed finite-element-based equivalent linearization approach for the analysis of random vibrations of geometrically nonlinear multiple degree-of-freedom structures is validated. The validation is based on comparisons with results from a finite element based numerical simulation analysis using a numerical integration technique in physical coordinates. In particular, results for the case of a clamped-clamped beam are considered for an extensive load range to establish the limits of validity of the equivalent linearization approach.

INTRODUCTION

Current efforts to extend the performance and flight envelope of high-speed aerospace vehicles have resulted in structures which may respond to the imposed loads in a geometrically nonlinear (large deflection) random fashion. This type of behavior can significantly degrade the structural fatigue life. Linear prediction techniques currently used in the design process are grossly conservative and provide little understanding of the nonlinear behavior. Without practical design tools capable of capturing the important dynamics, further improvements in vehicle performance and system design will be hampered.

Methods currently used to predict geometrically nonlinear random response include perturbation, Fokker-Plank-Kolmogorov (F-P-K), numerical simulation and stochastic linearization techniques. All have various limitations. Perturbation techniques are limited to weak geometric nonlinearities. The F-P-K approach [1, 2] yields exact solutions, but can only be applied to simple mechanical systems. Numerical simulation techniques using numerical integration provide time histories of the response from which statistics of the random response may be calculated. This, however, comes at a high computational expense due to the long time records or high number of ensemble averages required to get quality random response statistics. Statistical linearization methods (e.g. equivalent linearization (EL), see [2-6]) have seen the most broad application because of their ability to accurately capture the response statistics over a wide range of response levels while maintaining relatively light computational burden. Implementations of

[†] Aerospace Engineer

[‡] Former NRC Postdoctoral Research Associate

statistical linearization methods have been primarily limited to special purpose “in-house” computer codes. The first known implementation in a general-purpose code was developed in [7] using MSC/NASTRAN. In this study, an alternative implementation of EL based on the methods developed in [8] and [9] will be used. This implementation was previously validated using the F-P-K method for a few special cases including a Duffing oscillator and beam structure under a convenient, but non-physical loading condition. In the present study, results from the EL analysis will be compared with those from a finite element based numerical simulation analysis for the case of a clamped-clamped beam under random inertial loading. By studying a wide range of load levels, the range of applicability is established.

EQUIVALENT LINEARIZATION APPROACH

The equations of motion of a multiple degree-of-freedom, viscously damped geometrically nonlinear system can be written in the form:

$$M\ddot{X}(t) + C\dot{X}(t) + KX(t) + \Gamma(X(t)) = F(t) \quad (1)$$

where M , C , K are the mass, damping, and stiffness matrices, X is the displacement response vector and F is the force excitation vector, respectively. The nonlinear stiffness term $\Gamma(X)$ is a vector function which generally includes 2nd and 3rd order terms in X . An approximate solution to (1) can be achieved by formation of an equivalent linear system:

$$M\ddot{X}(t) + C\dot{X}(t) + (K + K_e)X(t) = F(t) \quad (2)$$

where K_e is the equivalent linear stiffness matrix.

The traditional (force error minimization) method of EL seeks to minimize the difference between the nonlinear force and the product of the equivalent linear stiffness and displacement response vector. Since the error is a random function of time, the required condition is that the expectation of the mean square error be a minimum, i.e.:

$$error = E[(\Gamma(X) - K_e X)^T (\Gamma(X) - K_e X)] \rightarrow \min \quad (3)$$

where $E[\dots]$ represents the expectation operator. Equation (3) will be satisfied if

$$\frac{\partial(error)}{\partial K_{eij}} = 0 \quad i, j = 1, 2, \dots, N$$

In this study, consideration is limited to the case of Gaussian, zero-mean excitation and response to simplify the solution. With these assumptions and omitting intermediate derivations, the final form for the equivalent linear stiffness matrix becomes (see for example [3] and [4]):

$$K_e = E \left[\frac{\partial \Gamma}{\partial X} \right] \quad (4)$$

An alternative approach based on potential (strain) energy error minimization was proposed in [5] and [6], where mostly single degree-of-freedom systems were considered. A generalization for multiple degree-of-freedom systems is developed in [8] and [9]. For the sake of brevity, the present paper will present the formulation and results from the force error minimization only.

Applying the modal coordinate transformation

$$X = \Phi q$$

to equation (2) yields a set of coupled modal equations with reduced degrees of freedom, where Φ is generally a subset ($L \leq N$) of the linear eigenvectors, and q are the modal coordinates. This coupled set is expressed as:

$$[I]\ddot{q} + [2\zeta_r \omega_r]\dot{q} + [\omega_r^2] + [k_e]q = f \quad (5)$$

where ω_r are the undamped natural frequencies, $[I]$ is the unit matrix, $[2\zeta_r \omega_r]$ is the diagonal modal damping matrix, $[\omega_r^2]$ is the diagonal modal stiffness matrix, and $[k_e]$ is the fully populated equivalent stiffness matrix given by:

$$[k_e] = \left[E \left[\frac{\partial \gamma}{\partial q} \right] \right] \quad (6)$$

The nonlinear terms may be represented in the following form:

$$\gamma_r(q_1, q_2, \dots, q_L) = \sum_{j,k=j}^L a'_{jk} q_j q_k + \sum_{j,k=j,l=k}^L b'_{jkl} q_j q_k q_l \quad (7)$$

where a'_{jk} and b'_{jkl} are nonlinear stiffness coefficients with $j = 1, 2, \dots, L$, $k = j, j+1, \dots, L$, and $l = k, k+1, \dots, L$. This form of the nonlinear terms facilitates the solution of equations (5) when the forces and displacements are random functions in time.

Iterative Solution

Because the equivalent stiffness matrix k_e is a function of the unknown modal displacements, the solution takes an iterative form. The time variation of the modal displacements and forces may be expressed as:

$$q_r(t) = \sum_n \hat{q}_r e^{i\omega_n t} \quad f_r(t) = \sum_n \hat{f}_r e^{i\omega_n t} \quad (8)$$

where $(\hat{})$ indicates the dependency on ω_n . Applying (8) to (5) and writing in iterative form gives:

$$\hat{q}^m = [H^{m-1}] \hat{f} \quad (9)$$

where m is the iteration number and

$$[H^{m-1}] = [-\omega_n^2 [I] + i\omega_n [2\zeta_r \omega_r] + [\omega_r^2] + [\alpha k_e^{m-1} + \beta k_e^{m-2}]]^{-1} \quad (10)$$

The introduction of the weightings α and β are to aid in the convergence of the solution, with the condition that $\alpha + \beta = 1$.

For stochastic excitation, (9) is rewritten as:

$$[S_{qq}^m] = [H^{m-1}] [S_{ff}] [\bar{H}^{m-1}]^T \quad (11)$$

and

$$E[q_r q_s]^m = \sum_n S_{\hat{q}_r \hat{q}_s}^m \Delta \omega_n$$

The diagonal elements of $[S_{qq}^m]$ are the variances of the modal displacements. For the first iteration, $[k_e]$ is zero yielding the covariance matrix $E[q_r q_s]$ of the linear system. For subsequent iterations ($m > 1$), $[k_e^m]$ is determined from (6) as:

$$[k_e^m] = \left[E \left[\frac{\partial \gamma}{\partial q} \right] \right]^m = \begin{bmatrix} E \left[\frac{\partial \gamma_1}{\partial q_1} \right] & \cdots & E \left[\frac{\partial \gamma_1}{\partial q_L} \right] \\ \vdots & \ddots & \vdots \\ E \left[\frac{\partial \gamma_L}{\partial q_1} \right] & \cdots & E \left[\frac{\partial \gamma_L}{\partial q_L} \right] \end{bmatrix}^m \quad (12)$$

where (from (7)),

$$\left[E \left[\frac{\partial \gamma}{\partial q} \right] \right]^m = \begin{bmatrix} \sum_j^L a_{j1}^1 E[q_j] + \sum_{j,k=j}^L b_{jk1}^1 E[q_j q_k] & \cdots & \sum_j^L a_{jL}^1 E[q_j] + \sum_{j,k=j}^L b_{jkL}^1 E[q_j q_k] \\ \vdots & \ddots & \vdots \\ \sum_j^L a_{jL}^L E[q_j] + \sum_{j,k=j}^L b_{jkL}^L E[q_j q_k] & \cdots & \sum_j^L a_{jL}^L E[q_j] + \sum_{j,k=j}^L b_{jkL}^L E[q_j q_k] \end{bmatrix}^{m-1} \quad (13)$$

Recall a zero-mean response is assumed, i.e. $E[q] = 0$, which reduces (13) to:

$$\left[E \left[\frac{\partial \gamma}{\partial q} \right] \right]^m = \begin{bmatrix} \sum_{j,k=j}^L b_{jk1}^1 E[q_j q_k] & \cdots & \sum_{j,k=j}^L b_{jkL}^1 E[q_j q_k] \\ \vdots & \ddots & \vdots \\ \sum_{j,k=j}^L b_{jkL}^L E[q_j q_k] & \cdots & \sum_{j,k=j}^L b_{jkL}^L E[q_j q_k] \end{bmatrix}^{m-1} \quad (14)$$

The iterations continue until convergence of the equivalent stiffness matrix such that

$$\| [k_e^m] - [k_e^{m-1}] \| < \varepsilon$$

The value of ε typically used is 0.1%. Following convergence, the $N \times N$ covariance matrix of the displacements in physical coordinates is recovered from

$$E[X_i X_j] = \Phi E[q_r q_s] \Phi^T \quad (15)$$

and root-mean-square values are the square roots of the diagonal terms in (15). Further post-processing to obtain power spectral densities of displacements, stresses, strains, etc., may be performed by substituting the converged equivalent stiffness matrix into (5) and solving in the usual linear fashion.

Implementation

The EL procedure as outlined above was recently implemented within the context of MSC/NASTRAN using the DMAP programming language [10]. The implementation entails first performing a normal modes analysis (solution 103) to obtain the modal matrices, from which a subset of L modes are chosen. Since the form of the nonlinear stiffness terms are not explicitly known, the nonlinear stiffness coefficients a'_{jk} and b'_{kl} must be determined numerically. To accomplish this, a series of inverse problems are performed by prescribing displacement fields as linear combinations of modes to the linear static (solution 101) and nonlinear static (solution 106) solutions. The nonlinear stiffness coefficients are then determined from the resulting linear and nonlinear nodal forces. The process by which this is done is covered in detail in [8] and [9]. The iterative solution is performed within a standalone DMAP alter, which has as its output the root-mean-square displacements in physical coordinates, the cross covariance in modal coordinates, and the sum of the linear and equivalent linear modal stiffness matrices. The latter may be substituted for the linear modal stiffness in the modal frequency response analysis (solution 111) for post-processing.

NUMERICAL SIMULATION APPROACH

A numerical simulation analysis was performed to generate time history results from which response statistics could be calculated. The particular method used was finite element based with the integration performed in physical coordinates. Two different integration methods were used depending on the response level. For lower level responses, an implicit integration method was taken which allowed for larger time steps compared with the explicit method. Because the implicit scheme is unconditionally stable, a convergence study on the time step was undertaken at each response level to ensure adequacy of the time step. This was done by halving the Δt used until the time history response over the calculation period was unchanged. As the response level became higher at the higher excitation levels, the Δt required to obtain a converged solution became smaller. When the Δt required was on the order of the time step required for the explicit method, it became more efficient to perform the explicit integration. Both methods produced identical results, so the particular choice of implicit versus explicit was dictated solely by the time required to run each analysis. In both the implicit and explicit methods, the nonlinear deformation was handled using a corotational scheme [11]. The program NONSTAD [12] was used to generate the numerical simulation results.

Loading Time History

The time history of the load was generated by summing equal amplitude sine waves with random phase within a specified bandwidth using a discrete inverse Fourier transform. This generated a pseudo-random time history with a specified amplitude and period T . The period was specified by $2^n \Delta t$. In this study, $\Delta t = 50 \mu s$ and $n = 16$, giving a period of $1.6384 s$ in duration. The selected Δt corresponded with that needed for the implicit integration scheme used for the lower loading levels. The explicit integration scheme used for the higher load levels interpolated the signal between points such that the specified loading at each Δt interval was maintained. A radix-2 number of time history samples was chosen to facilitate use of radix-2 FFT algorithms employed for the subsequent analysis. An ensemble of time histories was generated by specifying different seeds to the random number generator.

A typical time history corresponding to an inertial load of $0.05g$ RMS is shown in Figure 1. The corresponding probability density function is also shown with the Gaussian distribution. The power spectral density for 10 ensemble averages gives a spectrum level of $1.67 \times 10^{-6} g^2/Hz$ over a $1500 Hz$ bandwidth as shown. A sharp roll-off of the input spectrum practically eliminates excitation of the structure outside the frequency range of interest.

Transient Response Processing

The structure is assumed to be at rest at the beginning of each loading. An initial transient in the structural response is therefore induced before the response becomes fully developed. This transient must be eliminated to ensure the proper response statistics are recovered.

The approach taken to eliminate the transient is shown graphically in Figure 2. Because the loading is pseudo-random, it is possible to apply multiple periods of the load and generate the same statistics for periods of length T beginning at any point in time. For example, the statistics of the load are the same for the period $0 - T$ as they are for the period $T/4 - 5T/4$. In a like manner, for the linear condition, the response statistics are the same for any period T following the initial transient. Therefore, by computing the desired statistic for a moving window of period T , it is possible to identify a point in time t_o after which the response statistics do not change significantly. In the present study, the root-mean-square response was monitored and a time of $t_o = 0.5s$ was found suitable. For each loading history, a total response of $T + 0.5s = 2.1384s$ was calculated and the first $0.5s$ was discarded. Note that a similar argument for the nonlinear condition does not hold because the nonlinear response is not periodic over T . Nevertheless, the above approach was employed with satisfactory results.

Response Statistics

Response statistics were generated from an ensemble of $N=10$ time histories at each load level. Estimates of the displacement root-mean-square served as the basis for comparison with the EL method, which essentially had the RMS as its basic unknown. Additionally, confidence intervals for the mean value of the RMS estimate were generated to quantify the degree of uncertainty in the estimate [13] using:

$$\left[\bar{x} - \frac{st_{n;\alpha/n}}{\sqrt{N}} \leq \mu_x < \bar{x} + \frac{st_{n;\alpha/n}}{\sqrt{N}} \right], \quad n = N - 1$$

where \bar{x} and s^2 are the sample mean and variance of the RMS estimates from N ensembles, and t_n is the Student t distribution with n degrees of freedom, evaluated at $\alpha/2$. For the 90% confidence intervals calculated, $\alpha = 0.1$.

Estimates of the displacement mean, skewness, and kurtosis were also computed to help ascertain the degree to which the assumptions made in the development of the equivalent linearization method were followed. Power spectral density and probability density functions of the displacement were computed for similar purposes.

RESULTS

Validation studies were conducted using an 18-in. x 1-in. x 0.09in. ($l \times w \times h$) clamped-clamped aluminum beam with material properties:

$$E = 10.6 \times 10^6 \text{ psi}, \quad G = 4.0 \times 10^6 \text{ psi}, \quad \rho = 2.588 \times 10^{-4} \frac{\text{lb}_f \cdot \text{s}^2}{\text{in}^4}$$

The beam was subjected to an inertial loading over a computational bandwidth of 1500 Hz, as shown in Figure 1. This bandwidth was in excess of the desired bandwidth of 1000 Hz to allow for the contribution of the higher order modes in the EL solution. This is especially important for capturing the anti-resonant behavior. The numerical simulation analysis utilized the same loading for consistency, although the effect of the higher order modes are automatically realized since the computations are performed in physical coordinates. Since the loading was uniformly distributed, only symmetric modes were included in the analysis. In general, any combination of symmetric and non-symmetric modes may be included.

The NASTRAN model used in the EL analysis was comprised of thirty-six 1/2-in. long CBEAM elements. The EL analysis used a four-mode solution comprised of the first four symmetric bending modes. Damping was chosen to be consistent with the mass-proportional damping of the numerical simulation analysis and at a level sufficiently high so that a good comparison could be made at the peaks of the PSD. This dictated a critical damping of 2.0%, 0.37%, 0.15%, and 0.081% for the first four symmetric modes. The finite element model used in the numerical simulation analysis was also comprised of thirty-six 1/2-in. long beam elements. Both EL and simulation finite

element models were checked for convergence by running additional analyses with models consisting of 1/4-in. elements.

Analysis was performed at load levels of 0.8, 3.2, 12.8, 51.2, and 204.8 g RMS, giving a dynamic range of 48 dB. Figure 3 shows the normalized RMS out-of-plane (w) deflection at the beam center as a function of load level. The numerical simulation results are shown with 90% confidence intervals of the RMS estimate. At the lowest load level of 0.8 g RMS, the response is linear as can be seen by the comparison with results from a strictly linear analysis (NASTRAN solution 111). A small, but noticeable, difference between the linear and nonlinear response is noted at the 3.2g RMS load level. The degree of nonlinearity increases with load level, as expected. At the highest load level, the nonlinear response calculations predict a RMS center deflection of 2.5 times the thickness compared with the nearly 11 times the thickness from the linear analysis.

In order to gain greater insight into the nonlinear dynamics, plots of the time history, PSD, and PDF are shown for three load levels, 0.8, 51.2 and 204.8g RMS, in Figure 4 through Figure 6, respectively. Data in the time history and PDF plots correspond solely to numerical simulation results. Data in the PSD plots correspond to numerical simulation and EL results, where the EL results were generated by running a linear analysis (NASTRAN solution 111) using the equivalent linear stiffness generated by the EL process described above. Also shown in the figures are plots of the normalized RMS deflection shape for both numerical simulation and EL analyses.

Results for the 0.8g RMS excitation level are shown in Figure 4. This excitation level was shown (see Figure 3) to produce a linear response. As expected, the PDF mimics the normally distributed PDF of the input shown in Figure 1. The averaged PSD and normalized deflected shape show excellent agreement between the EL and numerical simulation results. This agreement helps to establish the confidence in making comparisons between these two fundamentally different analyses.

Figure 5 shows a nonlinear response associated with the 51.2g RMS excitation level. The time history of the center displacement has a visibly higher peak probability and the PDF exhibits a flattening at the peak. The PSD from both the numerical simulation and EL analyses both show the shifting of peaks to higher frequencies compared with the linear solution. This shifting is associated with a hardening spring type of nonlinearity. Note that the frequencies associated with the peaks of the EL solution are the natural frequencies of the equivalent linear system. The numerical simulation results correctly show the peak broadening effect, which the EL analysis is unable to capture. Also distinguishable in the numerical simulation results are contributions of harmonics. The effect of nonlinearity is somewhat over predicted in the EL result, as seen in the normalized deflection shape.

The highest degree of nonlinearity is shown in Figure 6, corresponding to the 204.8g RMS load. The time history is further peak oriented and the PDF is nearly flat. The peak broadening in the PSD of the numerical simulation results is severe, and nearly flattens the spectrum above 350 Hz. Of particular interest is flattening of the normalized deflection shape, which both the EL and numerical simulation results reflect. This is likely to have a significant effect on the strain distribution. It is unclear why the results at the 204.8g RMS load level compare more favorably than those at the 51.2g RMS level. This behavior warrants further investigation.

Moments of the center displacement were calculated from the numerical simulation results for all load levels. They are provided in Table 1 with the RMS center displacement from the EL analysis. The EL and numerical simulation results agree well, thus validating the EL analysis over a substantial load range. The validity of assumptions made in the development of the EL method are ascertained by observing the mean, skewness and kurtosis. The mean value is effectively zero for all load levels, indicating the assumption of zero mean response has not been violated. Although the PDF is more or less skew-symmetric, the shape is flattened at the higher load levels as indicated by a decreasing kurtosis from the linear value of 3. The decreasing kurtosis values indicate a violation of the Gaussian response assumption. However, even with this non-Gaussian response distribution, the EL analysis gives a good prediction of the RMS response.

Table 1: Moments of the center displacement.

Load (g) _{RMS}	Mean (in.)	EL RMS (in.)	Numerical Simulation RMS (90% Confidence Interval) (in.)	Skewness	Kurtosis
0.8	-6.54×10^{-8}	0.0038	$0.00379 \leq \text{RMS} < 0.00381$	0.0197	3.05
3.2	-5.26×10^{-6}	0.0147	$0.01438 \leq \text{RMS} < 0.01532$	0.0190	2.82
12.8	-1.62×10^{-5}	0.0458	$0.04680 \leq \text{RMS} < 0.05350$	-0.0017	2.47
51.2	-4.93×10^{-6}	0.1078	$0.11268 \leq \text{RMS} < 0.12325$	-0.0002	2.25
204.8	3.78×10^{-4}	0.2285	$0.21654 \leq \text{RMS} < 0.23216$	-0.0058	2.29

DISCUSSION

The RMS random response predictions from the EL implementation have been validated through a wide range of load levels. Comparisons with numerical simulation results are good, even when the assumption of Gaussian response has been violated.

Differences that do exist warrant some discussion. It is seen that the EL approach slightly over-predicts the degree of nonlinearity compared to the numerical simulation results. This does not appear to be due to a violation of the assumption of a Gaussian response because the over-prediction does not correlate with increasing kurtosis of response. The likely reason for the difference is in the error minimization approach used. Results previously

computed using the alternative strain-energy error minimization technique, not included here, indicated better comparison with the exact F-P-K solution than the conventional force-based error minimization undertaken here [9]. The improved comparison of strain-energy error minimization and simulation results was also seen in a different EL implementation for the problem of a beam on an elastic foundation [6]. The strain-energy analysis is beyond the scope of this paper and is left as an area for further investigation.

Some implications on the use of the EL technique as a basis for fatigue life calculations are worth mentioning. First, assuming that stresses or strains from the EL technique will compare equally well with the fully nonlinear results, a simple fatigue-life calculation based on RMS levels will be much less conservative than calculations based on linear analyses. This offers the potential for substantial weight savings for structures designed using nonlinear methods. Secondly, it appears that a nonlinear analysis, EL or otherwise, is required to accurately calculate the RMS deflected shape. Use of a linear RMS deflected shape scaled to the nonlinear level would inaccurately reflect the spatial distribution. Simple fatigue-life calculations based on the RMS stress or strain could be significantly affected as these quantities depend on the spatial distribution of the deformation. Lastly, use of the EL derived PSD response in a more sophisticated fatigue-life calculation requires careful investigation. Recall that peaks in the equivalent linear PSD may occur at different frequencies than the fully nonlinear PSD, as shown in Figure 5 and Figure 6. Methods such as spectral fatigue analysis [14], which take moments of the PSD, may incorrectly account for the contribution a particular frequency component in the cycle counting scheme. It is not known, for example, if the narrowly shaped, higher fundamental frequencies of the equivalent linear PSD result in conservative or non-conservative estimates of fatigue life relative to predictions made using the fully nonlinear PSD with more broadly shaped, lower fundamental frequencies. An assessment of this effect is left as an area for further study.

The question of computational efficiency has not been addressed in this paper because the differing analyses were performed on different computer platforms. What can be stated is that the computational burden for the EL approach will increase only slightly with an increase in the size of the physical model for the same number of modes used in the solution. This increase is associated with the solution of a larger linear eigenvalue problem. The expense of the numerical simulation solution, however, will increase dramatically with an increase in physical system size.

ACKNOWLEDGEMENTS

The authors wish to thank Professor James F. Doyle of Purdue University for providing the finite element code NONSTAD used for the numerical simulation analysis and for his advice on its use. The authors also thank

Travis Turner and Jay Robinson of NASA Langley Research Center for helpful discussions and comments.

REFERENCES

1. Bolotin, V.V., Statistical methods in structural mechanics. 1969: Holden-Day, Inc.
2. Lin, Y.K., Probabilistic theory of structural dynamics. 1976, Malabar, FL: R.E. Krieger.
3. Roberts, J.B. and Spanos, P.D., Random vibration and statistical linearization. 1990, New York, NY: John Wiley & Sons.
4. Atalik, T.S. and Utku, S., Stochastic linearization of multi-degree-of-freedom nonlinear systems, *Earthquake engineering and structural dynamics*, 1976, **4**, pp. 411-420.
5. Elishakoff, I. and Zhang, R. Comparison of new energy-based versions of the stochastic linearization technique. In *IUTAM Symposium*, Turin, Springer-Verlag, 1992, pp. 201-211.
6. Fang, J. and Elishakoff, I., Nonlinear response of a beam under stationary excitation by improved stochastic linearization method, *Applied Mathematical Modelling*, 1995, **19**, pp. 106-111.
7. Robinson, J.H., Chiang, C.K., and Rizzi, S.A., Nonlinear Random Response Prediction Using MSC/NASTRAN, NASA TM 109029, October 1993.
8. Muravyov, A.A., Turner, T.L., Robinson, J.H., Rizzi, S.A. A new stochastic linearization implementation for prediction of geometrically nonlinear vibrations. In *40th AIAA/ASCE/AHS/ASC Structures, Structural Dynamics and Materials Conference*, St. Louis, MO, AIAA, 1999, pp. 1489-1497.
9. Muravyov, A.A. Determination of nonlinear stiffness coefficients for finite element models with application to the random vibration problem. In *MSC Worldwide Aerospace Conference Proceedings*, Long Beach, MacNeal-Schwendler Corp., 1999, pp. 1-14.
10. Bella, D. and Reymond, M., eds. *MSC/NASTRAN DMAP Module Dictionary*. Version 68 ed. . 1994, MacNeal-Schwendler Corporation: Los Angeles, CA.
11. Crisfield, M.A., Nonlinear finite element analysis of solids and structures. Vol. 2. 1997: Wiley.
12. Doyle, J.F., Lecture Notes: AAE 546 - Static and dynamic analysis of thin-walled structures. 1999: Purdue University.
13. Bendat, J.S. and Piersol, A.G., Random data: Analysis and measurement procedures. 1971: Wiley-Interscience.
14. Bishop, N.W.M. and Sherratt, F., A theoretical solution for the estimation of rainflow ranges from power spectral density data, *Fat. Fract. Engng. Mater. Struct.*, 1990, **13**, pp. 311-326.

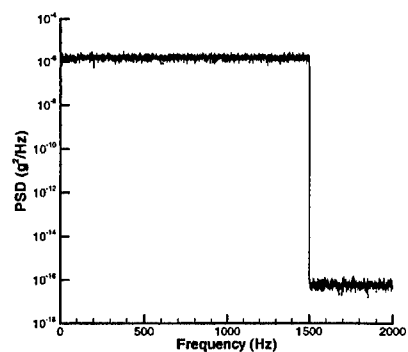
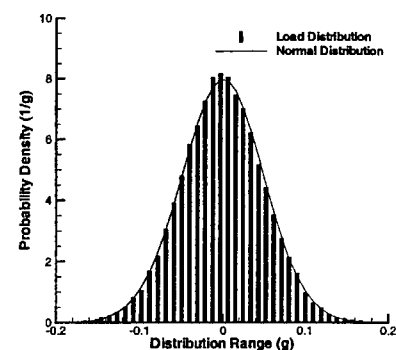
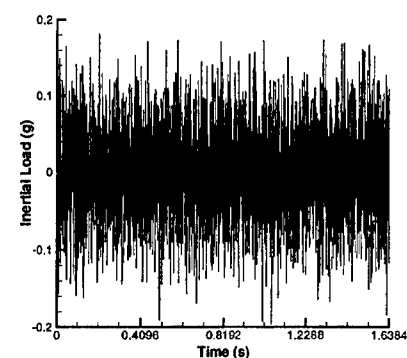


Figure 1: Typical loading time history, probability density, and power spectral density.

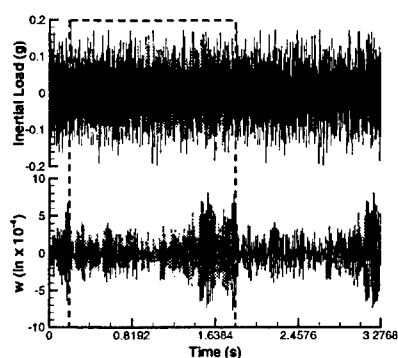


Figure 2: Transient response processing.

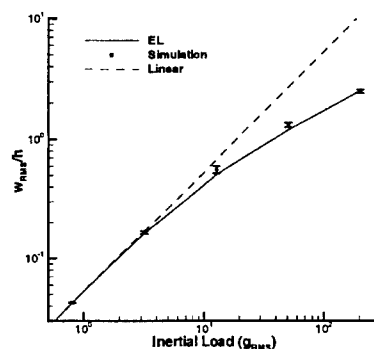


Figure 3: Normalized RMS center deflection as a function of inertial load

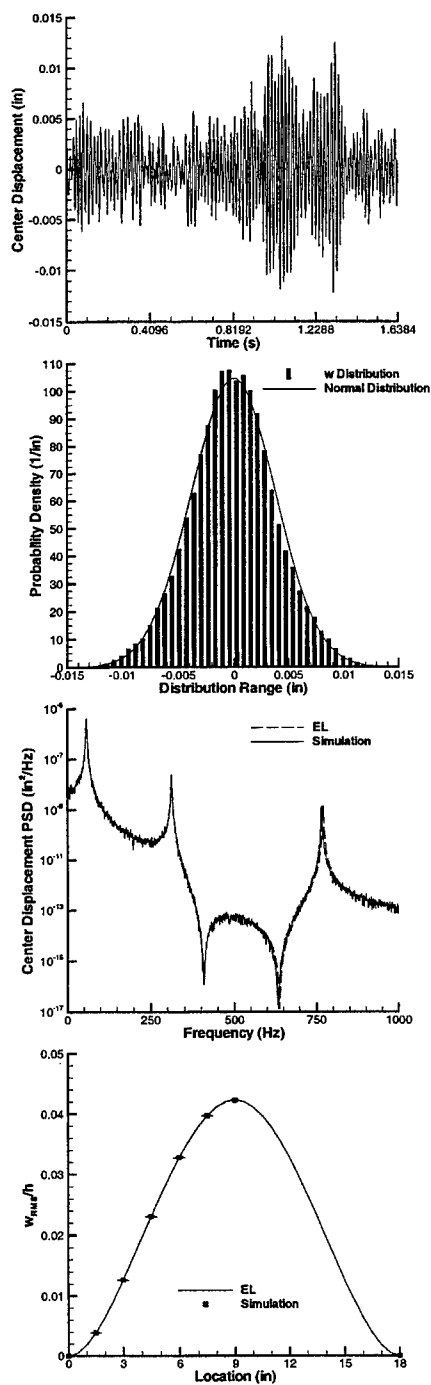


Figure 4: Center deflection response and normalized deflection shape at 0.8g RMS inertial load.

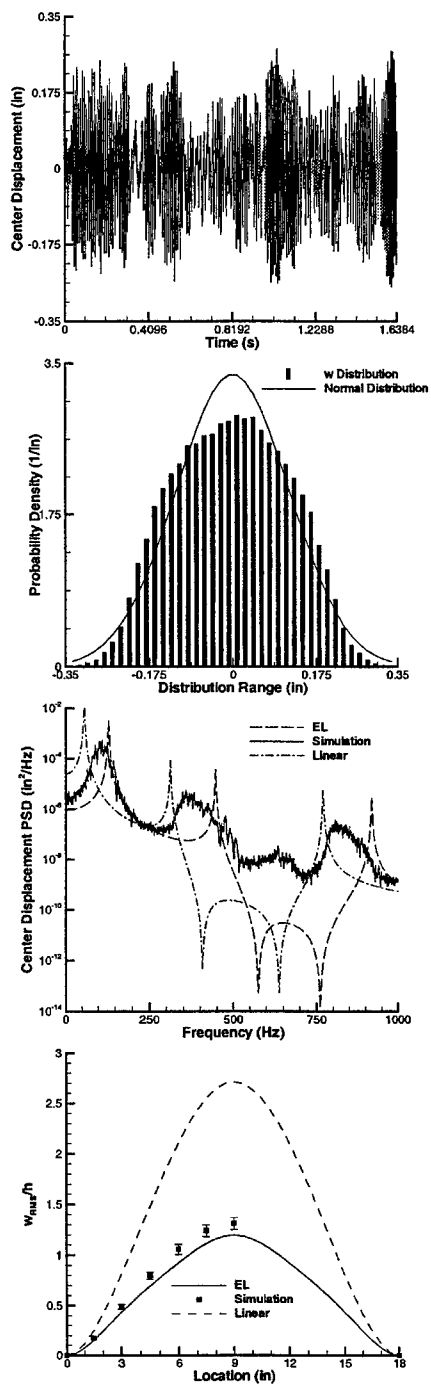


Figure 5: Center deflection response and normalized deflection shape at 51.2g RMS inertial load.

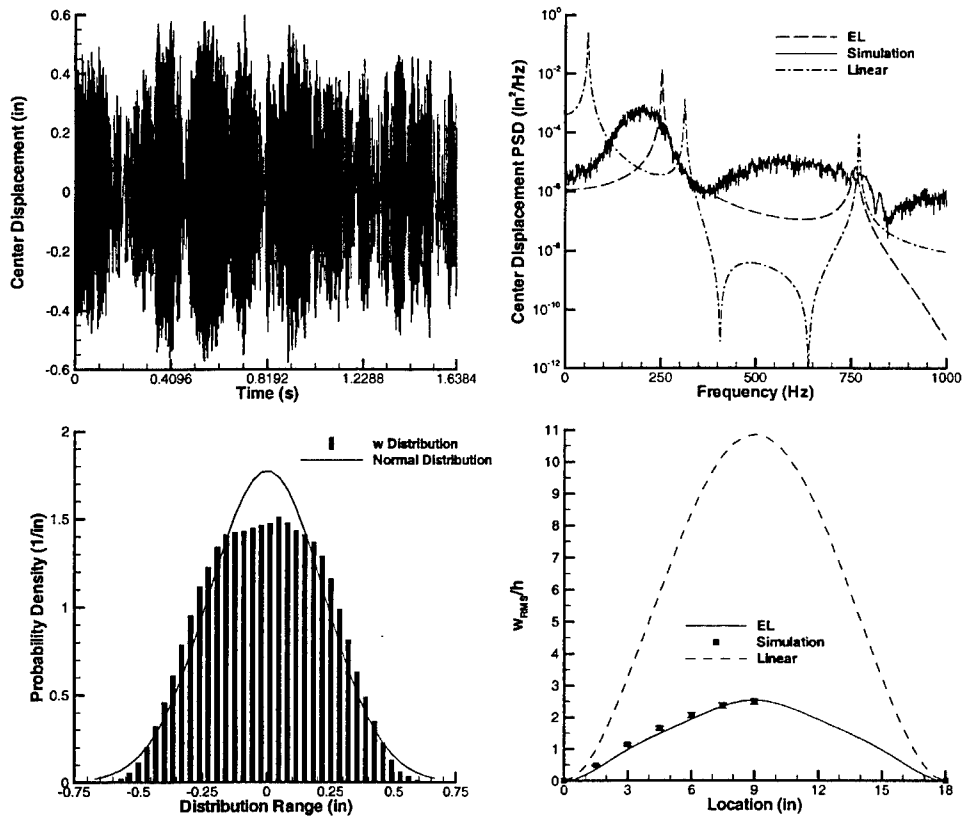


Figure 6: Time history, PSD, and PDF of center deflection response and normalized deflection shape at 204.8g RMS inertial load.

Effects of temperature dependent physical properties on the response of thermally buckled plates

Jon Lee

Air Force Research Laboratory (VASS)

Wright-Patterson Air Force Base, OH 45433, USA

jon.lee@wpafb.af.mil

Abstract

Under plate heating by a uniform temperature rise above the ambient temperature, we have obtained simple analytical expressions of static single-mode analysis to include the temperature-dependent physical properties. The critical buckling temperature is lowered but the post-buckled plate displacement is raised as the plate temperature increases. This qualitatively confirms the numerical computations of previous investigators. We have further found that the temperature-dependent properties decrease the static normal x-stress and increase the static x-strain based on the post-buckled plate displacements. Surprisingly, when we formulate a single-mode stochastic dynamics, the RMS x-stress and x-strain are also decreased and increased by the temperature-dependent physical properties. More than that, the percent decreases in static and RMS x-stress are nearly the same, so are the percent increases in static and RMS x-strain.

Nomenclature

$a_{i,j}$	= Fourier amplitudes for w
C_0, C_1, C_2	= quadratic constants for $\hat{\sigma}$ and $\hat{\epsilon}$
D	= $Et^3/12(1-\mu^2)$
E, E_1	= Young modulus, fractional increment of E per a degree of temperature
$f(t)$	= $\hat{f}p_{1,1}/(\rho h^2/\gamma^2)$
$\hat{f}p_{i,j}$	= Fourier amplitudes for p
F	= dimensionless power input for white-noise excitations
G	= $\omega^2(s-1)\sqrt{2\lambda/\kappa F}$
h	= plate thickness
L_x, L_y	= plate sides in x and y coordinates
p	= externally applied pressure
$P(\hat{x}), P(r)$	= Fokker-Planck distributions
q	= $a_{1,1}/h$
Q	= $a_{1,1}$
s	= t_o/T^*
t, τ	= time, dimensionless time t/γ
t_o	= uniform plate temperature above the reference

	temperature
T^*	= critical buckling temperature
x, y, z	= plate coordinates (x and y normalized by L_x and L_y)
w	= transverse displacement
Z	= z/h
α, α_1	= thermal expansion coefficient, fractional increment of α per a degree of temperature
β	= L_y/L_x
γ	= $\sqrt{\rho h L_y^4 / \pi^4 D_r}$
$\varepsilon_{(x,y,xy)}$	= normal strain tensor components
$\hat{\varepsilon}$	= $\varepsilon_x L_y^2 / \pi^2 h^2$
ζ	= damping coefficient
κ	= cubic stiffness
λ	= $2\zeta\omega$
μ	= Poisson's ratio
ρ	= plate mass density
$\sigma_{(x,y,xy)}$	= normal stress tensor components
$\hat{\sigma}$	= $\sigma_x L_y^2 / \pi^2 h^2 E_r$
φ_i	= beam mode functions
Ψ	= Airy stress function
ω	= square root of linear stiffness
subscript 'a'	= actual temperature
subscript 'r'	= reference temperature
$\langle \dots \rangle$	= statistical average

1. Introduction

For the thermal-acoustic structural fatigue analysis, one estimates the statistical responses of displacement and stress/strain on metallic and composite plates under the intense heating up to 2000°F and huge acoustic loading over 170 dB. In spite of a large temperature variation, the physical properties, such as the thermal expansion coefficients, Young's moduli of elasticity, and Poisson's ratios, are usually assumed temperature independent. Hence, constant physical property values at the reference (room) temperature have been used in analyses for simplicity (e.g., Ref. [1–3]). Since Poisson's ratios are not susceptible to temperature variation [4], we shall call in this paper only thermal expansion coefficient and Young's modulus the temperature-dependent physical properties.

In fact, the physical properties do not change much with temperature. For instance, the thermal expansion coefficient increases by 2.75%/100°F for aluminum and 1.25%/100°F for Silicon-Carbon-Titanium. On the other hand, a typical Young's modulus decreases by 3.75%/100°F for aluminum and 2%/

100°F for Silicon-Carbon-Titanium [4–6]. Although the incremental changes are small, total variations over many multiples of 100°F cannot be ignored. Since Hoff [7] first drew attention to the temperature-dependent physical properties at high temperature buckling in 1957, temperature dependency has been addressed in a variety of structural analyses [8–13]. We however consider here only those pertaining to thermally buckled plates [5, 11, 12].

By a static analysis, Kamiya & Fukui [11] first showed that the maximum displacement is raised by temperature-dependent physical properties for simply-supported and clamped square aluminum plates. They have remarked in passing that the critical buckling temperatures are decreased by temperature-dependent properties. Later, Chen & Chen [12] carried out a parametric study to demonstrate that the temperature-dependent physical properties always lower critical buckling temperatures. More recently, Mei et al. [5] have recomputed the maximum post-buckled displacement of a clamped square aluminum plate, together with the static bending and membrane stresses. However, since the changes wrought by temperature-dependent physical properties are so slight, they have dismissed the effects of temperature dependency as insignificant.

The main purpose of this paper is to demonstrate how the temperature-dependent physical properties would affect the static and stochastic dynamic responses of thermally buckled plates. As already shown [1], the formulation of heated plates involves three thermal terms; (i) a uniform plate temperature rise above the reference temperature, (ii) a local temperature variation over the mid-plate plane superposed on (i), and (iii) a temperature gradient across the plate thickness. The first two thermal terms represent total plate temperature over the mid-plate, and hence they contribute to thermal buckling. On the other hand, the third term inducing thermal moment provides an additional forcing, and hence brings about asymmetry in the potential energy well. Since the first thermal term contributes mostly to thermal buckling, we shall restrict the present analysis (Sec. 2) to a heated plate whose temperature is raised uniformly over the mid-plate above the reference temperature. Besides, the inclusion of the other thermal terms will complicate the analysis, and thereby obscuring the first-order effects of temperature-dependent physical properties.

From a single-mode static analysis in Sec. 4, we first present simple analytical expressions for the critical buckling temperature and post-buckled plate displacement. Based on the latter, we compute the normal components of static x -stress and x -strain. In Sec. 5 we pose a stochastic dynamic problem for the single-mode equation under a random white-noise forcing. We then compute the RMS x -stress and x -strain to compare with the static analysis counterparts.

2. The plate equations under a uniform temperature heating

In our previous work [1], we have considered the heating of thin plate in a general temperature field $T(x, y, z)$ consisting of a uniform temperature rise

above the reference (room) temperature, a temperature variation over the mid-plate, and a linear temperature gradient across the plate thickness. We shall consider here plate heating by

$$T(x, y, z) = t_o, \quad (1)$$

where t_o is a uniform temperature rise above the reference temperature.

The formulation of [1] involves the transverse displacement w and Airy stress function Ψ , instead of the two in-plane displacements. Under the uniform temperature heating (1), thermal terms do not appear explicitly in the equations for w and Ψ . Written in the normalized coordinates x and y ranging over $(0, 1)$, we have

$$\begin{aligned} \rho h \frac{\partial^2 w}{\partial t^2} + \rho h \zeta \frac{\partial w}{\partial t} - p + \frac{D}{L_y^4} \left[\beta^4 \frac{\partial^4 w}{\partial x^4} + 2\beta^2 \frac{\partial^4 w}{\partial x^2 \partial y^2} + \frac{\partial^4 w}{\partial y^4} \right] = \\ \frac{\beta^2}{L_y^4} \left[\frac{\partial^2 w}{\partial x^2} \frac{\partial^2 \Psi}{\partial y^2} + \frac{\partial^2 w}{\partial y^2} \frac{\partial^2 \Psi}{\partial x^2} - 2 \frac{\partial^2 w}{\partial x \partial y} \frac{\partial^2 \Psi}{\partial x \partial y} \right], \end{aligned} \quad (2)$$

$$\left[\beta^2 \frac{\partial^4 \Psi}{\partial x^4} + 2 \frac{\partial^4 \Psi}{\partial x^2 \partial y^2} + \beta^{-2} \frac{\partial^4 \Psi}{\partial y^4} \right] = Eh \left[\left(\frac{\partial^2 w}{\partial x \partial y} \right)^2 - \frac{\partial^2 w}{\partial x^2} \frac{\partial^2 w}{\partial y^2} \right], \quad (3)$$

where ρ is the mass density of plate, h the plate thickness, p the externally applied pressure forcing. Also, $D = Eh^3/12(1-\mu^2)$, where E is Young's modulus, μ Poisson's ratio, and $\beta = L_y/L_x$ is the aspect ratio of plate sides L_y and L_x . We have introduced here viscous structural damping $\rho h \zeta (\partial w / \partial t)$ with the damping ratio ζ .

The pair of (2) and (3) is same as the familiar von Karman-Chu-Herrmann equations of large-deflection plate under no plate heating [14]. However, the plate heating by (1) enters through the integral constraints of zero plate-edge displacement

$$\begin{aligned} \int_0^1 \int_0^1 \left\{ \frac{1}{Eh} \left[\frac{\partial^2 \Psi}{\partial y^2} - \mu \beta^2 \frac{\partial^2 \Psi}{\partial x^2} \right] + \alpha L_y^2 t_o - \frac{\beta^2}{2} \left(\frac{\partial w}{\partial x} \right)^2 \right\} dx dy = 0, \\ \int_0^1 \int_0^1 \left\{ \frac{1}{Eh} \left[\beta^2 \frac{\partial^2 \Psi}{\partial x^2} - \mu \frac{\partial^2 \Psi}{\partial y^2} \right] + \alpha L_y^2 t_o - \frac{1}{2} \left(\frac{\partial w}{\partial y} \right)^2 \right\} dx dy = 0, \end{aligned} \quad (4)$$

where α is the thermal expansion coefficient [15]. In terms of w and Ψ , we have the stress tensor

$$\begin{aligned} \sigma_x &= \frac{1}{hL_y^2} \frac{\partial^2 \Psi}{\partial y^2} - \frac{Ez}{L_y^2(1-\mu^2)} \left[\beta^2 \frac{\partial^2 w}{\partial x^2} + \mu \frac{\partial^2 w}{\partial y^2} \right], \\ \sigma_y &= \frac{\beta^2}{hL_y^2} \frac{\partial^2 \Psi}{\partial x^2} - \frac{Ez}{L_y^2(1-\mu^2)} \left[\frac{\partial^2 w}{\partial y^2} + \mu \beta^2 \frac{\partial^2 w}{\partial x^2} \right], \end{aligned}$$

$$\sigma_{xy} = -\frac{\beta}{hL_y^2} \frac{\partial^2 \Psi}{\partial x \partial y} - \frac{\beta E z}{L_y^2(1+\mu)} \frac{\partial^2 w}{\partial x \partial y}, \quad (5)$$

from which the strain tensor follows

$$\varepsilon_x = \frac{1}{E}(\sigma_x - \mu \sigma_y) + \alpha t_o, \quad \varepsilon_y = \frac{1}{E}(\sigma_y - \mu \sigma_x) + \alpha t_o, \quad \varepsilon_{xy} = \frac{1+\mu}{E} \sigma_{xy}. \quad (6)$$

In this paper, we let the temperature-dependent E and α of the form

$$E = E_r E_a, \quad \alpha = \alpha_r \alpha_a, \quad (7)$$

where the subscript 'r' refers to the reference temperature and subscript 'a' to actual plate temperature. In particular, we assume a linear temperature dependency

$$E_a = (1 - E_1 t_o), \quad \alpha_a = (1 + \alpha_1 t_o), \quad (8)$$

where E_1 and α_1 denote the fractional changes per unit degree of temperature rise t_o [11, 12]. We however ignore the temperature dependency of μ , for it is in comparison quite insignificant.

3. The Galerkin procedure

By the Galerkin procedure, we eliminate the spatial dependency of (2) and (3) on x and y , and thereby obtain modal equations that are the ordinary differential equations. We begin with the following expansions for four symmetric plate modes

$$\begin{Bmatrix} w \\ p \end{Bmatrix} = \sum_{i=1,3} \sum_{j=1,3} \begin{Bmatrix} a_{i,j} \\ f p_{i,j} \end{Bmatrix} \phi_i(x) \phi_j(y), \quad (9)$$

in which the plate modal function $\phi_i(x)\phi_j(y)$ is a product of the beam mode $\phi_n(\xi)$ with the appropriate end boundary conditions. We need not specify $\phi_n(\xi)$ at this point, other than requiring $\int_0^1 \phi_m(\xi) \phi_n(\xi) d\xi = \delta_{m,n}$. Also, we introduce the cosine expansion for the Airy function

$$\Psi = -\frac{1}{2} C_x L_y^2 y^2 - \frac{1}{2} C_y L_x^2 x^2 + E h \sum_{\substack{p=0,2,\dots \\ (p \neq 0)}} \sum_{q=0,2,\dots} f_{p,q} \cos(p\pi x) \cos(q\pi y). \quad (10)$$

In the Galerkin (spectral) procedure we first express $f_{p,q}$ in terms of the quadratic $a_{i,j}$ by (3). We then evaluate the constant C_x and C_y through the integral constraint (4).

$$\begin{aligned} C_x &= \frac{E h \alpha t_o}{(1-\mu)} - \frac{E h}{2(1-\mu^2) L_y^2} \{ \beta^2 \langle w_{,x}^2 \rangle + \mu \langle w_{,y}^2 \rangle \}, \\ C_y &= \frac{E h \alpha t_o}{(1-\mu)} - \frac{E h}{2(1-\mu^2) L_x^2} \{ \beta^2 \mu \langle w_{,x}^2 \rangle + \langle w_{,y}^2 \rangle \}, \end{aligned} \quad (11)$$

where $\langle w_x^2 \rangle = (a_{1,1}^2 + a_{1,3}^2) d_{1,1,0} + 2(a_{1,1} a_{3,1} + a_{1,3} a_{3,3}) d_{1,3,0} + (a_{3,1}^2 + a_{3,3}^2) d_{3,3,0}$,
 $\langle w_y^2 \rangle = (a_{1,1}^2 + a_{3,1}^2) d_{1,1,0} - 2(a_{1,1} a_{1,3} + a_{3,1} a_{3,3}) d_{1,3,0} + (a_{1,3}^2 + a_{3,3}^2) d_{3,3,0}$,
 $d_{i,j,k} = \int_0^1 \varphi_i'(\xi) \varphi_j'(\xi) \cos(k\pi\xi) d\xi$. Lastly, we sort out the modal equations for $(a_{1,1}, a_{1,3}, a_{3,1}, a_{3,3})$ from (2) after inserting (9) and (10). Although the details of Galerkin procedure are quite tedious [1], the laborious manipulation has recently been carried out by a symbolic manipulation software, such as MATHEMATICATM [16].

Later on, for a simply-supported plate we use $\varphi_i(\xi) = \sqrt{2} \sin(i\pi\xi)$ of the usual simply-supported-beam modes. For a clamped plate, we shall use for simplicity the trigonometric clamped-beam modes, $\varphi_1(\xi) = \sqrt{\frac{8}{3}} \zeta_1(\xi)$,
 $\varphi_2(\xi) = 2\zeta_2(\xi)$, $\varphi_3(\xi) = \sqrt{\frac{24}{5}} \zeta_3(\xi) + \sqrt{\frac{8}{15}} \zeta_1(\xi)$, where $\zeta_n(\xi) = \frac{1}{2}(\cos(i-1)\pi\xi - \cos(i+1)\pi\xi) = \sin(n\pi\xi)\sin(\pi\xi)$, rather than the true clamped-beam modes [17].

4. The static analyses of thermal buckling

For static analyses, we drop the inertial and damping and forcing terms in the left-hand side of (2) and write the remaining as

$$D_r E_a (\beta^4 \frac{\partial^4 w}{\partial x^4} + 2\beta^2 \frac{\partial^4 w}{\partial x^2 \partial y^2} + \frac{\partial^4 w}{\partial y^4}) - \beta^2 (\frac{\partial^2 w}{\partial x^2} \frac{\partial^2 \Psi}{\partial y^2} + \frac{\partial^2 w}{\partial y^2} \frac{\partial^2 \Psi}{\partial x^2} - 2 \frac{\partial^2 w}{\partial x \partial y} \frac{\partial^2 \Psi}{\partial x \partial y}) = 0, \quad (12)$$

where $D_r = E_r h^3 / 12(1 - \mu^2)$. Upon introducing (11) into (10), we find

$$\Psi = - \frac{h}{2(1-\mu)} (L_y^2 y^2 + L_x^2 x^2) E_r E_a \alpha_r \alpha_a t_o + \text{Quadratic in } a_{n,m}. \quad (13)$$

Here, the first term is multiplied by t_o and the second term denotes a multitude of quadratic expressions in $a_{n,m}$. Hence, when (13) is inserted into (12) we would end up with a set of cubic algebraic equations involving $a_{1,1}$, $a_{1,3}$, $a_{3,1}$, and $a_{3,3}$. First we consider only the first right-hand side term in (13). Then the resulting linear system determines the balance between plate bending and thermal expansion αt_o . The plate temperature at which thermal expansion exactly counteracts the bending of a particular mode is called the critical buckling temperature T^* . Although there are critical buckling temperatures for each of the modes $a_{n,m}$, we mean by the critical buckling temperature the lowest one for the primary mode $a_{1,1}$. In the absence of external pressure forcing ($p=0$), (12) admits only zero displacement below the critical buckling temperature. In contrast, above the critical buckling temperature, (12) has non-zero post-buckled plate displacements even under $p=0$. To see this, we must consider (13) in its entirety and hence investigate a system of cubic algebraic equations, to be presented shortly.

4.1 The critical buckling temperature

We express the linear algebraic equation for $a_{1,1}$ resulting from (12) in a compact form $(d_1\alpha_a t_o - d_2)a_{1,1} = 0$, where $d_1 = 12L_x^2\beta^2(1+\mu)\alpha_r$ and $d_2 = \pi^2 h^2(1+\beta^2)$ for simply-supported plate, and $d_1 = 9L_x^2\beta^2(1+\beta^2)(1+\mu)\alpha_r$ and $d_2 = \pi^2 h^2(3+2\beta^2+3\beta^4)$ for clamped plate. Since $a_{1,1} \neq 0$, we demand $d_1\alpha_a t_o - d_2 = 0$ and solve for $t_o = d_2/d_1\alpha_a$, which is the critical buckling temperature T^* .

$$T^* = \frac{d_2}{d_1\alpha_a} = \frac{T_r^*}{\alpha_a} \approx \frac{T_r^*}{(1+\alpha_1 t_o)} \approx T_r^*(1 - \alpha_1 t_o). \quad (14)$$

We need to explain the series of equalities. Of course, the first equality in (14) is by definition. In the second equality, we define $T_r^* = d_2/d_1$ as the critical buckling temperature of the reference state. Now, the third equality involves a pivotal approximation, in which we replace α_a by (8). To be exact, we should have written $T^* = T_r^*/(1+\alpha_1 T^*)$, which would then result in a quadratic equation for T^* . This is why T^* is determined by iterative schemes in the finite-element formulations of Chen & Chen [12] and Mei et al. [5]. It is evident by the third equality that T^*/T_r^* never exceeds unity and, in fact, is a decreasing function of t_o . By retaining only the leading terms in the expansion, in the last equality it is rendered a linear decrease, in which $\alpha_1 t_o$ represents a fractional decrease in T^*/T_r^* .

Returning to the quadratic equation, we now write the positive root

$$T^* = \frac{1}{2\alpha_1} (\sqrt{1+4\alpha_1 T_r^*} - 1). \quad (15)$$

Expanding the square root by the power exponent $\frac{1}{2}$, the leading-term expansion is $T^* \approx T_r^*(1 - \alpha_1 T_r^*)$ for $\alpha_1 T_r^* \ll 1$. This clearly asserts that the last equality of (14) is also valid for $\alpha_1 t_o \ll 1$. That $T_r^* \geq T^*$ for $\alpha_1 t_o > 0$ means that the critical buckling temperature is always lowered by the temperature-dependent physical properties. This has been supported by the finite-element analysis of Chen & Chen [12] for the simply-supported and clamped composite plates. In particular, Fig. 4 and 5 of Ref. [12] show that the difference of T_r^* and T^* increases with the aspect ratio $\beta^{-1} = L_x/L_y$ in the range of (0.3, 3). This is indeed in qualitative agreement with (15) for T^* , which is displayed in Fig. 1 with respect to $\beta^{-1} = L_x/L_y$ of a clamped plate. Here, we use $\alpha_r = 1.23 \cdot 10^{-5}/^\circ\text{F}$ for an aluminum plate of $\mu = \sqrt{0.1}$ and $L_x/h = 64$. Also, we estimate $\alpha_1 = 0.000275/^\circ\text{F}$ from α being increased by 11%/400°F in Fig. 8 of Ref. [5]. We also note that in Fig. 7 of Ref. [12] the decrease in T^* is nearly independent of the ratio of moduli of elasticity for a composite plate. This may be explained by that (15) does not at all involve E .

Without presenting the detail, we point out that the critical buckling temperature $T^* = \pi^2 h^2 (\beta^2 + 1) / 12 \alpha \beta^2 L_y^2 (1 + \mu)$ of a simply-supported plate is not affected by the presence of other Fourier amplitudes ($a_{1,3}$, $a_{3,1}$, $a_{3,3}$). On the other hand, $T^* = \pi^2 h^2 (3\beta^4 + 2\beta^2 + 3) / 9 \alpha \beta^2 (\beta^2 + 1) L_y^2 (1 + \mu)$ of a clamped plate is reduced by the factor 0.9975, when all four Fourier amplitudes ($a_{1,1}$, $a_{1,3}$, $a_{3,1}$, $a_{3,3}$) are included in (12).

4.2 The post-buckled maximum displacement

Into (12) we introduce (13) in its entirety. For the primary mode $a_{1,1} \equiv Q$, we obtain a cubic equation

$$\varpi^2 (1 - s) Q + \kappa Q^3 = 0, \quad (16)$$

where $\varpi^2 = (1 + \beta^2)^2$ and $\kappa = 6(1 + \beta^4 + 2\mu\beta^2) + 3(1 + \beta^4)(1 - \mu^2)$ for simply-supported plate, and $\varpi^2 = \frac{16}{9}(3 + 2\beta^2 + 3\beta^4)$ and $\kappa = \frac{32}{3}(1 + \beta^4 + 2\mu\beta^2) + \frac{16}{27}\beta^4(1 - \mu^2)\{17(1 + \beta^{-4}) + 32(1 + \beta^2)^{-2} + 8(4 + \beta^2)^{-2} + 8(1 + 4\beta^2)^{-2}\}$ for clamped plate. Also, we let $s = t_o / T^*$ in (16). For a pre-buckled plate ($s < 1$), (16) admits only zero displacement $Q = 0$. For $s > 1$ the post-buckled plate displacements are given by $Q = \pm \varpi \sqrt{(s - 1) / \kappa}$. Then, by (14) we express temperature dependency through s

$$Q = \pm \varpi \sqrt{\frac{1}{\kappa} (s_r (1 + \alpha_1 T_r^* s_r) - 1)}, \quad (17)$$

where $s_r = t_o / T_r^*$. Note that $s = s_r$ for $\alpha_1 = 0$, and hence the reference state displacement is $Q_r = \pm \varpi \sqrt{(s - 1) / \kappa}$.

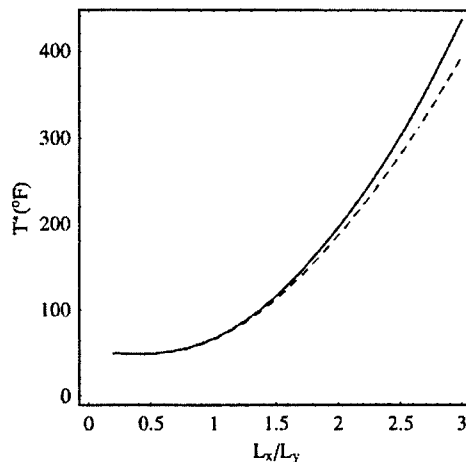


Figure 1. Critical buckling temperature of a clamped aluminum plate; — T_r^* , --- T^* .

Clearly, by (17) we have $Q > Q_r$ for a heated plate, since $\alpha_1 t_o > 0$. In other words, the post-buckled plate displacement is always raised by the temperature-dependent physical properties. This is confirmed by Fig. 2 of Kamiya & Fukui [11], in which the maximum displacements are always larger under the temperature-dependent properties than the temperature-independent counterparts. We now compute the Q and Q_r for a square clamped plate of $\beta=1$, as shown in Fig. 2. With $\alpha_r = 1.23 \cdot 10^{-5}/^\circ\text{F}$ for a clamped aluminum plate of $\mu = \sqrt{0.1}$ and $L_x/h = 64$, the critical buckling temperature is $T_r^* \approx 67^\circ\text{F}$. In Fig. 2 and the remaining figures, we always consider the reduced temperature range of $s_r = (1, 5)$. That is, we raise t_o up to five times the critical buckling temperature, and this corresponds to the actual temperature range of $(140^\circ\text{F}, 420^\circ\text{F})$ when both the reference temperature and T_r^* are assumed 70°F . We see in Fig. 2 that the final increase $Q/Q_r \approx 1.06$ (6% increase) is reached toward the upper temperature limit $s_r = 5$. In contrast, Fig. 9 of Mei et al. [5] shows only a minute increase of Q over Q_r for clamped square aluminum plate. Hence, they concluded no appreciable effect of temperature-dependent physical properties on the maximum deflections.

With all four amplitudes $(a_{1,1}, a_{1,3}, a_{3,1}, a_{3,3})$, (16) expands to a set of cubic algebraic equations which has very complex root configurations. However, we only need to trace the roots along $Q = \pm \varpi \sqrt{(s-1)/\kappa}$. Here we simply point out that the inclusion of higher-order amplitudes lowers the maximum displacement for $a_{1,1}$, yet $Q = \pm \varpi \sqrt{(s-1)/\kappa}$ remains a good approximation for both the simply-supported and clamped plates. The detail will be reported elsewhere.

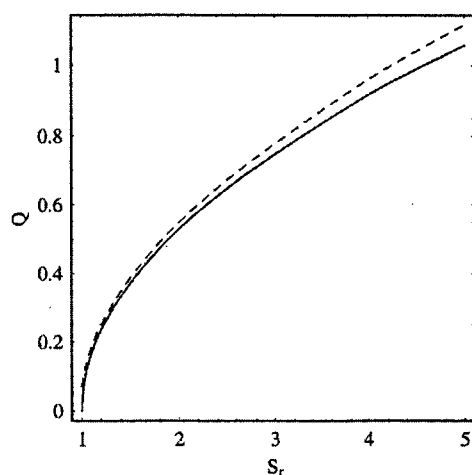


Figure 2. Post-buckled plate displacement; — Q_r , --- Q .

4.3 The normal components of x-stress and x-strain

Typically, we consider the normal components in x-coordinate of σ_x and ε_x , involving only the primary amplitude $a_{1,1}$. After normalizing σ_x by $\pi^2 h^2 E_r / L_y^2$, we denote it by $\hat{\sigma} = \sigma_x L_y^2 / \pi^2 h^2 E_r$, and similarly $\hat{\varepsilon} = \varepsilon_x L_y^2 / \pi^2 h^2$. In view of (8), the quadratic expression for $\hat{\sigma}$ becomes

$$\hat{\sigma} = (1 - E_1 T_r^* s_r)(C_0 + C_1 a_{1,1} + C_2 a_{1,1}^2), \quad (18)$$

where $C_0 = -(3+2\beta^2+3\beta^4)s_r(1+\alpha_1 T_r^* s_r)/9(1+\beta^2)(1-\mu^2)$,
 $C_1 = 16Z(\mu \cos 2\pi y \sin^2 \pi x + \beta^2 \cos 2\pi x \sin^2 \pi y) / 3(1-\mu^2)$,
 $C_2 = 2(\beta^2 + \mu)/3(1-\mu^2) + \frac{2}{9}\beta^2\{-4 \cos 2\pi y + \cos 4\pi y +$
 $8 \cos 2\pi x \cos 2\pi y / (1+\beta^2)^2 - 4 \cos 4\pi x \cos 2\pi y / (1+4\beta^2)^2 -$
 $16 \cos 2\pi x \cos 4\pi y / (4+\beta^2)^2\}$

and $Z = z/h$ for a clamped plate. In Fig. 3 we present the maximum $\hat{\sigma}$ at $Z = x = y = \frac{1}{2}$ based on the post-buckled displacement $a_{1,1} = Q$. Here, we use the same parameter values of Fig. 2 and estimate $E_1 = 0.000375/^\circ\text{F}$ from 15%/400°F decrease in E from Fig. 7 of Ref. [5]. In Fig. 3 we see that $\hat{\sigma} \approx \hat{\sigma}_r$ up to $s_r \approx 3$, but then $\hat{\sigma}$ falls below the temperature-independent $\hat{\sigma}_r$, so that $\hat{\sigma}/\hat{\sigma}_r \approx 0.94$ (6% decrease) at $s_r = 5$. We believe that $\hat{\sigma}$ falls below $\hat{\sigma}_r$ for $s_r > 3$, because E_a is a decreasing function of t_o . In contrast, in Fig. 10 and 11 of Mei et al. [5] the bending and membrane stresses of a clamped aluminum plate are not at all affected by the temperature-dependent physical properties.

Next, we compute the normalized x-strain by the quadratic expression

$$\hat{\varepsilon} = C_1 a_{1,1} + C_2 a_{1,1}^2, \quad (19)$$

where $C_1 = -\frac{16}{3} Z \beta^2 \cos 2\pi x \sin^2 \pi y$,

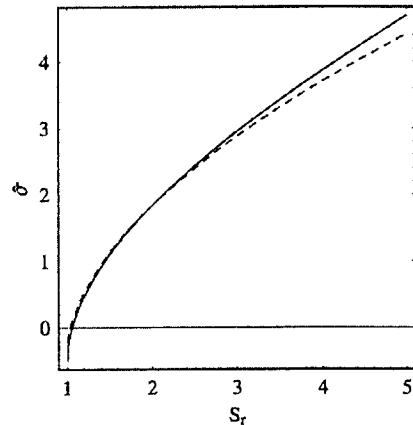


Figure 3. Maximum normal x-stress;
 — $\hat{\sigma}_r$, --- $\hat{\sigma}$.

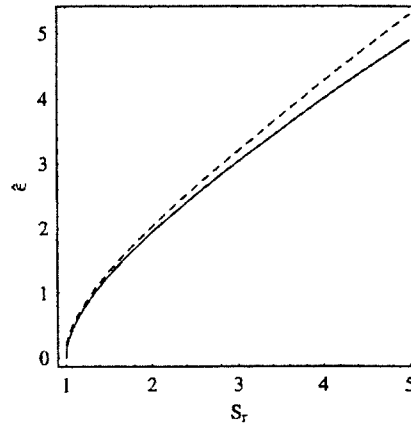


Figure 4. Maximum normal x-strain;
 — $\hat{\varepsilon}_r$, --- $\hat{\varepsilon}$.

$$C_2 = \frac{2}{3}\beta^2 + \frac{2}{9}\beta^2 \{-4\cos 2\pi y + \cos 4\pi y + 8\cos 2\pi x \cos 2\pi y / (1+\beta^2)^2 - \\ 4\cos 4\pi x \cos 2\pi y / (1+4\beta^2)^2 - 16\cos 2\pi x \cos 4\pi y / (4+\beta^2)^2 - \\ \beta^2 \mu [\cos 4\pi x \beta^{-4} - 4\cos 2\pi x \beta^{-4} + 8\cos 2\pi x \cos 2\pi y / (1+\beta^2)^2 - \\ 16\cos 4\pi x \cos 2\pi y / (1+4\beta^2)^2 - 4\cos 2\pi x \cos 4\pi y / (4+\beta^2)^2]\}$$

for clamped plate. We see in Fig. 4 that $\hat{\epsilon}$ is always larger than $\hat{\epsilon}_r$, and the final ratio $\hat{\epsilon}/\hat{\epsilon}_r \approx 1.08$ (8% increase) is approached at $s_r = 5$.

5. Statistical responses of displacement and stress/strain

Recall that the cubic equation (16) is the single-mode representation of (12), which is nothing but the time-independent part of displacement equation (2). We now present the complete single-mode equation in a standard oscillator form

$$\frac{d^2 q}{d\tau^2} + 2\zeta\varpi \frac{dq}{d\tau} - E_a \varpi^2 (s-1)q + E_a \kappa q^3 = f(\tau). \quad (20)$$

It is nondimensionalized by $\tau = t/\gamma$, $q = a_{1,1}/h$, $f(\tau) = fp_{1,1}/(\rho h^2/\gamma^2)$, where $\gamma = (\rho h L_y^4/\pi^4 D_r)^{1/2}$. Besides, ϖ , κ , and s are already given in Sec. 4 for a clamped plate. The damping coefficient $\zeta = 0.01$ is used in the subsequent computation. We split q into the buckled displacement Q and fluctuations \hat{x}

$$q = Q + \hat{x}, \quad (21)$$

and compute total moments

$$\begin{aligned} \langle q \rangle &= Q + m_1, & \langle q^2 \rangle &= Q^2 + 2Qm_1 + m_2, \\ \langle q^3 \rangle &= Q^3 + 3Q^2 m_1 + 3Qm_2 + m_3, \\ \langle q^4 \rangle &= Q^4 + 4Q^3 m_1 + 6Q^2 m_2 + 4Qm_3 + m_4. \end{aligned} \quad (22)$$

Here $m_i = \langle \hat{x}^i \rangle$, where $\langle \dots \rangle$ denotes ensemble average.

Now, inserting (21) into (20) gives the fluctuation equation

$$\frac{d^2 \hat{x}}{d\tau^2} + \lambda \frac{d\hat{x}}{d\tau} + E_a \Omega \hat{x} + 3E_a \kappa Q \hat{x}^2 + E_a \kappa \hat{x}^3 = f(\tau), \quad (23)$$

where $\lambda = 2\zeta\varpi$ and $\Omega = 2\varpi^2(s-1)$. Under the white-noise excitations with a delta-function correlation $\langle f(t)f(\tau) \rangle = 2F\delta(t-\tau)$, where F is the total power input of forcing, the stationary Fokker-Planck distribution is given by [18, 19]

$$P(\hat{x}) = \exp\left\{-\frac{\lambda}{F} E_a \left(\frac{1}{2}\Omega \hat{x}^2 + \kappa Q \hat{x}^3 + \frac{1}{4}\kappa \hat{x}^4\right)\right\}.$$

Hence, the moments are $M_n = \int_{-\infty}^{\infty} P(\hat{x}) \hat{x}^n d\hat{x}$ for all n . For computation it is more convenient to have a symmetric distribution which follows from the transformations $\hat{x} = \hat{y}(2F/\kappa\lambda)^{1/4}$ and $\hat{y} = r - \sqrt{g/2}$, where $g = \varpi^2(s-1)\sqrt{2\lambda/\kappa F}$.

Hence, $M_n = \left(\frac{2F}{\kappa\lambda}\right)^{\frac{n+1}{4}} \int_{-\infty}^{\infty} P(r) \left(r - \sqrt{\frac{g}{2}}\right)^n dr$, where $P(r) = \exp\left\{-\frac{E_a}{2}\left(r^2 - \frac{g}{2}\right)^2\right\}$.

Since the symmetric $P(r)$ has zero odd moments, we have the normalized moments $m_i = M_i/M_0$

$$\begin{aligned} m_1 &= -Q, & m_2 &= J_2 + Q^2, \\ m_3 &= -3QJ_2 - Q^3, & m_4 &= J_4 + 6Q^2J_2 + Q^4, \end{aligned} \quad (24)$$

where $J_n = \left(\frac{2F}{\kappa\lambda}\right)^{\frac{n}{4}} \int_{-\infty}^{\infty} P(r) r^n dr / \int_{-\infty}^{\infty} P(r) dr$. Upon inserting (24) into (22), we find simple expressions for the even moments, $\langle q^n \rangle = J_n$ for $n = 2, 4$, whereas all odd moments are zero, $\langle q^n \rangle = 0$ for $n = 1, 3$. Note that temperature dependency on α and E is introduced by $g = \varpi^2 \left(s_r(1 + \alpha_1 T_r^* s_r) - 1\right) \sqrt{2\lambda/\kappa F}$ and $E_a = 1 + E_1 T_r^* s_r$. In Fig. 5 and 6, we present the second and fourth-order moments of q under a dimensionless power input of forcing $F = \frac{1}{2}$. Note that both moments are boosted by the temperature-dependent physical properties, approaching $\langle q^2 \rangle / \langle q_r^2 \rangle \approx 1.12$ and $\langle q^4 \rangle / \langle q_r^4 \rangle \approx 1.24$ at $s_r = 5$, respectively.

The second and fourth-order moments are needed to compute the root-mean-square (RMS) values of x-stress and x-strain. By squaring and averaging (18), we obtain

$$\text{RMS}(\hat{\sigma}) = (1 - E_1 T_r^* s_r) \sqrt{C_0^2 + (C_1^2 + 2C_0C_2) \langle q^2 \rangle + C_2^2 \langle q^4 \rangle}.$$

In Fig. 7 the $\text{RMS}(\hat{\sigma})$ is decreased by the temperature-dependent physical properties, giving rise to the final ratio of $\text{RMS}(\hat{\sigma})/\text{RMS}(\hat{\sigma}_r) \approx 0.93$ (7% decrease) at $s_r = 5$. This should be compared with the final 6% decrease for the static x-stress in Fig. 3. Similarly, squaring and averaging (19) yields

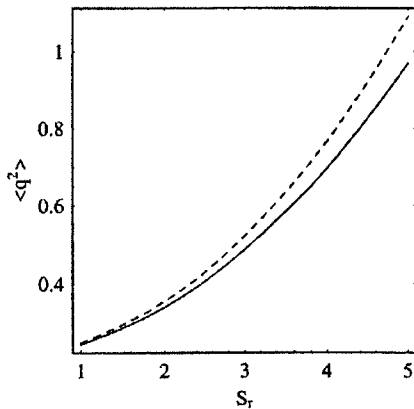


Figure 5. The second moment for $F=0.5$;
— $\langle q_r^2 \rangle$, --- $\langle q^2 \rangle$.

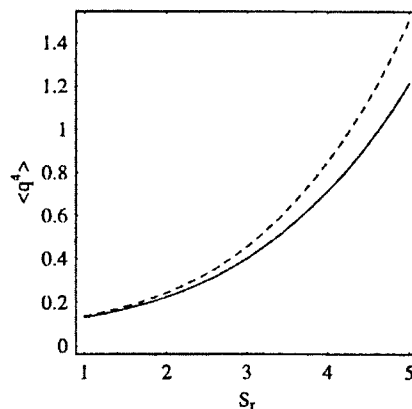


Figure 6. The fourth moment for $F=0.5$;
— $\langle q_r^4 \rangle$, --- $\langle q^4 \rangle$.

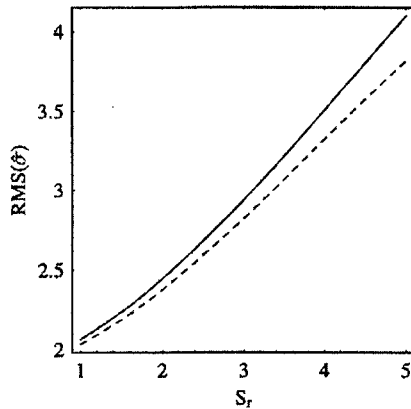


Figure 7. RMS normal x-stress for $F=0.5$;
—— $\langle \hat{\sigma}_r \rangle$, ---- $\langle \hat{\sigma} \rangle$.

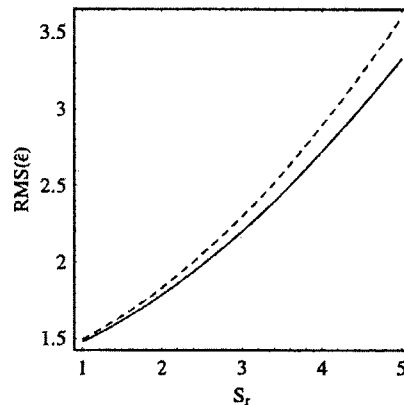


Figure 8. RMS normal x-strain for $F=0.5$;
—— $\langle \hat{\epsilon}_r \rangle$, ---- $\langle \hat{\epsilon} \rangle$.

$$\text{RMS}(\hat{\epsilon}) = \sqrt{C_1^2 \langle q^2 \rangle + C_2^2 \langle q^4 \rangle}.$$

We see in Fig. 8 the $\text{RMS}(\hat{\epsilon})$ is increased by the temperature-dependent physical properties. The final increase of 8% ($\text{RMS}(\hat{\epsilon})/\text{RMS}(\hat{\epsilon}_r) \approx 1.08$) at $s_r=5$ is same as that of the static x-strain shown in Fig. 4.

6. Summary

It is shown experimentally that Young's moduli for several aluminum alloys decrease with temperature, but the decrease is almost linear over the temperature range of (50°C, 400°C) [4]. Mei et al. [5] have compiled typical temperature variations of E and α for aluminum in their Fig. 7 and 8, respectively, over the temperature range of (70°F, 470°F). We estimate the linear decrease in E of 13% and the increase in α of 9.6% over the range of 350°F. To compare with the previous work [5, 11, 12], we consider here a square clamped aluminum plate of $L_x/h=64$, so that the critical buckling temperature turns out about 70°F. In this paper, the uniform plate heating temperature is varied over five times the critical buckling temperature, i.e., 350°F. Hence, the actual temperature range considered is (70°F, 420°F) when the reference temperature of nominal 70°F is assumed.

To establish a frame of reference, we have derived from a static single-mode analysis simple analytical expressions for the critical buckling temperature and post-buckled plate displacement. As we raise the plate temperature by 350°F, the critical buckling temperature decreases by 9.6% and the post-buckled plate displacement increases by 6%. This is in qualitative agreement with the numerical computations of Kamiya & Fukui [11] and Chen & Chen [12] on thermally buckled aluminum and composite plates. We have further computed the normal x-stress and x-strain based on the static post-buckled plate displacements. Here, the static x-stress is decreased by 6% and

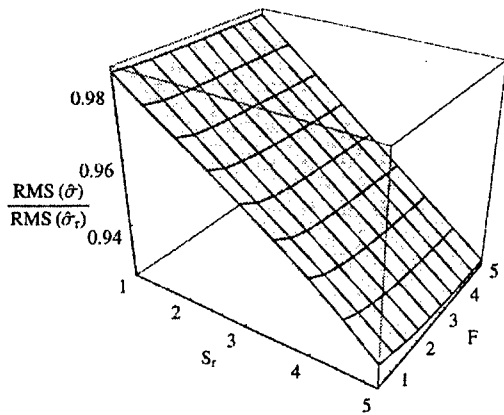


Figure 9. Ratio of the RMS x-stresses

x-strain is increased by 8% when the temperature dependency of E and α is taken into account over 350°F . For comparison, we also compute the RMS x-stress and x-strain of stochastic dynamics analysis based on the single-mode Fokker-Planck distribution. Surprisingly, the temperature-dependent E and α decrease the RMS x-stress and increase the RMS x-strain, just as in the static x-stress and x-strain. More important, over the plate temperature range of 350°F , the RMS and static x-stresses are decreased by 6–7%, and both RMS and static x-strains are increased by the same 8%. It is indeed reassuring to observe such close agreements between the static and stochastic dynamic analyses.

For a qualitative comparison, we have thus far based statistical estimates on a forcing power input of $F=0.5$ for the Fokker-Planck distribution. Note that F is nondimensional, rather than a physical power input as expressed by, say, deci-Bell units, as in Ref. [20]. We therefore summarize in Fig. 9 and 10 how the RMS x-stress and x-strain are affected when F is varied over a decade range of (0.5, 5). In Fig. 9, a linear decrease in $\text{RMS}(\hat{\sigma})/\text{RMS}(\hat{\sigma}_r)$ with

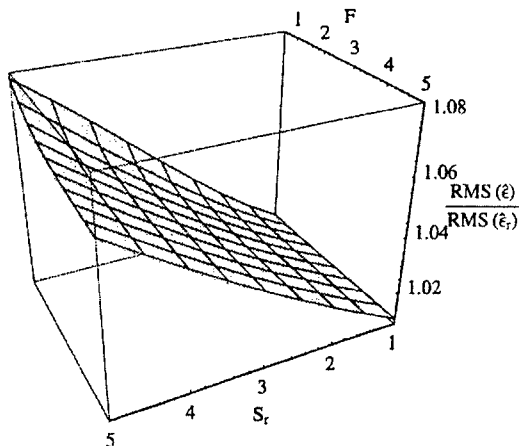


Figure 10. Ratio of the RMS x-strains.

temperature is not altered significantly by F over the range of 350°F. On the other hand, Fig. 10 shows the final increase in $\text{RMS}(\hat{\epsilon})/\text{RMS}(\hat{\epsilon}_r)$ at $s_r=5$ falls off from 1.08 to 1.065 as F increases from 0.5 to 5, respectively.

Acknowledgments

This work was supported in part by the Air Force Office of Scientific Research New World Vista. Also, thanks to Howard Wolfe for his comments on the first draft of this paper.

References

1. Lee, J., Large amplitude plate vibration in an elevated thermal environment, *Appl. Mech. Rev.*, 1993, **46**(2), S242-54.
2. Vaicaitis, R., Nonlinear response and sonic fatigue of national aerospace plane surface panels, (survey paper), *J. Aircraft*, 1994, **31**(1), 10-18.
3. Moorthy, J., Mei, C. and Shirahatti, U., Numerical simulation of acoustically induced nonlinear variations of a plate with temperature gradient, 36th SDM Conf., 1844-54, AIAA-95-1378-CP, New Orleans, LA, Apr., 1995.
4. Takeuti, Y., Komori, S., Noda, N. and Nyuko, H., Thermal-stress problems in industry. 3: temperature dependency of elastic moduli for several metals at temperatures from -196 to 1000°C, *J. Thermal Stresses*, **2**, 1979, 233-50.
5. Mei, C., Duan, B., Zhong, Z. and Wolfe, H.F., *Large thermal deflections of composite plates with temperature dependent material properties*, AFRL-VA-WP-TR-1999-3036, Wright-Patterson AFB, OH, March, 1999.
6. Duan, B., Progress report "large thermal deflections of thin composite plates with temperature-dependent material properties" submitted to H.F. Wolfe, Sept. 1998.
7. Hoff, N.J., Buckling at high temperature, *J. Roy. Aeronautical Soc.*, 1957, **61**, 756-74.
8. Nowinski, J., Transient thermoelastic problem for an infinite medium with a spherical cavity exhibiting temperature-dependent properties, *J. Appl. Mech.*, 1962, **29**(11), 399-407.
9. Kamiya, N. and Kameyama, E., On the effect of boundary conditions on finite deflections of heated annuli exhibiting temperature-dependent properties, *Nuclear Engr. Design*, 1980, **61**, 187-96.
10. Miller, C.J., Millavec, W.A. and Kither, T.P., Thermal stress analysis of layered cylindrical shells, *AIAA J.*, 1981, **19**, 523-30.
11. Kamiya, N. and Fukui, A., Finite deflection and post buckling behavior of heated rectangular plates with temperature-dependent properties, *Nuclear Engr. Design*, 1982, **72**, 415-20.
12. Chen, L.W. and Chen, L.Y., Thermal buckling behavior of laminated composite plates with temperature-dependent properties, *Composite Structures*, 1989, **13**, 275-87.

-
13. Noor, A.K. and Burton, W.S., Three-dimensional solutions for the thermal buckling and sensitivity derivatives of temperature-sensitive multilayered angle-ply plates, *J. Appl. Mech.*, 1992, **59** (12), 848-56.
 14. Chu, H.N. and Herrmann, G., Influence of large amplitudes on free flexural vibrations of rectangular elastic plates, *J. Appl. Mech.*, 1956, **23** (12), 532-40.
 15. Bolotin, V.V., *Nonconservative problems of the theory of elastic stability*, MacMillan, NY, 1963.
 16. Wolfram, S., *The MATHEMATICA book*, 4th ed., Wolfram Media, Wolfram Research, IL, 1999.
 17. Lee, J., *Qualitative analysis of the strain energy of thermally buckled plates*, The manuscript, Jan. 2000.
 18. Caughey, T.K., Derivation and application of the Fokker-Planck equation to discrete nonlinear dynamical systems subjected to white random excitations, *J. Acoust. Soc. Am.*, 1963, **35**(11), 1683-92.
 19. Lee, J., Random vibration of thermally buckled plates: I Zero temperature gradient across the plate thickness, in *Aerospace Thermal Structures and Materials of a New Era*, ed. Thornton, E.A., Progress in Astronautics and Aeronautics Vol. 168, AIAA, 1995, 41-67.
 20. Lee, J., Displacement and strain statistics of thermally buckled plates, *J. Aircraft*, 2000, **37**(2), xxx.

FE AND APPLICATIONS

FREQUENCY MODAL ANALYSIS OF SUPRAGLOTTAL VOCAL TRACT

Karel Dedouch

Czech Technical University Prague, Faculty of Mechanical Engineering
Technická 4, 166 07 Prague 6, Czech Republic, E-mail: dedouch@fsik.cvut.cz

Jaromír Horáček

Institute of Thermomechanics, Academy of Sciences
Dolejškova 5, Prague 8, Czech Republic, E-mail: jaromirh@it.cas.cz

Jan Švec

MEDICAL HEALTHCOM, Ltd., Centre for communication disorders
Řešovská 10/491, 181 00 Prague 8, Czech Republic
E-mail: svecjan@mbox.vol.cz

Keywords :

Biomechanics of human voice, modal analysis of acoustic spaces, natural frequencies, damping and mode shapes of vibration, vibroacoustics

ABSTRACT

The subject of the paper is modal analysis of acoustic space relevant to the human supraglottal vocal tract. The influence of the wall impedance is taken into consideration in the numerical analysis. The finite element (FE) method is used for modelling of the vocal tract. Several lowest natural frequencies, damping ratios and natural mode shapes of vibration are calculated. The agreement between the computed first two lowest natural frequencies and the values of the formant frequencies found in the literature are good in all cases studied.

INTRODUCTION

In accordance with the established source-filter theory of voice [1], the vocal tract serves as an acoustic filter, which modifies the primary voice signal, produced by the voice source, the vocal folds. The vocal tract encompasses the acoustic space in between the vocal folds and the lips and, since the speech articulation takes place here, may be varied. The relationship between the shape of the vocal tract and its resonance properties has been the subject of interest in various disciplines related to voice, such as phonetics, speech analysis and synthesis, voice physiology, research on singing, etc. The present study explores a FE mathematical model in order to get more detailed information on the natural frequencies, damping ratio and natural mode shapes of vibration of the air column in the vocal tract. To the authors' knowledge, it is the first attempt to model the shape of the vocal tract as used in the Czech language.

The subjects of particular importance here are the properties of the two lowest resonant frequencies of the vocal tract, so called formants F_1 and F_2 . These

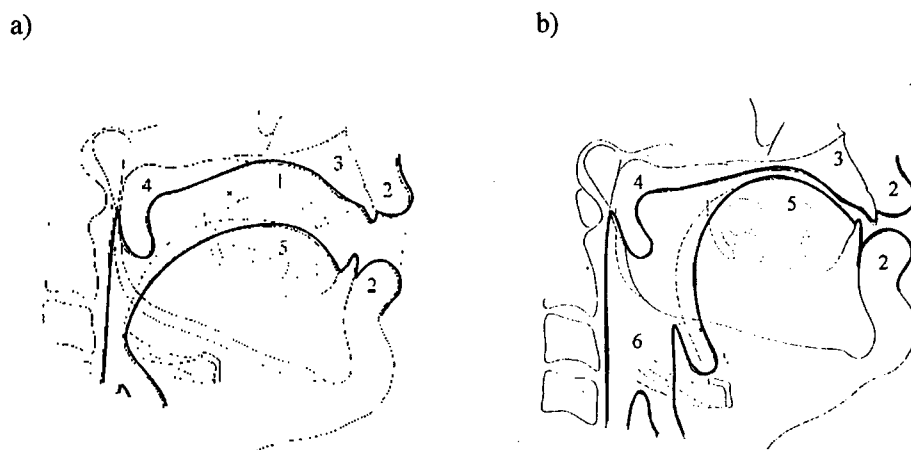


Fig. 1 – Vocal tract profiles based on data obtained from X-ray photographs of the vocal tract during the phonation of Czech vowels: a) /a/ and b) /i/; 1 – mouth resonance cavity, 2 – lips, 3 – hard palate with front teeth, 4 – soft palate, 5 – tongue, 6 – throat. Reproduced from [4].

two formants are crucial for the production of vowels [2]. The developed mathematical models represent a male supraglottal vocal tract. The considered geometry and volume of the acoustic space correspond to English and Czech vowels /a/ and /i/. The length of the vocal tract is assumed from the lips to the glottal end. The geometry of the investigated models is evaluated from the data published by Story et al. [3] for English vowels and by Hála and Polland [4] for Czech vowels. The supraglottal tract is considered as an acoustic space composed of a number of narrow truncated cones. The total length of the vocal tract is 174.58 mm (in accordance with Story) and it is composed of 43 sections of the length 4.06 mm each. The first cross-section (1) corresponds to the lips. The glottal end is at the last cross-section (44). The data published by Story et al. in [3] for the English vowels /a/ and /i/ were obtained by using the magnetic resonance imaging (MRI) method. The shape of the vocal tract for the Czech vowels was taken from the X-ray study of Hála & Polland [4]. This study offers the only available set of data on the vocal tract shapes for Czech vowels. Unfortunately, the X-ray images of Hála & Polland provide information on the part of the vocal tract around the tongue only; the information on the lower part (especially the laryngeal cavity) and on the shape of the lips is missing. Therefore, in order to construct a complete model of the vocal tract, the data from Story et al. for the US-English vowels were used and attached to the original data of Hála & Polland. Although such a compilation of two sets of data is not absolutely correct, it allows for a first approximation of the properties of the vocal tract, before actual data on the vocal tract shapes for the Czech vowels become available.

The geometrical data for the Czech vowels for the medium part of the vocal tract (mouth) were evaluated from the published pictures of the vocal tract profiles (see Fig. 1). Equivalent transversal measures (radii r_i) corresponding to each cross-section are given in Table 1 for all studied cases.

Cross-Section	Coordinate $z_i \cdot 10^{-3}$ [m]	vowel /a/		vowel /i/	
		Story $r_i \cdot 10^{-2}$ [m]	Hála - Story $r_i \cdot 10^{-2}$ [m]	Story $r_i \cdot 10^{-2}$ [m]	Hála - Story $r_i \cdot 10^{-2}$ [m]
1	0.000	1.265	1.265	0.709	0.709
2	4.060	1.222	1.222	0.800	0.800
3	8.120	1.166	1.166	0.810	0.810
4	12.180	1.163	1.163	0.733	0.733
5	16.240	1.147	1.147	0.495	0.495
6	20.300	1.110	1.100	0.370	0.370
7	24.360	1.223	1.100	0.258	0.258
8	28.420	1.296	0.95	0.378	0.350
9	32.480	1.375	0.92	0.288	0.260
10	36.540	1.413	0.98	0.259	0.230
11	40.600	1.415	1.08	0.293	0.180
12	44.660	1.444	1.11	0.160	0.200
13	48.720	1.384	1.14	0.178	0.240
14	52.780	1.273	1.15	0.259	0.270
15	56.840	1.210	1.15	0.324	0.290
16	60.900	1.093	1.11	0.352	0.320
17	64.960	0.980	1.06	0.479	0.390
18	69.020	0.954	1.02	0.600	0.520
19	73.080	0.941	1.00	0.677	0.590
20	77.140	0.903	1.00	0.733	0.610
21	81.200	0.816	0.99	0.818	0.690
22	85.260	0.718	1.00	0.974	0.780
23	89.320	0.578	1.06	1.057	1.050
24	93.380	0.618	0.94	1.138	1.138
25	97.440	0.458	0.500	1.149	1.149
26	101.500	0.357	0.35	1.189	1.189
27	105.560	0.298	0.30	1.224	1.224
28	109.620	0.304	0.304	1.193	1.193
29	113.680	0.319	0.319	1.189	1.189
30	117.740	0.271	0.271	1.197	1.197
31	121.800	0.299	0.299	1.117	1.117
32	125.860	0.288	0.288	1.095	1.095
33	129.920	0.352	0.352	1.087	1.087
34	133.980	0.448	0.448	0.956	0.956
35	138.040	0.520	0.520	0.883	0.883

36	142.100	0.597	0.597	0.959	0.959
37	146.160	0.578	0.578	1.000	1.000
38	150.220	0.324	0.324	0.736	0.736
39	154.280	0.309	0.309	0.383	0.383
40	158.340	0.319	0.319	0.451	0.451
41	162.400	0.259	0.259	0.324	0.324
42	166.460	0.288	0.288	0.339	0.339
43	170.520	0.252	0.252	0.309	0.309
44	174.580	0.378	0.378	0.324	0.324

Table 1 – Geometry of the vocal tract for all studied cases.

FINITE ELEMENT MODEL

The acoustic field inside a closed space is described by the following wave equation for the pressure p :

$$\nabla^2 p = \frac{1}{c_0^2} \frac{\partial^2 p}{\partial t^2} , \quad (1)$$

where c_0 is the speed of sound.

The boundary condition associated with the rigid boundary area is

$$\frac{\partial p}{\partial \mathbf{n}} = 0 , \quad (2)$$

and at the open end of the acoustic space it is supposed

$$p = 0 . \quad (3)$$

The application of the finite element method to an investigation of acoustic fields requires a discretization of the wave equation. Each node of the acoustic finite element has one degree of freedom, i.e., the magnitude of the acoustic pressure. The equation of motion for acoustic pressure in the acoustic space can be written in FE formulation as

$$\mathbf{M} \ddot{\mathbf{P}} + \mathbf{B} \dot{\mathbf{P}} + \mathbf{K} \mathbf{P} = \mathbf{0} , \quad (4)$$

where

\mathbf{M} - mass matrix in global co-ordinate system

\mathbf{B} - acoustic boundary damping matrix in global co-ordinate system

\mathbf{K} - stiffness matrix in global co-ordinate system

\mathbf{P} - vector of acoustic pressures in global co-ordinate system.

The damping matrix \mathbf{B} is associated with the pressure degrees of freedom. The acoustic boundary damping is defined as an acoustic resistance of the elements – dampers between the fluid and structural mesh or a mesh on the boundary areas. This element resistance per unit surface area can be in the range from

zero for no sound absorption up to a value of fluid characteristic impedance $\rho_0 c_0$, e.g., for air in the vocal tract $\rho_0 c_0 = 400 \text{ Nsm}^{-3}$, where ρ_0 is the fluid density. The acoustic damping modelled here by the coefficient μ of the boundary admittance is associated with the fluid-structure interface on the boundary between the air and the walls (tissues) of the vocal tract. The coefficient μ is a dimensionless quantity between 0 and 1 that is equal to the ratio of the real component of the specific acoustic impedance (resistance term x) associated with the sound absorbing material to the fluid characteristic impedance [10]:

$$\mu = x / \rho_0 c_0. \quad (5)$$

Another frequently used characteristic of the sound absorption of the material is dimensionless absorption coefficient α which is related to the boundary admittance coefficient μ by the following equation:

$$\alpha = \frac{1}{0,5 + 0,25(\mu + 1/\mu)}, \quad (6)$$

e.g., for $\rho_0 c_0 = 400 \text{ kgm}^{-2}\text{s}^{-1}$ and $x = 6 \text{ kgm}^{-2}\text{s}^{-1}$ *) is $\mu \doteq 0,015$ and $\alpha \doteq 0,06$.

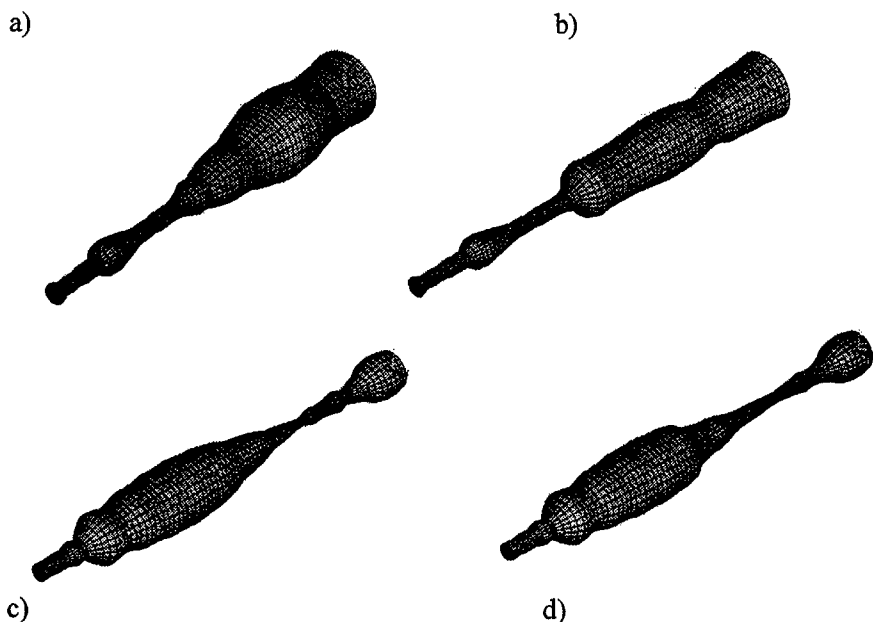


Fig. 2 – FE models of the human vocal tract for: a) English vowel /a/, b) Czech vowel /a/, c) English vowel /i/, d) Czech vowel /i/.

*) This value corresponds to soft tissues (according to the measurement of Mišun V. et al. [11]).

The finite element model of the supraglottal vocal tract is designed by applying the FE code. Each section of the vocal tract is modelled using a truncated cone and acoustic finite elements are used for the fluid. Investigated FE models are shown in Fig. 2. The straight acoustic space is composed of 43 truncated cones.

In the plane that corresponds to the lips the acoustic pressure is presumed to be zero. The plane of the vocal folds (co-ordinate $z=174,58$ mm) is considered to be acoustically hard. All other walls (tissues) of the acoustic volume are generally considered as absorbent ($\mu>0$). The Lanczos unsymmetrical complex eigenvalue solver was used for the modal analysis.

RESULTS OF NUMERICAL CALCULATIONS

The investigation of the influence of the boundary admittance μ on the complex eigenfrequencies: $F_j = F_{j\text{real}} + iF_{j\text{imag}}$ and damping characteristics (damping ratios): $D_j = F_{j\text{real}} / \sqrt{F_{j\text{real}}^2 + F_{j\text{imag}}^2}$ of the vocal tract FE models was the main aim of this study. The results of such numerical calculations are presented in Tables 2 – 5 for the formants F_1 and F_2 for all cases studied. The associated fundamental acoustic mode shapes of the vocal tract are presented in the Figs. 3 - 6. First several eigenfrequencies belong to the acoustic modes, which are excited in the direction of z -axis of the global coordinate system (see Figs. 3-6). The 9th and 10th eigenfrequencies correspond to transversal acoustic modes excited in the direction of x and y -axis (see Fig.7).

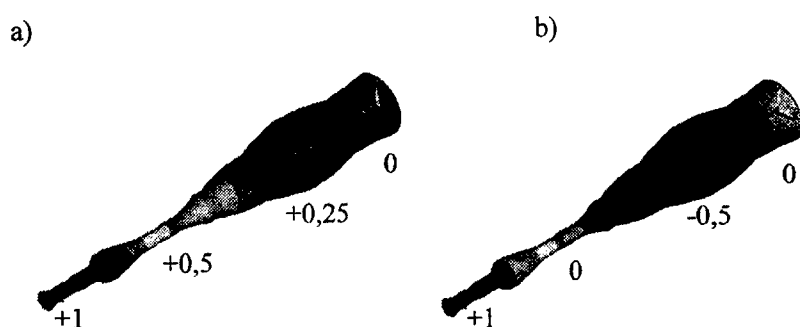


Fig. 3 – First two acoustic eigenmodes of vibration for the English vowel /a/:
a) 1st formant – $F_1=789,8$ Hz, b) 2nd formant – $F_2=1183,8$ Hz for $\mu=0$.

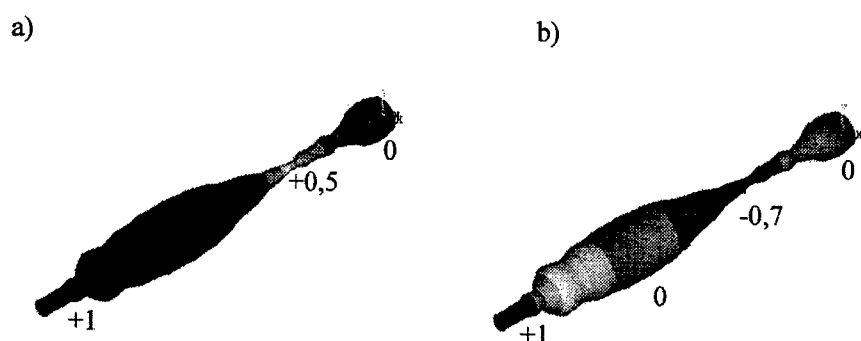


Fig. 4 – First two acoustic eigenmodes of vibration for the English vowel /i/:
a) 1st formant - $F_1=204,4$ Hz, b) 2nd formant - $F_2=2290,3$ Hz for $\mu=0$.

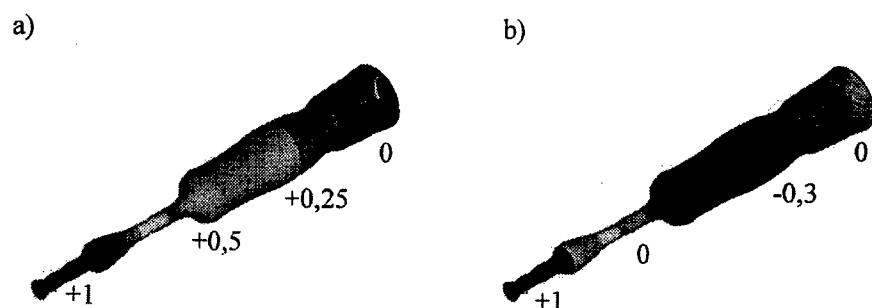


Fig. 5 – First two acoustic eigenmodes of vibration for the Czech vowel /a/:
a) 1st formant - $F_1=753,3$ Hz, b) 2nd formant - $F_2=1146,4$ Hz for $\mu=0$.

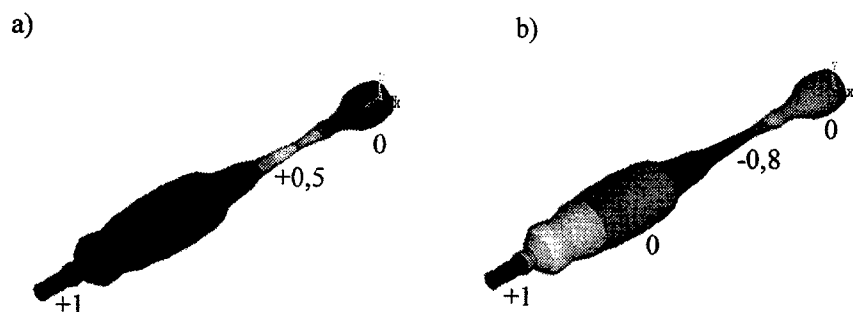


Fig. 6 – First two acoustic eigenmodes of vibration for the Czech vowel /i/:
a) 1st formant - $F_1=203,5$ Hz, b) 2nd formant - $F_2=2360$ Hz for $\mu=0$.

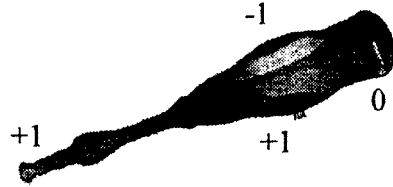


Fig. 7 – Ninth acoustic eigenmode of vibration for the English vowel /a/,
 $F_9 = 7809$ Hz.

The dependence of the half power 3dB bandwidths:

$$\Delta F_i = 2F_{0i}D_i = -2F_{i,real} \quad (i = 1, 2) \quad (5)$$

on the coefficient of the boundary admittance μ is shown in Fig. 8 for the formants F_1 and F_2 for English vowels /a/ and /i/.

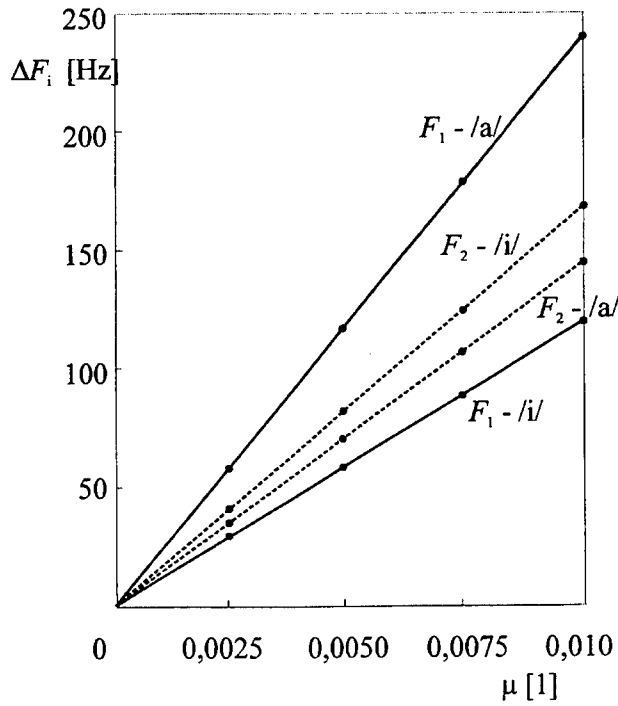


Fig. 8 – Half power 3dB bandwidths versus the coefficient of the boundary admittance the formants F_1 and F_2 of the English vowels /a/ and /i/.

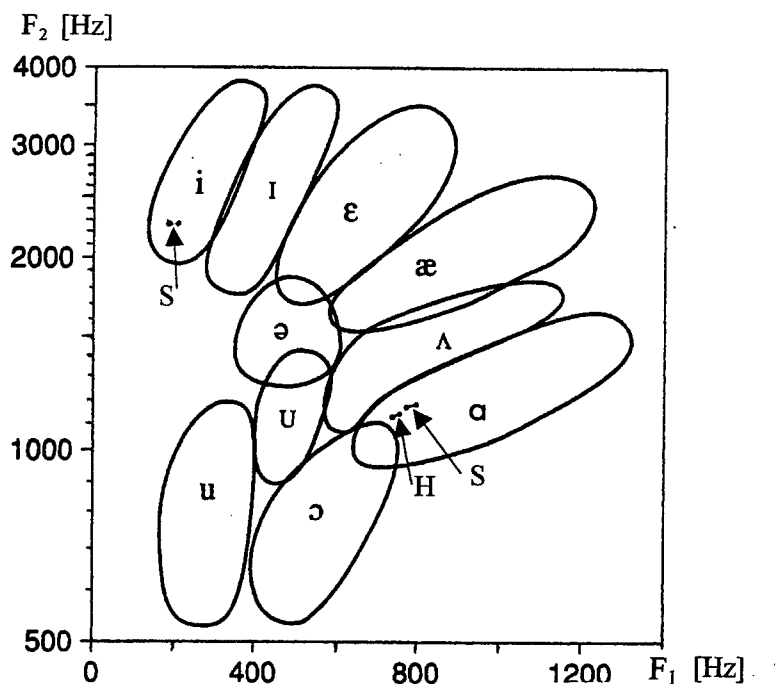


Fig. 9 – Experimentally obtained frequency of second formant F_2 versus frequency F_1 of first formant for 10 English vowels [5]. Results of the FE calculations: S – FE model according to STORY et al. [3], H – FE model according to HÁLA [4].

DISCUSSION OF THE RESULTS

The calculated acoustic eigenfrequencies of the vocal tract for the vowel /a/ reflect the difference between the shapes of the vocal tract for Czech and English vowels. For the vowel /i/ the difference in the eigenfrequencies is not large since the shapes of the vocal tract in the FE models for the Czech and English vowel /i/ are very similar. The reason for that was mentioned above. A reliable measurement of the vocal tract geometry for Czech vowels is needed. All calculated first two eigenfrequencies for both the vowels /a/ and /i/ are in the regions of first two formant frequencies reproduced here in Fig. 9 from the reference [5] where men, women and children were taken into account for ten English vowels (see Fig. 9).

The calculated eigenfrequencies for the Czech vowels are compared in Table 6 with the values published in [6,7].

The agreement between calculated and published frequencies is good for the vowel /a/, however, poor for the vowel /i/, probably caused by insufficiently accurate geometry of the vocal tract.

Concerning the acoustic damping of the vowels, there is no important difference between the results for Czech and English vowels (see Tables 2-5). The acoustic mode shapes of vibration in Figs. 3-6 are also very similar.

absorption		1 st FORMANT /a/ (STORY)			2 nd FORMANT /a/ (STORY)		
μ [1]	α [1]	F_1 real [Hz]	F_1 imag [Hz]	D_1 [1]	F_2 real [Hz]	F_2 imag [Hz]	D_2 [1]
0.0000	0.000	0.000	789.8	0.000	0.000	1183.8	0.000
0.0025	0.010	-30.75	789.4	0.039	-18.18	1183.4	0.015
0.0050	0.020	-61.61	788.1	0.078	-36.26	1182.3	0.031
0.0075	0.030	-92.68	785.9	0.117	-54.14	1180.5	0.046
0.0100	0.039	-124.0	782.7	0.157	-71.73	1178.0	0.061
0.0125	0.049	-155.8	778.5	0.196	-88.96	1174.8	0.076
0.0150	0.058	-188.0	773.1	0.236	-105.7	1171.2	0.090

Table 2 – Calculated complex natural frequencies and damping ratios for English vowel /a/.

absorption		1 st FORMANT /i/ (STORY)			2 nd FORMANT /i/ (STORY)		
μ [1]	α [1]	F_1 real [Hz]	F_1 imag [Hz]	D_1 [1]	F_2 real [Hz]	F_2 imag [Hz]	D_2 [1]
0.0000	0.000	0.000	204.4	0.000	0.000	2290.3	0.000
0.0025	0.010	-15.05	203.8	0.074	-21.80	2290.2	0.010
0.0050	0.020	-30.11	202.2	0.147	-43.60	2290.1	0.019
0.0075	0.030	-45.17	199.4	0.221	-65.41	2289.8	0.029
0.0100	0.039	-60.23	195.4	0.295	-87.23	2289.4	0.038
0.0125	0.049	-75.30	190.1	0.368	-109.1	2288.9	0.048
0.0150	0.058	-90.37	183.4	0.442	-130.9	2288.3	0.057

Table 3 – Calculated complex natural frequencies and damping ratios for English vowel /i/.

A linear relation was found between the considered absorption coefficient of the living tissue and the calculated damping ratios for the acoustic modes in all cases studied. An interesting result is that the damping of the acoustic modes for the first formant is much higher for the vowel /a/ than for the vowel /i/ (see Fig. 8).

The range of real damping (formant bandwidths ΔF_i) is not well known. The calculated half power 3dB bandwidths ΔF_i for the formants F_1 and F_2 are somewhat higher than the values of the formant bandwidths published by Jovičič [8] and Fant [9]. Fant notes that $\Delta F = 40 - 250$ Hz are probable limits for the first three formants and that $\Delta F = 100$ Hz is a typical average value (compare it to Fig. 8). Jovičič found that ΔF is higher than 100 Hz for first two

formants for whispered vowels ($\Delta F_1 = 160$ Hz for /i/ and $\Delta F_1 = 116,5$ Hz for /a/) and that the mean formant bandwidths for voiced vowels are much smaller ($\Delta F_1 = 45,8$ Hz for /i/ and $\Delta F_1 = 63$ Hz for /a/). Hence the calculated bandwidths ΔF presented in Fig. 8 are probably somewhat overestimated and the range of μ should be considered from $\mu \approx 0,005$ to $\mu \approx 0,0075$.

absorption		1 st FORMANT /a/ (HÁLA - STORY)			2 nd FORMANT /a/ (HÁLA - STORY)		
μ [1]	α [1]	$F_{1 \text{ real}}$ [Hz]	$F_{1 \text{ imag}}$ [Hz]	D_1 [1]	$F_{2 \text{ real}}$ [Hz]	$F_{2 \text{ imag}}$ [Hz]	D_2 [1]
0.0000	0.000	0.000	753.3	0.000	0.000	1146.4	0.000
0.0025	0.010	-27.00	753.0	0.036	-22.98	1145.8	0.020
0.0050	0.020	-54.10	752.2	0.072	-45.86	1144.2	0.040
0.0075	0.030	-81.41	750.9	0.108	-68.54	1141.5	0.060
0.0100	0.039	-109.0	748.9	0.144	-90.92	1137.7	0.080
0.0125	0.049	-137.1	746.3	0.181	-112.9	1132.9	0.099
0.0150	0.058	-165.7	743.0	0.218	-134.3	1127.1	0.118

Table 4 – Calculated complex natural frequencies and damping ratios for Czech vowel /a/.

absorption		1 st FORMANT /i/ (HÁLA - STORY)			2 nd FORMANT /i/ (HÁLA - STORY)		
μ [1]	α [1]	$F_{1 \text{ real}}$ [Hz]	$F_{1 \text{ imag}}$ [Hz]	D_1 [1]	$F_{2 \text{ real}}$ [Hz]	$F_{2 \text{ imag}}$ [Hz]	D_2 [1]
0.0000	0.000	0.000	203.5	0.000	0.000	2360.0	0.000
0.0025	0.010	-15.31	202.9	0.075	-23.47	2360.0	0.010
0.0050	0.020	-30.63	201.2	0.151	-46.94	2359.8	0.020
0.0075	0.030	-45.95	198.3	0.226	-70.42	2359.6	0.030
0.0100	0.039	-61.27	194.1	0.301	-93.91	2359.2	0.040
0.0150	0.058	-91.93	181.6	0.452	-141.0	2358.2	0.060

Table 5 – Calculated complex natural frequencies and damping ratios for Czech vowel /i/.

Czech vowel	1 st formant		2 nd formant	
	HÁLA [7]	FE model	HÁLA [7]	FE model
/a/	700-1100 Hz	753 Hz	1100-1500 Hz	1146 Hz
/i/	300-500 Hz	204 Hz	2000-2800 Hz	2360 Hz

Table 6 – Comparison of the calculated and published formants for the Czech vowels /a/ and /i/.

CONCLUSIONS

The presented results of modal analysis of the human supraglottal vocal tract indicate that the magnitude of the acoustic boundary admittance has significant influence on the eigenfrequencies of the FE model. For further analysis it is necessary to verify the values of boundary admittance for the soft tissues in the human vocal tract. The agreement between the calculated first two eigenfrequencies and first two formant frequencies is very good.

REFERENCES

1. Fant, G.M., *Acoustic theory of speech production*. Mouton and Company, Gravenhage, 1960.
2. Peterson, G.E. and Barney, H.L., Control methods used in study of the vowels. *J. Acoust. Soc. Am.*, 1952, **24**, 175-184.
3. Story, B. H., Titze, I. R. and Hoffman, E.A., Vocal tract area functions from magnetic resonance imaging. *J. Acoust. Soc. Am.*, 1996, **100** (1), 537-554.
4. Hála, B., Pollard, B., *Articulation of Czech sounds in X-ray pictures*. ČAVU Prague, 1926 (in Czech).
5. Titze, I. R., *Principles of voice production*. Prentice – Hall, London, 1994.
6. Palková, Z., *Fonetika a fonologie češtiny*. Charles University, Karolinum, Prague, 1994 (in Czech).
7. Hála, B., *Uvedení do fonetiky češtiny na obecném fonetickém základě*. ČSAV, Prague, 1962 (in Czech).
8. Jovičič, S. T., Formant feature difference between whispered and voiced sustained vowels. *Acustica – acta acustica*, 1998, **84**, 739-743.
9. Fant, G.M., On the predictability of formant levels and spectrum envelopes from formant frequencies. In *For Roman Jakobson*, eds. Halle, M., Lunt, H. and MacLean M., Mouton and Company, Gravenhage, The Netherlands, 1956, pp. 109-120.
10. Nový, R., *Noise and vibration*. ČVUT, Prague, 1995 (in Czech).
11. Mišun, V. and Ryndová A., Absorptive characteristics of vocal tract soft tissues. In *Proceedings of the Seminar Interaction and Feedbacks'99*, Nov. 23-24, 1999, Prague, Institute of Thermomechanics, Academy of Sciences of the Czech Republic, pp. 127-134 (in Czech).

The research is supported by the Grant Agency of the Czech Republic by the project No 106 / 98 / K 019.

Combined influence of cutouts and initial stresses on the free vibration response of general, double curvature shell structures

Giuseppe Catania

*Diem, Dept. of Mechanical and Aeronautical Engineering,
University of Bologna, Bologna I-40136, Italy*

ABSTRACT

The stiffening effect experimentally exhibited by locally damaged, thin walled structures such as plates and shells, is investigated. This effect is related to a positive shift of some eigenfrequencies whenever damage is present, i.e. some natural frequencies tend to increase with respect to the same values obtained in sound conditions. In this paper, the stress concentration around a small cutout such as a hole is investigated, and its effect on the modification of structural stiffening is studied and taken into account. It is shown that in some cases this secondary effect may prevail on the damage added flexibility reverse effect, so that some natural frequencies may increase, despite the commonly expected reverse behaviour.

A numerical simulation approach, based on a finite element (F.E.) program developed by the author, is described, and results concerning the free vibrations of a thin walled, initially loaded shell structure, locally damaged by a small circular cutout, are reported and discussed in detail.

1. INTRODUCTION

Free-vibration response of mechanical structures is a well developed area of research from both the modeling-simulation and the machine health conditioning-diagnostics standpoint. Modal parameters, such as eigenfrequencies and eigenshapes, may correctly model the dynamical behaviour of a mechanical component under many ordinary conditions, just as usually employed stiffness and inertia structural parameters generally do. As a matter of fact, small variations of eigenfrequencies and shapes may be used as indicators of local stiffness and inertia structural modifications. Since minor damage can be generally related to some local slight structural modification, a change of the free-vibration response of the whole structure is generally expected. Scientific and technical literature provides plenty of diagnostic tools and procedures to detect structural damages such as cracks and cutouts starting from measured forced or free vibrations [1,2]. Some methods simply rely on complex signal (*signature*) analysis techniques, mainly considering the mechanical system as an unknown "*black box*", while other techniques are model-oriented, being based on the before mentioned correspondence between structural and modal models. Identification of damage parameters, such as type, position and dimensions, can be obtained in this latter case by measuring the free response of the whole structure and then employing an inverse,

identification technique on a previously defined, effective model of a damaged structure. Many analytical and numerical methods have been proposed in the past to accomplish this task, some results being by now well known and quite accepted by the scientific community. It has been found analytically and experimentally that the presence of damage locally decreases structure stiffness and inertia, so that modal mass and stiffness parameters decrease as well. On the other hand, real damage such as a crack only tends to exhibit a low variation of inertia, while local flexibility may be greatly increased. This means that in practical circumstances a decrease of some eigenfrequencies is expected, according to local structural eigen-sensitivity. Nevertheless, the experience of the author [3] and other researchers [4,5] show that under some experimental circumstances an increase of some eigenfrequencies can result, even if the structural inertia was not modified, i.e. minor damage, such as a thin cutout or a crack, results. It should be pointed out that these relative eigenvalue differences are generally small, but are not generally related to computational or experimental errors. Moreover, even low eigenfrequencies may exhibit this behaviour.

The most commonly accepted interpretation of this phenomenon may be obtained by differentiating the standard expression of eigenvalue ω_i^2 , as a function of modal stiffness k_i and modal mass m_i :

$$\omega_i^2 = \frac{k_i}{m_i}, \quad (1.1)$$

$$\Rightarrow d\omega_i = \frac{1}{2 \cdot \omega_i \cdot m_i} \cdot \left(dk_i - \frac{k_i}{m_i} \cdot dm_i \right). \quad (1.2)$$

Thus, when low mode index i is taken into account, positive (small) variations of i^{th} natural frequency ω_i are associated with usually large negative variations of modal mass m_i , since:

$$d\omega_i > 0 \Rightarrow dm_i < \frac{m_i}{k_i} \cdot dk_i = \frac{dk_i}{\omega_i^2}. \quad (1.3)$$

As a matter of fact, numerical experiences carried out by the author of this paper seem to point out that this effect may only occur if large cutouts or high frequency modes ($\omega_i \nearrow$) are considered.

In other cases, a different interpretation could be given. The presence of a cutout may consistently alter the structural dynamic behaviour, as happens when damage is localized close to some physical constraints, e.g. the clamp connections to the ground [5]. In this case, boundary conditions are modified and model structure may change as well.

Moreover, it should be pointed out that strange results may also be obtained while trying to simulate the dynamic behaviour of thin-walled structures by employing commercial, F.E. packages. When trying to obtain the numerical solution of eigen-problems related to a *sound* and a similar but damaged structure, very low eigenfrequency differences are expected. Efficient, iterative procedures adopted by these programs may give wrong

results, since errors referring to mode i^{th} are commonly related to the previous $(i-1)^{\text{th}}$ mode. As a matter of fact, there is no effective way to check against the absolute error, and to verify that this error is small with respect to expected eigenfrequency difference values. The same can also apply when numerical models concerning *sound* and damaged structures are too different, e.g. F.E. meshing and model algebraic dimensions (number of degrees of freedom) are not the same. Even in this case, numerical results may not be consistent at all.

In this paper, effective modeling of the free vibration response of a shell structure, damaged by a cutout, is considered, with the main concern being addressed to give a physical interpretation of the previously mentioned effect. Known research in the modeling and diagnosis contexts is mainly concentrated on the eigenvalue variation of simple damaged structures such as beam, plates and single curvature (circular cylinders) shells, generally under a few standard boundary conditions; eigenshape variation is studied as well, but difficulties and errors in practical testing can make this approach less attractive from an experimental point of view. Nevertheless, these approaches seem to suffer from the modeling standpoint, since only unrealistic, simple case-structures are considered; moreover they also seem to be lacking in some testing verifications, since the previously cited secondary stiffening effect is not modeled at all.

To account for stiffening effect, local stress field modification that occurs in proximity of the physical damage is taken into account. Since large stress concentrations are generally expected, stress stiffening may result, and some eigenvalues are expected to increase, despite the added flexibility due to damage. To justify this assumption, initial stresses are needed, as happens for example in most civil and aerospace structures which are pre-loaded for stiffening purposes. On the other hand, it should be pointed out that initial loading may also occur if structural weight is not negligible, or even if residual stresses due to some technological process are taken into account.

An *ad hoc*, finite element program, based on a library of isoparametric shell elements was developed and implemented to obtain the dynamical model of a damaged, general shell structure, under some initial external loading. The combined influence of initial stresses and cutouts is considered to correctly interpret the stiffening behaviour. An automatic, parametric mesh fitting procedure was studied to allow nearly rectangular and elliptical cutouts be modeled. Initial stresses were then taken into account by evaluating the element geometric stiffness matrix K_g . Natural frequencies of the same structure, undamaged and damaged by a circular cutout, are numerically obtained and compared, showing that some eigenfrequencies may increase under some loading conditions.

2. FINITE ELEMENT MODELING APPROACH

A family of standard, Mindlin-type shell elements was developed and implemented to allow general double curvature, thin and moderately thick structures to be modeled. Quadrilateral, iso-parametric formulation was

adopted [6], and linear, quadratic, cubic polynomial interpolation form functions were chosen to obtain a family of five different quadrilateral elements (linear, 4 nodes; quadratic, serendipity 8 nodes; quadratic, full 9 nodes; cubic, serendipity 12 nodes; cubic, full 16 nodes). In all of the family elements, five degrees of freedom (d.o.f.) per node were chosen, according to standard references [6].

Quadratic and cubic elements were initially preferred to effectively model curved shells without further mesh refinement, i.e. with a limited number of d.o.f.s. Since meshing of large, isoparametric shell elements tends to stiffen (*locking*), a selective integration rule was adopted [7]. To prevent numerical increase of element rigid modes (*mechanisms*, [8]) due to the adoption of low order integration rules, an original stiffening rule, based on algebraic Singular Value Decomposition (SVD) conditioning of stiffness element matrix K , was defined and implemented; details of it can be found in [9].

An accurate solution of the generalized eigenproblem related to the free vibration problem (2.1):

$$(K_{\text{ass}} - \omega_i^2 \cdot M_{\text{ass}}) \cdot \Xi_i = 0, \quad i = 1 \dots m, \quad (2.1)$$

being M_{ass} , K_{ass} the assembled structural mass and stiffness matrices and ω_i^2, Ξ_i the i^{th} eigenvalue and eigenvector, was obtained by evaluating the Crout decomposition of positive definite mass matrix $M_{\text{ass}} = L \cdot L^T$, then solving the standard eigenproblem (2.2) by reducing the real symmetric matrix $(L^{-1} \cdot K_{\text{ass}} \cdot (L^{-1})^T)$ to a symmetric tridiagonal matrix using orthogonal similarity transformations; eigenvalues are then evaluated using Sturm sequences [10]:

$$(L^{-1} \cdot K_{\text{ass}} \cdot (L^{-1})^T - \omega_i^2 \cdot I) \cdot \Psi_i = 0, \quad \Xi_i = (L^{-1})^T \cdot \Psi_i, \quad i = 1 \dots m. \quad (2.2)$$

Although this historical algorithm performs poorly from an efficiency standpoint, especially with respect to other usually employed procedures, such as sub-space iteration techniques [11], more accurate results can be obtained with it when high frequency modes are considered.

Elements were then tested and validated by comparing numerically evaluated natural frequencies with reference values computed by analytical closed form (C.F.) expressions allowable from literature [12]; only plate and circular cylinder structures under standard boundary conditions were considered. Numerical validation showed that analytical C.F. modes were effectively modeled, and that a relative low eigenfrequency error (less than 1%) can be easily obtained for the first 50 modes starting from moderately fine meshes.

Although better results were obtained with cubic, 12 and 16 node elements, especially with respect to their behaviour against the before mentioned locking effect, the 8 node, 40 d.o.f., parabolic, serendipity element was preferred instead, because of its inherent, low computational load. As a

matter of fact, a smaller number of d.o.f.s is generally obtained with lower order elements by using standard meshing techniques.

A simplified, automatic mesh generation scheme was then adopted, based on the generalization of classical algorithm [13]. Starting from a complex, single patch B-spline model Φ of surface geometry Γ (2.3):

$$\Phi(\xi, \eta): Q \rightarrow \Gamma, \quad Q = \{[0,1] \times [0,1]\} \subset \mathbb{R}^2, \quad \Gamma \in \mathbb{R}^3, \quad (2.3)$$

Φ being obtained by point interpolation or fitting [14], the final mesh can be obtained by decomposing \mathbb{R}^2 square domain Q in n rows \times m columns rectangular sub-domains q_{ij} :

$$Q = \{ \{ [0 \equiv \xi_0, \xi_1], [\xi_1, \xi_2], \dots, [\xi_{n-1}, \xi_n \equiv 1] \} \times \{ [0 \equiv \eta_0, \eta_1], \dots, [\eta_{m-1}, \eta_m \equiv 1] \} \} = \{ q_{11}, q_{12}, \dots, q_{ij}, \dots, q_{nm} \}; \quad (2.4)$$

$$q_{ij} = [\xi_{i-1}, \xi_i] \times [\eta_{j-1}, \eta_j], \quad \begin{cases} 0 = \xi_0 < \xi_1 < \dots < \xi_n = 1 \\ 0 = \eta_0 < \eta_1 < \dots < \eta_m = 1 \end{cases}$$

Element γ_{ij} can then be obtained as the \mathbb{R}^3 image of \mathbb{R}^2 domains q_{ij} :

$$\gamma_{ij} = \Phi(q_{ij}). \quad (2.5)$$

To effectively mesh a rectangular or curved cutout, the following scheme, illustrated in figs.1-2 and previously implemented for plane geometry (plates) [3], was adopted. A single \mathbb{R}^2 rectangular domain q_{ij} is refined in $4 \times s(+1)$ rectangular sub-elements:

$$q_{ij} = \{ \omega_{\text{left}}, \omega_{\text{up}}, \omega_{\text{right}}, \omega_{\text{down}}, (\omega_0) \}, \quad r = 1 \dots s; \quad (2.6)$$

element vertices (external nodes) being built on main diagonal straight lines of rectangle $q_{ij} \subset \mathbb{R}^2$ parameter domain.

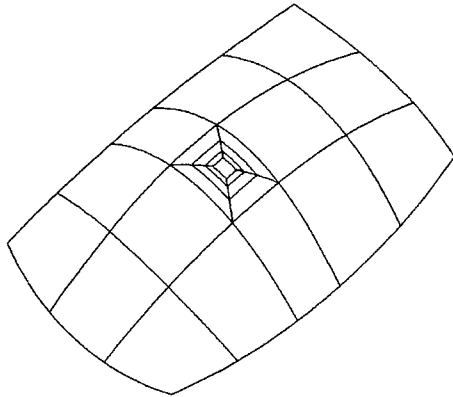


Figure 1: rectangular slot.

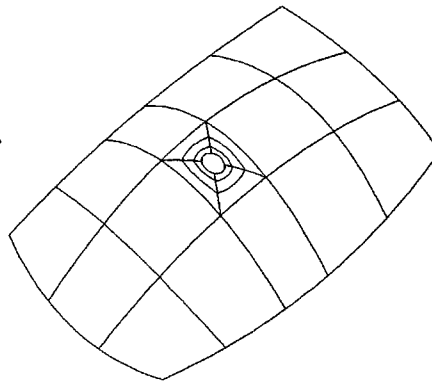


Figure 2: elliptical slot.

The position of internal nodes is thus evaluated by linearly interpolating the positions of internal nodes of reference domain q_{ij} , and those referring to internal element ω_b . Element ω_b refers to cutout geometry, and only belongs

to sound structure Γ ; instead, only external 4xs refined elements belong to damaged structure Γ_{dam} . Since parabolic interpolation functions were adopted, rectangular (slot) and elliptical (hole) cutouts can be modeled by correctly positioning ω_0 internal nodes. Damaged and undamaged finite element models Γ_{dam} and Γ are thus similar, meaning that the same degrees of freedom are considered in both cases.

Since iso-parametric quadrilateral elements may behave critically when distorted [15], an iterative check is also done to ensure that angle α between any contiguous curved element sides is not too small ($\alpha \geq 15^\circ$) or close to a flat angle ($\alpha \leq 165^\circ$). Side ratio r between the length of any contiguous couple of element sides is also evaluated and checked ($0.2 \leq r \leq 5$).

Stress stiffening is modeled by adding a geometric stiffness matrix K_g to the stiffness element matrix K . Many formulations of matrix K_g are known and may be found in literature, but local formulations are generally taken into account, depending on the particular problem studied (Kirchoff plates, cylindrical shells, etc.). Since Mindlin type elements employed in this work can consistently model transverse shear deformations, a more general expression is preferred. Moreover, it should be taken into account that even simple initial stress fields, such as one-dimensional, uniform membrane stress field, are expected to change and become fully 3-dimensional stress fields in proximity of a cutout.

A general formulation of K_g is thus adopted, as results from adding the work done by the initial stress field σ_0 on the non linear, second order (Lagrange) deformation components ϵ^{II} to the local element elastic energy Π ; this means that elastic work done by any stress field can be evaluated. This formulation does not seem new, since [16] first seems to have proposed this generalization, and other researchers [15] state the same concepts, but in the author's knowledge there does not seem to be any published reference to successful implementations of such general formulation.

Following standard notations employed in variational formulation of elasticity problems [15], the contribution Π_g to the full potential energy Π' and algebraic expression of K_g can be obtained as results from the following:

$$\Pi' = \Pi + \Pi_g, \quad \Pi = \frac{1}{2} \cdot \delta^T \cdot K \cdot \delta + \delta \cdot M \cdot \tilde{\delta}; \quad (2.7)$$

$$\begin{aligned} \Pi_g &= \int_{\gamma} \sigma_0^T \cdot \epsilon^{\text{II}} \cdot d\gamma = \frac{1}{2} \delta^T \cdot \int_{\gamma} (H \cdot N)^T \begin{bmatrix} \underline{\sigma}_0 & 0 & 0 \\ 0 & \underline{\sigma}_0 & 0 \\ 0 & 0 & \underline{\sigma}_0 \end{bmatrix} H \cdot N \cdot d\gamma \cdot \delta = \\ &= \frac{1}{2} \delta^T \cdot K_g \cdot \delta; \end{aligned} \quad (2.8)$$

$$K_g = \int_{\gamma} (H \cdot N)^T \begin{bmatrix} \underline{\sigma}_0 & 0 & 0 \\ 0 & \underline{\sigma}_0 & 0 \\ 0 & 0 & \underline{\sigma}_0 \end{bmatrix} H \cdot N \cdot d\gamma; \quad (2.9)$$

where:

K: element stiffness matrix,

M: element mass matrix,

δ : element d.o.f. vector,

γ : finite element domain,

$\mathbf{u} = \{u, v, w\}^T$: displacement vector,

N: interpolation (form) vector function ($\mathbf{u} = \mathbf{N} \cdot \delta$);

$$\sigma_0 = \{\sigma_{x_0}, \sigma_{y_0}, \sigma_{z_0}, \tau_{xy_0}, \tau_{yz_0}, \tau_{zx_0}\}^T, \quad \underline{\sigma}_0 = \begin{bmatrix} \sigma_{x_0} & \tau_{xy_0} & \tau_{zx_0} \\ \tau_{xy_0} & \sigma_{y_0} & \tau_{yz_0} \\ \tau_{zx_0} & \tau_{yz_0} & \sigma_{z_0} \end{bmatrix};$$

$$H = \begin{bmatrix} h_x \\ h_y \\ h_z \end{bmatrix}, \quad h_\chi = \begin{bmatrix} \partial/\partial\chi & 0 & 0 \\ 0 & \partial/\partial\chi & 0 \\ 0 & 0 & \partial/\partial\chi \end{bmatrix}, \quad \chi = x, y, z;$$

$$H \cdot \mathbf{u} = H \cdot \mathbf{N} \cdot \delta = \left\{ \frac{\partial u}{\partial x}, \frac{\partial u}{\partial y}, \frac{\partial u}{\partial z}, \frac{\partial v}{\partial x}, \frac{\partial v}{\partial y}, \frac{\partial v}{\partial z}, \frac{\partial w}{\partial x}, \frac{\partial w}{\partial y}, \frac{\partial w}{\partial z} \right\}^T;$$

$$\varepsilon^{\Pi} = \begin{bmatrix} \varepsilon_x^{\Pi} \\ \varepsilon_y^{\Pi} \\ \varepsilon_z^{\Pi} \\ \gamma_{xy}^{\Pi} \\ \gamma_{yz}^{\Pi} \\ \gamma_{zx}^{\Pi} \end{bmatrix} = \begin{bmatrix} \frac{1}{2} \left(\frac{\partial u}{\partial x}^2 + \frac{\partial v}{\partial x}^2 + \frac{\partial w}{\partial x}^2 \right) \\ \frac{1}{2} \left(\frac{\partial u}{\partial y}^2 + \frac{\partial v}{\partial y}^2 + \frac{\partial w}{\partial y}^2 \right) \\ \frac{1}{2} \left(\frac{\partial u}{\partial z}^2 + \frac{\partial v}{\partial z}^2 + \frac{\partial w}{\partial z}^2 \right) \\ \frac{\partial u}{\partial x} \cdot \frac{\partial u}{\partial y} + \frac{\partial v}{\partial x} \cdot \frac{\partial v}{\partial y} + \frac{\partial w}{\partial x} \cdot \frac{\partial w}{\partial y} \\ \frac{\partial u}{\partial y} \cdot \frac{\partial u}{\partial z} + \frac{\partial v}{\partial y} \cdot \frac{\partial v}{\partial z} + \frac{\partial w}{\partial y} \cdot \frac{\partial w}{\partial z} \\ \frac{\partial u}{\partial z} \cdot \frac{\partial u}{\partial x} + \frac{\partial v}{\partial z} \cdot \frac{\partial v}{\partial x} + \frac{\partial w}{\partial z} \cdot \frac{\partial w}{\partial x} \end{bmatrix}.$$

3. APPLICATION

A numerical example is reported, concerning the double curvature shell structure shown in fig.3. The shell main surface geometry is obtained from a curved, quadrilateral patch, initially meshed by the automatic procedure previously referred, so that an initial mesh of 50 elements results. Both external loading and constraints are distributed along the four sides of the original surface patch. Load is uniformly applied along one direction, on a single side only; constraints are modeled as elastic, and distributed along the

four sides of the patch, to obtain a clamp-like constraint (five d.o.f.s elastically constrained) on one side, and a rolling, support-like elastic constraint on the opposite loaded side and on the other lateral sides. Main dimensions can be expressed by the length along the load direction $\ell \cong 1200\text{mm}$, transverse width $b \cong 300\div 500\text{mm}$, and uniform thickness $t=2\text{mm}$. Material is high strength aluminium alloy, density $\rho = 2800\text{kg/m}^3$, Young modulus $E = 7.2 \times 10^{10}\text{N/m}\cdot\text{s}^2$, and Poisson coefficient $\nu = 0.33$.

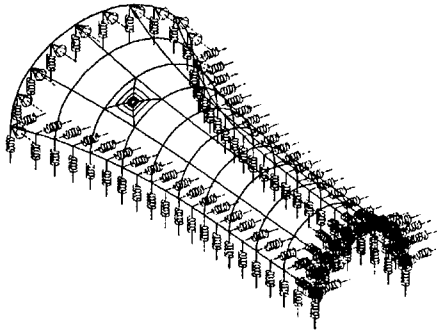


Figure 3: geometry and boundary conditions.

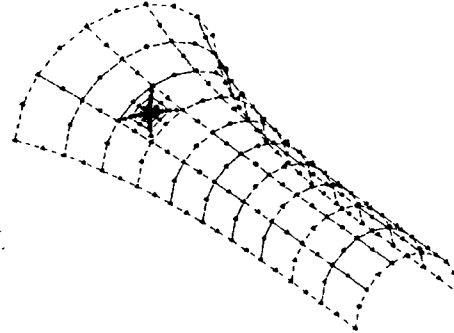


Figure 4: F.E. mesh.

Damage is modeled by an interior circular cutout, diameter $d=10\text{mm}$; automatic meshing is done, and a locally fitted mesh, consisting of $n_e=69+1$ elements, $n_d=241$ nodes, $n=1205$ d.o.f.s, was obtained by choosing the previously defined mesh refinement parameter $s=5$ (fig.4).

4. NUMERICAL RESULTS

Natural frequencies $f_k^{(\Gamma)}$, $f_k^{(\Gamma_{\text{dam}})}$ ($k=1\dots m$) and mode shapes $\Xi_k^{(\Gamma)}$, $\Xi_k^{(\Gamma_{\text{dam}})}$ of undamaged (Γ) and damaged (Γ_{dam}) structures previously defined in §3 were first evaluated with no external loading, to outline the sensitivity of free vibration modes to the modeled damage.

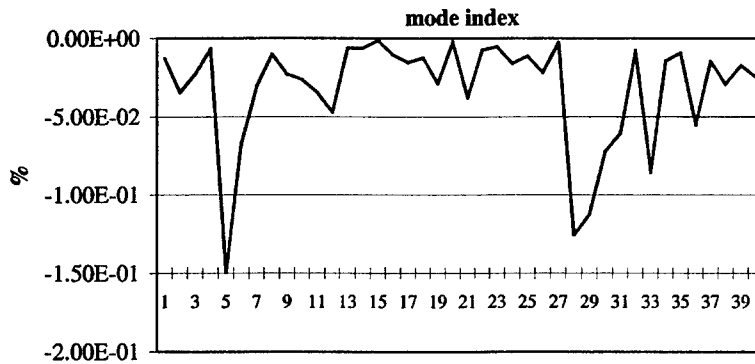


Figure 5: $\Delta_k = \frac{\Delta f_k}{f_k^{(\Gamma)}}$, $q=0$ (no load).

It was checked that first $m=40$ mode shapes are essentially the same, and also result in the same order, if ordering is made with respect to crescent, eigenfrequency values. Tab.1 shows first $m=40$ natural frequencies $f_k^{(\Gamma)}$ and difference $\Delta f_k = f_k^{(\Gamma_{\text{dam}})} - f_k^{(\Gamma)}$, while fig.5 refers to the relative frequency difference parameter $\Delta_k = \frac{\Delta f_k}{f_k^{(\Gamma)}}$, plotted against (discrete) mode index k . It can be shown that only null or negative relative differences are obtained, as is expected.

Tab.1: $f_k^{(\Gamma)}$, Δf_k ($q=0$).

f[1]=	2.1798e+02 Hz => Δf =	-2.77e-02 Hz
f[2]=	2.5863e+02 Hz => Δf =	-8.86e-02 Hz
f[3]=	3.4367e+02 Hz => Δf =	-7.82e-02 Hz
f[4]=	4.0340e+02 Hz => Δf =	-2.67e-02 Hz
f[5]=	4.8517e+02 Hz => Δf =	-7.24e-01 Hz
f[6]=	5.3488e+02 Hz => Δf =	-3.60e-01 Hz
f[7]=	6.3750e+02 Hz => Δf =	-1.94e-01 Hz
f[8]=	6.5811e+02 Hz => Δf =	-6.63e-02 Hz
f[9]=	7.4484e+02 Hz => Δf =	-1.68e-01 Hz
f[10]=	7.8470e+02 Hz => Δf =	-2.05e-01 Hz
f[11]=	8.0178e+02 Hz => Δf =	-2.75e-01 Hz
f[12]=	9.0053e+02 Hz => Δf =	-4.22e-01 Hz
f[13]=	9.3622e+02 Hz => Δf =	-5.73e-02 Hz
f[14]=	1.0082e+03 Hz => Δf =	-6.31e-02 Hz
f[15]=	1.0261e+03 Hz => Δf =	-1.12e-02 Hz
f[16]=	1.1134e+03 Hz => Δf =	-1.18e-01 Hz
f[17]=	1.1582e+03 Hz => Δf =	-1.77e-01 Hz
f[18]=	1.1892e+03 Hz => Δf =	-1.47e-01 Hz
f[19]=	1.3075e+03 Hz => Δf =	-3.75e-01 Hz
f[20]=	1.4161e+03 Hz => Δf =	-2.99e-02 Hz
f[21]=	1.5028e+03 Hz => Δf =	-5.68e-01 Hz
f[22]=	1.5206e+03 Hz => Δf =	-1.12e-01 Hz
f[23]=	1.5945e+03 Hz => Δf =	-8.43e-02 Hz
f[24]=	1.6541e+03 Hz => Δf =	-2.64e-01 Hz
f[25]=	1.6636e+03 Hz => Δf =	-1.88e-01 Hz
f[26]=	1.8135e+03 Hz => Δf =	-3.95e-01 Hz
f[27]=	1.8343e+03 Hz => Δf =	-4.28e-02 Hz
f[28]=	1.8806e+03 Hz => Δf =	-2.35e+00 Hz
f[29]=	1.9930e+03 Hz => Δf =	-2.24e+00 Hz
f[30]=	2.0211e+03 Hz => Δf =	-1.46e+00 Hz
f[31]=	2.0691e+03 Hz => Δf =	-1.25e+00 Hz
f[32]=	2.1336e+03 Hz => Δf =	-1.60e-01 Hz
f[33]=	2.2542e+03 Hz => Δf =	-1.93e+00 Hz
f[34]=	2.3212e+03 Hz => Δf =	-3.35e-01 Hz
f[35]=	2.4205e+03 Hz => Δf =	-2.20e-01 Hz
f[36]=	2.4789e+03 Hz => Δf =	-1.37e+00 Hz
f[37]=	2.5163e+03 Hz => Δf =	-3.66e-01 Hz
f[38]=	2.5782e+03 Hz => Δf =	-7.49e-01 Hz
f[39]=	2.6768e+03 Hz => Δf =	-4.57e-01 Hz
f[40]=	2.8100e+03 Hz => Δf =	-6.93e-01 Hz

Tab.2: $f_k^{(\Gamma)}$, Δf_k ($q=100 \text{ N/mm}$).

f[1]=	2.5378e+02 Hz => Δf =	1.71e-02 Hz
f[2]=	2.8921e+02 Hz => Δf =	5.66e-03 Hz
f[3]=	3.9215e+02 Hz => Δf =	-1.00e-01 Hz
f[4]=	4.4588e+02 Hz => Δf =	8.28e-02 Hz
f[5]=	5.3033e+02 Hz => Δf =	-2.98e-01 Hz
f[6]=	5.7781e+02 Hz => Δf =	-3.76e-01 Hz
f[7]=	6.9284e+02 Hz => Δf =	7.31e-02 Hz
f[8]=	6.9819e+02 Hz => Δf =	-6.96e-02 Hz
f[9]=	7.5964e+02 Hz => Δf =	-1.48e-01 Hz
f[10]=	8.3718e+02 Hz => Δf =	-2.52e-01 Hz
f[11]=	8.7812e+02 Hz => Δf =	-6.05e-02 Hz
f[12]=	9.3703e+02 Hz => Δf =	5.06e-02 Hz
f[13]=	9.6282e+02 Hz => Δf =	-3.12e-01 Hz
f[14]=	1.0454e+03 Hz => Δf =	-8.90e-02 Hz
f[15]=	1.0664e+03 Hz => Δf =	-1.44e-02 Hz
f[16]=	1.1526e+03 Hz => Δf =	-1.34e-01 Hz
f[17]=	1.2173e+03 Hz => Δf =	-1.73e-01 Hz
f[18]=	1.2574e+03 Hz => Δf =	-1.66e-01 Hz
f[19]=	1.3793e+03 Hz => Δf =	-3.95e-01 Hz
f[20]=	1.4654e+03 Hz => Δf =	4.12e-03 Hz
f[21]=	1.5507e+03 Hz => Δf =	-1.53e-01 Hz
f[22]=	1.5944e+03 Hz => Δf =	-3.58e-01 Hz
f[23]=	1.6509e+03 Hz => Δf =	-4.64e-02 Hz
f[24]=	1.6677e+03 Hz => Δf =	-4.44e-01 Hz
f[25]=	1.7034e+03 Hz => Δf =	-5.10e-02 Hz
f[26]=	1.8599e+03 Hz => Δf =	1.23e-02 Hz
f[27]=	1.8837e+03 Hz => Δf =	1.37e+00 Hz
f[28]=	1.9613e+03 Hz => Δf =	-1.99e+00 Hz
f[29]=	2.0604e+03 Hz => Δf =	-4.74e-01 Hz
f[30]=	2.0759e+03 Hz => Δf =	-1.37e+00 Hz
f[31]=	2.1188e+03 Hz => Δf =	-1.11e+00 Hz
f[32]=	2.1833e+03 Hz => Δf =	2.84e-01 Hz
f[33]=	2.3512e+03 Hz => Δf =	-2.10e+00 Hz
f[34]=	2.3748e+03 Hz => Δf =	-1.32e-01 Hz
f[35]=	2.4407e+03 Hz => Δf =	1.87e-02 Hz
f[36]=	2.5456e+03 Hz => Δf =	-1.21e+00 Hz
f[37]=	2.5829e+03 Hz => Δf =	1.68e+00 Hz
f[38]=	2.6396e+03 Hz => Δf =	-3.93e-02 Hz
f[39]=	2.7870e+03 Hz => Δf =	-4.95e-01 Hz
f[40]=	2.8524e+03 Hz => Δf =	-5.42e-01 Hz

The same steps are repeated, but distributed load $q=100 \text{ N/mm}$ is applied (§3). Static evaluation of initial stresses σ_0 was first performed, in order to evaluate K_g :

$$\delta \subset \delta_{\text{ass}} = (K_{\text{ass}}^{-1} \cdot F_{\text{ass}}),$$

$$\sigma_0 = D \cdot \mathcal{L} \cdot N \cdot \delta;$$

where new symbols now refer to:

$K_{\text{ass}}, F_{\text{ass}}, \delta_{\text{ass}}$: F.E. assembled stiffness matrix, force and d.o.f. vectors;

D : material, constitutive property matrix ($\sigma = D \cdot \varepsilon$);

\mathcal{L} : first order deformation differential operator matrix ($\varepsilon = \mathcal{L} \cdot u = \mathcal{L} \cdot N \cdot \delta$).

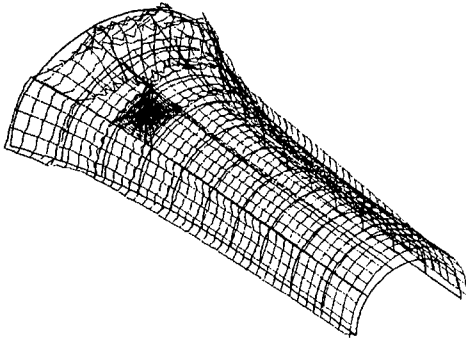


Figure 6: σ_z stress plot.

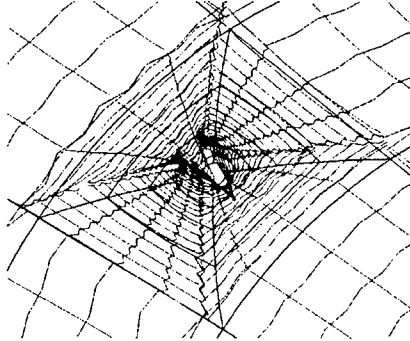


Figure 7: σ_z plot around the hole.

Figures 6,7 refer to the graphical plot of σ_z stress component along the main loading direction, showing that high stress concentration occurs in proximity of the hole.

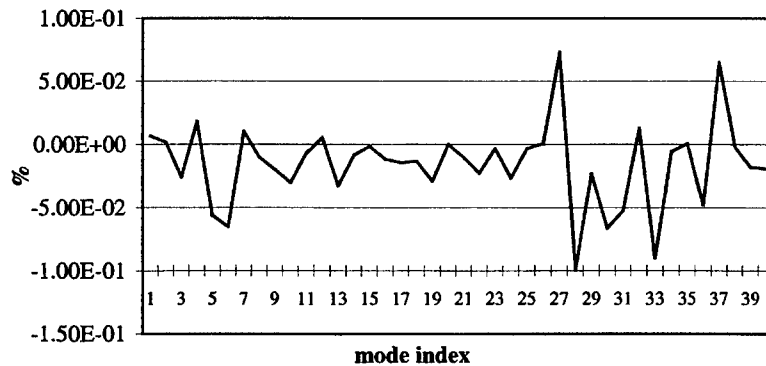


Figure 8: $\Delta_k = \frac{\Delta f_k}{f_k^{(\Gamma)}}$, $q=100 \text{ N/mm}$.

Also in this case it was checked that the effect of damage does not modify either mode shapes or relative ordering while referring to the same loading condition. Nevertheless, it was also found that the same does not apply if unloaded, and loaded structure mode shapes are compared. As a matter of fact, initial stresses tend to mostly stiffen the structure along the loading direction, so that related natural frequencies may increase as well.

Tab.2 and fig.8 report the results. In this case, positive relative differences are obtained with respect to some index modes, showing that the previously defined stiffening effect may occur and prevail on the reverse, damage added flexibility effect.

5. DISCUSSION AND CONCLUSIONS

The stiffening effect, experimentally found by the author in some past experiences, was considered, and a physical interpretation of this effect is also proposed. A numerical approach, based on a finite element analysis based on Mindlin, iso-parametric shell elements, was used. Since standard, F.E. packages may suffer from loss in accuracy while evaluating structural properties and resulting eigen-parameters, an *ad-hoc* program was developed and implemented to accomplish this task.

Numerical results, obtained on a thin walled structure case example, showed that in some cases such stiffening effect may result. Moreover, it was shown that this effect could also be obtained at low frequency values, i.e. when low order free vibration modes are taken into account.

Real damage, such as cracks, is not considered in this paper, and more effort is thus required to consistently model both the stress field and the added flexibility due to a real crack. Nevertheless, it should be pointed out that the aim of this paper was to analytically demonstrate that the stiffening effect can result. Quantitative results about real, cracked structures still need to be achieved: some work is actually in progress to obtain an effective F.E. formulation of a cracked, iso-parametric finite element [9].

Experimental verification of numerical results was previously obtained for plate-like structures, and details can be found in a previous paper [3]. However, experimental validation is also needed in the general curved, shell context, to assess the limits of applicability of eigenfrequency-based condition monitoring techniques. Such extension could be a new related topic to investigate in the future.

6. REFERENCES

1. Cawley, P., Adams, R.D., The location of defects in structures from measurements of natural frequencies, *J. of Strain Analysis*, 1979, **14** (2), 49-57.
2. Catania, G., Maggiore, A., Meneghetti, U., Monitoring rotors by sensitivity analysis, Proc. of Conditioning Monitoring Conf., Swansea, Pineridge Press, 1994, 253-64.

3. Catania, G., Meneghetti, U., Effect of initial stresses on eigenfrequencies of a damaged plate, Proc. of 16th DAS Symposium on Experimental Methods in Solid Mechanics, 1999, Cluj-Napoca.
4. Ahmad, A.Q., Meneghetti, U., Crack detection in plates by sensitivity analysis, Proc. of the 15th IMAC, 1997.
5. Natke, H.G., Cempel, C., Fault detection and localisation in structures: a discussion, *Mechanical Systems and Signal Processing*, 1991, 5 (5), 345-56.
6. Ahmad, S., Irons, B., Zienkiewicz, O.C., Analysis of thick and thin shell structures by curved finite elements, *International Journal of Numerical Methods in Engineering*, 1970, 2 (3), 419-51.
7. Zienkiewicz, O.C., Taylor, R.L., Too, J.M., Reduced integration technique in general analysis of plates and shells, *International Journal of Numerical Methods in Engineering*, 1971, 3 (2), 275-90.
8. Verhegge, B., Powell, G.H., Control of zero-energy modes in 9-node plane element, *International Journal of Numerical Methods in Engineering*, 1986, 23 (5), 863-69.
9. Vitali, A., Modellazione dinamica di un guscio criccato mediante il metodo dell'elemento finito, Master thesis, University of Bologna, 1999.
10. Wilkinson, J.H., Reinsch, C., Handbook for automatic computation, vol.II, Linear Algebra, Part 2, 1971, Springer-Verlag, Berlin.
11. Dhatt, G., Touzot, G., The finite element method displayed, 1984, John Wiley & sons, Chichester.
12. Leissa, A.W., Vibrations of shells, 1973, NASA SP 288.
13. Zienkiewicz, O.C., Phillips, D.V., An automatic mesh generation scheme for plane and curved surfaces by isoparametric coordinates, *International Journal of Numerical Methods in Engineering*, 1971, 3, 519-28.
14. Catania, G., Molari, P.G., A prototype CAD-CAM environment for design and manufacturing of mechanical moulds and dies, Proc. of the 36th Anipla conference, Genova, Pirella ed., 1992, III, 211-25.
15. Cook, R.D., Malkus, D.S., Plesha, M.E., Concepts and applications of finite element analysis, 1989, John Wiley & sons, Singapore.
16. Przemieniecki, J.S., Theory of matrix structural analysis, 1968, McGraw-Hill, New York.

ON THE IDENTIFICATION OF NATURAL FREQUENCIES OF THICK PORTAL FRAMES

S. E. Hirdaris
School of Engineering Sciences
Ship Science
University of Southampton
Highfield, Southampton, SO17 1BJ, U.K.
E-mail: spyros @ ship.soton.ac.uk

AND

A. W. Lees
Department of Mechanical Engineering
University of Wales -Swansea
Singleton Park, Swansea, SA2 8PP, U.K.
E-mail: a.w.lees@swansea.ac.uk

ABSTRACT

Portal frames are a common feature in many engineering structures and in this paper an approach is given to model their dynamic behaviour adequately. Whilst the eigen-frequencies of continuous systems comprising of slender beam structures can be identified, in most cases of practical interest, by means of Euler or Timoshenko beam theory, for thick portal frame models this is not true. The present paper attempts to approach this problem by means of 2D planar finite element analysis. Two plane stress finite element representations of conforming and non-conforming form are suggested and their differences are examined. Using the results of a new conforming 32dof per element representation some insight is gained into the motion of such structures, particularly with respect to the strain field around the joints.

INTRODUCTION

Many engineering structures such as ships, aeroplanes, turboalternator foundations, rotors...etc. can be modeled with sufficient accuracy using beam models and extensive research on the basic theory has spanned almost three centuries. Most of the work is based on the so-called Bernoulli hypothesis according to which structural cross-sections remain undeformed in the deformed state of the beam and differ in the way the relationships between the displacements, rotations and corresponding strain measures are defined. The *Euler's elastica* [1] denotes a planar beam with no axial and shear strains so that the bending stresses couple, being proportional to the curvature, while the *Kirchoff's beam* [2] consists a spatial generalization of the former with the torsional stress couple being proportional to the torsional curvature. When some small axial strain is added the *Kirchoff-Love beam theory* [3] is being used to simulate the structure sufficiently. Due to the absence of shear strains at the centroid of each plane of the structure in all of these theories the cross-sections remain orthogonal to the centroidal axis of the beam. In contrast, the presence of shear strains introduces a change of the angle between a cross-section and the centroidal axis, so that the deformed configuration of a beam is defined by (i) *the deformed centroidal axis* and (ii) *the set of orientations of cross-sections with respect to their un-deformed positions*. Such a beam, in which the fields of lateral displacements and rotations are considered as independent, is generally referred as the *Timoshenko beam* [4].

Although the Euler equation consists good representation of the vibrational behaviour of a slender beam at lower aspect ratios the Timoshenko theory, involving shear and rotary inertia effects, provides a better description. But this improved representation has only a limited range of applications for continuous systems, such as frame models, as the structure deviates from its fundamental beam properties.

These deviations from the ideal behaviour are investigated in this work by means of finite elements and, indeed, by representing the cross section of the continuous system as an assembly of in-plane stress rectangular elements. The authors have recently suggested [5] that for those cases, where shear effects become important, a fully conforming finite element could become necessary to achieve reliable results.

Along these lines a new fully conforming 32dof rectangular finite element, which allows for the shear effects to be simulated more reliably at the corners of the portal frame structure, was derived. Conforming, non-conforming and 1D beam element results were compared for various aspect ratios. The relevant computational algorithms have been developed by using MATLAB computational environment for a mild steel structure ($E = 200 \times 10^9 \text{ N/m}^2$, $\rho = 7860 \text{ kg/m}^3$, $\nu = 0.3$). The model consists an example for those cases where beams meet at right angles so that the transverse forces in one member interact

with the extensional forces of the adjoining structure. This is a situation with wide general importance in structural dynamics, ship building and in the supporting structures for large rotating machines.

LITERATURE REVIEW

The problem of flexural vibrations of frames and particularly that of finding their fundamental natural frequency is of primary importance in engineering design practice. As expected, there has been extensive research into the vibration of such systems in many different configurations and complexities. The majority of published work has been in the area of what may be described as closed frames [6].

Some representative examples include the Rayleigh-Ritz treatment of a portal frame under support conditions that range from clamped or pinned [6,7,8] to elastically supported. The latter is due to Filipitch et.al. [9], in case of symmetric vibrations, and to Laura and Valegra de Greco [10], in the case of antisymmetric dynamics. These cases have also been treated by using a more analytical approach by Filipitch and Laura [11]. Portal frames with cross bracing including axial deformation in the members were investigated by Chang et.al. [12], while Mottershead et.al. [13] have reported on the experimental identification of portal frame dynamics. More recently, Lee and Ng [14] have used the Rayleigh -Ritz method to treat portal frames, H frames and T frames. Clough and Penzien [15] include a two member closed frame as an example. Alexandropoulos et.al. [16] analysed the free vibration of a closed two bar frame carrying a concentrated mass capturing the dynamic couplings of the system precisely.

It is widely recognized that the traditional Bernoulli-Euler theory for beam vibration leads to erroneous results for cases of a large ratio of radius of gyration of cross-section to length. Hence, it is proposed that the errors may be corrected by including the effects of rotary inertia and shear deformation of beams. It is true that frame systems behave in a slightly different manner due to the interaction between the transverse forces of one member to the extensional forces of the span. Thus, the effects of the mass of the joints, the inertia properties and slenderness ratios become important parameters for the accurate identification of the fundamental frequency of the system.

In treating the problem a usual simplified approach is to assume that the frame girders are infinitely rigid (very rigid as compared to the column's rigidities). Another method is to transform the structure into an equivalent lumped parameter system. However, replacing the mass of the columns by lumped masses at their ends and neglecting the flexibility of the girders leads to serious errors in identifying the fundamental frequency [17]. In considering the effects of longitudinal vibration on the lateral vibration eigenfrequencies the mass of the portal frame joint as well as the shear effects have to be considered.

The present investigation suggests a more unified approach to such problems. The use of a fully conforming, 8dof finite element of bi-cubic nature, which allows for the shear effects to be simulated sufficiently at the corners of the portal frame structure, could suggest an alternative to the existing analytical solutions. The validation of the model was achieved by comparing the one and two-dimensional finite element idealisations. The important aspects related to this process are explained in the following paragraphs.

ONE DIMENSIONAL FINITE ELEMENT SIMULATIONS

A considerable number of Timoshenko beam finite elements for use in vibration problems has been described in literature. In a critical review of many of those they may be classified as simple, having two degrees of freedom at each of two end nodes, or complex, with either additional degrees of freedom or nodal points which improve their accuracy. However, if an inappropriate complex element is chosen, its accuracy may be proved to be poor. Furthermore, the additional degrees of freedom at the end nodes may introduce significant complications when used in structures (such as frames) with elements joining at arbitrary angles and changes of beam cross-section [18]. Thus, for the purposes of this project the Przemieniencki form of the typical McCalley Timoshenko beam element has been adopted [19]. This is a 2-node, 4dof (one transverse displacement and one rotation per node) element which has been widely accepted in literature.

Three significant factors namely (i) the mass distribution, (ii) the shear distortion of the joints and (iii) the shear coefficient for the rigid structure should be considered in the 1D simulations. The first one is associated with the design and manufacturing of the structure and it should be realistically justified when comparing the 1D rigid frame to the 2D planar frame finite element model. The *shear distortion* of the joints is measure of the realistic representation of the distortion angles at the frame corners. Physically frames are not rigid in the sense that a bending moment is transmitted at the corners of the structure. The shear distortion causes a discrepancy between the angles of rotation of the two beam ends, thus failing to fulfil the assumption of a unique value of nodal rotation. To a first approximation the magnitude of the discrepancy in the angles is equal to the overall mean value of shear strain at the web region, γ_w . If the beams are relatively short the joint flexibility arising from shear distortion contributes significantly to the overall flexibility of the frame, and must be accounted for in order to obtain accurate values of bending moments, especially at the vicinity of the joints. For the simple, unbracketed structure examined an insertion of a very stiff rotational spring connecting the two beams could provide a linear elastic moment resisting any increase or decrease in the angle of the joint. The spring is not an 'element' in the usual sense because it has no physical size, but it does connect two independent degrees of freedom (θ_1, θ_2) and it supplies rotational stiffness between them (see fig.1). It therefore may be incorporated in the 1D finite element model by means of a 2×2 stiffness



Fig.1 Representation of (i) joint shear deformation by an elastic rotational spring (ii) inner web region of a joint.

matrix having the same form of that of a linear spring $k = k_j \begin{bmatrix} 1 & -1 \\ -1 & 1 \end{bmatrix}$, where k_j is the spring stiffness of the joint defined as the net total moment acting on the joint divided by the resulting shear angle.

Although the exact distribution shear strain would depend on the local geometry an approximate qualitative estimate of the joint stiffness on the basis of the mean value of shear stress within the joint region could be obtained. Milchert [21] has shown that for a joint subject to applied moments M_v , M_j the joint stiffness is given by $k_j = \varphi \frac{Gt_w h_i h_j}{\alpha_w + \frac{1}{\alpha_w}}$, where $\alpha_w = h_i/h_j$ and φ is an empirically derived factor

based upon the boundary conditions (e.g. bending moments) applied upon the structure. For the case examined optimisation of the k_j was not possible. This is a weak point of the 1D flexible simulation, which may be overcome by means of the 2D planar finite element analysis. Comparison, however, of the variation of natural frequencies of the 1D system for Mindlin torsional stiffness of $\varphi=1$ consists a clear indication that the fundamental natural frequency of the system is realistically lower than this given by 1D rigid Timoshenko simulation (see table 1). Joint flexibility, however, due to shear is a separate and distinct phenomenon from bending flexibility (or its inverse namely bending rigidity). The selection of an appropriate dimensionless k factor, however, is not a straightforward matter. According to the commonly accepted definition, k is the ratio of the average shear strain on a section to the shear strain at the centroid. For beams of rectangular cross-section Cowper [22] suggests that $k = 10(1+\nu)/(12+11\nu)$.

Mode no.	Mindlin k , with $\varphi=1$	Rigid structure
Mode 1	7.30	7.31
Mode 2	28.00	28.03
Mode 3	45.44	45.54
Mode 4	47.01	47.15

Table 1. 1D flexible versus 1D rigid portal frame idealisation (Material: mild steel, $L/t = 1:10$).

This expression results from direct integration of the mathematical formulae describing the three-dimensional elasticity theory. The nature of the approximation, regarding the shear stress, suggests that such value would be satisfactory for static and long wavelength, low frequency deformations of beams. Indeed a comparison to the k values suggested by Mindlin and Goodman give an indication of the bandwidth of variation of their effective values with frequency (see table 2).

Source	k
Mindlin	0.822
Goodman	0.870
Cowper	0.85

Table 2. Shear coefficient alternatives for a solid beam of rectangular cross section (Mild steel, $E = 200 \times 10^9 \text{ N/m}^2$, $\rho = 7860 \text{ kg/m}^3$, $\nu = 0.3$)[22].

Whilst the value proposed by Mindlin is appropriate for small effect vibrations, Goodman's factor could be considered as more appropriate for frame structures in the sense that it provides more reliable high spectrum eigen-frequencies. In fact the deviations from Timoshenko's equations for such a continuous system may suggest a small arbitrarily optimised increase of k so as to simulate more accurately the shear effects (see table 2).

Shear factor	$k = 0.822$	$k = 0.85$	$k = 0.87$	$k = 0.89$
	Mindlin	Cowper	Goodman	arbitrary
Mode 1	7.30	7.31	7.31	7.31
Mode 2	28.00	28.02	28.03	28.04
Mode 3	45.44	45.50	45.54	45.58
Mode 4	47.05	47.10	47.15	47.20

Table 3. Effects on natural frequencies (Hz) with increasing shear coefficient. Mild steel rigid portal frame of $L/t = 10:1$.

FOUR NODED RECTANGULAR FINITE ELEMENTS

Initial studies were made using the standard in-plane element used in many FE packages. This allows for a linear displacement in each of the two directions and consequently has a total of 8 degrees of freedom. Although this simple rectangular element is economic and subject to simple mathematical manipulations, numerical analysis has proved [23] that it is not accurate even for the dynamic approximation of a simple cantilevered beam structure. For comparisons with beam elements having cubic displacement function this is not surprising. Further study was performed by deriving an element similar to that proposed by Schmidt, Bogner & Fox which has been proved to give results with excellent convergence rate, for bending analysis [24]. The element has six

degrees of freedom per node, which are distributed in a form of a bi-cubic field with six nodal degrees of freedom namely $u, v, \frac{\partial u}{\partial x}, \frac{\partial u}{\partial y}, \frac{\partial v}{\partial x}, \frac{\partial v}{\partial y}$ and displacement model in the form of an *incomplete* fourth order polynomial function as shown below:

$$u = A_0 + xA_1 + yA_2 + \dots + y^3xA_{11}$$

$$v = A_{12} + xA_{13} + yA_{14} + \dots + y^3xA_{23}$$

After evaluating the displacement differentials at each of the nodal points it was customary to establish the 24 by 24 displacement field matrix and hence formulate the stiffness and mass effects of the element by means of energy differentials.

In solving a structural problem whatever the type of structure, loading or material three separate arguments namely equilibrium, compatibility and stress-strain law need to be deployed (see fig.2).

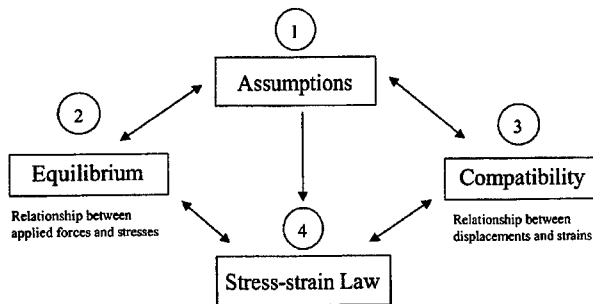


Fig.2 Fundamental properties used in the derivation of an FEA model

Along these lines Lees and Hirdaris [5] have recently demonstrated that for frame structures the Schmidt, Bogner & Fox *non-conforming* finite element is inadequate. The absence of the following highlighted higher order polynomial terms in the derivation of this element become significant.

$$\begin{array}{ccccccc}
 & & & & 1 & & \\
 & & & & x & & y \\
 & & x^2 & & xy & & y^2 \\
 x^3 & & x^2y & & xy^2 & & y^3 \\
 & x^3y & & x^2y^2 & & xy^3 & \\
 & & x^3y^2 & & x^2y^3 & & \\
 & & & x^3y^3 & & &
 \end{array}$$

Hence, for frame models the bi-cubic variation in strain along each of the structures' sides is affected while the continuity of slope conditions is violated. A solution to the problem could be given by means of a fully conforming finite element having 8dof of freedom per node namely $u, v, \frac{\partial u}{\partial x}, \frac{\partial u}{\partial y}, \frac{\partial v}{\partial x}, \frac{\partial v}{\partial y}, \frac{\partial^2 u}{\partial x \partial y}, \frac{\partial^2 v}{\partial x \partial y}$. The displacement field models in this case become:

$$u(x, y) = A_0 + xA_1 + yA_2 + x^2A_3 + \dots + x^3y^3A_{15}$$

$$v(x, y) = A_{16} + xA_{17} + yA_{18} + x^2A_{19} + \dots + x^3y^3A_{31}$$

In this case the second order partial differentials are believed to account for the distortion at the corners of the frame model especially at lower aspect ratios whilst the convergence and continuity criteria in C^0 space are not violated.

In both cases the mass and the stiffness effects of the structure were calculated under plain stress conditions by means of energy integrals and MATHEMATICA software program. The elements of the stiffness and mass matrices were expressed as functions of the dimensions of the rectangular element (a, b), Young's modulus (E) and Poisson's ratio (ν) and are not included in this report due to length and complexity. Using MATLAB the process was completed. In applying the boundary conditions it was necessary to reassure that the shape functions of the model behave adequately at the clamped edges. In this sense $u, v, \frac{\partial u}{\partial y}, \frac{\partial v}{\partial x}, \frac{\partial^2 v}{\partial x \partial y}$ dof were constrained wherever appropriate at the clamped edges of the structure.

In all the following work, the simple Euler element is referred as R1, the Timoshenko rigid beam element simulation as R2, the Timoshenko 1D flexible finite element idealization as R2*, Schmidt, Bogner & Fox plate representation is termed R3 and the Hirdaris-Lees 32dof conforming element as R4.

NUMERICAL ANALYSIS

Initial studies for the case of a free-free beam of $L/t = 10:1$ and solid cross-section have led to the conclusion that the 2D conforming finite simulation provides lower results than the non-conforming idealisation as well as Timoshenko's theory (see table 4). Considering that these deviations from the Timoshenko theory should become more significant due to shear distortion effects in portal frame analysis R4 approximation could be realistic.

In comparing the results the two dimensional approximation was assumed to form the basis of the overall numerical interpretation, mainly because of the fact that it is much more realistic than the 1D rigid-type simulation which is becoming rather weak at lower aspect ratios (L/t).

<i>Element type</i>	<i>R1</i>	<i>R2</i>	<i>R3</i>	<i>R4</i>
Rigid modes	0,0	0,0	0,0,0	0,0,0
Mode 1	52.05	50.31	50.30	50.30
Mode 2	143.52	131.31	131.04	131.03
Mode 3	281.54	241.41	239.52	239.43
Mode 4	466.08	373.38	253.09	253.09

Table 4. Comparison between the 1D and 2D simulation for a uniform free-free beam structure of aspect ratio $L/t = 10:1$ (frequencies in Hz).

The torsional spring flexible 1D idealisation was used as a reference point in justifying that, depending on the adjustment of a suitable shear strain factor, lower natural frequencies could be achieved even when Timoshenko beam models are being used. As the angle of distortion is increasing the effects of rotary inertia and shear deformation could be approximated in a better way by means of a two dimensional mesh providing more realistic projections towards the expected values.

Before proceeding to the actual comparison between the one and two dimensional finite element idealizations it is useful to note that as the number of elements in the discretized structure is increasing the level of approximation is improving, a fact necessary for the validity of the 2D finite element analysis of the structure. In demonstrating this effect two alternative mesh types were used. In the crude one each beam was assumed to have $(L \text{ by } 1) \times (L \text{ by } 1) \times (L \text{ by } 1)$ number of elements. In the refined mesh model the number of elements was doubled for each beam giving $(L \text{ by } 2) \times (L \text{ by } 2) \times (L \text{ by } 2)$ discretization level. Hence four rectangular elements were used to idealize the corners of the structure and the shear strain results were simulated in a more precise manner. For the purposes of the 1D simulation a constant discretization level of the order of $(L+0.5) \times L \times (L+0.5)$ was used mainly for reference purposes (see table 5).

<i>Mode no.</i>	<i>R4 crude model</i> (32 elem., 520 d.o.f.)	<i>R4 refined</i> (56 elem., 696 d.o.f.)
Mode 1	8.6	8.45
Mode 2	33.21	32.91
Mode 3	52.64	51.88
Mode 4	58.81	57.81

Table 5. The effects of Mesh refinement for a mild steel portal frame of $L/t = 10:1$ (all frequencies in Hz).

It is reasonable to suppose that the comparison between the one and two-dimensional approximations can be valid if the two-dimensional eigenfrequencies are compared to the one-dimensional results obtained when

the centerline of the frame is considered (see fig. 3). For instance, in order to simulate successfully a symmetrical portal frame with ratio $L/t = 10:1$ the one-dimensional approximation was based upon a structure with $L = 9.5$, $t = 1$ while the horizontal member corresponding to beam 2 was of length 8. Mass correction factors of the order of $0.5\rho/(L-0.5)$ and $\rho/(1-L)$ (since $A = 1 \text{ m}^2$) were implemented in order to account for the mass distribution along the legs and span of the frame respectively. Shear factors of the order of 0.87, as suggested by Goodwin, and 0.89 as it could be arbitrarily suggested were used (see table 6).

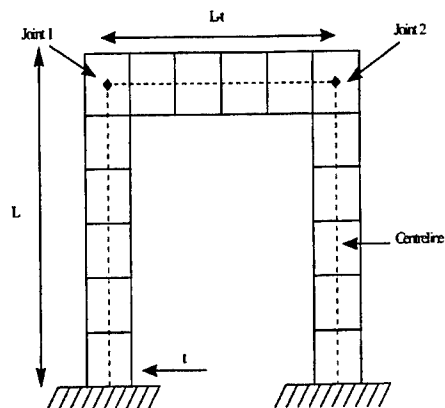


Fig. 3. 1D vs 2D portal frame FE simulation

Aspect ratio (L/t)	Mode no.	R1	R2 (Goodwin)	R2 (arbitrary)	R3	R4
10:1	1	8.58	8.44	8.45	8.56	8.45
	2	34.55	33.47	33.55	33.26	32.91
	3	53.09	50.19	50.41	52.40	51.88
	4	57.23	53.63	53.93	57.98	57.81
5:1	1	39.91	37.13	37.36	38.11	37.09
	2	154.31	138.08	139.28	137.27	133.59
	3	205.20	182.79	184.55	200.84	188.92
	4	227.93	190.11	192.78	206.04	197.50
3:1	1	136.31	112.24	113.87	118.93	108.11
	2	390.89	359.61	365.66	351.74	303.47
	3	461.27	392.07	394.94	403.97	347.64
	4	510.80	425.65	429.33	446.72	401.55

Table 6. Comparison between the 1D and 2D simulation for a portal frame structure over a variety of aspect ratios (all frequencies in Hz).

As expected, the effects of rotary inertia and shear deformation become more important from lower aspect ratios. From table 6 it becomes apparent that R4 simulation approximates the fundamental frequency of the system (frequency at 1st mode of vibration) much better than the non-conforming R3 element. This effect becomes more apparent as the frame aspect ratio is decreasing and the effects of shear, particularly at the corners of the frame model become more significant. An arbitrary increase of the order of 0.02 of the Goodwin shear factor may lead to better results even for slender frame aspect ratios of the order of 10:1.

CONCLUSIONS

The dynamic behaviour of thick beam structures is not adequately described using either Euler or Timoshenko theory. Planar elements have been shown to give better and more realistic results. A suitable fully two-dimensional 32dof conforming element has been derived and the numerical results have been compared to 1D rigid and flexible frame simulations. The idealisation was proved to be particularly advantageous for thick beam structures although at higher discretisation levels the element could become slightly '*uneconomic*'. It was also suggested that care is needed in choosing the most appropriate shear factor in beam model representations. Since most problems of such nature are degree of freedom limited future work will be concentrated in comparing the present finite element model with alternative 2D plate elements having the same total number of degrees of freedom. The fact that most non-academic finite element practitioners may prefer, at the moment, to resolve such problems by means of 3D solid finite element idealisations is also acknowledged. Along these lines comparison of the Hirdaris-Lees 2D conforming idealisation over the commercial 3D solid models will be performed especially for the cases of lower aspect ratio. An experimental verification of the model will also be carried out.

ACKNOWLEDGEMENTS

Mr. Spyridon Hirdaris is pleased to acknowledge financial support from the European Union and the School of Engineering sciences of the University of Southampton. British Energy plc. and BNFL (Magnox Generation) jointly fund Professor Arthur Lees.

REFERENCES

- [1] Euler, L. (1744); Methodus inveniendi Lieas curvas maximi minimive proprietate gaudentes.; Additamentum I; De Curvis elasticis; In Opera Omnia (ed. C. Caratherodory); I-24 (1952); pp.231-297. Bern: Auctoritate et Impensis Societatis Scientiarum Naturalium Helveticae.
- [2] Kirchhoff, G. (1859); Uber des Gleichgewicht und die Bewegung einwa unedlich dunnen elastischen staves ; J. Reine. Angew. Math. (Grelle) ; Vol.56; pp.285-313.

-
- [3] Love, A.E.H (1944) ; The mathematical theory of elasticity. New York: Dover.
- [4] Timoshenko & Goodier (1975); Theory of elasticity;3rd edition ; Mc Graw Hill.
- [5] Lees, A.W. , Hirdaris, S.E. (1999); Models of beams and Frames; International modal analysis conference (IMAC99); Orlando (Florida)-USA.
- [6] Oguamanam D.C.D., Hansen, J.S., Heppler, G.R. (1998); Vibration of arbitrarily oriented two member open frames with tip mass; Journal of Sound and Vibration ; Vol. 107; pp. 652 – 669.
- [7] Rieger, N.F. and McCallion, H. (1965); The natural frequencies of portal frames – I; International Journal of Mechanical science; Vol. 7; pp.253-261.
- [8] Rieger, N.F. and McCallion, H. (1965); The natural frequencies of portal frames – II; International Journal of Mechanical science; Vol. 7; pp.263-276.
- [9] Filipitch, C.P., Valerga de Greco, B.H. and Laura, P.A.A. (1987); ; A note on the analysis of symmetric mode of vibrations of portal frames ; Journal of sound and vibration; Vol. 117, pp.198-201.
- [10] Laura, P.A.A and Valerga de Greco, B.H. (1987); In plane vibrations of frames carrying concentrated masses; Journal of sound and vibration; Vol. 117; pp.447-458.
- [11] Filipitch, C.P. and Laura, P.A.A. (1987); In plane vibrations of portal frames with end supports elastically restraint against rotation and translation; Journal of sound and vibration; Vol. 117; pp.467-474.
- [12] Chang, C.H., Wang, P.Y. and Lin Y.W. (1987); Vibration of X-braced portal frames; Journal of sound and vibration; Vol. 117; pp.233-248.
- [13] Mottershead, J.E., Tee T.K. and Foster C.D. (1990); An experiment to identify the structural dynamics of a portal frame ; Journal of Vibration and acoustics; Vol. 112; pp. 78-83.
- [14] Lee, H.P., and Ng, T.Y. (1994); In plane vibration of planar frame structures; Journal of sound and vibration ; Vol. 172; pp.420-427.
- [15] Clough, R.W. and Penzien, J. (1975); Dynamics of structures; New York: McGraw Hill.
- [16] Alexandropoulos, A., Michaliatsos, G. and Kounadis, K. (1986); The effect of longitudinal motion and other parameters on the bending eigenfrequencies of a simple frame; Journal of sound and vibration; Vol.106, pp.153-159.

[17] Rogers, G.L. (1959) ; An introduction to the dynamics of frame structures; New York: John Willey.

[18] Lees, A.W. and Thomas, D.L. (1982); A unified Timoshenko beam finite element; Journal of sound and vibration; Vol. 80; pp.355-366.

[19] Thomas, D.L., Wilson, J.M., Wilson, R.R. (1973); Timoshenko beam finite elements; Journal of sound and vibration; Vol.31(3),pp.315-330.

[20] Cowper, G.R. (1966); The shear coefficient in Timoshenko's beam theory; Transactions of the ASME; Journal of applied mechanics; Vol.33; pp.335-339.

[21] Ship structural design – An optimised rationally based approach (1992); The Society of Naval Architects and Marine engineers; SNAME publications, New York.

[22] D.J.Dawe,; Matrix and finite element displacement analysis of structures, 1st edition, Oxford Engineering Science Series, 1988.

[23] Schmit, L.A., Bogner, F.K., Fox, R.L (1968); Development and evaluation of energy search methods of non linear structural analysis; Air force dynamic laboratories, Patterson air force base Ohio; Report no. TR65/115.

A new multiple-layer finite element shell incorporating very thin damping layers: application to a multilayered cylindrical shell

C.Remillat - G.R. Tomlinson

Department of Mechanical and Process engineering
University of Sheffield
Sheffield S1 3JD, UK

R.Lewin

ROLLS-ROYCE plc
Derby DE24 8BJ, UK

Abstract

This paper is concerned with a multilayer finite shell element, which incorporates very thin layers of viscoelastic materials. The element is a conforming quadrilateral element with a variable number of nodal degrees of freedom, depending on the number of layers. Results are presented for a cylindrical shell, even though the formulation can handle general shapes. Two different examples are presented which show good agreement between the finite element calculus and experimental results.

1. INTRODUCTION

Shell type structures are well spread, in the aerospace industries for example, and therefore there have been a lot of effort put into their finite element modeling ([1, 2, 3, 4, 5]). To avoid fatigue failure due to vibrations in these components, one common practice is to apply damping coatings. The difficulty is then to achieve a good damping level without compromising the stiffness of the original structure. A good compromise can be obtained by using coatings made with very thin constrained layers of viscoelastic materials.

Modeling complex structures with embedded viscoelastic layers is not an easy task. Being much softer than elastic ones, the viscoelastic layers induce additional shearing in the structure. The damping is then directly related to the shearing energy in the damping layers.

Taking into account this phenomenon to predict dynamical behavior requires special care. Analytical expressions of the dynamic equations are extremely complicated, and can only be solved for special kinds of boundary conditions, and simple geometries. This is why finite element modeling is more convenient in most practical cases where the structure is geometrically complicated.

However, modeling damped structures using commercial codes is rather restricting. Complex mode calculation are generally not allowed, and there is no element dedicated to layered structures incorporating viscoelastic layers. The behavior of such structures is completely different from that of elastic layered structures, and so it is incorrect to use the layered finite element shells provided in these codes. It is necessary to employ 3D elements to properly model the viscoelastic layers effect. This leads to an increased number of degrees of freedom required to model the structure. When very thin layers of viscoelastic materials are involved, the meshing should be so refined that it is almost impossible to perform the analysis. Special elements are then required to accurately and efficiently handle the problem.

In this paper, a formulation for a multi-layered shell element is proposed. It is based on thin shell assumptions, and can incorporate several damping layers. The element is an extension of a previous work from Macé [6]. First the potential and kinetic energies in each layers are calculated based on the proposed kinematic assumptions. The problem is then discretized using conforming polynomials for each displacement. Where an exact equation for the reference surface of the shell exists, no geometrical discretization is involved. Two examples are finally given which compare the predicted and experimental behavior of a three-layered and a five-layered cylindrical shell.

2. GENERAL ASSUMPTIONS

The theoretical formulation is done in a classical way, by calculating the potential and kinetic energies in each layers. The main assumptions made are the following:

1. The multi-layer shell is a thin shell and therefore it is considered that
 - (a) one of the geometrical dimensions of the shell is much smaller than the other ones,
 - (b) the shell deflections are assumed to be small,
 - (c) the stress in the direction normal to the thin dimension is negligible,
 - (d) a line originally normal to the shell reference surface will remain normal to the undeformed reference surface.

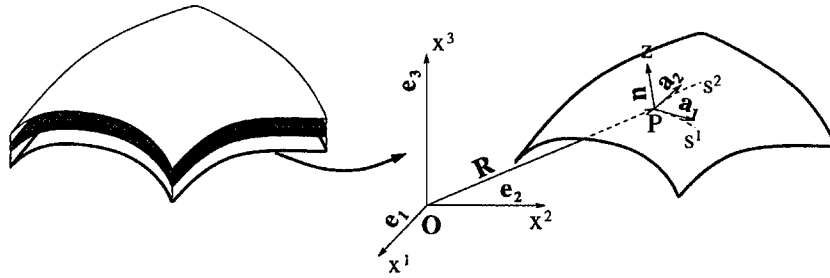


Figure 1: Shell reference surface and shell coordinates

2. There is no shearing in the elastic layers.
3. The thickness of the viscoelastic layers is nearly zero,

$$h_v \simeq 0$$

, so that each of these layers are represented by a sliding surface Σ_v

Assumption 1.(d) above implies that the displacement must be linear in the thickness coordinate. This means that the displacement of any point in the shell can be determined from a corresponding point on a reference surface. This reference surface can be chosen for convenience. It is usual to select the middle surface of the shell as the reference surface, but in our case it is simpler to just take one of the outer surfaces as the reference surface, as the studied shell is a multi-layered one (see Figure 1). Let the triplet (x^1, x^2, x^3) be the Cartesian coordinates related to the base vectors (e_1, e_2, e_3) , and (s^1, s^2, z) be the local or shell coordinates with respect to the base vectors of the reference surface a_1, a_2, n . The position vector R can be expressed by

$$\begin{aligned} R(x^1, x^2, x^3) &= \vec{OP} \\ &= x^i e_i \end{aligned} \quad (1)$$

in the Cartesian coordinate system, and by

$$\begin{aligned} R(s^1, s^2, z) &= r(s^1, s^2) + zn \\ &= s^\alpha a_\alpha + zn \end{aligned} \quad (2)$$

in the shell coordinate system, where the Einstein summation convention was used, and a_α and n are given by:

$$a_\alpha = \frac{\partial r}{\partial s^\alpha} \quad (3)$$

and

$$n = \frac{a_1 \wedge a_2}{\|a_1 \wedge a_2\|} \quad (4)$$

Similarly, the base vectors associated with a surface at a distance z from the reference surface are

$$\mathbf{g}_\alpha = \frac{\partial \mathbf{R}}{\partial s^\alpha} \quad (5)$$

and

$$\mathbf{g} = \mathbf{n} \quad (6)$$

The thin shell assumptions 1.(a)-(d) enables one to assume the following displacement function in each elastic layer i :

$$\begin{cases} U_\alpha^{(i)}(s^1, s^2, s^3) = u_\alpha^{(i)}(s^1, s^2) + s^3 \beta_\alpha^{(i)}(s^1, s^2) \\ U_3^{(i)}(s^1, s^2, s^3) = w(s^1, s^2) \end{cases} \quad (7)$$

Moreover, It follows from assumption 2. that:

$$\beta_\alpha^{(i)} = -\Phi_\alpha^{(i)} \quad (8)$$

$$= -[w_{,\alpha} + b_\alpha^{\beta(i)} u_\beta^{(i)}] \quad (9)$$

Assumption 1. (c) can be expressed as

$$\sigma_{33} = 0 \quad (10)$$

in the whole multi-layer shell.

Assumption 3. provides information on the displacement field in each viscoelastic layer. If layers i and $i + 2$ are elastic layers and layer $i + 1$ is a viscoelastic one, when making the transition from the elastic layer i to the elastic layer $i + 2$ the displacement field is tangentially discontinuous. Following Macé's notation [6] this displacement jump is noted

$$[[U]]^{(i,i+2)} = U_\alpha^{(i+2)} - U_\alpha^{(i)} \quad (11)$$

Having clarified all the basic assumptions linked to the multi-layered shell element, one can now express the energy contribution in each layer, which is necessary to carry out a direct finite element formulation of the new element.

3. ENERGY CONTRIBUTION OF THE ELASTIC LAYERS

The elastic layers will contribute in two ways in the total energy of the shell

- with a potential energy E_{pe}
- with a kinetic energy E_{ke}

The potential energy can be expressed as follows:

$$E_{pe} = \frac{1}{2} \int_{\Omega_e} \sigma^{\alpha\beta} \varepsilon_{\alpha\beta} d\Omega_e \quad (12)$$

with Ω_e representing the volume of the layer and $d\Omega_e$ the elementary volume such that

$$d\Omega = \sqrt{\det [\underline{g}]} ds^1 ds^2 dz \quad (13)$$

$$\simeq \sqrt{\det [\underline{a}]} ds^1 ds^2 dz \quad (14)$$

$$(15)$$

\underline{a} is the metric tensor of the reference surface defined by

$$a_{\alpha\beta} = \mathbf{a}_\alpha \cdot \mathbf{a}_\beta \quad (16)$$

$\underline{\varepsilon}$ are the linearized deformations of the shell in the curvilinear coordinate system and can be expressed as (see [7], [8])

$$\begin{cases} \varepsilon_{\alpha\beta} = \gamma_{\alpha\beta} + s^3 \chi_{\alpha\beta} \\ \varepsilon_{3\beta} = \frac{1}{2} [\Phi_\alpha + \beta_\alpha] \end{cases} \quad (17)$$

where $\gamma_{\alpha\beta}$ are the linearized deformations of the shell reference surface, which are given by

$$\chi_{\alpha\beta} = -[w_{;\alpha\beta} + b_{\beta;\alpha}^\lambda u_\lambda + b_{\beta}^\lambda u_{\lambda;\alpha} + b_\alpha^\lambda u_{\lambda;\beta} - b_\alpha^\lambda b_{\lambda\beta} w] \quad (18)$$

\underline{b} is the curvature tensor given by

$$\begin{aligned} b_{\alpha\beta} &= \mathbf{n} \cdot \mathbf{a}_{\alpha,\beta} \\ &= -\mathbf{a}_\alpha \cdot \mathbf{n}_{,\beta} \end{aligned} \quad (19)$$

The stress-strain relations can be written as

$$\sigma^{\lambda\mu} = c^{\lambda\mu\alpha\beta} \varepsilon_{\alpha\beta} \quad (20)$$

where all the tensors are expressed in the curvilinear coordinate system. When the material is isotropic, the transformation law for the elasticity tensor between the curvilinear and Cartesian system takes the following form

$$c^{\lambda\mu\alpha\beta} = \frac{E\nu}{(1+\nu)(1-2\nu)} g^{\lambda\mu} g^{\alpha\beta} + G(g^{\lambda\alpha} g^{\mu\beta} + g^{\lambda\beta} g^{\mu\alpha}) \quad (21)$$

The kinetic energy in an elastic layer is given by

$$E_{ke} = \frac{1}{2} \int_{\Omega_e} g_{\alpha\beta} \dot{u}^\alpha \dot{u}^\beta d\Omega_e \quad (22)$$

so that in harmonic condition, it simplifies as

$$E_{ke} = -\frac{\omega^2}{2} \int_{\Omega_e} g_{\alpha\beta} u^\alpha u^\beta d\Omega_e \quad (23)$$

4. ENERGY CONTRIBUTION OF THE VISCOELASTIC LAYERS

According to assumption 3., the viscoelastic layer thickness is considered to be zero. This means that their only contribution in the energy balance will be in the potential energy. Equation 11 expresses the fact that the tangential component of the displacement vector is discontinuous when passing through a viscoelastic layer. On the other hand, the stress vector is continuous through Σ_v

$$[[\sigma]] \cdot \mathbf{n} = 0 \quad (24)$$

where \cdot stands for the contracted tensorial product. The stress vector on the surface Σ_v can be expressed by

$$\sigma = \sigma^{3\alpha} g_i \quad \alpha = 1, 2 \quad (25)$$

If the strains are assumed to be constant inside the viscoelastic, then

$$\varepsilon_{3\alpha} = \frac{[[U_i]]}{h_v} \quad \alpha = 1, 2 \quad (26)$$

with h_v the thickness of the viscoelastic layer. In the harmonic state, the components of the tangential stress on Σ_v can be expressed as

$$\sigma^{3\alpha} = G_v^* [[U_\alpha]] \quad \alpha = 1, 2 \quad (27)$$

with G_v^* the complex shear modulus of the viscoelastic material. The contribution of the viscoelastic layer to the total elastic energy can then be written as

$$E_{pv} = \int_{\Sigma_v} [[U]] \cdot \sigma \cdot \mathbf{n} d\Sigma_v \quad (28)$$

$$= \int_{\Sigma_v} \sigma^{3\alpha} [[U_\alpha]] \quad \alpha = 1, 2 \quad (29)$$

5. DISCRETIZATION OF THE PROBLEM

Using the previous results, the multi-layered shell element can be directly formulated using the principle of total energy for example

$$\delta \Pi = 0 \quad (30)$$

where Π is the total potential energy

$$\Pi = \sum_{\text{elastic layers}} E_{pe} + \sum_{\text{viscoelastic elastic layers}} E_{pv} + \sum_{\text{elastic layers}} E_{ke} \quad (31)$$

Π is then approximated using relevant piecewise continuous interpolation functions for the displacement field and the geometry if needed. In this paper, it is assumed to simplify the study that the equation of the reference surface is known exactly, so that it is only necessary to approximate the displacement components. Therefore, the discrete problem will be conforming for the displacement [9] if C^0 interpolation functions are chosen for the in-plane displacements and C^1 interpolation functions are chosen for the transverse displacement. To fulfill the previous conditions and to ensure that the same degree of accuracy for all the displacement components, the displacement field is approximated using the following relationship

$$\begin{cases} \tilde{u}_1 = N^t \bar{u}_1 \\ \tilde{u}_2 = N^t \bar{u}_2 \\ \tilde{w} = N^t \bar{w} \end{cases} \quad (32)$$

where N is the vector of interpolation functions, and $\bar{u}_1, \bar{u}_2, \bar{w}$ are the vectors of degrees of freedom related to each displacement component. To fulfill the continuity condition, the the two dimensional interpolation functions are the tensorial product of one dimensional Hermite polynomials given by

$$\begin{cases} H_{11}(s_i) = 1 - 3 \left\{ \frac{s_i}{l} \right\}^2 + 2 \left\{ \frac{s_i}{l} \right\}^3 \\ H_{12}(s_i) = 3 \left\{ \frac{s_i}{l} \right\}^2 - 2 \left\{ \frac{s_i}{l} \right\}^3 \\ H_{21}(s_i) = s_i - 2 \left\{ \frac{s_i^2}{l} \right\} + \frac{x^3}{l^2} \\ H_{22}(s_i) = -\frac{s_i^2}{l} + \frac{s_i^3}{l^2} \end{cases} \quad (33)$$

The corresponding finite element is then a quadrilateral with four nodes in the local coordinates. Each node has twelve degrees of freedom (four per displacement component). These degrees of freedom are the displacement component, its first derivatives and cross derivative with respect to the local coordinate system.

6. EXPERIMENTAL VALIDATION

Experimental work was carried out in order to validate the previous multi-layer shell element. Three different specimens were tested:

- an undamped single layer cylindrical shell
- a sandwich cylindrical shell
- a five layered cylindrical shell (two viscoelastic layers sandwiched between successive elastic layers)

All specimens share the following geometrical characteristics:

- length = 0.6 m
- radius of curvature = 0.132 m

All elastic layers are made of aluminium and 0.0015 m thick. All viscoelastic layers are made of a proprietary acrylic damping material ¹, and 0.000127 m thick. The stacking sequence for the multi-layer shells is aluminium-viscoelastic-aluminium and so on.

The experimental conditions are the following:

- the tested specimen is hung at point so that completely free boundary conditions are assumed
- a small accelerometer (B&K 4393) is attached at one point
- a roaming hammer is used to impact the specimen at different points

The figures 3, 4, 5 show the comparison between the calculated and experimental transfer functions at the same point. The accelerometer remaining in the same position at point 1 (see Figure 2) the specimen is impacted at point 2.

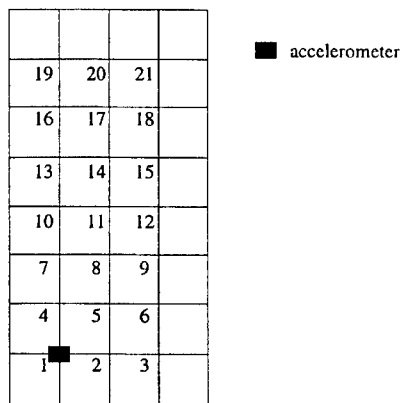


Figure 2: *Numbering convention for the experimental points*

The theoretical modeling has the same discretization as the experimental one (4x8 meshing).

For each specimen, a good agreement between theory and experiment is observed. One can notice that the damping introduced by the viscoelastic material is high, which is actually a good result with respect to the very small thickness of the damping layers. This is the reason why it was chosen to directly compare the transfer functions instead of the modal frequencies and damping factors. The high damping level

¹3M viscoelastic polymer 113

makes more difficult identification of the experimental values. In this particular case, the calculated average loss factor and stiffness reduction over the first five modes are respectively around 13% and 50%, which is very high in both cases. This is due to the fact that no attempt was made to optimize the structure at this point, as the main objective was to validate the proposed element. The damping material which was used has a shear modulus which varies between $2.8 \cdot 10^4 \text{ Pa}$ and $6.2 \cdot 10^5 \text{ Pa}$ in the frequency range of interest. A more reasonable stiffness reduction (around 20%) could be achieved by using a stiffer material (with an average shear modulus and loss factor over the frequency range of interest of respectively 10^6 Pa and 0.8) while keeping equivalent damping performance. It is worth noticing that the validation was carried out by comparing the transfer functions for each experimental point (20 points) and the results were equally good.

7. CONCLUSION

A new multi-layer finite element shell was presented. It is based on a real thin shell assumption and incorporates very thin layers of viscoelastic materials. The formulation is made in the shell coordinate system using the tensor theory. This feature enables one to only interpolate the displacement functions in the case when the equation of the reference surface is known exactly. Conforming interpolation functions were chosen to ensure a monotonous convergence of the element.

The element was experimentally validated for cylindrical shaped specimens, for various number of layers. The comparison between theory and experiment was satisfactory. The experimental tests also revealed that a very high level of damping could be achieved even using damping layers which were very thin.

Future work will be dedicated to the formulation of a geometrically conforming element for a general shaped shell.

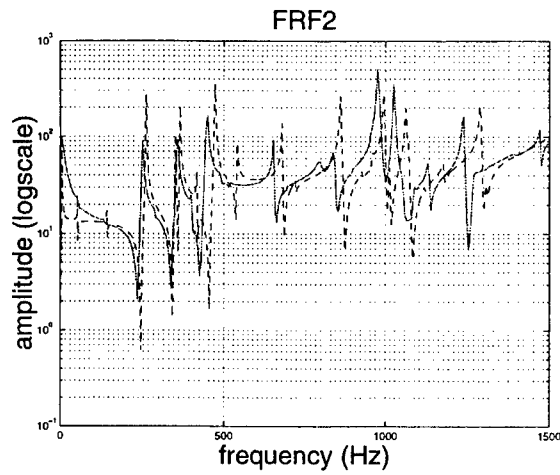


Figure 3: Theoretical — — and experimental — transfer function at point 2 for an undamped aluminium shell

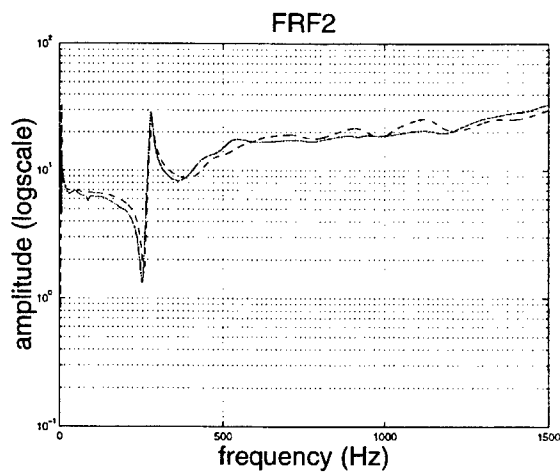


Figure 4: Theoretical — — and experimental — transfer function at point 2 for a three-layered aluminium shell

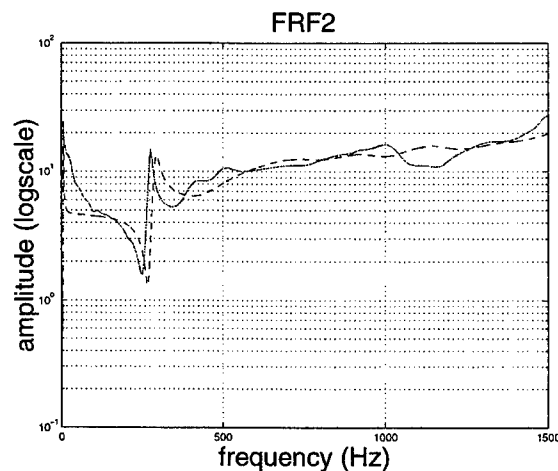


Figure 5: Theoretical — — and experimental — transfer function at point 2 for a five-layered aluminium shell

References

- [1] S. Ahmad, B. M. Irons, and O. C. Zienkiewicz. Analysis of thick and thin shell structures by curved finite element plates and shells. *International Journal for Numerical Methods in Engineering*, 2:pp. 419–451, 1970.
- [2] G. R. Cowper, G. M. Lindberg, and M. D. Olson. A shallow shell finite element of triangular shape. *International Journal of Solids and Structures*, 6:pp. 1133–1156, 1970.
- [3] G. Dupuis and J.-J. Göel. A curved finite element for thin elastic shells. *International Journal of Solids and Structures*, 6:1413–1428, 1970.
- [4] D. J. Dawe. High-order triangular finite element for shell analysis. *International Journal of Solids and Structures*, 11:1097–1010, 1975.
- [5] E. P. Popov and P. Sharifi. A refined curved element for thin shells of revolution. *International Journal for Numerical Methods in Engineering*, 3:495–508, 1971.
- [6] M. Macé. *Modlisation de structures amorties par film viscoélastique*. PhD thesis, Université Pierre et Maris Curie de Paris, 1991.
- [7] K. Washizu. *Variational methods in elasticity and plasticity*. Pergamon Press, 1982.
- [8] C. L. Dym. *Introduction to the theory of shells*. Pergamon Press, 1974.

-
- [9] P. G. Ciarlet. *The mathematics of finite elements and applications II*. Academic Press, 1974.

PREDICTING THE DYNAMIC STRESS INTENSITY FACTOR FOR A CIRCUMFERENTIAL CRACK IN A HOLLOW CYLINDER USING FRACTAL FINITE ELEMENT METHOD

D.K.L. Tsang, S.O. Oyadiji and A.Y.T. Leung

The Manchester School of Engineering, University of Manchester, Oxford Road, Manchester, M13 9PL, United Kingdom.

Abstract

The fractal finite element method predicts very accurate stress intensity factor (SIF). The method has been developed to study all kinds of 2D cracks and penny shaped 3D cracks. In this paper we extend our previous study to include dynamic effects on the stress intensity factor. We present the calculation of dynamic mode I stress intensity factors for complete circumferential cracks on the inner surface of a hollow cylinder subjected to time dependent axisymmetric loading. The effect of damping is also presented. The precise time integration scheme is used to perform the time integration. Our numerical results show that the fractal finite element method together with the precise time step integration method give very accurate dynamic SIF. The analysis is important in gun barrel design and in the design of pressure vessels and piping systems subjected to dynamic loading.

1. Introduction

It has been shown that the fractal finite element method [1, 2, 3, 4, 5 and 6] is an efficient and accurate technique for determining the stress intensity factor for various crack problems. The method divides a cracked elastic body into near field (singular) and far field (regular) regions. The far field is modelled by conventional finite elements. Within the near field, an extremely large number of finite elements is generated by self-similarity process to model the crack tip singular behaviour. These results in a large number of nodal displacements, which are, reduced effectively to a small set of global variables, with stress intensity factors as primary unknowns by the second level global interpolating transformation. As the global transformation can be performed at element level, the order of matrices involved is very small. Consequently, computer storage and solution times are reduced significantly. Furthermore, the stress intensity factors can be determined directly from the global variables without the need for any post-processing.

The response of a cracked solid which is subjected to rapidly applied loading is significantly affected by inertia effects. The influence of the loads is transferred to the crack by means of stress waves through the material. To understand whether or not a crack will propagate due to the stress wave loading, it is necessary to determine the transient driving force acting on the

crack. By using a suitable time integration method, it is possible to use fractal finite element in dynamic SIF calculation.

There are many time integration methods in the literature. They can be classified into two categories: explicit and implicit integration schemes. The explicit integration scheme is very efficient for one time step computation. However, to ensure stability of integration a very small time step size must be selected. The implicit integration scheme can be made unconditionally stable by proper selection of the integration parameters, such that a large value of the time step size can be selected. However, because the time step is larger, the vibration components with higher frequencies will be distorted after several integration steps. Therefore the system invariants, such as system energy or momentum in a conservation system, cannot be maintained.

The time integration scheme we used in this paper is a semi-analytical method by Zhong [7]: precise time step integration method. The method can give very accurate results, which usually coincide with exact solutions to several significant figures. The method is almost independent of the time step size for a wide range of step sizes. Also the main computations are all matrix multiplication and so can be efficiently executed on parallel computers.

A 4 cm long hollow cylinder, which represents a 0.22 gun barrel with an internal circumferential crack depth a is considered. The outer and inner diameter of the hollow cylinder are 1.27 cm and 0.56 cm respectively. Fractal finite element discretization is used for the space coordinates. The resulting ordinary differential equations are solved by the precise time step integration method. The effect of damping is included in the analysis.

2. The Fractal Finite Element Method

In the fractal finite element methods, the overall cracked problem is divided into near field and far field regions as shown in Figure 1. The curve that delineates the two regions is denoted as Γ_0 . The far field is modelled by conventional finite element method. In the near field, infinite numbers of layers of conventional finite element are generated layer by layer in a self-similar manner with a scaling ratio ϕ . It is convenient to take the crack tip as a centre of similarity. Assuming that ϕ lies between 0 and 1, that is $0 < \phi < 1$, an infinite set $\{\Gamma_1, \Gamma_2, \dots\}$ of curves similar to the shape of Γ_0 with proportionality constants $\{\phi^1, \phi^2, \dots\}$ are generated inside the singular region. The region in between any two consecutive curves is called the n th layer. The nodes located on the curve Γ_0 are called the master nodes. A set of straight lines that emanate from the similarity centre is connected to the master nodes. Thus each layer is divided into a set of elements with a similar pattern. All the nodes inside the curve Γ_0 are called the slave nodes. The grading of mesh inside the singular region can be controlled by the proportionality constant $0 < \phi < 1$. Higher

values of ϕ will produce finer grade of mesh and vice versa. This procedure is used to generate a fractal mesh.

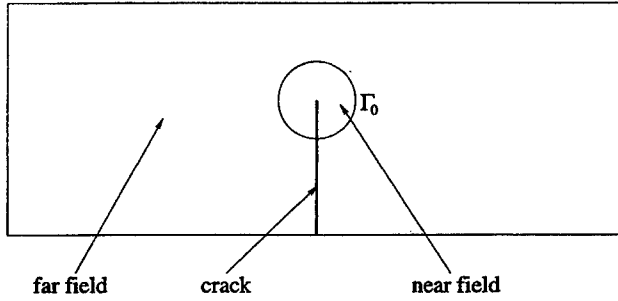


Figure 1: Far field and near field in a cracked material

Let r and z denote the radial and axial coordinates of a point respectively. Without loss of generality, a 6-noded triangular element is considered for axisymmetric stress analysis. The shape functions and the displacement function may be expressed in an isoparametric form as

$$x = \sum_{i=1}^6 N_i(\xi, \eta) x_i, \quad y = \sum_{i=1}^6 N_i(\xi, \eta) y_i \quad (1)$$

and

$$u = \sum_{i=1}^6 N_i(\xi, \eta) u_i, \quad v = \sum_{i=1}^6 N_i(\xi, \eta) v_i, \quad \mathbf{w} = \begin{pmatrix} u \\ v \end{pmatrix}, \quad (2)$$

where (x_i, y_i) and (u_i, v_i) are the nodal coordinates and the nodal displacements of an element respectively, \mathbf{w} is the displacement field and $N_i(\xi, \eta)$ are the shape functions. The resulting element stiffness equation is

$$\mathbf{K}\mathbf{w} = \mathbf{f}. \quad (3)$$

The associated stiffness matrix \mathbf{K} is calculated by

$$\mathbf{K} = \int \mathbf{B}^T \mathbf{D} \mathbf{B} dV, \quad (4)$$

where V is the volume of the element,

$$\mathbf{B} = (\mathbf{B}_1, \dots, \mathbf{B}_6), \quad \mathbf{B}_i = \begin{pmatrix} 0 & \frac{\partial N_i}{\partial z} \\ \frac{\partial N_i}{\partial r} & 0 \\ \frac{1}{r} N_i & 0 \\ \frac{\partial N_i}{\partial z} & \frac{\partial N_i}{\partial r} \end{pmatrix}, \quad i = 1, \dots, 6 \quad (5)$$

and

$$\mathbf{D} = \frac{E(1-\nu)}{(1+\nu)(1-2\nu)} \begin{bmatrix} 1 & \frac{\nu}{1-\nu} & \frac{\nu}{1-\nu} & 0 \\ \frac{\nu}{1-\nu} & 1 & \frac{\nu}{1-\nu} & 0 \\ \frac{\nu}{1-\nu} & \frac{\nu}{1-\nu} & 1 & 0 \\ 0 & 0 & 0 & \frac{1-2\nu}{2(1-\nu)} \end{bmatrix}, \quad (6)$$

where E and ν are Young's modulus and Poisson's ratio respectively.

The static equilibrium equation for regular region is

$$\begin{bmatrix} \mathbf{K}_{rr} & \mathbf{K}_{r0} \\ \mathbf{K}_{0r} & \mathbf{K}_{00} \end{bmatrix} \begin{Bmatrix} \mathbf{d}_r \\ \mathbf{d}_0 \end{Bmatrix} = \begin{Bmatrix} \mathbf{f}_r \\ \mathbf{f}_0 \end{Bmatrix}, \quad (7)$$

where \mathbf{d} and \mathbf{f} are displacements and force vector respectively. The subscript r and 0 represent the values in the regular region and on the boundary respectively. Similarly the static equilibrium equation of the layer n is

$$\begin{bmatrix} \mathbf{K}_{11}^n & \mathbf{K}_{12}^n \\ \mathbf{K}_{21}^n & \mathbf{K}_{22}^n \end{bmatrix} \begin{Bmatrix} \mathbf{d}_n \\ \mathbf{d}_{n+1} \end{Bmatrix} = \begin{Bmatrix} \mathbf{f}_n \\ \mathbf{f}_{n+1} \end{Bmatrix}. \quad (8)$$

The global static stiffness equation of the problem is

$$\begin{bmatrix} \mathbf{K}_{rr} & \mathbf{K}_{r0} & & & \\ \mathbf{K}_{0r} & \mathbf{K}_{00} + \mathbf{K}_{11}^1 & \mathbf{K}_{12}^1 & & \\ & \mathbf{K}_{21}^1 & \mathbf{K}_{22}^1 + \mathbf{K}_{11}^2 & \mathbf{K}_{12}^2 & \\ & & \ddots & \ddots & \ddots \\ & & & \mathbf{K}_{21}^\infty & \mathbf{K}_{22}^\infty \end{bmatrix} \begin{Bmatrix} \mathbf{d}_r \\ \mathbf{d}_0 \\ \mathbf{d}_1 \\ \vdots \\ \mathbf{d}_\infty \end{Bmatrix} = \begin{Bmatrix} \mathbf{f}_r \\ \mathbf{f}_0 \\ \mathbf{f}_1 \\ \vdots \\ \mathbf{f}_\infty \end{Bmatrix}. \quad (9)$$

Applying the transformation $\{\mathbf{d}_i\} = [\mathbf{T}_i]\{\mathbf{c}\}$, where $[\mathbf{T}_i]$ is evaluated from William's function and $\{\mathbf{c}\}$ is the vector of generalized coordinates to be determined, one has

$$\begin{bmatrix} \mathbf{K}_{rr} & \mathbf{K}_{r0} \\ \mathbf{K}_{0r} & \mathbf{K}_{00} + \mathbf{K}_{11}^1 & \mathbf{K}_{1s} \\ & \mathbf{K}_{s1} & \mathbf{K}_{ss} \end{bmatrix} \begin{Bmatrix} \mathbf{d}_r \\ \mathbf{d}_0 \\ \mathbf{c} \end{Bmatrix} = \begin{Bmatrix} \mathbf{f}_r \\ \mathbf{f}_0 \\ \mathbf{f} \end{Bmatrix}, \quad (10)$$

where $[\mathbf{K}_{1s}]^T = [\mathbf{K}_{s1}] = [\mathbf{K}_{21}][\mathbf{T}_0]$ and

$$\mathbf{K}_{ss} = \mathbf{T}_1^T \mathbf{K}_{22}^1 \mathbf{T}_1 + \sum_{k=2}^{\infty} (\mathbf{T}_k^T \mathbf{K}_{11}^k \mathbf{T}_k + \mathbf{T}_k^T \mathbf{K}_{12}^k \mathbf{T}_k + \mathbf{T}_k^T \mathbf{K}_{21}^k \mathbf{T}_k + \mathbf{T}_k^T \mathbf{K}_{22}^k \mathbf{T}_k) \quad (11)$$

Each entry of the last matrix is a function of the scaling factor ϕ . The unknowns now are \mathbf{d}_r and \mathbf{c} instead of \mathbf{d}_i , $i=1$ to ∞ . An additional advantage is that the SIFs are included in \mathbf{c} and no post-processing is required. Essentially, the original infinite matrices are compressed to a finite one by fractal transformation. The partially overlapped infinite layers have been replaced by completely overlapped finite layers.

In a fractal finite element, the nodal displacement \mathbf{w} is transformed to generalized co-ordinates

$$\mathbf{c} = \{a_0, a_1, \dots, b_0, b_1, \dots\}, \quad (12)$$

that is $\mathbf{w} = \mathbf{T}\mathbf{c}$, where \mathbf{T} is the transformation matrix. The static equilibrium equation can be transformed to

$$\mathbf{T}^T \mathbf{K} \mathbf{T} \mathbf{c} = \mathbf{T}^T \mathbf{f}. \quad (13)$$

After the transformation, the order of \mathbf{c} becomes much smaller than the original \mathbf{w} . Consequently, solving Equation (10) is much more efficient than solving Equation (9).

To perform a dynamic analysis of a bounded medium in the time domain, the mass matrix \mathbf{M} is required in addition to the static stiffness matrix \mathbf{K} . The analytical expression for the mass matrix is

$$\mathbf{M} = \int \mathbf{N}^T \rho \mathbf{N} dV. \quad (14)$$

The mass matrix is transformed using a procedure which is similar to that used for the stiffness matrix.

3. The Precise Time Step Integration Method

It is common practise when analysing an engineering structure under shock, gust or similar loading to perform a transient analysis to check its time history behaviour. The usual dynamic equation is

$$\mathbf{M} \frac{d^2 \mathbf{x}}{dt^2} + \mathbf{G} \frac{d\mathbf{x}}{dt} + \mathbf{K} \mathbf{x} = \mathbf{r}(t), \quad (15)$$

with the initial condition being the given vectors $\mathbf{x}(0)$ and $\dot{\mathbf{x}}(0)$, where \mathbf{M} , \mathbf{K} and \mathbf{G} are mass, stiffness and damping matrices respectively, \mathbf{x} is the displacement vector to be solved for, $\mathbf{r}(t)$ is the given external force vector and the dot means differentiation with respect to time, t . For time-invariant systems, that is ones for which \mathbf{M} , \mathbf{K} and \mathbf{G} are independent of t , the precise time integration method gives highly precise results, even when \mathbf{G} is a general damping matrix. The scheme does not give an analytical expression but its numerical results are highly precise. Numerical error is solely due to computer round-off error.

We define $\mathbf{D} = \mathbf{M}^{-1}$, $\mathbf{p} = \mathbf{M}\mathbf{x} + \frac{\mathbf{G}\mathbf{x}}{2}$, $\mathbf{A} = -\frac{\mathbf{M}^{-1}\mathbf{G}}{2}$, $\mathbf{B} = -\left(\mathbf{K} - \frac{\mathbf{G}\mathbf{M}^{-1}\mathbf{G}}{4}\right)$

and $\mathbf{C} = -\frac{\mathbf{G}\mathbf{M}^{-1}}{2}$. Then, Equation (15) can be rewritten as

$$\dot{\mathbf{v}} = \mathbf{H}\mathbf{v} + \mathbf{r}_1, \quad (16)$$

where $\mathbf{v} = \begin{pmatrix} \mathbf{x} \\ \mathbf{p} \end{pmatrix}$, $\mathbf{H} = \begin{bmatrix} \mathbf{A} & \mathbf{D} \\ \mathbf{B} & \mathbf{C} \end{bmatrix}$ and $\mathbf{r}_1 = \begin{bmatrix} \mathbf{0} \\ \mathbf{r} \end{bmatrix}$.

Equation (15) is inhomogeneous. From the theory of ordinary differential equations, the general solution of its homogeneous equation should be found first. The general solution can be given as

$$\mathbf{v} = \exp(\mathbf{H} \times t) \times \mathbf{v}_0, \quad (17)$$

where $\mathbf{v}_0 = \mathbf{v}(0)$ is the initial conditions. Now let the time step be τ . Then $\mathbf{v}(\tau) = \mathbf{S} \times \mathbf{v}_0$, where $\mathbf{S} = \exp(\mathbf{H} \times \tau)$. After finding the matrix \mathbf{S} precisely, the time step integration is $\mathbf{v}_k = \mathbf{S} \times \mathbf{v}_{k-1}$, $k = 1, 2, \dots$. A precise computation algorithm for an exponential matrix is given in [8]. It uses the theorem of exponential function

$$\exp(\mathbf{H} \times \tau) = \left[\exp\left(\frac{\mathbf{H} \times \tau}{m}\right) \right]^m, \quad (18)$$

where m is an arbitrary integer. If $m = 2^N$ is selected, $\Delta t = \tau / m$ will be an extremely small time interval for $N \geq 20$. Therefore the following truncated Taylor series expansion can be used

$$\begin{aligned} \exp(\mathbf{H} \times \Delta t) &\cong \mathbf{I} + \mathbf{H} \times \Delta t + \frac{(\mathbf{H} \times \Delta t)^2}{2} + \frac{(\mathbf{H} \times \Delta t)^3}{3!} \\ &\quad + \frac{(\mathbf{H} \times \Delta t)^4}{4!} \\ &= \mathbf{I} + \mathbf{S}_a \end{aligned} \quad (19)$$

where $\mathbf{S}_a = \mathbf{H} \times \Delta t + (\mathbf{H} \times \Delta t)^2 \times \frac{\mathbf{I} + (\mathbf{H} \times \Delta t)/3 + (\mathbf{H} \times \Delta t)^2/12}{2}$. Also \mathbf{S} can be factorized as

$$\begin{aligned} \mathbf{S} &\cong (\mathbf{I} + \mathbf{S}_a)^{2^N} \\ &= (\mathbf{I} + \mathbf{S}_a)^{2^{(N-1)}} (\mathbf{I} + \mathbf{S}_a)^{2^{(N-1)}} \\ &= (\mathbf{I} + \mathbf{S}_a + \mathbf{S}_a + \mathbf{S}_a \times \mathbf{S}_a)^{2^{(N-1)}} \end{aligned} \quad (20)$$

and the factorization can be repeated recursively.

It is assumed that the inhomogeneous term is linear within time step (t_k, t_{k+1}) . Then, Equation (15) can be written as

$$\dot{\mathbf{v}} = \mathbf{H}\mathbf{v} + \mathbf{r}_0 + \mathbf{r}_1 \times (t - t_k), \quad (21)$$

where \mathbf{r}_0 and \mathbf{r}_1 are given vectors. Let $\mathbf{Y}(t - t_k)$ be the solution of the homogeneous equation

$$\dot{\mathbf{Y}} = \mathbf{H}\mathbf{Y}, \quad \mathbf{Y}(0) = \mathbf{I}. \quad (22)$$

The solution of equation (21) can be derived as

$$\mathbf{v} = \mathbf{Y}(t - t_k) \times \left\{ \mathbf{v}_k + \mathbf{H}^{-1}(\mathbf{r}_0 + \mathbf{H}^{-1}\mathbf{r}_1) \right\} - \mathbf{H}^{-1}(\mathbf{r}_0 + \mathbf{H}^{-1}\mathbf{r}_1) - (\mathbf{H}^{-1}\mathbf{r}_1) \times (t - t_k). \quad (23)$$

Now substituting $t = t_{k+1}$

$$\mathbf{Y}(t_{k+1} - t_k) = \mathbf{Y}(\tau) = \mathbf{S}, \quad (24)$$

then the one step integration equation is

$$\mathbf{v}_{k+1} = \mathbf{S} \times [\mathbf{v}_k + \mathbf{H}^{-1}(\mathbf{r}_0 + \mathbf{H}^{-1}\mathbf{r}_1)] - \mathbf{H}^{-1}(\mathbf{r}_0 + \mathbf{H}^{-1}\mathbf{r}_1 + \mathbf{r}_1 \times \tau) \quad (25)$$

4. Description of the Problem

In this paper, a 4 cm long hollow cylinder, which represents a 0.22 gun barrel, is considered. The configuration of the barrel is shown in Figure 2. It is assumed that a crack emerges at the middle of the barrel. The crack is a cm deep and the thickness of the barrel is $h = 0.355$ cm. We define a dimensionless parameter α as the ratio of the crack depth to the thickness of the barrel and β as the ratio of external to internal radius. It is assumed that uniform tensile (mode I) time dependant loading is applied at both ends of the barrel. The time history of the loading is shown in Figure 3. It is also assumed that the loading increases linearly with time for the first 1×10^{-4} s and then remains constant. The Poisson's ratio and Young's modulus of iron is 0.25 and 2.1×10^{11} Pa respectively.

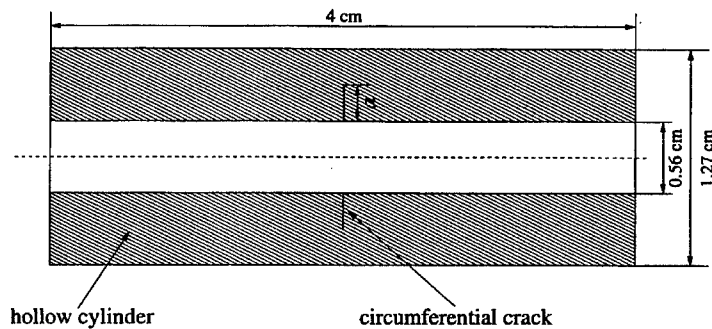


Figure 2: The problem layout

For the static case, Nied and Erdogan [9] presented numerical values of mode I SIF and displacements at the crack mouth for various geometric dimensions in an infinitely long cylinder. In their work the dimensionless SIF for $\beta = 0.4$ and $\alpha = 0.2, 0.4, 0.6$ and 0.8 are 1.003, 1.001, 1.099 and 1.411 respectively. In our study here β equal to 0.44 and the dimensionless SIF for $\alpha = 0.2, 0.4, 0.6$ and 0.8 are 0.979, 1.000, 1.099 and 1.423 respectively, which show very close agreement with Nied and Erdogan results.

Figures 4 and 5 show the mesh configurations for $\alpha = 0.8$ used in the present analysis. In previous work [10], a study was carried at on determining the optimum value of the similarity ratio ϕ and number of layers n . That study showed that a similarity ratio in the range $0.5 < \phi < 0.9$ with corresponding number of layers in the range $20 < n < 100$. Figure 4 shows the fractal finite element mesh, where the number of layers n and similarity ratio are 20 and 0.6

respectively. These values give accurate results without too much computational efforts. Figure 5 shows the far field finite element mesh. There are 772 elements and 1625 nodes before the transformation. But after the transformation the number of nodes reduces to 354. Therefore it is more efficient to solve.

5. Discussion of Numerical Results

Figure 6 depicts the variation of the dimensionless SIF with time for the loading conditions shown in Figure 3, and for values of the crack depth-to-thickness ratio $\alpha = 0.2, 0.4, 0.6$ and 0.8 , and for zero damping. It is seen that there are harmonic oscillations in the SIF profile. These oscillations are most likely due to multiple reflection from the crack and the ends of the cylinder. The figure also shows that the amplitude of the sinusoidal waves initially decreases as α increases from 0.2 to 0.6 . Thereafter the amplitude of the waves increase as α increases from 0.6 to 0.8 . Furthermore, it is seen that the final mean values of the dynamic SIF are approximately the same as the static SIF. These SIF values increase very slightly as α increases from 0.2 to 0.6 . But as α increases further to 0.8 , the SIF values increase rapidly.

In order to model damping effects on the solution, we use the so called Rayleigh damping, that is $\mathbf{G} = \theta \mathbf{M} + \rho \mathbf{K}$, where θ and ρ are two parameters. In this study we simplify the damping further by assuming that $\theta = \rho$. i.e., $\mathbf{G} = \theta(\mathbf{M} + \mathbf{K})$. Figures 7, 8 and 9 show SIF time history for $\theta = 1 \times 10^{-7}$, 1×10^{-6} and 1×10^{-5} respectively.

With $\theta = 1 \times 10^{-7}$, Figure 7 shows waves in the SIF profiles in the transit step stage and then harmonic oscillations in the constant stage. However the amplitude of these oscillatory waves decrease with time gradually due to the effect of the damping. As θ is increased to 1×10^{-6} , Figure 8 shows few oscillations at the beginning of each stage. The dynamic SIFs approach their static values at around 0.15 ms. Figure 9 shows SIF profiles when $\theta = 1 \times 10^{-5}$. It is seen that there are no oscillations in the SIF profiles. However the dynamic SIF values do not approach their static values. This is likely due to the damping coefficient being in excess of the critical damping value.

6. Concluding Remarks

In dynamic fracture mechanics, a subfield of fracture mechanics concerned with dynamic fracture phenomena, the role of material inertia is very significant. Inertial effects can arise either from rapidly applied loading on a cracked solid or from rapid crack propagation. Progress towards a thorough understanding of dynamic fracture phenomena has been impeded by several complicated factors. The inherent time dependence of a dynamic fracture process results in mathematical models that are more complex than the equivalent equilibrium models for the same configuration and material class.

There has been considerable amount of research directed towards the solution of problems in an effort to improve an understanding of the behaviour of material failure under dynamic loading. One of the main difficulties is the stress singularity around a crack tip. Usually numerous degrees of freedom or special singular elements have been used in order to accurately represent the stress field singularities. Another difficulty is the selection of a well-behaved time integration method, since there are so many different integration schemes in the literature.

In this paper, we extend our previous studies on the computation of SIF values for cracked solids subjected to static loading to include dynamic effects on the stress intensity factor. The calculations of dynamic mode I stress intensity factors for complete circumferential cracks on the inner surface of a hollow cylinder subjected to time dependent axisymmetric loading has been presented. The numerical result show that the fractal finite element method together with the precise time step integration method provides very accurate computation of dynamic SIF values.

Acknowledgement

This research is supported by EPSRC and British Aerospace, U.K.

References

1. Leung A.Y.T. and Su R.K.L., Mode I crack problems by fractal two-level finite element methods. *Engineering Fracture Mechanics*, 1994, **48**, 847-856.
2. Leung A.Y.T. and Su R.K.L., Body-force linear elastic stress intensity factor calculation using fractal two-level finite element method. *Engineering Fracture Mechanics*, 1995, **51**, 879-888.
3. Leung A.Y.T. and Su R.K.L., Mixed mode two-dimensional crack problems by fractal two-level finite element method. *Engineering Fracture Mechanics*, 1995, **51**, 889-895.
4. Leung A.Y.T. and Su R.K.L., Fractal two-level finite element analysis of cracked Reissner's plate. *Thin-Walled Structure*, 1996, **24**, 315-334.
5. Leung A.Y.T. and Su R.K.L., Fractal two-level finite element method for 2-D cracks. *Microcomputers in Civil Engineering*, 1996, **11**, 249-257.
6. Leung A.Y.T. and Su R.K.L., Fractal two-level finite element method for crack classical plates using DKT elements. *Engineering Fracture Mechanics*, 1996, **54**, 703-711.
7. Zhong W.X. and Williams F.W., A precise time step integration method. *Proc. Instn Mech. Engrs.*, 1994, **208**, 427-430.
8. Zhong W.X. and Yang. Z.S., On the computation of main eigenpairs of continuous-time linear quadratic control problem. *Appl. Math. Mech.*, 1991, **12**, 45-50.

9. Nied H.F. and Erdogan. F., The elasticity problem for a thick-walled cylinder containing a circumferential crack. International Journal of Fracture, 1983, **22**, 277-301.
10. Leung A.Y.T. and Tsang K.L., Mode III two-dimensional crack problem by two-level finite element method. Accepted by International Journal of Fracture.

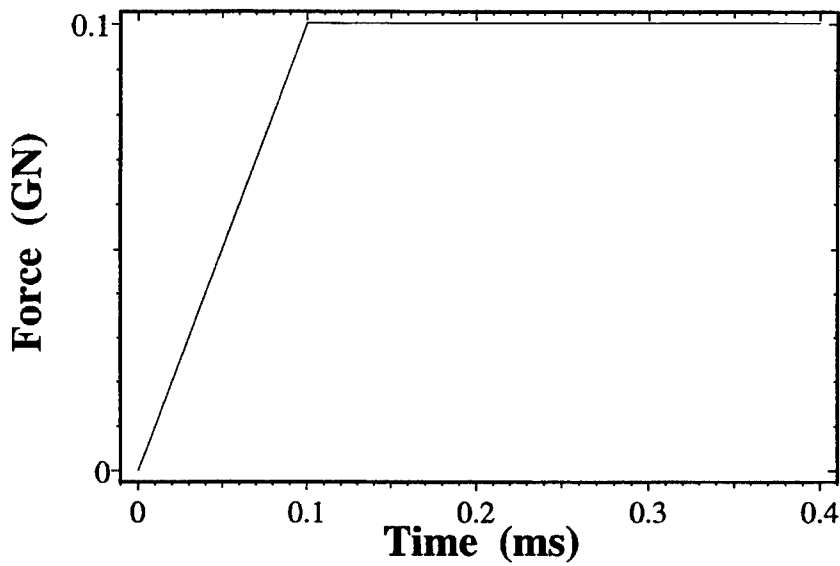


Figure 3: Force time history.

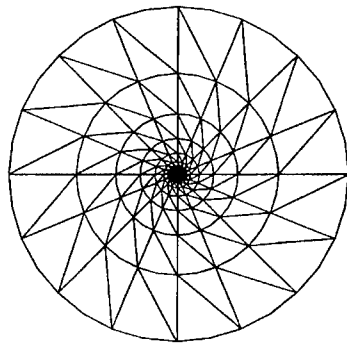


Figure 4: Fractal finite element mesh.

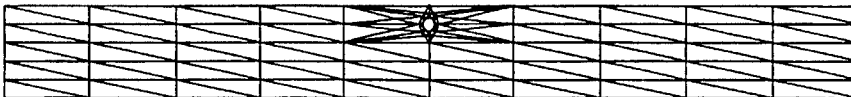


Figure 5: Far field finite element mesh.

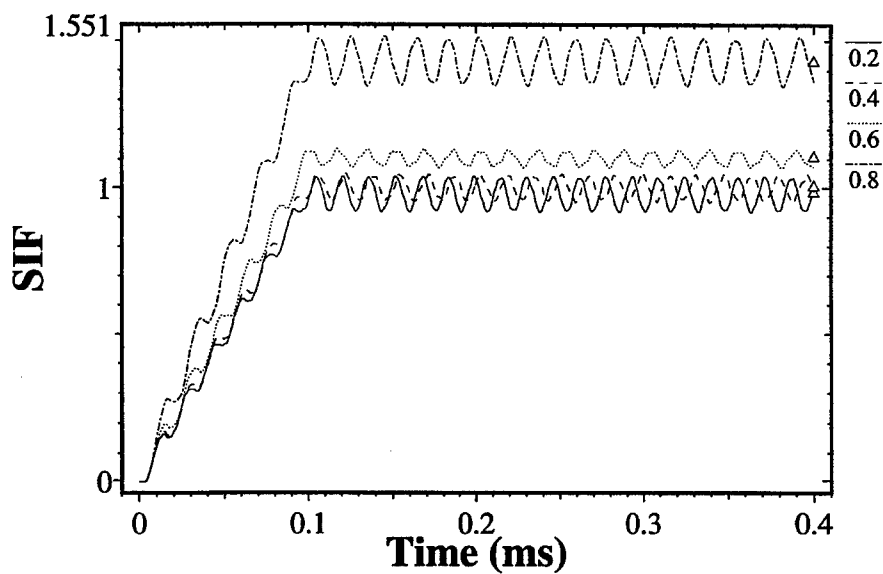


Figure 6: SIF time history without damping for $\alpha=0.2, 0.4, 0.6$ and 0.8 .

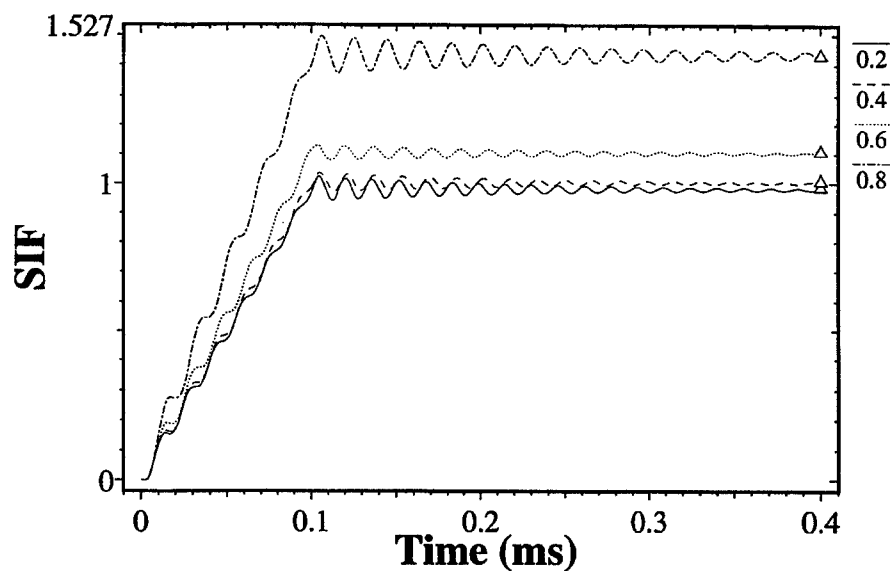


Figure 7: SIF time history with damping ($\theta=1 \times 10^{-7}$) for $\alpha=0.2, 0.4, 0.6$ and 0.8 .

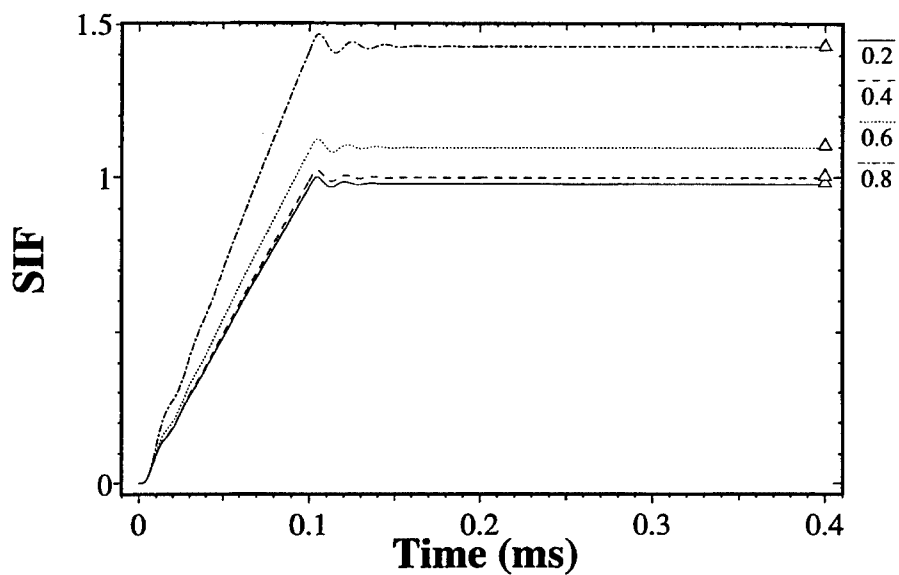


Figure 8: SIF time history with damping ($\theta=1\times10^{-6}$) for $\alpha=0.2, 0.4, 0.6$ and 0.8 .

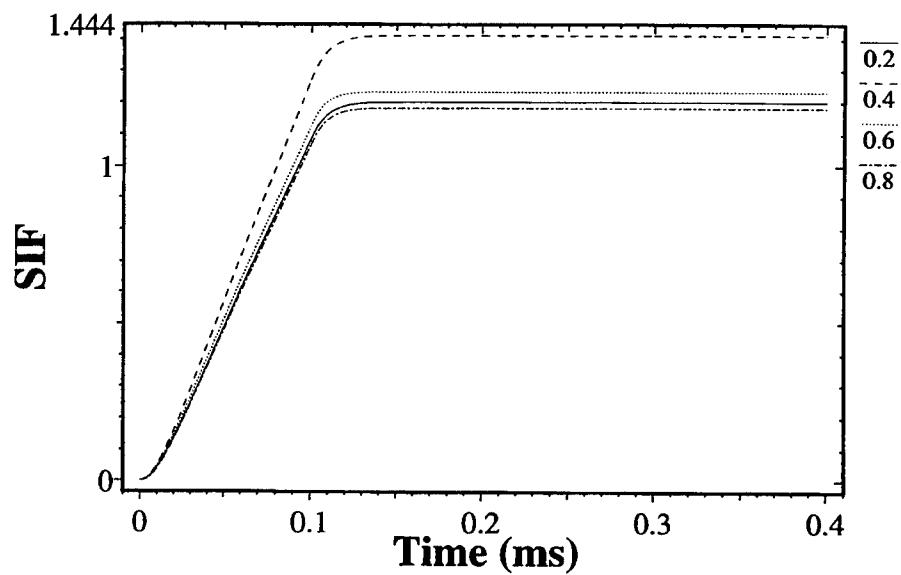


Figure 9: SIF time history with damping ($\theta=1\times10^{-5}$) for $\alpha=0.2, 0.4, 0.6$ and 0.8 .

SYSTEM IDENTIFICATION

A Geometric-Algebraic Approach to Identifying Second Order Continuous Systems.

S.D. Garvey[†], M.I. Friswell[‡] and J.E.T. Penny[¥]

[†] School of Mechanical, Materials, Manuf. Eng. & Management,
University of Nottingham, University Park, Nottingham NG7 2RD

[‡] Dept. of Mech. Eng. Univ. of Wales, Swansea, Singleton Park, Swansea, SA2 8PP

[¥] School of Engineering, Aston University, Aston Triangle, Birmingham, B4 7ET

ABSTRACT

Given a second-order system having N degrees of freedom, it is standard practice in virtually all identification procedures either to assume that it is a classically-damped system whose modes are real or to convert that system into a first order system having $2N$ degrees of freedom. Neither one of these is completely satisfactory. Assuming classical damping places an artificial constraint on the information which can be extracted and places a limit on how accurately that information can be obtained. Conversion into a first-order system produces a problem which has fewer constraints than it truly ought have (the natural link between displacement and velocity is weakened).

This paper examines the use the Clifford Algebra Cl_2 for the determination of system matrices from time-domain signals. In many of the established methods for determining state-space forms from time-domain signals, a block-Hankel matrix is formed. The decomposition of this block-Hankel matrix using Singular-Value Decomposition provides an indication of model order and state-space matrices can then be found. This paper outlines how at least one such method extends to the use of Clifford Numbers.

INTRODUCTION

Our interest in the use of Clifford Algebra began with a relatively mundane quest to improve the computational efficiency of algorithms for computing the characteristic roots of non-classically damped systems. The particular motivation for proceeding was founded on the faith that as the major "direct" methods achieve no computational advantage when the system being analysed is self-adjoint, there should be some other "direct" methods, by which this symmetry can be utilised. We use the term "direct" in this context to describe a method in which there is no iteration except in the solution of the eigenvalue problem. We have found such a method and we outline its essentials in summary here. Consider the following representation of a standard second-order system.

$$\mathbf{K}\mathbf{q} + \mathbf{D}\dot{\mathbf{q}} + \mathbf{M}\ddot{\mathbf{q}} = \mathbf{Q} \quad (1)$$

In (1), \mathbf{q} and \mathbf{Q} are the vectors of displacement and force coordinates respectively and \mathbf{K}, \mathbf{D} and \mathbf{M} are the system matrices. This system has solution pairs $\{s_k, \phi_k\}$ satisfying :

$$(\mathbf{K} + s_k \mathbf{D} + s_k^2 \mathbf{M})\phi_k = 0 \quad (2)$$

In order to determine the complete set of characteristic solutions, we normally set up and solve a $(2N \times 2N)$ generalised eigenvalue problem. The matrices comprising this problem may take different forms but we favour the following as a starting point :

$$\begin{bmatrix} \mathbf{E}_L & \mathbf{F}_L \\ \mathbf{G}_L & \mathbf{H}_L \end{bmatrix}^T \begin{bmatrix} \mathbf{0} & \mathbf{K} \\ \mathbf{K} & \mathbf{D} \end{bmatrix} \begin{bmatrix} \mathbf{E}_R & \mathbf{F}_R \\ \mathbf{G}_R & \mathbf{H}_R \end{bmatrix} = \begin{bmatrix} \mathbf{S}_1 & \mathbf{0} \\ \mathbf{0} & \mathbf{S}_2 \end{bmatrix} \quad (3)$$

$$\begin{bmatrix} \mathbf{E}_L & \mathbf{F}_L \\ \mathbf{G}_L & \mathbf{H}_L \end{bmatrix}^T \begin{bmatrix} \mathbf{K} & \mathbf{0} \\ \mathbf{0} & -\mathbf{M} \end{bmatrix} \begin{bmatrix} \mathbf{E}_R & \mathbf{F}_R \\ \mathbf{G}_R & \mathbf{H}_R \end{bmatrix} = \begin{bmatrix} \mathbf{I}_{(N \times N)} & \mathbf{0} \\ \mathbf{0} & \mathbf{I}_{(N \times N)} \end{bmatrix}$$

When system matrices $\{\mathbf{K}, \mathbf{D}, \mathbf{M}\}$ are symmetrical, the left and right characteristic vectors are identical and $\mathbf{E}_L = \mathbf{E}_R$, $\mathbf{F}_L = \mathbf{F}_R$, $\mathbf{G}_L = \mathbf{G}_R$, $\mathbf{H}_L = \mathbf{H}_R$. In general, $\mathbf{E}_L, \mathbf{F}_L, \mathbf{G}_L, \mathbf{H}_L, \mathbf{E}_R, \mathbf{F}_R, \mathbf{G}_R, \mathbf{H}_R, \mathbf{S}_1, \mathbf{S}_2$ are complex. We have shown [1], that through some relatively simple transformations, (3) can be written in the following equivalent form

$$\begin{bmatrix} \mathbf{W}_L^T & \mathbf{Y}_L^T \\ \mathbf{X}_L^T & \mathbf{Z}_L^T \end{bmatrix} \begin{bmatrix} \mathbf{0} & \mathbf{K} \\ \mathbf{K} & \mathbf{D} \end{bmatrix} \begin{bmatrix} \mathbf{W}_R & \mathbf{X}_R \\ \mathbf{Y}_R & \mathbf{Z}_R \end{bmatrix} = \begin{bmatrix} \mathbf{0} & \mathbf{\Omega} \\ \mathbf{\Omega} & 2\zeta\mathbf{\Omega} \end{bmatrix} \quad (4)$$

$$\begin{bmatrix} \mathbf{W}_L^T & -\mathbf{Y}_L^T \\ -\mathbf{X}_L^T & \mathbf{Z}_L^T \end{bmatrix} \begin{bmatrix} \mathbf{K} & \mathbf{0} \\ \mathbf{0} & \mathbf{M} \end{bmatrix} \begin{bmatrix} \mathbf{W}_R & \mathbf{X}_R \\ \mathbf{Y}_R & \mathbf{Z}_R \end{bmatrix} = \begin{bmatrix} \mathbf{I}_{(N \times N)} & \mathbf{0} \\ \mathbf{0} & \mathbf{I}_{(N \times N)} \end{bmatrix}$$

In this, $\mathbf{W}_L, \mathbf{X}_L, \mathbf{Y}_L, \mathbf{Z}_L, \mathbf{W}_R, \mathbf{X}_R, \mathbf{Y}_R, \mathbf{Z}_R, \mathbf{\Omega}, \zeta$ are all real and $\mathbf{\Omega}, \zeta$ are both diagonal. In the case of passive structural models, $\mathbf{K}=\mathbf{K}^T, \mathbf{D}=\mathbf{D}^T$ and $\mathbf{M}=\mathbf{M}^T$ and we have

$$\begin{aligned} \mathbf{W}_L &= \mathbf{W}_R = \mathbf{W}, & \mathbf{X}_L &= \mathbf{X}_R = \mathbf{X} \\ \mathbf{Y}_L &= \mathbf{Y}_R = \mathbf{Y}, & \mathbf{Z}_L &= \mathbf{Z}_R = \mathbf{Z} \end{aligned} \quad (5)$$

For such *self-adjoint* systems we can immediately see that the equations in (4) are perfectly symmetrical simply by transposing them. The nomenclature of real diagonal $\mathbf{\Omega}$ and ζ is deliberately chosen to invoke a connection with the quantities ω_n and ζ used to describe any general single-degree-of-freedom second order system. The transformations presented in (4) have the effect of decoupling the initial second order system into a set of N single-degree-of-freedom second order systems.

Clearly, (4) does not represent a generalised eigenvalue problem in the usual sense. However, if we represent each of the $(2N \times 2N)$ matrices of real numbers in (4) in alternative form as an $(N \times N)$ matrix of Clifford numbers from the algebra Cl_2 , it is found that (4) can be written in this elegant form.

$$\underline{U}_L^{*k} \underline{A} \underline{U}_R = \underline{A} \quad , \quad \underline{U}_L^{*i} \underline{B} \underline{U}_R = \underline{I} \quad (6)$$

The significance of each of the matrices in (6) can be appreciated from the isomorphism between the Clifford numbers of Cl_2 and the class of 2×2 matrices (see [2], [3]). The $*i$ and $*k$ operator notations denote two different conjugate transposes. The effect of the $*k$ operator at the $(2N \times 2N)$ level is a simple transpose. The effect of the $*i$ operator at this level is a transpose followed by a negation of the two off-diagonal $(N \times N)$ blocks.

We have found ways of using similarity transformations which point towards efficient solution of (6) in the domain of Clifford Numbers. Simplistically, the principal advantage of this computational approach derives from the fact that we can preserve symmetry in the analysis of self-adjoint systems whilst still avoiding the use of Complex numbers. With symmetry comes improved computational efficiency and accuracy. This paper extends the use of the Clifford Algebraic approach into the identification of self-adjoint second-order systems.

SELF-ADJOINT 1ST AND 2ND ORDER SYSTEMS IN STATE SPACE

Consider a first-order system in which the equations of motion do not involve any mass.

$$\mathbf{K} \mathbf{q} + \mathbf{D} \dot{\mathbf{q}} = \mathbf{Q} \quad (7)$$

There is a limited number of *terminals* at which forces may be applied and displacements measured. A *selection* matrix, \mathbf{S} , indicates the terminals. The vectors of forces and displacements at the terminals are \mathbf{r} and \mathbf{R} respectively.

$$\mathbf{r} = \mathbf{S}^T \mathbf{q} \quad , \quad \mathbf{Q} = \mathbf{S} \mathbf{R} \quad (8)$$

If this is set in state-space form with \mathbf{q} as the state vector we obtain :

$$\left. \begin{array}{l} \dot{\mathbf{q}} = \mathbf{A} \mathbf{q} + \mathbf{B} \mathbf{R} \\ \mathbf{r} = \mathbf{C} \mathbf{q} \end{array} \right\} \text{ with } \mathbf{A} = -\mathbf{D}^{-1} \mathbf{K}, \quad \mathbf{B} = \mathbf{D}^{-1} \mathbf{S}, \quad \mathbf{C} = \mathbf{S}^T \quad (9)$$

If we began with a self-adjoint system ($\mathbf{K} = \mathbf{K}^T$ and $\mathbf{D} = \mathbf{D}^T$), then we must find that the state space system is also self-adjoint (exhibits reciprocity) and this is manifest as

$$(\mathbf{C} \mathbf{A}^L \mathbf{B}) = (\mathbf{C} \mathbf{A}^L \mathbf{B})^T \quad \text{for every integer } L \quad (10)$$

If we intended to perform extensive response computations for a known first-order system, we would invariably solve the generalised eigenvalue problem for (\mathbf{K}, \mathbf{D}) in order to find a coordinate transformation such that the new \mathbf{A} matrix was diagonal.

$$\mathbf{U}^T \mathbf{K} \mathbf{U} = \mathbf{A} \quad \mathbf{U}^T \mathbf{D} \mathbf{U} = \mathbf{I} \quad \mathbf{q} = \mathbf{U} \mathbf{x} \quad (11)$$

Then a different state-space form is achievable

$$\left. \begin{array}{l} \dot{\mathbf{x}} = \mathbf{A} \mathbf{x} + \mathbf{B} \mathbf{R} \\ \mathbf{r} = \mathbf{C} \mathbf{x} \end{array} \right\} \text{ with } \mathbf{A} = -\mathbf{A}, \quad \mathbf{B} = \mathbf{U}^T \mathbf{S}, \quad \mathbf{C} = \mathbf{S}^T \mathbf{U} \quad (12)$$

The symmetry of this first-order system is then completely clear since the output matrix, \mathbf{C} , is the transpose of the input matrix, \mathbf{B} , and the \mathbf{A} matrix is diagonal. Moreover, if we are set the task of identifying the dynamic system given known terminal forces, $\mathbf{R}(t)$, and displacements, $\mathbf{r}(t)$, then it is attractive to identify it directly in this form.

We now present a similar form for self-adjoint second-order systems which both makes the symmetry perfectly clear and forms a natural structure in which to identify the complete system. The second order system of interest is represented by (1) and the same selection matrix \mathbf{S} applies to this system relating the terminal forces and displacements to the complete vector of forces and displacements according to (8).

To parallel the development above for 1st order systems, we write the “state-space” equation for the second order system using a double-differentiation thus :

$$\begin{aligned} \begin{bmatrix} \ddot{\mathbf{q}} \\ \dot{\mathbf{q}} \end{bmatrix} &= \begin{bmatrix} -\mathbf{M}^{-1}\mathbf{K} & -\mathbf{M}^{-1}\mathbf{D} \\ \mathbf{M}^{-1}\mathbf{D}\mathbf{M}^{-1}\mathbf{K} & \mathbf{M}^{-1}(\mathbf{D}\mathbf{M}^{-1}\mathbf{D} - \mathbf{K}) \end{bmatrix} \begin{bmatrix} \mathbf{q} \\ \dot{\mathbf{q}} \end{bmatrix} + \begin{bmatrix} 0 & \mathbf{M}^{-1} \\ -\mathbf{M}^{-1} & \mathbf{M}^{-1}\mathbf{D}\mathbf{M}^{-1} \end{bmatrix} \begin{bmatrix} \mathbf{S} & 0 \\ 0 & \mathbf{S} \end{bmatrix} \begin{bmatrix} \dot{\mathbf{R}} \\ \mathbf{R} \end{bmatrix} \\ \begin{bmatrix} \mathbf{r} \\ \dot{\mathbf{r}} \end{bmatrix} &= \begin{bmatrix} \mathbf{S}^T & 0 \\ 0 & \mathbf{S}^T \end{bmatrix} \begin{bmatrix} \mathbf{q} \\ \dot{\mathbf{q}} \end{bmatrix} \end{aligned} \quad (13)$$

Using (4) in much the same way as (11) was used above, we can find (see [4]),

$$\begin{aligned} \begin{bmatrix} \ddot{\mathbf{x}} \\ \ddot{\mathbf{y}} \end{bmatrix} &= \begin{bmatrix} 0 & -\Omega \\ -\Omega & 2\zeta\Omega \end{bmatrix} \begin{bmatrix} 0 & \Omega \\ \Omega & 2\zeta\Omega \end{bmatrix} \begin{bmatrix} \mathbf{x} \\ \mathbf{y} \end{bmatrix} + \begin{bmatrix} \mathbf{W}^T \mathbf{S} & \mathbf{Y}^T \mathbf{S} \\ \mathbf{X}^T \mathbf{S} & \mathbf{Z}^T \mathbf{S} \end{bmatrix} \begin{bmatrix} \dot{\mathbf{R}} \\ \mathbf{R} \end{bmatrix} \\ \begin{bmatrix} \mathbf{r} \\ \dot{\mathbf{r}} \end{bmatrix} &= \begin{bmatrix} \mathbf{S}^T \mathbf{W} & \mathbf{S}^T \mathbf{X} \\ \mathbf{S}^T \mathbf{Y} & \mathbf{S}^T \mathbf{Z} \end{bmatrix} \begin{bmatrix} \mathbf{x} \\ \mathbf{y} \end{bmatrix} \end{aligned} \quad (14)$$

In (14), \mathbf{x} and \mathbf{y} together comprise the state vector. Re-using the symbols \mathbf{A} , \mathbf{B} and \mathbf{C} now to represent the matrix quantities in (14) we have

$$\begin{aligned} \mathbf{A} &= \begin{bmatrix} 0 & -\Omega \\ -\Omega & 2\zeta\Omega \end{bmatrix} \begin{bmatrix} 0 & \Omega \\ \Omega & 2\zeta\Omega \end{bmatrix} \\ \mathbf{B} &= \begin{bmatrix} 0 & -\Omega \\ -\Omega & 2\zeta\Omega \end{bmatrix} \begin{bmatrix} \mathbf{W}^T \mathbf{S} & \mathbf{Y}^T \mathbf{S} \\ \mathbf{X}^T \mathbf{S} & \mathbf{Z}^T \mathbf{S} \end{bmatrix}, \quad \mathbf{C} = \begin{bmatrix} \mathbf{S}^T \mathbf{W} & \mathbf{S}^T \mathbf{X} \\ \mathbf{S}^T \mathbf{Y} & \mathbf{S}^T \mathbf{Z} \end{bmatrix} \end{aligned} \quad (15)$$

The symmetry is not yet as obvious as it was in (12) for the first-order system. To see it, represent \mathbf{A} , \mathbf{B} and \mathbf{C} using matrices $\underline{\mathbf{A}}$, $\underline{\mathbf{B}}$ and $\underline{\mathbf{C}}$ of Clifford Numbers (from Cl_2) whose dimensions are half of those of \mathbf{A} , \mathbf{B} and \mathbf{C} respectively. We then see that

$$\underline{\mathbf{A}} = \underline{\Omega}^* \underline{\Omega} \text{ with } \underline{\Omega} \text{ diagonal, } \underline{\Omega} = \underline{\Omega}^* \text{ and } \underline{\mathbf{A}}^* = \underline{\mathbf{A}}, \quad \underline{\mathbf{B}} = \underline{\Omega}^* \underline{\mathbf{C}}^* \quad (16)$$

Observing certain properties of the conjugate operators, we can combine (15) and (16) to find the following second order equivalent of (10)

$$(\underline{\mathbf{C}} \underline{\mathbf{A}}^L \underline{\mathbf{B}}) = (\underline{\mathbf{C}} \underline{\mathbf{A}}^L \underline{\mathbf{B}})^* \text{ for every integer } L \quad (17)$$

Equation (17) effectively reproduces a result about reciprocity of the system which could have been generated directly from (1) using arguments based on the symmetry of the dynamic stiffness matrix. However, the material above (in particular (16) and (17)) indicates an appropriate decomposition for certain matrices which occurring in the identification of second order systems.

IDENTIFYING MODELS FROM TIME-DOMAIN DATA

There are numerous established methods for performing this task – for example [5-9]. In almost all cases, a block-Hankel matrix is established and it is factorised into smaller full-rank terms through singular value decomposition. In this paper, we are interested in the decomposition of the particular block-Hankel matrix, \mathbf{H} , which relates $2L$ derivatives of \mathbf{r} to $2L$ derivatives of \mathbf{R} . For brevity, we present this for the specific case $L=3$ but the extension to different values of L is obvious.

$$\begin{bmatrix} \mathbf{r}^{(6)} \\ \mathbf{r}^{(7)} \\ \mathbf{r}^{(8)} \\ \mathbf{r}^{(9)} \\ \mathbf{r}^{(10)} \\ \mathbf{r}^{(11)} \end{bmatrix} = \begin{bmatrix} \mathbf{h}_1 & \mathbf{h}_2 & \mathbf{h}_3 & \mathbf{h}_4 & \mathbf{h}_5 & \mathbf{h}_6 \\ \mathbf{h}_2 & \mathbf{h}_3 & \mathbf{h}_4 & \mathbf{h}_5 & \mathbf{h}_6 & \mathbf{h}_7 \\ \mathbf{h}_3 & \mathbf{h}_4 & \mathbf{h}_5 & \mathbf{h}_6 & \mathbf{h}_7 & \mathbf{h}_8 \\ \mathbf{h}_4 & \mathbf{h}_5 & \mathbf{h}_6 & \mathbf{h}_7 & \mathbf{h}_8 & \mathbf{h}_9 \\ \mathbf{h}_5 & \mathbf{h}_6 & \mathbf{h}_7 & \mathbf{h}_8 & \mathbf{h}_9 & \mathbf{h}_{10} \\ \mathbf{h}_6 & \mathbf{h}_7 & \mathbf{h}_8 & \mathbf{h}_9 & \mathbf{h}_{10} & \mathbf{h}_{11} \end{bmatrix} \begin{bmatrix} \mathbf{R}^{(5)} \\ \mathbf{R}^{(4)} \\ \mathbf{R}^{(3)} \\ \mathbf{R}^{(2)} \\ \mathbf{R}^{(1)} \\ \mathbf{R}^{(0)} \end{bmatrix} \quad (18)$$

In this equation, $\mathbf{r}^{(6)}$ represents the 6th derivative of displacement vector \mathbf{r} with respect to time. We outline in the appendix one method whereby this matrix can be obtained from sampled-data but there are several possible routes to this and our emphasis is on the decomposition of \mathbf{H}_0 . The partitioning lines in (18) are introduced to emphasise the fact that the proposed decomposition will treat the large $(6M \times 6M)$ matrix, \mathbf{H}_0 , of (18) as a $(3M \times 3M)$ matrix, $\underline{\mathbf{H}}_0$, of Clifford numbers from Cl_2 (still assuming that $L=3$). Each Clifford Number will simultaneously represent four entries (ij) , $(iM+j)$, $(M+ij)$, $(M+iM+j)$ within one of the partitioned blocks.

In almost perfect parallel with established state-space identification methods, we can observe that $\underline{\mathbf{H}}_0$ has the structure :

$$\underline{\mathbf{H}}_0 = \underline{\mathbf{O}} \underline{\Omega}^* \underline{\mathbf{O}}^{*k} \quad \text{where} \quad (19)$$

$$\underline{\mathbf{O}}^{*k} = \begin{bmatrix} \underline{\mathbf{C}}^{*k} & (\underline{\Omega} \underline{\Omega}^*) \underline{\mathbf{C}}^{*k} & (\underline{\Omega} \underline{\Omega}^*)^2 \underline{\mathbf{C}}^{*k} \end{bmatrix}$$

Using $\underline{\mathbf{h}}_1, \underline{\mathbf{h}}_2, \underline{\mathbf{h}}_3$ etc. to denote the Cl_2 representations of the $(2M \times 2M)$ blocks containing $\{\underline{\mathbf{h}}_1, \underline{\mathbf{h}}_2, \underline{\mathbf{h}}_3\}$, $\{\underline{\mathbf{h}}_3, \underline{\mathbf{h}}_4, \underline{\mathbf{h}}_5\}$, $\{\underline{\mathbf{h}}_5, \underline{\mathbf{h}}_6, \underline{\mathbf{h}}_7\}$ etc. respectively, it is relatively straightforward to verify that (19) reproduces

$$\underline{\mathbf{h}}_1 = \underline{\mathbf{C}} \underline{\Omega} \underline{\mathbf{C}}^{*k}, \quad \underline{\mathbf{h}}_2 = \underline{\mathbf{C}} (\underline{\Omega}^* \underline{\Omega} \underline{\Omega}^*) \underline{\mathbf{C}}^{*k}, \quad \underline{\mathbf{h}}_3 = \underline{\mathbf{C}} (\underline{\Omega}^* \underline{\Omega} \underline{\Omega}^* \underline{\Omega} \underline{\Omega}^*) \underline{\mathbf{C}}^{*k} \quad (20)$$

Factorising $\underline{\mathbf{H}}_0$ into symmetrical factors using an eigenvalue-eigenvector decomposition (equivalent to singular value decomposition since $\underline{\mathbf{H}}_0$ is symmetric) begins the decomposition of (19) but this alone is not sufficient to distinguish the scaling of $\underline{\Omega}$ from the scaling of $\underline{\mathbf{O}}$. After this factorisation we have

$$\underline{\mathbf{H}}_0 = (\underline{\mathbf{O}} \underline{\mathbf{Q}}) (\underline{\mathbf{Q}}^{*k} \underline{\Omega}^* \underline{\mathbf{Q}}) (\underline{\mathbf{Q}}^{*k} \underline{\mathbf{O}}^{*k}) \quad \text{with} \quad \underline{\mathbf{Q}}^{*k} \underline{\mathbf{Q}} = \underline{\mathbf{I}} = \underline{\mathbf{Q}} \underline{\mathbf{Q}}^{*k} \quad (21)$$

in which each one of the bracketed terms is known but $\underline{\mathbf{Q}}$ is unknown. A suitable method for eliminating this unknown $\underline{\mathbf{Q}}$ involves setting up another block-Hankel matrix, $\underline{\mathbf{H}}_1$, beginning with $\underline{\mathbf{h}}_3$ rather than $\underline{\mathbf{h}}_1$. We know that this matrix must decompose according to

$$\underline{\mathbf{H}}_1 = (\underline{\mathbf{O}} \underline{\mathbf{Q}}) (\underline{\mathbf{Q}}^{*k} \underline{\Omega}^* \underline{\Omega} \underline{\Omega}^* \underline{\mathbf{Q}}) (\underline{\mathbf{Q}}^{*k} \underline{\mathbf{O}}^{*k}) \quad (22)$$

Then, knowing both $(\underline{\mathbf{Q}}^{*k} \underline{\Omega}^* \underline{\mathbf{Q}})$ and $(\underline{\mathbf{Q}}^{*k} \underline{\Omega}^* \underline{\Omega} \underline{\Omega}^* \underline{\mathbf{Q}})$, we can easily isolate $\underline{\mathbf{Q}}$.

The central proposition of this paper is that

- matrix $\underline{\mathbf{H}}_0$ is derived from measured data and should have dimensions to ensure that any further increase in dimension would lead to no increase in rank
- $\underline{\mathbf{H}}_0$ is decomposed according to (21) by solving a symmetric eigenvalue problem in Clifford Numbers (in fact, this problem can be solved in real numbers and then transformed). The bracketed terms in (21) are known but $\underline{\mathbf{Q}}$ is unknown.
- a second block-Hankel matrix, $\underline{\mathbf{H}}_1$ be compiled from almost the same original data (we discard $\underline{\mathbf{h}}_1$ and $\underline{\mathbf{h}}_2$ and we introduce $\underline{\mathbf{h}}_{4L}$ and $\underline{\mathbf{h}}_{4L+1}$) and by combining the previously obtained factors of $\underline{\mathbf{H}}_0$ with this, the identification can be completed.

EXAMPLE

In this example, we create \underline{H}_0 directly from the system matrices and then decompose it again – leaving out the very large step of transforming it into sampled time-domain data and processing this to obtain \underline{H}_0 . Rather than specify fully-populated system matrices and then generate a selection matrix \underline{S} comprising only 1's and 0's, we achieve the same generality by providing system matrices in compact form and fully-populated \underline{S} .

$$\begin{aligned} \underline{K} &= \text{diag}([0.7 \ 1.0 \ 4.0 \ 9.0]) \\ \underline{M} &= \text{diag}([1.0 \ 1.0 \ 1.0 \ 1.0]) \\ \underline{S}^T &= \begin{bmatrix} 1.0 & 0.0 & -0.5 & 0.2 \\ 0.2 & 0.4 & -0.2 & 1.0 \end{bmatrix} \end{aligned} \quad \underline{D} = \frac{1}{5} \begin{bmatrix} 9 & -5 & 4 & 2 \\ -5 & 8 & -8 & -2 \\ 4 & -8 & 10 & 2 \\ 2 & -2 & 2 & 6 \end{bmatrix}$$

The system $\{\underline{M}, \underline{D}, \underline{K}\}$ has two real roots and six complex roots. We can report these roots very compactly in pairs in Clifford form (c.f. eq. (4)) as :

	Pair #1	Pair #2	Pair #3	Pair #4
$\Omega(i,j)$	0.996910	1.599478	2.968223	1.060643
$(2\zeta\Omega)(i,j)$	0.892835	0.645556	1.090126	3.971482

Table 1. The characteristic roots of the example system quoted in Clifford form.

We create \underline{H}_0 directly with $L=4$ using (13) and when we decompose it using an eigenvalue-eigenvector decomposition, there are eight non-zero eigenvalues and eight zero eigenvalues. The non-zero eigenvalues are:

Index	Eigenvalue
1	1.594532E6
2	-1.865365E5
3	825.31521
4	-369.74480
5	-3.3634063
6	3.0802217
7	1.6935677
8	-1.1216953

Table 2. The eight non-zero eigenvalues of block-Hankel matrix \underline{H}_0 .

The \underline{Q} matrix found is quoted below (as an (8x8) matrix of reals rather than as a (4x4) matrix of Cl_2 numbers) so that the reader may verify that the decomposition of (21) is genuinely present.

2.6706637E-7	-8.5102806E-7	-2.1793478E-6	3.5413063E-3
-1.6451464E-6	8.5036854E-6	2.0190596E-5	-9.0754426E-2
6.9526035E-5	8.2083564E-4	-1.5038911E-3	5.4845103E-4
-3.4079385E-4	9.0501618E-5	-5.5262937E-6	-3.6418997E-4
-1.4377507E-7	1.4600324E-7	3.0822257E-6	-1.1761670E-2
-5.2901497E-6	7.0910964E-6	-9.2217792E-6	9.6747687E-2
-1.8487094E-4	-2.0470132E-3	-3.2037966E-3	1.2119063E-3
1.1774319E-3	-3.1268006E-4	1.9093465E-5	8.3512013E-4

Table 3. Columns 1-4 of the matrix Q (of 22).

-2.3744078E-2	4.6930695E-1	5.3557326E-1	-3.5748764E-1
1.3610172E-1	4.3493127E-2	1.7102556E-1	-3.0369552E-2
1.4174212E-3	3.9874863E-4	7.5470619E-4	-2.5903587E-4
2.9735962E-4	-6.0976298E-2	1.5549770E-2	1.3762340E+0
-4.5314227E-3	-6.2787429E-1	2.5438795E-1	3.7041249E-1
9.3499225E-2	-8.1329521E-2	4.7792015E-2	4.7678405E-2
-1.4015367E-3	6.8620482E-4	-7.9961759E-4	-5.2663892E-4
-2.3120215E-3	1.7005093E-2	-6.4478923E-3	-3.9792984E-1

Table 4. Columns 5-8 of the matrix Q (of 22).

CONCLUSIONS

It is established that Geometric (Clifford) Algebra has much to offer as a natural language in which to express and analyse the dynamics of generally-damped self-adjoint second order systems. This paper examines the implications of using Geometric Algebra in the context of identifying second order systems. The time-domain behaviour of a general second order system is set out in a format similar to the normal state-space format. The distinction is that where the normal state-space equation would express the first derivative of the state vector in terms of the inputs and current state vector, we express the second derivative of state. From this point on, we have paralleled developments in conventional state-space methods for identification. We have exposed a coordinate transformation such that the so-called "state-matrix" is diagonal. We have then progressed from this point to show that the block-Hankel matrix which relates high derivatives of displacement to low derivatives of forcing (c.f. (18)) can be decomposed in a particular fashion to yield the complete system identification.

We have not, in the body of the paper, even begun to address how the block-Hankel matrix of interest can be obtained from measured data. A possible route is described in the Appendices for completeness. Accepting that there are practical methods for obtaining this matrix, the following major outcome is then available.

If we can decompose this block-Hankel matrix using Clifford Algebra according to (21), we have directly identified a realisable second order system.

This is in stark contrast with other available methods for identifying second order systems. They identify state-space representations of the second order system which may not correspond to realisable second order systems and they must subsequently perform some non-trivial computations to force the system into second-order realisability. After this, they must extract the second order system from the state-space representation.

ACKNOWLEDGEMENT

Dr.s Garvey and Friswell gratefully acknowledge the contribution of the EPSRC to this work through their award of a research grant on *Applications of Geometric Algebra in Engineering Dynamics* and through their grant of an Advanced Research Fellowship to Dr. Friswell.

REFERENCES

1. S.D. Garvey, M.I. Friswell & J.E.T. Penny *An Old Algebra Newly Applied to Dynamics*. Paper re-submitted to Proc. Royal Society, Nov. '99 (following original submission in August 1997).
2. P. Lounesto. *Clifford Algebra & Spinors*. Cambridge University Press, 1997.
3. A. N. Lasenby, *Introduction to Geometric Algebra*. Presented at "Geometric Algebra in Engineering Dynamics", Aston University, Jan 6th, 1999.
4. S.D. Garvey, M.I. Friswell & J.E.T. Penny *A Clifford-Algebraic Perspective on Second-Order Linear Systems*. AIAA Journal of Guidance, Control, and Dynamics. To appear.
5. M. Aoki. *State Space Modelling of Time Series*. Springer Verlag. 1990
6. P. H. Kirkegaard & P. Anderson. *State Space Identification of Civil Engineering Structures from Output Measurements*. IMAC XV, Orlando, Fl. pp889-893, Feb. '97
7. J. Lardies. *Estimation of Parameters and Model Order in State Space Innovation Forms*. 2nd International Conf. on Identification in Engineering Systems. Swansea, March 21-23. p693-702, 1999
8. J. Lardies. *Modal Parameter Estimation and Model Order Selection of a Randomly Vibrating System*. Mechanical Systems and Signal Processing, Vol. 12, No.6 pp825-838, 1998.
9. M. J. Desforges, J. E. Cooper and J. R. Wright. *Spectral and Modal Parameter Estimation from Output-Only Measurements*. Mechanical Systems and Signal Processing, Vol. 9, No.2 pp169-186, 1995.

APPENDIX I. Processing Measurements to Obtain the Block-Hankel Matrix.

Begin by considering a general discrete-time system represented as

$$\begin{aligned} \mathbf{x}(k+1) &= \mathbf{A}\mathbf{x}_k + \mathbf{B}\mathbf{u}_k \\ \mathbf{y}_k &= \mathbf{C}\mathbf{x}_k + \mathbf{D}\mathbf{u}_k \end{aligned} \quad (\text{A1})$$

Vector \mathbf{u}_k contains a set of inputs to the dynamic model at the k^{th} time instant and it may be measured in some cases. Vector \mathbf{x}_k is the state vector at instant k . Vector \mathbf{y}_k contains a set of outputs from the dynamic model and this is measured – almost by definition. Let M , N and O represent the dimensions of input, state and output vectors. Initially, take it that $N=1=M=O$. From (A1)

$$\begin{aligned} y_i &= c x_i + d u_i & x_{i+1} &= a x_i + b u_i \\ y_{i+1} &= c x_{i+1} + d u_{i+1} & x_{i+2} &= a x_{i+1} + b u_{i+1} \\ y_{i+2} &= c x_{i+2} + d u_{i+2} & x_{i+3} &= a x_{i+2} + b u_{i+2} \\ y_{i+3} &= c x_{i+3} + d u_{i+3} \end{aligned} \quad (\text{A2})$$

Through some straightforward substitutions, we can eliminate $x_i, x_{i+1}, x_{i+2}, x_{i+3}$

$$\begin{aligned} y_{i+1} - a y_i &= (c b - a d) u_i + d u_{i+1} \\ y_{i+2} - a y_{i+1} &= (c b - a d) u_{i+1} + d u_{i+2} \\ y_{i+3} - a y_{i+2} &= (c b - a d) u_{i+2} + d u_{i+3} \end{aligned} \quad (\text{A3})$$

Assuming that $\{u_i \dots u_{i+3}\}$ and $\{y_i \dots y_{i+3}\}$ are available, (A3) comprises three simultaneous linear equations in three unknowns $\dots \{a, (c.b-a.d), d\}$ which can be solved with ease. We can write (A3) in matrix form thus :

$$[(c.b-a.d) \quad a \quad d \quad -1] \begin{bmatrix} u_i & u_{i+1} & u_{i+2} \\ y_i & y_{i+1} & y_{i+2} \\ u_{i+1} & u_{i+2} & u_{i+3} \\ y_{i+1} & y_{i+2} & y_{i+3} \end{bmatrix} = 0 \quad (\text{A4})$$

Extending (A4) to the case of system matrices is straightforward provided that some matrix \mathbf{G} exists such that

$$\mathbf{GC} = \mathbf{CA} \quad (\text{A5})$$

In this case, it is invariably possible to find the following equivalent of (A4)

$$[(CB - GD) \quad G \quad D \quad -I] \begin{bmatrix} \mathbf{u}_i & \mathbf{u}_{i+1} & \mathbf{u}_{i+2} & \dots \\ \mathbf{y}_i & \mathbf{y}_{i+1} & \mathbf{y}_{i+2} & \dots \\ \mathbf{u}_{i+1} & \mathbf{u}_{i+2} & \mathbf{u}_{i+3} & \dots \\ \mathbf{y}_{i+1} & \mathbf{y}_{i+2} & \mathbf{y}_{i+3} & \dots \end{bmatrix} = \mathbf{0} \quad (\text{A6})$$

From this, we can choose an appropriate coordinate set to separate CB into the factors C and B . Then, knowing C , the corresponding A can be extracted as

$$A = C^+ G C \quad (\text{A7})$$

A suitable G satisfying (A5) can be found if and only if the row space of C spans N -space. In most cases, C is not square and it has substantially fewer rows than its N columns (i.e. $O < N$). The state vector \mathbf{x}_k is not then observable from a single vector of outputs, \mathbf{y}_k . In such cases, we can consider creating an augmented vector of outputs, \mathbf{z}_k and a corresponding augmented vector of inputs \mathbf{v}_k defined as

$$\mathbf{v}_k = \begin{bmatrix} \mathbf{u}_k \\ \mathbf{u}_{k-1} \\ \vdots \\ \mathbf{u}_{k+1-Q} \end{bmatrix}, \quad \mathbf{z}_k = \begin{bmatrix} \mathbf{y}_{k+1} \\ \mathbf{y}_{k+2} \\ \vdots \\ \mathbf{y}_{k+R} \end{bmatrix} \quad (\text{A8})$$

Here, Q , is chosen as the minimum integer sufficient to form \mathbf{v}_k containing N independent inputs capable of influencing \mathbf{x}_{k+1} and R as the minimum integer sufficient to form \mathbf{z}_k containing N independent outputs observing \mathbf{x}_{k+1} . Clearly, we can assemble a set of dynamic equations in very similar form to (A1) as

$$\begin{aligned} \mathbf{x}_{k+1} &= A \mathbf{x}_k + B' \mathbf{v}_k \\ \mathbf{z}_k &= C \mathbf{x}_k + H \mathbf{v}_k \end{aligned} \quad \text{.. with ..} \quad C' = \begin{bmatrix} C \\ CA \\ \vdots \\ CA^{R-2} \\ CA^{R-1} \end{bmatrix} \quad (\text{A9})$$

$$B' = [B \quad AB \quad \dots \quad A^{Q-1}B]$$

$$H = \begin{bmatrix} CA^0 B & CA^1 B & CA^2 B & \dots & CA^{Q-1} B \\ CA^1 B & CA^2 B & CA^3 B & \dots & CA^{Q+0} B \\ CA^2 B & CA^3 B & CA^4 B & \dots & 0 \\ \vdots & \vdots & \vdots & \ddots & \vdots \\ CA^{R-1} B & CA^{R+0} B & CA^{R+1} B & \dots & CA^{R+Q-2} B \end{bmatrix}$$

Note, that by beginning the definition of \mathbf{z}_k at time-instant $(k+1)$, any effects of direct feed-through (matrix D in (A1)) are avoided.

APPENDIX II Extension to continuous time.

The above appendix outlined the block-Hankel matrix \mathbf{H} could be obtained. There are two ways (at least!) in which such methods developed for discrete-time systems can be applied to continuous-time systems. One of these is the trivial operation of approximating a derivative by a finite-difference expression involving values of a function at two consecutive instants in time. Provided that the time-interval between these instants is very small compared with all of the time-constants of the continuous system, the approximation will be a good one mathematically. If the time-interval is too small, problems arise associated with the finite precision representation of numbers.

An alternative possibility – much preferred by the authors – is that derivatives of the input and output vectors function are deduced from a sequence of values of the function. For any general function, $f(t)$, we can use a Taylor (McLauren) series to relate the values of this function at a sequence of values of t about the instant $t=t_0$, to the derivatives of the function at $t=t_0$.

$$\begin{bmatrix} f(t_0 + h_1) \\ f(t_0 + h_2) \\ \vdots \\ f(t_0 + h_M) \end{bmatrix} \approx \begin{bmatrix} 1 & h_1 & h_1^2/2 & \dots & h_1^N/N! \\ 1 & h_2 & h_2^2/2 & \dots & h_2^N/N! \\ \vdots & \vdots & \vdots & \ddots & \vdots \\ 1 & h_M & h_M^2/2 & \dots & h_M^N/N! \end{bmatrix} \begin{bmatrix} f(x_0) \\ \left. \frac{df}{dt} \right|_{t_0} \\ \vdots \\ \left. \frac{d^N f}{dt^N} \right|_{t_0} \end{bmatrix} \quad (\text{B1})$$

Inverting the expansion matrix instantly provides expressions for the derivatives in terms of time-sampled values. Assuming that all requisite derivatives are available, we can parallel the method in Appendix I perfectly.

To set this in context, suppose that we require to obtain the block-Hankel matrix of equation (18) in the main body of the text. We would use six different levels of differentiation of the displacement (output) vector ($\mathbf{r}^{(6)}$ up to $\mathbf{r}^{(11)}$) and six levels of differentiation of the force (input) vector ($\mathbf{R}^{(0)}$ up to $\mathbf{R}^{(5)}$). The extraction of derivatives zero through five of \mathbf{R} for any given reference time would involve at least six values of \mathbf{R} at instants around the reference time. The computation of the derivatives six through eleven of \mathbf{r} would take place in two stages. Firstly, we would compute the sixth derivative of \mathbf{r} at each one of the reference times of interest. Then, we would use the same differentiation process as was used for finding derivatives zero through five of \mathbf{R} on this already-differentiated data.

The maximum number of levels of differentiation required is determined by the order of the system which we require the process to be capable of detecting and by the rank of the input and output matrices. Note that in the case of structural identification, the rank of the input and output matrices is necessarily identical.

COMPARISON BETWEEN SECOND AND HIGHER ORDER SPECTRAL ANALYSIS IN DETECTING STRUCTURAL DAMAGES

Alessandro RIVOLA

DIEM, University of Bologna - Viale Risorgimento, 2 I-40136 Bologna, Italy
Phone: +39 051 209 3440 Fax: +39 051 209 3446
alessandro.rivola@mail.ing.unibo.it

ABSTRACT

The aim of this paper is to compare the results of the traditional linear spectral analysis to those of the bispectral analysis in the case of experimental tests carried out on a straight beam with a fatigue crack. The tests are performed on a simply supported beam attached to a vibration shaker fed with Gaussian noise. An accelerometer is used to measure the acceleration of the free end of the beam. The excitation and the system response are used to compute a number of quantities for the system in the two operating states: without damage and with the presence of a fatigue crack. In particular, the power spectrum, the frequency response function, the second-order coherence function and the third-order spectrum are estimated. These measures are compared and the results are discussed. Fatigue cracks open and close depending on the vibration direction, causing the time-variation of the physical system parameters. Therefore, the cracked beam exhibits non-linear behaviour. Consequently, the traditional linear spectral analysis is of limited value in studying the beam response because non-linearities are involved. On the contrary, higher order spectra are of great importance in the analysis of non-linear vibrations where the generation and interactions of non-linear resonance modes are of major concern. Since the system, which is excited by random signal, tends to distribute the energy between frequencies in a way that reflects the type of non-linearity contained in the system itself, particular effort is spent in order to relate information obtained from higher order spectra to the signal frequency content.

INTRODUCTION

The development of techniques based on vibration measurements for monitoring the integrity of structures has received increasing attention in recent years. As a matter of fact, these techniques offer an effective and fast means of detecting structural damages. Therefore they play an important role in ensuring the integrity of machine elements and structures.

A range of research has been conducted into the area of detecting cracks

in structures. Some researchers assume that cracks are always open during the vibration. In their works, the cracks are detected from alterations in natural frequencies and modes of vibration, as well as amplitude of forced vibrations [1-3]. However, the modal parameters may change due to not only structural damage, but also other factors, such as temperature. Besides, many studies have illustrated that it is important to consider the crack closure. In [4] the author pointed out that the change in natural frequencies due to a real fatigue crack is much lower than the drop caused by a narrow notch. Therefore, it is important to take into account the non-linear nature of the system. The beam, in fact, exhibits a non-linear behaviour because of the time-variation of the physical system parameters due to the crack opening and closing. Several studies were conducted into the field of non-linear cracks in beams: models of beams with closing cracks were developed by [5-9]. In these works the authors employed the linear spectra analysis, such as the power spectrum of the beam vibration and/or the frequency response function, in order to detect and identify the structural damages.

The second-order spectrum, that is the power spectrum, is very satisfactory in many studies of vibrations, but it is obviously of limited value in other studies of vibrations where non-linearities are involved [10, 11]. Nevertheless, the traditional linear spectral analysis can be employed in studying vibrations of non-linear systems. As a matter of fact, the second-order frequency response function and the coherence function are commonly used to detect deviations from linearity of a system [6, 12]. However, their computation require two measurement sensors.

On the other hand, there is another area of signal processing that is gaining importance in studying non-linear systems and has a wide variety of practical applications (vibration analysis, underwater acoustics, speech processing, chaos and condition monitoring). It deals with Higher Order Spectra (HOS) which are the natural extension of the ordinary linear spectral analysis. In particular, the HOS can be viewed as the frequency domain equivalent of higher order statistical moments [13-18]. Accordingly, they are used to explore statistical relationships between several spectral components. Therefore, the HOS are of great importance in the analysis of non-linear vibrations where the generation and interactions of non-linear resonance modes are of major concern. In such cases, HOS are necessary to investigate and characterise the non-linear phenomena. An important feature of HOS is that their computation can be performed from a single signal measurement.

The aim of this paper is to compare the results of the traditional linear spectral analysis to those of the third-order spectra analysis in the case of experimental tests carried out on a straight beam in two operating states: without damage and with the presence of a fatigue crack. The system is a simply supported beam attached to a vibration shaker fed with Gaussian noise. The beam response is measured by an accelerometer located at the free end of the beam. The excitation and the system response are used to compute a

number of quantities. In particular, the power spectrum of the beam response, the frequency response function and the second-order coherence function between the input and the output of the system, and the normalised version of the third-order spectrum of the response are estimated. These measures are compared and the results are discussed. The system, which is excited by random signal, tends to distribute the energy between frequencies in a way that reflects the type of non-linearity. Particular effort is then spent in order to relate information obtained from third-order spectra to the signal frequency content and to the system's physical characteristics.

DEFINITIONS

With reference to two discrete time series $x(n)$ and $y(n)$ representing stationary random processes, the power spectrum (i.e. the auto-spectrum), S_{xx} , and the cross-spectrum, S_{xy} , can be described by the signal's Discrete Fourier Transform (DFT) as

$$S_{xx}(k) = E[X^*(k)X(k)], \quad S_{xy}(k) = E[X^*(k)Y(k)]. \quad (1)$$

The symbol $E[\cdot]$ denotes the expectation operator, and k is the discrete frequency variable [13].

For a linear time invariant system the function that relates the response to a given excitation, at each frequency, is the system's Frequency Response Function (FRF). If $X(k)$ and $Y(k)$ are respectively the DFT of the input and output of the system, the FRF is defined as

$$H(k) = \frac{Y(k)}{X(k)}. \quad (2)$$

Measured FRF are the basic data for several techniques for frequency domain identification of the dynamic characteristics of structural systems [12, 13, 19]. They are employed to such technologies as experimental modal analysis, structural systems identification, and force determination to name a few. The measured input and output can be obviously affected by noise that depends on the environment in which the dynamic test is taking place. Background disturbances such as ambient vibrations and instrumentation noise may excite the structure without being accounted for in the measured force or, on the other hand, they may affect the measured response without being related to the physical excitation of the system. By converting measured data from the time domain into the frequency domain using appropriate windowing functions, the FRF is obtained from relations between the auto-spectra and cross-spectra of the excitation and response signals. The most popular methods of estimating the FRF for uncorrelated input and output noise are [13, 19, 20]

$$H_1(k) = \frac{S_{xy}(k)}{S_{xx}(k)}, \quad H_2(k) = \frac{S_{yy}(k)}{S_{yx}(k)}. \quad (3)$$

It may be shown that the estimator H_1 is the least square solution for the true FRF which minimises the bias effects of output noise. Conversely, the estimator H_2 is the least square estimate of H which minimises the effects of input noise [13, 20]. It should be noted that at the resonances the output SNR is high, thus the noise to be minimised is that which affects the excitation. Therefore, the estimator H_2 is more accurate at the resonances. On the contrary, at the anti-resonances the better estimator is H_1 because the SNR of the output drops causing the H_2 to overestimate the true FRF substantially.

As a measure of how well the output is linearly related to the input at each frequency, one uses the ordinary coherence function [13, 19, 20]. In other words, the coherence function is a measure of the linearity of the system. It is rated on a 0 to 1 scale and is defined as

$$\gamma^2(k) = \frac{H_1(k)}{H_2(k)} = \frac{|S_{xy}(k)|^2}{S_{xx}(k) S_{yy}(k)}. \quad (4)$$

The conventional linear spectral analysis uses the lowest order spectra; that is, it investigates the statistical relationship between two spectral components. The next extension of linear spectral analysis to higher order is the bispectral analysis. It investigates the statistical relationship between three spectral components. The bispectrum of a discrete time series $x(n)$ is defined by the DFT as [16]

$$B_x(k, l) = E[X(k) X(l) X^*(k + l)]. \quad (5)$$

The bispectrum contains phase information and is a function of two independent frequencies. Equation (5) shows that the bispectrum is a statistical average of a product of three spectral components. Therefore, the bispectrum is of great importance in the study of those non-linear vibrations where the relationships between three spectral components are in question, such as the generation of combinational resonance modes or quadratic mode couplings [10, 14, 18]. An important feature of bispectrum is the fact that it is able to measure the extent of joint statistical dependency of various combinations of three spectral components and their statistical degree without reference to the spectral amplitudes. In addition, the bispectrum, i.e. the third-order spectrum, can be viewed as the decomposition of the third statistical moment (skewness) of a signal over frequency and as such can detect non-symmetric non-linearities

[11, 18, 21]. Moreover, it is noteworthy that the bispectrum computation requires a single signal measurement.

Due to several symmetries it can be shown that, for a discrete time process with no aliasing, it is necessary to compute the bispectrum only over a limited bifrequency region given by

$$\{k, l\}: 0 \leq k \leq \frac{f_s}{2}, 0 \leq l \leq k, k + l \leq \frac{f_s}{2} \quad (6)$$

where f_s is the sampling frequency [22].

In order to estimate the bispectrum, the data is divided into N segments, an appropriate window is applied to each segment to reduce leakage, the quantity in eq. (5) is computed for each segment by using the DFT and, finally, the bispectrum is averaged across segments in order to reduce the variance of the estimator. The main disadvantage in computing the HOS is the data length needed in order to ensure statistical confidence. Reference [16] stated that the segment size should be the square root of the total length of the data. This means that for the computation of the bispectrum by using a DFT size of 512, the data length should be $512^2=262144$, causing problems due to the fact that the data should be stationary over the measurement period.

Unfortunately, the variance of the bispectrum estimator depends not only on the data length but is also proportional to the triple product of the power spectra of eq. (5) [14]. Consequently, the second-order properties of the signal could dominate the estimate, which can result in a misleading interpretation of the bispectrum as discussed in [21]. For this reason the bispectral analysis often deals with normalised versions of the bispectrum. One method for normalising the bispectrum employs the bicoherence, $b^2(k, l)$, which is defined by [14] as

$$b^2(k, l) = \frac{|B_x(k, l)|^2}{E[|X(k)X(l)|^2] E[|X(k+l)|^2]}. \quad (7)$$

The bicoherence is bounded between 0 and 1 and quantitatively measures the fraction of the power of the signal due to the quadratic interaction between frequency components [21]. Since it is related to the skewness of the signal, the bicoherence is sensitive to the non-symmetric non-linearities. Therefore, if the signal is Gaussian, i.e. it has a Gaussian probability density function, the bicoherence will take zero-value over the whole bifrequency plane.

It is noteworthy that the bicoherence is just a method of normalisation for the bispectrum. In this sense, it should not be confused with the second-order coherence function defined by the eq. (4). The second-order coherence function is also employed to detect deviations from linearity of a system, but its computation requires two measurement sensors; on the contrary, the

bicoherence can be computed from a single signal.

EXPERIMENTAL TEST

The experimental test is carried out on a 450 mm long straight beam with a uniform 10x10 mm cross section; the beam material is cold-drawn bronze. The beam is supported and excited by a vibration shaker; the beam response is measured by means of an accelerometer mounted at the free end of the beam (see Fig. 1). The excitation is a random signal; in particular, it is a Gaussian white noise. The signal analysis is limited to the frequency range 0-1000 Hz where the integral beam has five resonant modes measured at about 23, 170, 420, 500, and 890 Hz. Actually, within the examined frequency range, the clamped beam should have only four resonant frequencies, but the supporting fixture shifts the resonances and introduces another mode of vibration.

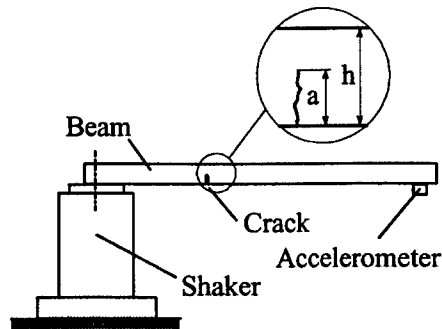


Fig. 1 - Set-up of the experimental apparatus.

The tests are performed in two different conditions: when the beam is integral and with a fatigue crack at 300 mm from the free end. The crack was initiated by denting a V 0.5 mm-deep notch. It was propagated on a high frequency fatigue testing machine. More details on the test can be found in [18]. The severity of the structural damage is expressed in terms of the ratio between its depth, a , and the height of the beam, h (see Fig. 1). In this paper only the cases $a/h = 0.0$, that is no crack is present, and $a/h = 0.6$ are considered and discussed.

RESULTS AND DISCUSSION

Two experimental signals are analysed: the voltage across the shaker and the beam's acceleration response. The sampling frequency is 2560 Hz and a signal length of 32768 points is taken into account.

Some higher order statistical moments of the beam acceleration response are firstly computed. In particular, the skewness and the kurtosis are considered: their values are reported in Table 1. These measures, which give an overall measure of system non-linearity, in this case do not provide clear information about the beam condition because of their small changes.

When a non-linear system is excited by random input, it usually generates response at frequencies that are multiples and/or combinations of the structural resonance frequencies (sometimes it generates sub-harmonic frequencies as well). The power spectra of the beam acceleration response are then considered in order to look for the generation of non-linear modes. The power spectra are computed by averaging 32 segments which have 1024 points each (Hanning window is employed); the results are shown in Fig. 2. The presence of the crack causes only small changes in the auto-spectra. The resonant frequencies decrease in the case of cracked beam and there is a change in the peak amplitude. The differences are particularly evident for the third and fourth beam's resonances, but they do not provide much information about the nature of the system, that is, they do not tell anything about the generation of combinational components due to the non-linearity. This confirms that the power spectrum is of limited value in studying the behaviour of non-linear systems.

Table 1 - Features of the beam acceleration response.

a/h	0.0	0.6
Skewness	-0.00113	0.00488
Kurtosis	2.884	2.976

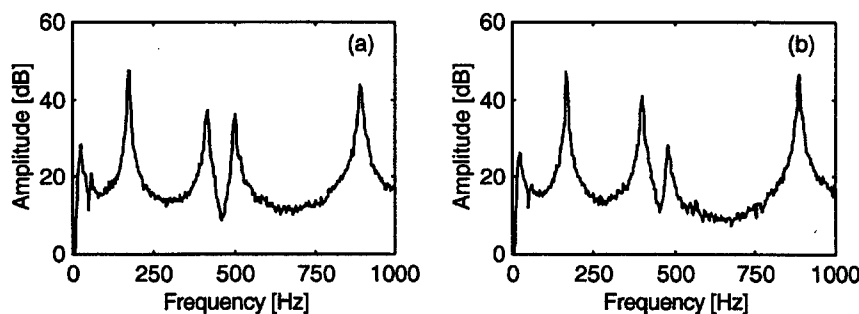


Fig. 2 - Power spectrum of the beam acceleration: a) integral beam; b) cracked beam.

In order to detect the non-linearity introduced by the crack, the FRF and the second-order coherence function have been estimated. The processing parameters are the same as in the case of power spectrum, that is, the frequency resolution is identical (2.5 Hz). Figures 3 and 4 show the results for the integral and the cracked beam, respectively. The FRF is computed by means of the estimator H_2 . As a matter of fact, the method H_2 should be better than H_1 from the point of view of the detection of components due to the interaction between the system resonances which takes place in the case of cracked beam (H_2 is

better than H_1 at the resonances).

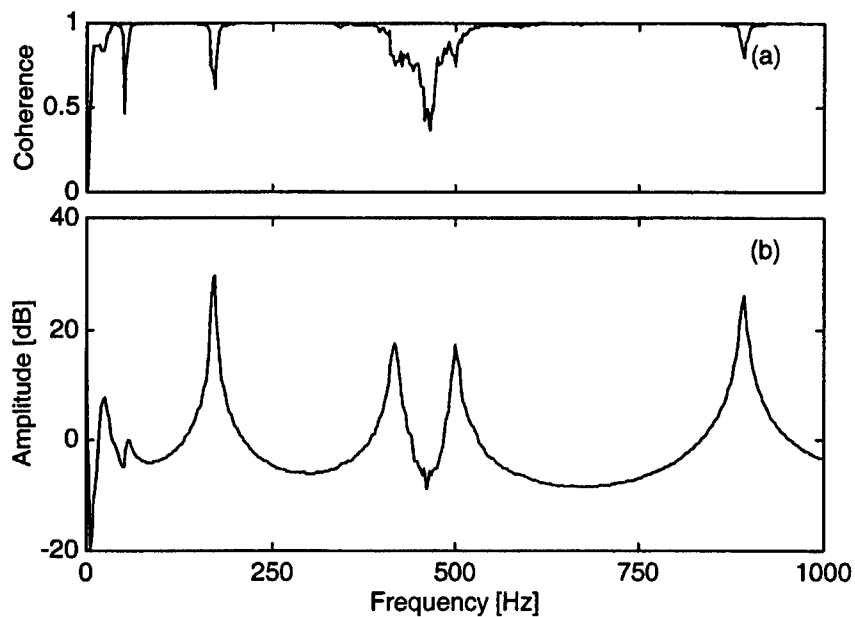


Fig. 3 - Integral beam: a) FRF H_2 between input and output of the system; b) second-order coherence function.

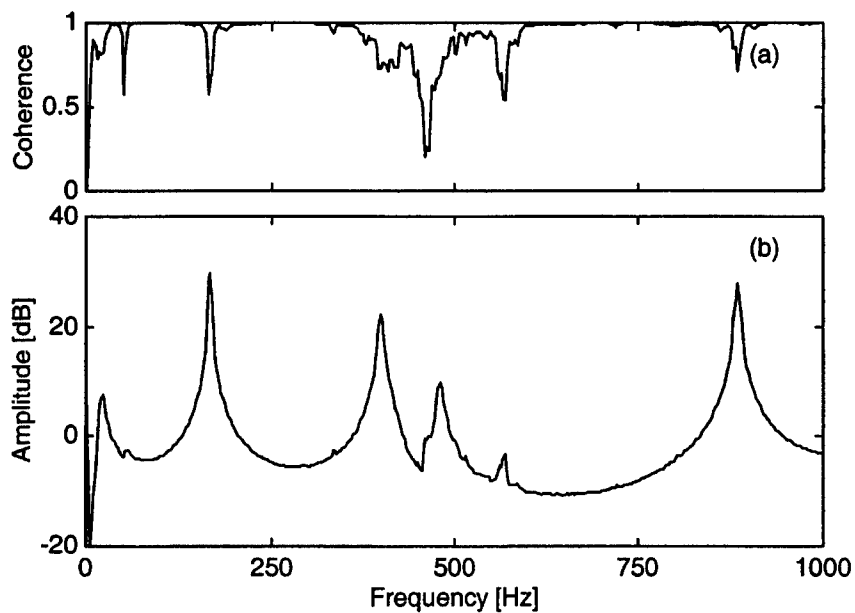


Fig. 4 - Cracked beam: a) FRF H_2 between input and output of the system; b) second-order coherence function.

The comparison between Fig. 3(b) and Fig. 4(b) shows that the estimator H_2 is, in fact, sensible to peaks due to the non-linear behaviour of the beam with the structural damage. In particular, there is a clear "non-linear" peak at the frequency 570 Hz and, in addition, two small peaks at about 335 Hz and 515 Hz are visible. Moreover, one can observe that in the case of cracked beam the fourth resonance, which is the more affected by the damage, seems to be modulated (lateral bands are present). As a matter of fact, the time-variation of the beam stiffness, due to the crack opening and closing, results in a frequency modulation phenomenon.

On the contrary, by means of the estimator H_1 it is quite impossible to see the effect of the system non-linearities (see Fig. 5). However, this does not mean that H_1 is useless: it will be shown that the second-order coherence function, which implicitly makes use of the estimator H_1 , is very sensitive to the damage.

Therefore, one may conclude that the FRF estimators give more informations about non-linearities than those given by the power spectra. Actually, the peak at 570 Hz also appears in the power spectrum of Fig. 2(b), but in that case it was practically indistinguishable.

At the frequencies of the combinational components, the beam response is not correlated to the input of the system; consequently, the coherence will be less than unity at those frequencies. This is particularly evident at the frequency 570 Hz where a non-linear effect takes place for the cracked beam: the coherence decreases substantially [see Fig. 3(a) and Fig. 4(a)]. Actually, there are other coherence drops; they appear for both the integral and damaged beam. Some of them are located at the anti-resonances, as it was expected; others are at the resonances and are due to resolution bias errors in the estimation [13].

As a conclusion, the second-order FRF and the coherence function give a clear indication about the presence of non-linearity. However, it is noteworthy that a comparison between the damaged and integral case is needed. In other words, only the observation of the changes of these functions between the two beam states makes it possible to obtain information related to the non-linearity of the system. If these second-order functions were unknown for the integral beam, the crack monitoring would be impossible. The non-linear effects could be investigated by employing different amplitude of the excitation, because when the amplitude of the excitation increases the beam response goes further into the non-linear regime. However, in general this is not the case; an alternative procedure is therefore required.

The HOS can be used as non-linearity detectors [11, 17]. In [18] the authors stated that a beam with a fatigue crack has a bilinear nature, that is, the system has a non-symmetric non-linearity. Therefore the bispectrum should be expected to be sensitive to the damage, as well as its normalised version, i.e. the bicoherence. As a matter of fact, when the beam is integral the Gaussian

excitation operates on a linear system; thus, the resulting output will also be Gaussian. On the contrary, the output results as non-Gaussian for the cracked beam. The bicoherence, that takes non-zero values only in the case of signals which have a non-symmetric probability density function, should be able to extract information regarding the presence of the fatigue crack.

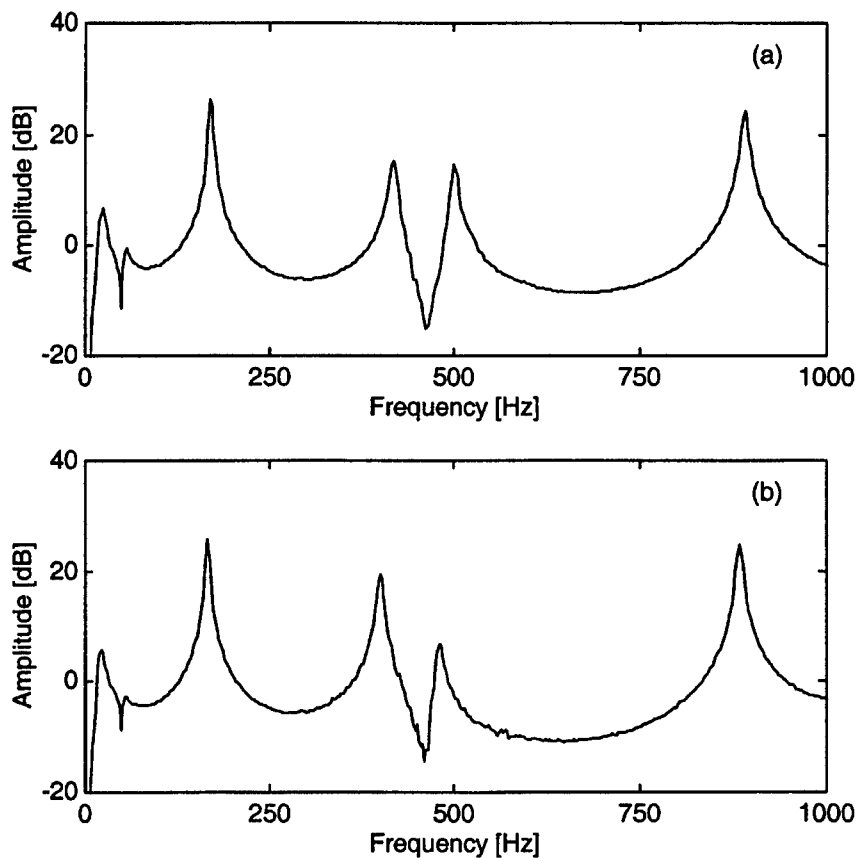


Fig. 5 - FRF H_1 between input and output of the system: a) integral beam; b) cracked beam.

Figure 6 plots the bicoherence of the beam response in case of the undamaged structure and when the fatigue crack is present. The bicoherence is computed from the total data length with a DFT size of 128 points. It clearly appears that the bicoherence is very sensitive to the damage: the bicoherence rises in the case of the cracked beam, thus showing a significant coupling between frequencies due to the system non-linearities. This illustrates a practical aspect of the bispectral analysis. Since the bicoherence measures the normalised degree of statistical dependency without reference to spectral

amplitudes, it detects the non-linear interactions even in those cases where the resultant spectral component is hardly noticeable, as in the power spectrum of Fig. 2(b).

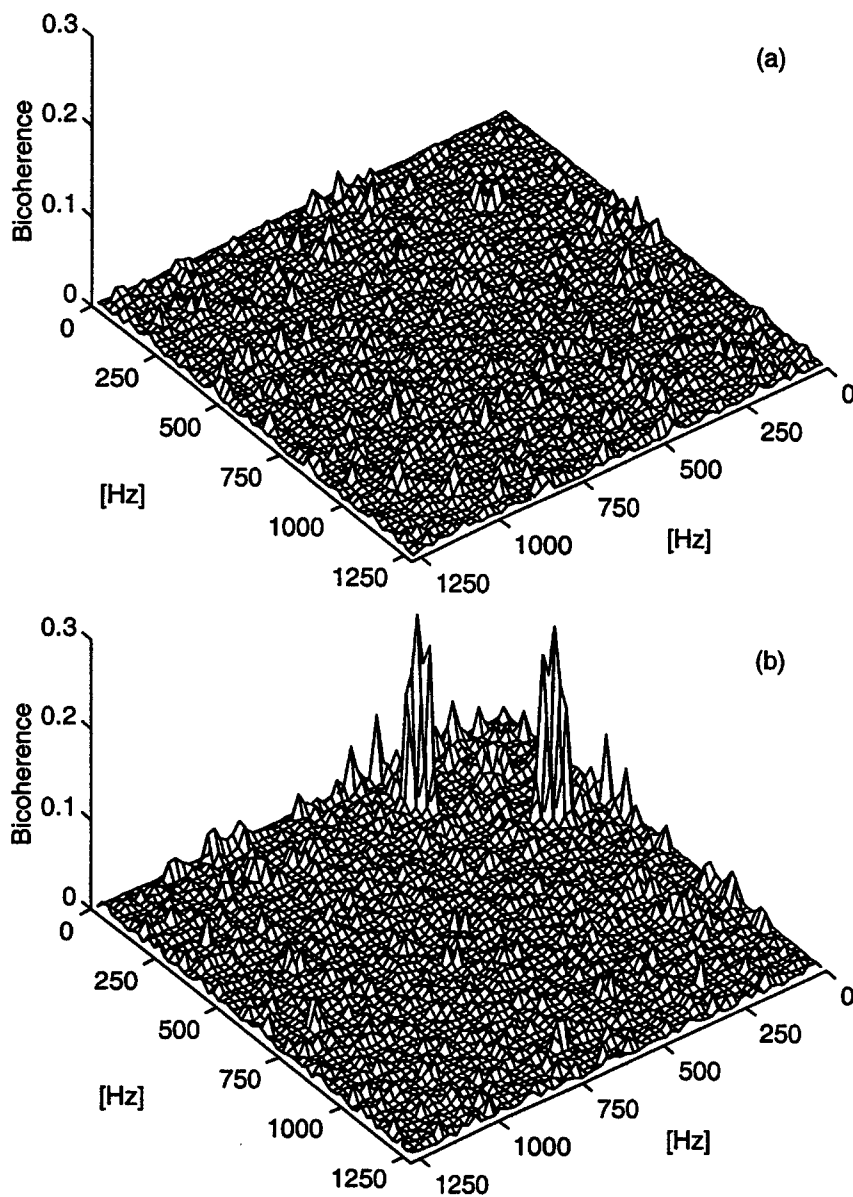


Fig. 6 - Bicoherence of the beam acceleration: a) integral beam; b) cracked beam.

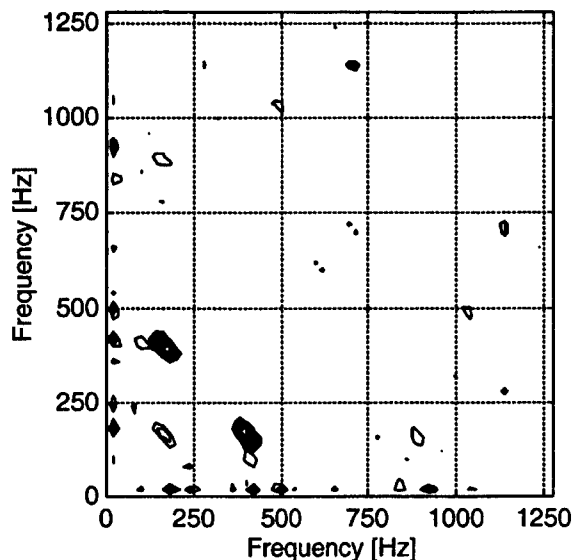


Fig. 7 - Cracked beam: contour plot of the bicoherence of the beam acceleration response.

Since the bicoherence of the response takes non-zero values only in the case of the non-linear system, the bicoherence peaks are undoubtedly related to the presence of the structural damage. As a consequence, by using the bicoherence it is not necessary the comparison with the integral case. This is a clear advantage with respect to the approaches that employ second-order FRF and/or the coherence function. Moreover, it is noteworthy that the bicoherence computation requires one signal, whilst the FRF and coherence estimate needs two measurements. In addition, it is interesting to note that the bicoherence of Fig. 6 has a frequency resolution which is much lower than that of FRF and coherence functions of the Figs. 3, 4, and 5. Nevertheless, it has higher sensitivity to the statistical dependency of spectral components than that of the second-order functions.

By observing the bicoherence's contour plot of Fig. 7, it is possible to understand how the system resonances interact causing the birth of non-linear components in the case of the damaged beam. The highest bicoherence peak is located at the frequency pair (170, 400) Hz. This indicates a coupling between frequency components at the triplet (170, 400, 570) Hz, and is a manifestation of the fact that the two modes at frequency 170 Hz, and 400 Hz interact and lead to the combinational resonance at 570 Hz. In fact, the non-linear component, which is visible in the FRF plot of Fig. 4(b), rises just around to the frequency 570 Hz. Figure 7 shows other couplings between spectral components, but these occurrences are not visible in the FRF of Fig. 4(b).

In conclusion, the bispectral analysis provide additional insight for

identifying the dynamic response of structural's non-linear systems.

CONCLUSIONS

The dynamic behaviour of a beam with a breathing crack is studied by means of linear and higher order spectral analysis. In particular, the study is devoted to inspect the non-linearity of the damaged structure. The power spectrum is of limited value in detecting the system non-linearities. On the contrary, the second-order FRF and coherence functions are able to give a clear indication about the presence of non-linearity. However, the comparison between the damaged and integral case is needed, that is, if these second-order functions were unknown for the integral beam, the crack monitoring would be impossible. Moreover, the FRF and coherence estimates need two signals. Conversely, the bicoherence function, which is the normalisation of the third-order spectrum, can be evaluated from a single sensor measurement. From the bicoherence it is possible to say whether or not non-linearities occur in the system or, in other words, this signal processing technique is able to detect the presence of a structural damage in the beam. Since the bicoherence measures the degree of statistical dependency between spectral components without reference their amplitudes, it detects the non-linear interactions even in those cases where the resultant spectral component are hardly noticeable in the second-order functions, such as the power spectra. In addition, the bispectral approach is not affected by environmental factors, therefore this procedure may be used to improve the reliability and effectiveness of damage diagnostic techniques.

REFERENCES

1. Cawley, P. and Adams, R. D., The Location of Defects in Structures from Measurements of Natural Frequencies. *Journal of Strain Analysis*, 1979, **14**, 49-57.
2. Rizos, F., Aspragathos, N. and Dimarogonas, A. D., Identification of Crack Location and Magnitude in a Cantilever Beam from the Vibration Modes. *Journal of Sound and Vibration*, 1990, **138**(3), 381-388.
3. Al-Qaisia, A. and Meneghetti, U., Crack Localization in Stepped Beams. *Meccanica*, 1997, **32**, 315-325.
4. Gudmunson, P., The Dynamic Behaviour of Slender Structures with Cross-Sectional Cracks. *Journal of Mechanics and Physics of Solids*, 1983, **31**(4), 329-345.
5. Ibrahim, A., Ismail, F. and Martin, H. R., Modelling of the Dynamics of Continuous Beam including Nonlinear Fatigue Crack. *Journal of Analytical, Experimental Modal Analysis*, 1987, **2**, 76-82.
6. Ismail, F., Ibrahim, A. and Martin, H. R., Identification of Fatigue Cracks from Vibrating Testing. *Journal of Sound and Vibration*, 1990, **140**(2), 305-317.
7. Friswell, M. I. and Penny, J. E. T., A Simple Nonlinear Model of a Cracked Beam. *Proceedings of X International Modal Analysis Conference, San Diego, CA*, 1992,

- 1, 516-521.
8. Chu, Y. C. and Shen, M. H. H., Analysis of Forced Bilinear Oscillators and the Application to Cracked Beam Dynamics. *AIAA Journal*, 1992, 30(10), 2512-2519.
9. Krawczuk, M. and Ostachowicz, W., Forced Vibrations of a Cantilever Timoshenko Beam with a Closing Crack. *Proceedings of ISMA 19, Leuven, Belgium*, 1994, 3, 1067-1078.
10. Choi, D., Chang, J., Stearman, R.O. and Powers, E.J., Bispectral Identification of Nonlinear Mode Interactions. *Proceedings of 2nd International Modal Analysis Conference, Orlando, FL*, 1984, 2, 602-609.
11. Rivola, A. and White, P. R., Detecting system non-linearities by means of higher order statistics. *Proceedings of the 3rd International Conference on Acoustical and Vibratory Surveillance Methods and Diagnostic Techniques, Senlis, France*, 1998, 1, 263-272.
12. McConnell, K.G., *Vibration Testing: Theory and Practice*, John Wiley & Sons, New York, 1995.
13. Bendat, J. S. and Piersol, A. G., *Engineering Applications of Correlation and Spectral Analysis*, John Wiley & Sons, New York, 1980.
14. Kim, Y. C. and Powers, E. J., Digital Bispectral Analysis and its Applications to Nonlinear Wave Interactions. *IEEE Transactions on Plasma Science*, 1979, PS-7, 120-131.
15. Fackrell, J. W. A. and McLaughlin, S., The Higher Order Statistics of Speech Signals. *Proceedings of the IEE Colloquium on Techniques in Speech Signal Processing, London, UK*, 1994, 138(7), 1-6.
16. Fackrell, J. W. A., White, P. R., Hammond, J. K., Pinnington, R. J. and Parsons, A. T., The Interpretation of the Bispectra of Vibration Signals: Part 1: Theory. *Mechanical Systems and Signal Processing*, 1995, 9(3), 257-266.
17. Fackrell, J. W. A., White, P. R., Hammond, J. K., Pinnington, R. J. and Parsons, A. T., The Interpretation of the Bispectra of Vibration Signals: Part 2: Experimental Results and Applications. *Mechanical Systems and Signal Processing*, 1995, 9(3), 267-274.
18. Rivola, A. and White, P. R., Bispectral Analysis of the Bilinear Oscillator with Application to the Detection of Fatigue Cracks. *Journal of Sound and Vibration*, 1998, 216(5), 889-910.
19. Ewins, D. J., *Modal Testing: Theory and Practice*, Research Studies Press, Letchworth, 1984.
20. Mitchell, L.D., Improved Methods for the Fast Fourier Transform (FFT) Calculation of the Frequency Response Function. *Journal of Mechanical Design*, 1982, 104, 277-279.
21. Collis, B., White, P. R. and Hammond, J. K., Higher Order Spectra: the Bispectrum and Trispectrum. *Mechanical Systems and Signal Processing*, 1998, 12(3), 375-394.
22. Chandran, V. and Elgar, S., A General Procedure for the Derivation of Principle Domains of Higher Order Spectra. *IEEE Transactions on Signal Processing*, 1994, 42(1), 229-233.

PARAMETER IDENTIFICATION OF A SINGLE DEGREE OF FREEDOM DYNAMICAL SYSTEM BASED ON PHASE SPACE VARIABLES

Nikola Jakšić¹, Miha Boltežar², Anton Kuhelj³

¹MSc, postgraduate student, ²Lecturer in Mechanics, ³Professor of Mechanics, all University of Ljubljana,
Faculty of Mechanical Engineering, Aškerčeva 6, 1000 Ljubljana, Slovenia

ABSTRACT

A new method of parameter identification for a single-degree-of-freedom (s.d.o.f.) system is presented. It uses free responses of the system's phase space to derive the acceleration. When the state space is reconstructed, the parameters of the equation of motion of the model under consideration can be estimated by solving a system of algebraic equations. The idea is based on the fact that the differential equation of motion is an algebraic equation, if the parameters are considered to be unknowns. The method has been tested on a Duffing oscillator with different sets of parameters, at different sampling rates of the signals of the phase space and at different signal to noise ratios – SNRs.

1. INTRODUCTION

The estimation of model parameters of mechanical systems is an area which attracts considerable attention. To predict the behaviour of the dynamical system a mathematical model of the system should be deduced. The task is to determine the parameters of the model's equation of motion on the basis of information contained in the system's dynamical response. There are several ways of model parameter identification based on the system's behaviour.

The study of the parameter identification of a forced system with combined viscous damping and Coulomb dry friction in the resonant region has been achieved by curve fitting of the data presented in the Kennedy-Pancu plot [1,2]. This method is suitable for lightly damped systems. On the other hand, a number of studies consider the free vibrations of the single-degree-of-freedom (s.d.o.f.) system with combined viscous damping and Coulomb dry friction [3-5]. These approaches use only amplitude decay of the displacement response of the system. Any other information in the signal is neglected. A completely different approach to parameter identification of assumed polynomials for the description of non-linearities in restoring and damping forces within a forced dynamical system has been used in [6]. This approach uses approximation theory with the polynomials of Tschebishev, but is unable to deal with dry friction and the properties of the system that depend on the combination of displacement and velocity. The results of the methods in [3-6] are obtained in the time domain. Another class of methods that can be used for parameter identification includes the input-output models of NARMAX [7] and AVD [8,9]. The NARMAX model provides the output variable and the FRFs. It offers a way of achieving parameter identification of a non-linear system by knowing the model and time series of displacement and velocity. It has been shown [8,9] that the AVD model gives more accurate results in the time and frequency domain, but still requires simultaneous data of the displacement, velocity and acceleration. Both

methods need far more points than the number of parameters of the model to be estimated. An experimental method, which provides a means of identifying the linear and non-linear damping for a s.d.o.f. system, is proposed in [10] using analysis in the frequency domain.

In this paper a new method is proposed that is simple and could be used on different classes of problems concerning parameter identification of second-order autonomous differential dynamical systems. The single-degree-of-freedom (s.d.o.f.) mechanical systems were taken into consideration using their free vibration responses including both the displacement and velocity. The method is based on a geometrical representation of the solutions of the differential equation of motion. The solutions consist of a family of curves governed by two parameters. Only one curve (trajectory) is realised with the initial conditions. Each of the points on the trajectory in the state space satisfies the solution of the differential equation of motion. On the other hand, the differential equation of motion can be represented by an algebraic equation, if the parameters are considered to be unknowns. Hence, to estimate n parameters of the model's equation of motion, theoretically only n points on the trajectory in the state space are needed, and the problem is transformed to one of solving a system of algebraic equations. The preliminary results [11] show that the method gives usable results even when the simplest algorithms for reconstructing the acceleration are used.

2. THE METHOD

The task is to characterise a dynamical system with a chosen dynamical model. Let us consider that the type of differential equation of motion is known and the phase space portrait of the system under consideration is also known. The latter assumes that the discrete values of the phase space variables (displacement and velocity) of the system are measured.

The method for identification of the parameters of autonomous s.d.o.f. systems can be divided into two parts:

Reconstruction of the state space, meaning the reconstruction of the missing signal of the acceleration and smoothing the noisy measured time series of the phase space by means of interpolation and/or approximation. In this paper several kinds of splines are used in order to numerically derive acceleration and to smooth noisy data. Cubic splines [12,13,16], Hermitian splines of the 5th degree [12,16] and Splines of the 5th degree are used to derive acceleration from the phase space portrait of the system in the case of a high SNR. In the case of a low or medium SNR the Cubic approximation splines [12] are added in order to derive acceleration and to smooth the time series.

Computation of the parameters can be achieved by a least squared fit of the chi squared merit function deduced from the equation of motion since the system of the equation is predefined. Another way is to compute n parameters from n equations at n points of state space. To improve the statistics of the estimated parameters one can further average the estimates using different sets of points. We will refer to the first approach as regression solving and to the second approach as equation solving.

The equation of free vibration of the s.d.o.f. system can be written as:

$$\ddot{\varphi} + F(\dot{\varphi}, \varphi, a_1, \dots, a_n) = 0 \quad (1)$$

where φ is a variable, F is the scalar function and a_1, \dots, a_n are n coefficients to be estimated. If the substitution of the phase space variables is applied:

$$\begin{aligned} x &= \varphi \\ y &= \dot{\varphi} \end{aligned} \quad (2)$$

the equation of motion can be written as:

$$z + F(y, x, a_1, \dots, a_n) = 0. \quad (3)$$

where z denotes acceleration and x, y and z are in fact the state space variables.

If the acceleration is known or can be estimated, then since the trajectory in the phase space is known, the chi squared merit function can be written as:

$$\chi^2 = \sum_{i=1}^m [z + F(y_i, x_i, a_1, \dots, a_n)]^2 \quad (4)$$

where m is number of points of the responses, usually $m > n$. The maximum likelihood estimation of the parameters is reached by minimising the merit function over the parameters.

On the other hand, in the predefined system of equations, only the set of n algebraic equations to calculate n coefficients at n different points of the state space could be chosen and written as:

$$\begin{aligned} z_1 + F(y_1, x_1, a_1, \dots, a_n) &= 0 \\ &\vdots \\ z_n + F(y_n, x_n, a_1, \dots, a_n) &= 0 \end{aligned} \quad (5)$$

where (x_i, y_i) represents a point on the trajectory in the phase space and z_i is known or estimated acceleration at point i . The method enables one to estimate n parameters by knowing only n points in the phase space. To improve the statistics of the estimated parameters one can further average the estimates using different sets of points. If there are m points in the phase space at which the acceleration is known or could be estimated then the total number of different sets of parameters is given by the binomial coefficient $C_m^{(n)}$:

$$C_m^{(n)} = \binom{m}{n} = \frac{m!}{n!(m-n)!} \quad (6)$$

Hence, there are $C_m^{(n)}$ averages of the parameters possible for improving the statistics of the estimated parameters. So estimated parameters could be further smoothed by neglecting the estimates that are not within the interval of ± 1 standard deviation around the original mean value. The new mean value, as the estimated value of the parameter, is computed from the remaining estimates.

3. METHOD TESTING

The method has been tested on a strongly non-linear Duffing oscillator. The equation of motion is:

$$\ddot{\varphi} + 2\delta\omega_0\dot{\varphi} + \omega_0^2\varphi + \varepsilon\varphi^3 = 0 \quad (7)$$

and can be rewritten as:

$$z + 2\delta\omega_0 y + \omega_0^2 x + \varepsilon x^3 = 0 \quad (8)$$

where δ corresponds to the viscous damping ratio of a linearised system, ω_0 corresponds to the non-damped natural frequency of a linearised system, and ε is the coefficient of non-linearity of a spring in a Duffing system.

A positive value of ε characterises a hardening spring, negative value characterises a softening spring and a value of zero for ε characterises a linear spring. The parameters δ , ω_0 , ε are called natural parameters.

The Parameters governing the equation of motion can also be chosen as:

$$\begin{aligned} a &= 2\delta\omega_0 \\ b &= \omega_0^2 \\ c &= \varepsilon \end{aligned} \quad (9)$$

and named method parameters. The equation of motion can then be given in the form:

$$z + ay + bx + cx^3 = 0. \quad (10)$$

The task is to compute parameters a , b and c from the dynamic responses of displacement and velocity. The responses have been numerically integrated with the Runge-Kutta method with an error estimation of $O(h^5)$, where h denotes the constant integration step. The used variables had an extended precision of 80 bits. In Figure 1, the displacement, velocity and acceleration are shown for the natural parameters $\omega_0 = 1$ rad/s, $\delta = 0.1$, $\varepsilon = 1.5$ rad/m²s², and initial conditions $x(0) = 1$ m and $y(0) = 0$ m/s. This has been chosen as the default set of natural parameters. In the same Figure, the phase portrait is shown. The integration step has been chosen as $h = 10^{-4}$ s to minimise the integration error. The maximum integration error of displacement and velocity has been estimated to be $e_x = 1.2 \cdot 10^{-19}$ m and $e_y = 3.5 \cdot 10^{-19}$ m/s respectively.

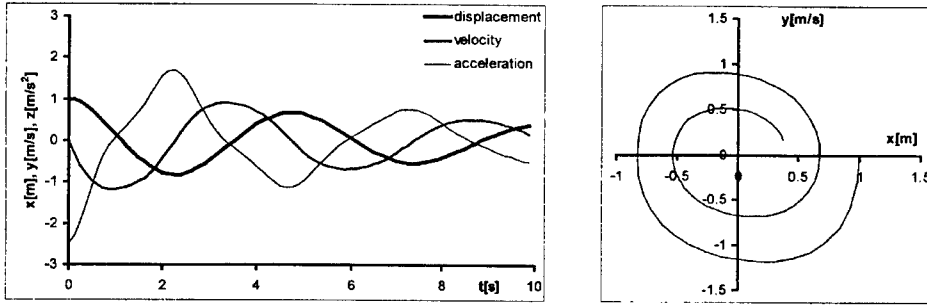


Figure 1: The responses of a Duffing system at $\omega_0 = 1$, $\delta = 0.1$, $\varepsilon = 1.5$ and the phase portrait

The method's behaviour has been tested on Duffing systems by varying: the values of damping ratio δ , the number of samples per cycle and the SNR of the phase portrait.

3.1 The influence of varying the damping ratio δ

The responses for different values of δ have been resampled to 40 samples in 10 seconds, which gives approximately 20 samples per cycle for the default parameter set. The responses for several values of $\delta = 1.0$, 0.5, 0.0 and -0.1 are depicted in Figure 2 and for the value $\delta = 0.1$ in Figure 1.

The non-linear nature of the Duffing oscillator is best seen in the shape of the acceleration signal. The Duffing system has only one equilibrium point at the origin of the phase plane in the case of a non-negative value of ε . The negative damping ratio gives rise to amplitude values and shortens the cycle time with increasing amplitudes, Figure 2a. The equilibrium point is an unstable focus. Zero damping relates to the conservative system in which

the amplitudes and periods are constant, Figure 2b. There is a centre in the origin of the phase plane. In the case of positive damping the amplitude decay of the responses is visible, Figures 1, 2c, 2d. There is a stable focus at the origin of the phase plane in the case of $0 < \delta < 1$, an inflected node in the case of $\delta = 1$ and a node in the case of $\delta > 1$. The acceleration has been reconstructed by derivation of Cubic splines and Splines of the 5th degree interpolation of velocity time series and by derivation of Hermitian splines of the 5th degree interpolation of both the displacement and velocity time series. In the case of the Cubic splines interpolation of velocity the zero 3rd derivatives and in case of Hermitian splines the zero 4th derivatives at the boundary points have been used to describe the boundary conditions. In the case of Splines of the 5th degree the not-a-node condition for the 1st and $(m-1)$ th point and zero 4th derivatives at boundary points have been used to specify boundary conditions. It is also important to note that both approaches, regression and equation solving, have been applied in order to compute the method parameters a , b and c . The boundary points have not been included in the computation of these parameters.

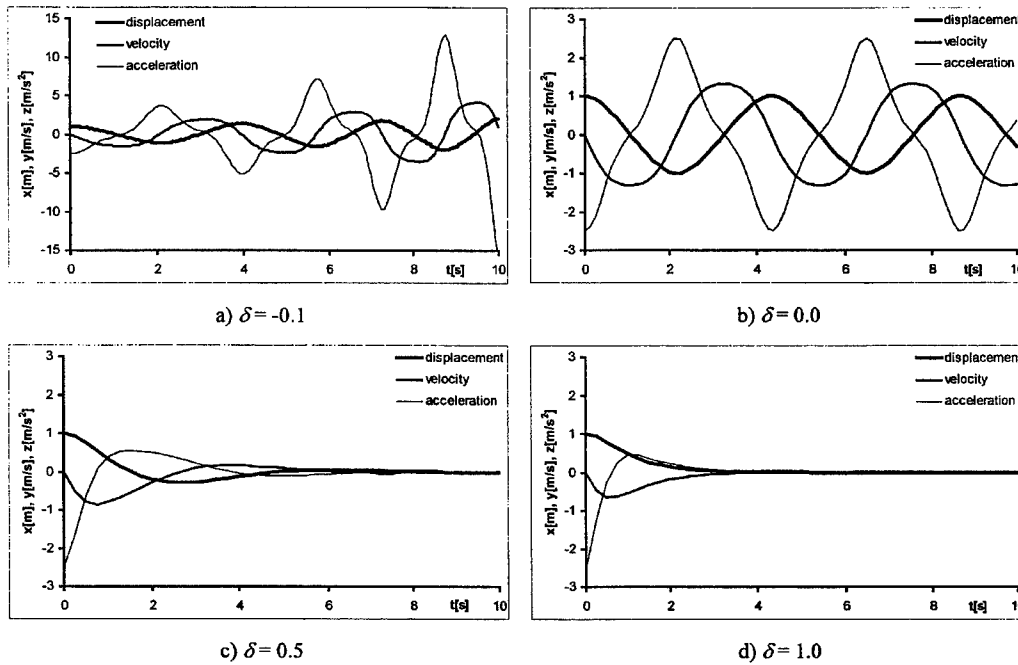


Figure 2: The responses of Duffing system at different δ and $\omega_0 = 1$, $\varepsilon = 1.5$

The results of parameter identification of the system at various values of δ are shown in Table 1. The relative errors of the estimated values of the parameters are presented in Table 2. In both Tables the variations of δ are given in the first column, true values of the method parameters a , b and c are given in the second column for given δ . Each column of the different spline interpolations is divided into two halves. The left half, denoted as equation, presents results obtained by equation solving and the right half, denoted as regression, presents results obtained by regression solving.

In Table 2, the row at $\delta=0$ is shaded and true values are placed there since the relative error can not be computed for the zero valued parameter. It can be seen that the estimates of parameter c are somewhat poorer when compared with the other two at higher damping, implying that the method should be used in regions of the time series where the transients have not, from the engineering point of view, died out.

δ	a	Cubic splines		Hermitian splines of the 5 th degree		Splines of the 5 th degree	
	b	equation	regression	equation	regression	equation	regression
	c						
1	2	1.9997	1.9888	2.0000	2.0021	2.0000	2.0602
	1	0.9997	0.9843	1.0000	1.0030	0.9999	1.0758
	1.5	-2.7501	1.5118	1.3340	1.4976	1.3400	1.4643
0.5	1	1.0001	1.0012	1.0000	1.0000	1.0000	1.0008
	1	1.0000	0.9973	1.0000	0.9999	0.9999	0.9980
	1.5	1.5162	1.5277	1.4942	1.5005	1.4755	1.5170
0.1	0.2	0.1999	0.1993	0.2000	0.2000	0.2000	0.1998
	1	0.9999	1.0007	0.9999	0.9996	0.9999	0.9993
	1.5	1.5049	1.5012	1.4999	1.5011	1.5023	1.5027
0	0	-0.0064	-0.0002	0.0003	0.0000	0.0013	-0.0002
	1	1.0163	1.0122	0.9986	0.9985	1.0101	1.0015
	1.5	1.4833	1.4837	1.5019	1.5022	1.4954	1.4983
-0.1	-0.2	-0.2026	-0.2039	-0.2001	-0.2001	-0.2012	-0.2000
	1	1.0307	1.1070	0.9958	0.9928	1.0014	1.0232
	1.5	1.4860	1.4436	1.5018	1.5041	1.4987	1.4880

Table 1: The influence of varying δ on parameter identification for different spline interpolations and for different approaches to parameter computation

δ	a	Cubic splines		Hermitian splines of the 5 th degree		Splines of the 5 th degree	
	b	equation	regression	equation	regression	equation	regression
	c						
1	2	0.00 %	-0.56 %	0.00 %	0.10 %	0.00 %	3.01 %
	1	0.00 %	-1.57 %	0.00 %	0.30 %	-0.01 %	7.58 %
	1.5	0.00 %	0.79 %	-11.07 %	-0.16 %	-10.67 %	-2.38 %
0.5	1	0.01 %	0.12 %	0.00 %	0.00 %	0.00 %	0.08 %
	1	0.00 %	-0.27 %	0.00 %	-0.01 %	-0.01 %	-0.20 %
	1.5	1.08 %	1.85 %	-0.39 %	0.03 %	-1.63 %	1.13 %
0.1	0.2	0.00 %	-0.35 %	0.00 %	0.00 %	0.00 %	-0.10 %
	1	-0.01 %	0.07 %	-0.01 %	-0.04 %	-0.01 %	-0.07 %
	1.5	0.33 %	0.08 %	-0.01 %	0.07 %	0.15 %	0.18 %
0	0	-0.0064	-0.0002	0.0003	0.0000	0.0013	-0.0002
	1	1.63 %	1.22 %	-0.14 %	-0.15 %	1.01 %	0.15 %
	1.5	-1.11 %	-1.09 %	0.13 %	0.15 %	-0.31 %	-0.11 %
-0.1	-0.2	1.30 %	1.95 %	0.05 %	0.05 %	0.60 %	0.00 %
	1	3.07 %	10.70 %	-0.42 %	-0.72 %	0.14 %	2.32 %
	1.5	-0.93 %	-3.76 %	0.12 %	0.27 %	-0.09 %	-0.80 %

Table 2: The relative errors in parameter identification influenced by varying δ for different spline interpolations and for different approaches to parameter computation

In Figure 2c one can see that after 7s, and in Figure 2d after 4s, the transients practically die out. One can also see that the results are slightly better for low damping than for zero or negative damping. This happens because the peak amplitudes of acceleration become increasingly sharp with descending values of δ and are therefore more difficult to simulate with polynomial splines. The results in Table 2 indicate that errors rarely give rise to values of more than a few percent. The regression solving has no real advantage with respect to the quality of results when compared to equation solving, but the latter needs much more computational effort and has failed to estimate parameter c at $\delta = 1$ for Cubic splines. As a consequence, the cells in Table 1 and 2 are shaded for $\delta = 1$ with Cubic splines.

3.2 The influence of varying the number of samples per cycle

The responses for the default parameter set have been resampled to 10, 20, 40, 80 samples in 10 seconds which gives approximately 5, 10, 20 and 40 samples per cycle respectively, Figure 3.

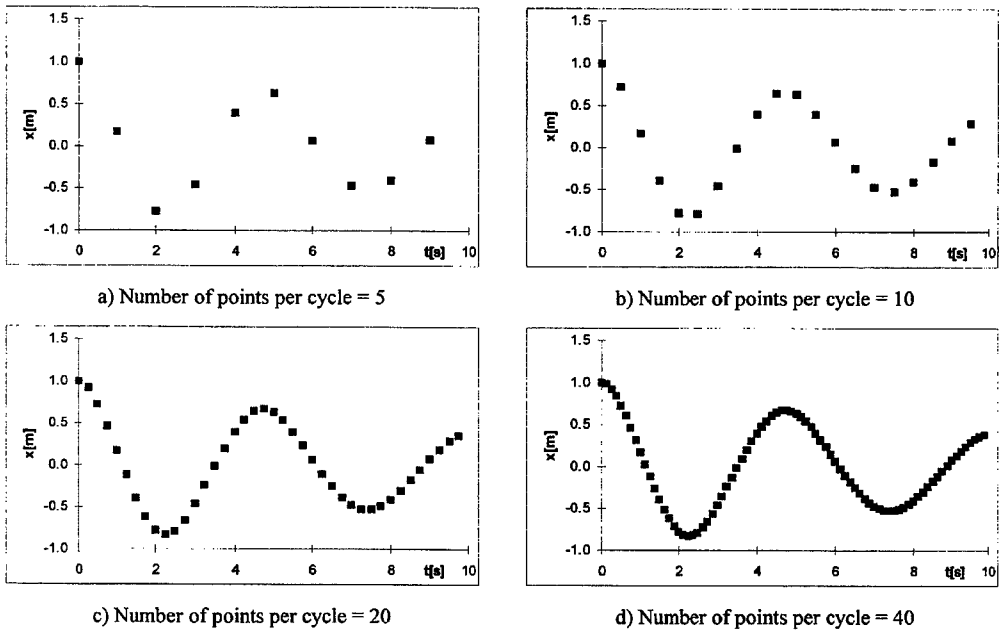


Figure 3: The responses of Duffing system for a default set of parameters and different sampling rates

The acceleration has been reconstructed using the same techniques as in section 3.1 and the parameters have been computed using both approaches. The results of parameter identification of the system for various values of samples per cycle are shown in Table 3. The relative errors of the estimated values of the parameters are presented in Table 4. In both Tables, the variations of samples per cycle are given in the first column, true values of the method parameters are given in the second column for the default parameter set. Each column of different spline interpolations is again divided into two halves, one denoted as equation and the other denoted as regression, and presents the results obtained by equation solving and regression solving respectively.

It can be seen that the estimates of parameters are well within 10% as soon as the sampling rate is greater than or equal to 10 samples per cycle. At a sampling rate of 20 samples per cycle or more, the errors of the estimation fall below 1%. The 5 samples per cycle represents a very poor sampling rate, Figure 3a, and the method fails to produce results, even from the engineering point of view, unless the Hermitian splines are used. They produced estimates of parameters with an error of less than 1%, but as will be demonstrated in the next section, the Hermitian splines are extremely sensitive to noise. It is clear that sampling rates of 10 samples per cycle or more should be used. One can see again that regression solving gives the same quality of results as equation solving but that the latter needs much more computational effort.

Samp. per cycle	<i>a</i>	Cubic splines		Hermitian splines of the 5 th degree		Splines of the 5 th degree	
	<i>b</i> <i>c</i>	equation	regression	equation	regression	equation	regression
5	0.2	0.1487	0.1576	0.2018	0.1998	0.1579	0.1718
	1	1.3996	1.5504	1.0054	1.0106	1.3729	1.5600
	1.5	0.3060	0.0932	1.4873	1.4710	0.4173	0.1191
10	0.2	0.2042	0.2002	0.1995	0.1993	0.1994	0.1959
	1	1.0344	1.0476	0.9991	0.9975	1.0121	1.0217
	1.5	1.3562	1.3748	1.4968	1.5033	1.4053	1.4494
20	0.2	0.1999	0.1993	0.2000	0.2000	0.2000	0.1998
	1	0.9999	1.0007	0.9999	0.9996	0.9999	0.9993
	1.5	1.5049	1.5012	1.4999	1.5011	1.5023	1.5027
40	0.2	0.2000	0.2000	0.2000	0.2000	0.2000	0.2000
	1	1.0000	0.9996	1.0000	0.9999	1.0000	1.0000
	1.5	1.5001	1.5013	1.5000	1.5002	1.5000	1.5001

Table 3: The influence of the number of samples per cycle on parameter identification for different spline interpolations and for different approaches to parameter computation

Samp. per cycle	<i>a</i>	Cubic splines		Hermitian splines of the 5 th degree		Splines of 5 th degree	
	<i>b</i> <i>c</i>	equation	regression	equation	regression	equation	regression
5	0.2	-25.65 %	-21.20 %	0.90 %	-0.10 %	-21.05 %	-14.10 %
	1	39.96 %	55.04 %	0.54 %	-0.25 %	37.29 %	50.00 %
	1.5	-79.60 %	-93.89 %	-0.85 %	0.22 %	-72.18 %	-92.06 %
10	0.2	2.10 %	0.10 %	-0.25 %	-0.35 %	-0.30 %	-2.05 %
	1	3.44 %	4.76 %	-0.09 %	-0.25 %	1.21 %	2.17 %
	1.5	-9.59 %	-8.35 %	-0.21 %	0.22 %	-6.31 %	-3.37 %
20	0.2	0.00 %	-0.35 %	0.00 %	0.00 %	0.00 %	-0.10 %
	1	-0.01 %	0.07 %	-0.01 %	-0.04 %	-0.01 %	-0.07 %
	1.5	0.33 %	0.08 %	-0.01 %	0.07 %	0.15 %	0.18 %
40	0.2	0.00 %	0.00 %	0.00 %	0.00 %	0.00 %	0.00 %
	1	0.00 %	-0.04 %	0.00 %	-0.01 %	0.00 %	0.00 %
	1.5	-0.01 %	0.09 %	0.00 %	0.01 %	0.00 %	0.01 %

Table 4: The relative errors in parameter identification influenced by varying the number of samples per cycle for different spline interpolations and for different approaches to parameter computation

3.3 The influence of varying the SNR

The noise is added to the time series by means of simulating the A/D conversion. The A/D converter used in this case rounds the real values of the integrated time series to the nearest quantization level. The full-scale level of the A/D converter X_m has been optimally chosen for each signal separately. The quantization error e_n is defined as the difference between the quantized sample and true sample value and so it follows that:

$$-\Delta/2 < e_n \leq \Delta/2 \quad (11)$$

where Δ is the step size of the quantizer defined as:

$$\Delta = \frac{2X_m}{2^{B+1}} = \frac{X_m}{2^B} \quad (12)$$

where $B+1$ stands for the number of bits of the quantizer. The quantization error e_n is assumed to be a uniformly distributed white-noise sequence having zero mean and a variance of:

$$\text{var}(e) = \Delta^2/12. \quad (13)$$

The signal to noise ratio (SNR) in dB is defined as [14]:

$$\text{SNR} = 10 \cdot \log \left(\frac{\text{var}(x)}{\text{var}(e)} \right) \approx 6B - 1.25 \quad (14)$$

where $\text{var}(x)$ is the variance of the signal under consideration.

The responses for different values of SNR have been resampled to 40 samples in 10 seconds, which gives approximately 20 samples per cycle for the default parameter set. The responses for several values of SNR are shown in Figure 4.

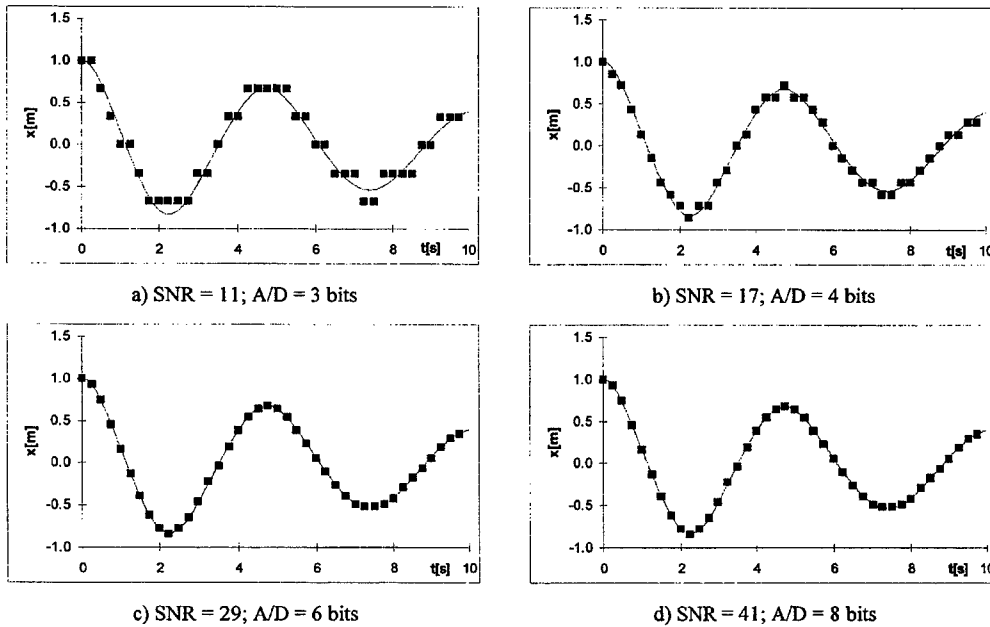


Figure 4: The responses of a Duffing system for default parameter set and at different SNR levels

It can be seen in Figure 4 that the noise signal from the 3 and 4 bit A/D conversions visually differs from the noise free signal. The difference is hard to see for the 6-bit conversion and can not be seen for higher bit conversions.

Approximation cubic splines [12] are added to the known reconstruction techniques of the previous two sections. The Approximation splines are used to smooth the displacement and velocity time series and to derive acceleration from velocity. In all the cases of using the Approximation cubic splines the zero 3rd derivatives at boundary points are used. The parameters have been computed using both equation and regression solving. The boundary points have not been included in the computation of the parameters.

The results of parameter identification of the system at various SNR values are shown in Table 5. The relative errors of the estimated values of the parameters are presented in Table 6. In both Tables the variations of SNR are given in the second column, the corresponding values of the bits of the A/D converter are given in the first column and the true values of the method parameters are given in the third column. Each column of different spline interpolations is again divided into two halves, one denoted as equation and the other denoted as regression. They present the results obtained by equation solving and regression solving respectively. The estimated parameters from the real noisy state space are given in the last two columns.

The shaded cells in Tables 5 and 6 identify the combination of parameters where the method fails to produce any reasonable results. The true power of regression solving is revealed when dealing with noisy signals. Not only does the regression solving need much less computational effort than the equation solving, the latter failed to produce any reasonable results for A/D conversions up to 6 bits, except when using the Approximation cubic splines. One can see that the Hermitian splines are extremely sensitive to noise. The results for a $\text{SNR} \geq 30$ dB are in the error range of less than 5 % and for a $\text{SNR} \geq 65$ dB the noise does not significantly influence the results, the errors are predominantly due to the estimation of acceleration. The method is capable of computing only a rough estimation of the parameters for a SNR smaller than 20 dB within some 30 % of the true value by using the approximation splines.

A/D bits	SNR dB	a b c			Cubic splines		Hermitian splines of the 5 th degree		Splines of the 5 th degree		Approximation cubic splines		Original state space	
					equation	regression	equation	regression	equation	regression	equation	regression	equation	regression
3	11	0.2			-1e20	0.1177	-5e20	0.8131	5e19	0.1147	0.1624	0.1476	-8e17	0.1118
		1			7e17	0.8152	1e18	-1.9882	5e17	0.8288	0.6269	1.0522	2e18	0.9861
		1.5			5e10	2.1571	-1e18	20.8706	6e17	2.1185	3.0953	1.6643	3e15	1.2656
4	17	0.2			-2e14	0.1597	-6e14	0.1560	-1e14	0.1612	0.1517	0.1461	8e11	0.1793
		1			4e15	0.7590	-2e16	-1.8094	5e15	0.7401	0.9071	0.9526	1e15	0.9865
		1.5			-7e15	2.1959	6e16	11.6000	4e14	2.2321	2.4400	1.8113	-2e14	1.5292
6	29	0.2			0.1189	0.1918	-0.4443	0.2404	0.1109	0.1924	0.1821	0.1928	0.2052	0.2016
		1			2e10	1.0287	-2e10	0.1508	5e10	1.0290	1.0343	1.0396	3e9	1.0108
		1.5			-7e11	1.4240	1e14	3.8021	-7e11	1.4262	1.4364	1.4324	3e12	1.4652
8	41	0.2			0.1994	0.1999	0.2029	0.2224	0.2002	0.2000	0.1925	0.1995	0.2029	0.1999
		1			-2.2581	1.0154	-4.4654	1.0955	-0.4225	1.0152	1.0694	1.0195	0.9490	1.0071
		1.5			2.5541	1.4753	1.2371	1.1581	2.6814	1.4731	1.5226	1.4676	1.7472	1.4985
12	65	0.2			0.2000	0.1993	0.2033	0.1992	0.1999	0.1998	0.2000	0.1994	0.2000	0.2000
		1			1.0002	1.0008	0.9891	0.9986	1.0000	0.9994	1.0001	1.0008	1.0000	1.0002
		1.5			1.4982	1.5006	1.4605	1.5060	1.4967	1.5024	1.4986	1.5007	1.4995	1.4990

Table 5: The influence of SNR on parameter identification for different spline interpolations and for different approaches to parameter computation

A/D bits	SNR dB	a b c			Cubic splines		Hermitian splines of the 5 th degree		Splines of the 5 th degree		Approximation cubic splines		Original state space	
					equation	regression	equation	regression	equation	regression	equation	regression	equation	regression
3	11	0.2				-41.15 %				-42.65 %	-1.88 %	-26.20 %		-44.10 %
		1				-18.48 %				-17.12 %	-37.31 %	5.22 %		-1.39 %
		1.5				43.81 %				41.23 %	106.35 %	10.95 %		-15.63 %
4	17	0.2				-20.15 %				-19.40 %	-24.15 %	-26.95 %		-10.35 %
		1				-24.10 %				-25.99 %	-9.29 %	4.74 %		-1.35 %
		1.5				46.39 %				48.81 %	62.67 %	20.75 %		1.95 %
6	29	0.2				-4.10 %				-3.80 %	-8.95 %	-3.60 %		0.80 %
		1				2.87 %				2.90 %	3.43 %	3.96 %		1.08 %
		1.5				-5.07 %				-4.92 %	-4.24 %	-4.51 %		-2.32 %
8	41	0.2				-0.05 %				0.00 %	-3.75 %	-0.25 %		-0.05 %
		1				1.54 %				1.52 %	6.94 %	1.95 %		0.71 %
		1.5				-1.65 %				-1.79 %	1.51 %	-2.16 %		-0.10 %
12	65	0.2				0.00 %				-0.05 %	0.00 %	-0.30 %		0.00 %
		1				0.02 %				0.00 %	0.01 %	0.08 %		0.00 %
		1.5				-0.12 %				-0.22 %	-0.09 %	0.05 %		-0.07 %

Table 6: The relative errors in parameter identification influenced by varying SNR for different spline interpolations and for different approaches to parameter computation

4. CONCLUSIONS

In this paper a new parameter identification method for the second-order autonomous differential dynamical systems is proposed. The method follows the idea of computing the parameters of the differential equation of motion, which can be represented as an algebraic equation, if the parameters are considered to be unknowns. The single-degree-of-freedom (s.d.o.f.) mechanical systems were taken into consideration using their free vibration responses including both the displacement and velocity.

It was shown that the method works well on different sets of parameters with errors generally well below 5 %. Sharp peak amplitude or decaying transients make reconstruction of the acceleration with polynomial splines difficult and less accurate. This may give rise to errors in the estimated parameters. The sampling rate of 10 samples per cycle is generally the lowest rate to ensure errors of the estimated parameters are below 5 % with the Splines of the 5th degree and under 10 % with the Cubic splines unless, the Hermitian splines are used at a high SNR. The lower degree of the spline polynomial seldom means higher accuracy. Noise makes the Hermitian splines practically unusable, and for a SNR less than 20 dB the parameters could be estimated only to within some 30 % of the true value by using the Approximation splines. The results for a $\text{SNR} \geq 30$ dB are in the error range of less than 5 % and for a $\text{SNR} \geq 65$ dB, noise does not significantly influence the results, the errors are predominantly due to the estimation of the acceleration. The results show that for a $\text{SNR} < 65$ dB the regression method should be used. It needs much less computational effort than the equation solving for all sets of points in state space and is therefore the recommended approach.

The results show that the method offers parameters estimation with good quality using a modest number of points for a wide range of s.d.o.f. systems. It offers easy ways for computing the parameters from the free vibrations' responses of s.d.o.f. systems. The method uses the complete information of signals for the parameter estimation. It is insensitive to initial conditions, and only the type of differential equation of motion needs to be known. It has been shown that for modest quality of parameter estimates only a few points of the phase space are needed at reasonably low sampling rates.

The main draw back of the method is in its sensitivity to noise. Free vibrations of s.d.o.f. systems tend to be simple. Only two types of attractor are known to exist [15], point attractor and limit cycle. Hence, filtering of a signal should not be an impossible task to perform and could help to improve the results of the parameter estimation.

5. REFERENCES

- [1] G.R. TOMLINSON, J.H. HIBBERT 1979 *Journal of Sound and Vibration* 64(2), 233-242. Identification of the dynamic characteristics of a structure with coulomb friction.
- [2] G.R. TOMLINSON 1980 *Journal of Sound and Vibration* 71(3), 443-451. An analysis of the distortion effects of coulomb damping on the vector plots of lightly damped systems.
- [3] P.H. MARKHO 1980 *Transactions of the ASME - Journal of Dynamic Systems, Measurement, and Control* 102, 283-286. On free vibrations with combined viscous and Coulomb damping.
- [4] F. BADRAKHAN 1985 *Journal of Sound and Vibration* 100(2), 243-255. Separation and determination of combined dampings from free vibration.

-
- [5] C.A. DE HILLERIN 1989 *Proceedings of the 7th international modal analysis conference, Las Vegas* **2**, 1123-1127. Free response to an initial displacement for a s.d.o.f system in the presence of dry friction and viscous damping.
- [6] H.G. NATKE, M. ZAMIROWSKI 1990 *ZAMM – Z. angew. Math. Mech.* **70**(10), 415-420. On methods of structure identification for the class of polynomials within mechanical systems.
- [7] S. CHEN, S.A. BILLINGS 1989 *International Journal of Control* **49**(3), 1013-1032. Representation of non-linear systems: the NARMAX model.
- [8] Q. CHEN, G.R. TOMLINSON 1994 *Mechanical Systems and Signal Processing* **8**(5), 531-549. A new type of time series model for the identification of non-linear dynamical system.
- [9] Q. CHEN, G.R. TOMLINSON 1996 *Transactions of the ASME - Journal of Vibration and Acoustic* **118**, 252-263. Parametric identification of systems with dry friction and nonlinear stiffness using a time series model.
- [10] H.J. RICE, J.A. FITZPATRICK 1991 *Transactions of the ASME - Journal of Vibration and Acoustic* **113**, 132-140. The measurement of nonlinear damping in single-degree-of-freedom system.
- [11] N. JAKŠIČ, M. BOLTEŽAR, A. KUHELJ 1999 *Congress of the Slovenian society of mechanics, Kuhljevi dnevi '99, Zemono, September 30th – October 1st*, 87-94. Identification of parameters of the autonomous dynamical systems of 2nd order in the phase space. (in Slovene)
- [12] G. ENGELN-MUELLGES, F. UHLIG: 1996, *Numerical algorithms with C*, Springer Verlag.
- [13] W.H. PRESS, B.P. FLANNERY, S.A. TEUKOLSKY, W.T. VETTERLING: 1992, *Numerical Recipes in Pascal, The Art of Scientific Computing*, Cambridge University Press.
- [14] A.V. OPPENHEIM, R.W. SCHAFFER: 1989, *Discrete-time Signal Processing*, Prentice-Hall.
- [15] J.M.T. THOMPSON, H.B. STEWART 1991 *Nonlinear dynamics and chaos, geometrical methods for engineers and scientists*. Chichester, New York, Brisbane, Toronto, Singapore: John Wiley and Sons.
- [16] J. PETRIŠIČ 1999 *Interpolation and computer graphics basics*. University of Ljubljana, Faculty of Mechanical Engineering. (In Slovene)

DAMAGE LOCALISATION USING NOVELTY INDICES

K. Worden, G. Manson & C. Remillat

Dynamics Research Group
Department of Mechanical Engineering
University of Sheffield
Mappin Street
Sheffield S1 3JD
United Kingdom

Abstract

One approach to the problem of damage detection is to use a novelty index to signal departures from normal condition. The object of the present paper is to investigate if the approach can yield information about damage location if more than one index is used. The novelty index here is constructed using outlier analysis. The approach is demonstrated on a simple Finite Element model of a framework structure.

INTRODUCTION

The problem of damage detection can be addressed at several levels. At the lowest level one wishes to know only if damage is present or not. It is to solve this problem that the discipline of *novelty* or *anomaly detection* has emerged recently. The technique - which has its roots firmly embedded in classical condition monitoring - seeks first to establish a description of normal condition for a system or structure and then to signal statistically significant departures from this condition.

There are numerous approaches to novelty detection, these include methods based on simple distance measures [1], probability density estimation (Gaussian mixture models and Parzen windows) [2, 3, 4] and artificial neural networks [5, 6, 7]. The method used in this paper is one of the simpler methods based on outlier statistics [8, 9], this simply uses Mahalanobis distance to measure the distance between a new measurement and the normal condition data.

The paper attempts to extend the use of novelty indices to the problem of damage localisation. The idea is to have a network of indices, one for each region of the structure and to use a neural network to interpret the patterns of firing for the indices when damage is present. The idea was motivated by the work in [10], where it was observed that transmissibilities

measured on different parts of a framework model were selectively sensitive to damages in different areas. In order to simplify matters here, the structure of interest will be a Finite Element model of a two-dimensional truss structure and the data used to construct the novelty indices will once again consist of measured transmissibilities.

The layout of the paper is as follows: Section Two will describe the truss structure and show examples of transmissibility data. Section Three will discuss briefly the theoretical basis of outlier analysis and Section Four will describe how a neural network is used to localise the damage.

THE FRAMEWORK MODEL

The structure of interest is a two-dimensional cantilever truss as shown in Figure 1. The supports are rigid and the joints between members are assumed to be pinned.

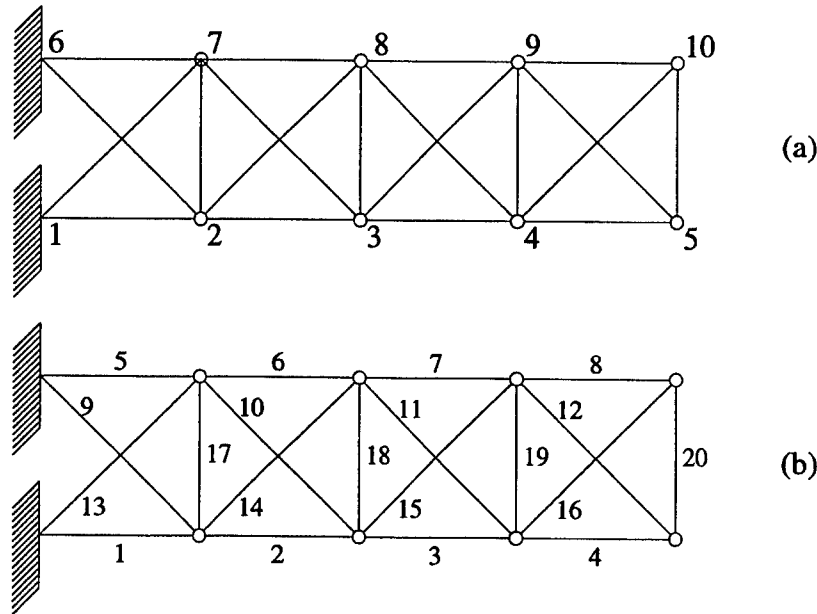


Figure 1. The framework structure: (a) node labelling, (b) element labelling.

Each member is considered to be made from 25.4 mm \times 6.4 mm aluminium strip and the framework is overall 1 m long by 0.25 m high. Each bay is square. The system was modelled using the ABAQUS Finite Element analysis system, all members are simple bar elements. The analysis provided displacement spectra for the responses at all nodes to a white noise excitation at node 5. A frequency range of 0 to 4000 Hz was adopted in order to encompass the first eight natural frequencies of the structure.

The displacement spectra were used to form the displacement transmissibilities across each member i.e. if nodes i_1 and i_2 bound member i , then the corresponding transmissibility T_i is simply Y_{i_2}/Y_{i_1} . For members 1, 5, 9 and 13 which have encastred ends, the displacement spectrum of the free end is used as a feature. Figure 2 shows an example - the transmissibility T_7 across element 7.

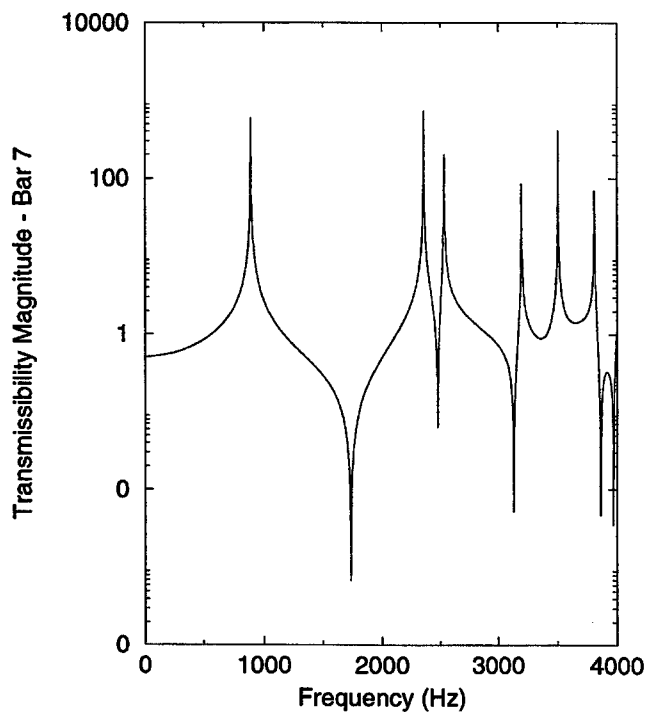


Figure 2. Transmissibility T_7 .

The undamaged natural frequencies were as follows:

Mode	Natural Frequency (Hz)
1	181.3
2	815.5
3	821.3
4	1837.2
5	2486.2
6	2799.1
7	3372.0
8	3424.6

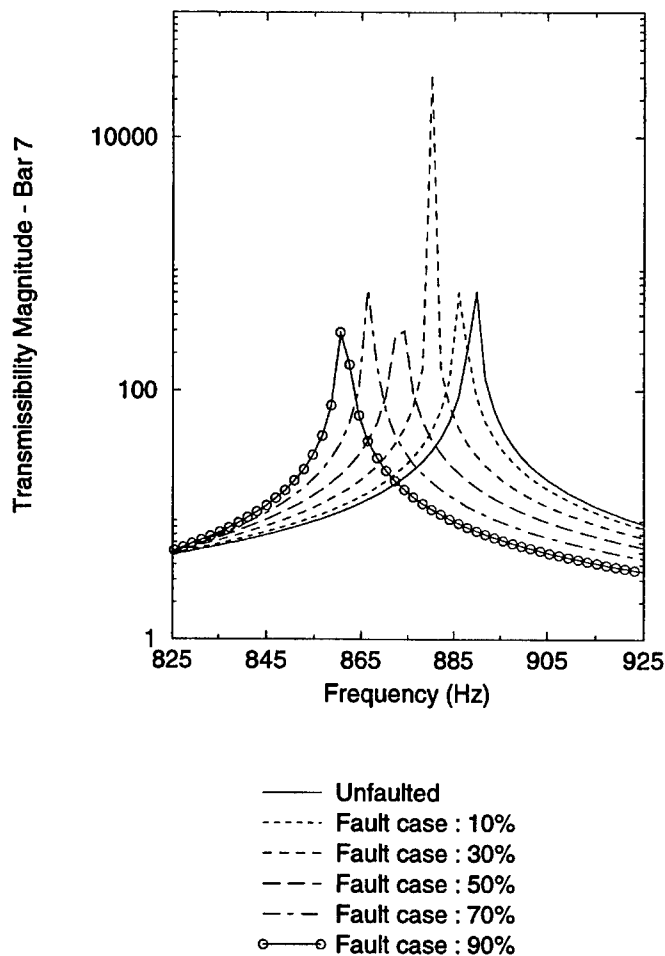


Figure 3. Selected pattern from Transmissibility T_7 .

In order to construct data which allowed the possibility of damage quantification as well as localisation, a large number of simulations were made. Each member in turn was subjected to a 10%, 30%, 50%, 70% and 90% reduction in stiffness and all the corresponding transmissibilities were generated. In order to obtain a diagnostic which was robust against noise, each pattern was copied a number of times and each copy was corrupted by a unique Gaussian noise vector - the RMS of the noise was taken as 1% of the peak transmissibility in each case. Each transmissibility was inspected visually in order to select for each a mode which showed significant *and* systematic movement in frequency as the damage progressed. Once a mode was identified, a 50-point window was taken about the relevant frequency to give a pattern for the novelty detector. Figure 3 shows the

mode selected for transmissibility T_7 and displays how it changes as damage severity increases.

In order to consider the localisation problem alone. Only the severity case of a 10% reduction in stiffness was used here.

This framework model was investigated in a previous paper [11]. In that study, the objective was to use strain measurements taken on the vertical and horizontal members to diagnose *complete removal* of the diagonal members. The current study is considerably more ambitious in that it seeks to locate 10% damage in *any* of the members. The price paid for the extra facility is the additional overhead on signal processing.

OUTLIER ANALYSIS

The problem of outlier detection is fairly simply stated: an outlier in set of observations is a point which is *discordant* with the rest i.e. sufficiently different to raise the suspicion that it was generated by a different mechanism to the rest. The theory is well-developed and only the briefest survey is given here; the reader is referred to [12] for more details.

The case of outlier detection in univariate data is fairly straightforward in that outliers must 'stick out' from one end or other of the data set. There are numerous discordancy tests but the most common, and the one whose extension to multivariate data is simplest is based on the deviation statistic and given by,

$$z_\zeta = \frac{|x_\zeta - \bar{x}|}{s} \quad (1)$$

where x_ζ is the potential outlier and \bar{x} and s the mean and standard deviation of the sample respectively. The latter two values may be calculated with or without the potential outlier in the sample. The statistic is then compared to some threshold value and the observation declared, or not, to be an outlier. The standard threshold values are based on the assumption that the underlying distribution of the data is Gaussian and are usually taken to be 3 or 4.

The discordancy test which is the multivariate equivalent of equation (1) is the Mahalanobis squared distance measure given by,

$$D_\zeta = (\{x_\zeta\} - \{\bar{x}\})^T [S]^{-1} \{x_\zeta\} - \{\bar{x}\} \quad (2)$$

where $\{x_\zeta\}$ is the potential outlier, $\{\bar{x}\}$ is the mean of the sample observations and $[S]$ the sample covariance matrix. The observations are assumed to be patterns in a p -dimensional space and to be n in number.

In order to label a multivariate observation as an outlier or an inlier there needs to be some threshold value against which the discordancy

value can be compared. This value is dependent on both the number of observations and the number of dimensions of the problem being studied.

A Monte Carlo method is typically used to arrive at the threshold value. The procedure is to construct a $p \times n$ matrix with each element being a randomly generated number from a zero mean and unity standard deviation normal distribution. The Mahalanobis squared distances are calculated for all the elements, using equation (2) where $\{\bar{x}\}$ and $[S]$ are inclusive measures (i.e. include the potential outlier), and the largest value stored. This process is repeated i.e. 1000 times whereupon the array containing all the largest Mahalanobis squared distances is ordered in terms of magnitude. The critical values for 5% and 1% tests of discordancy for a p -dimensional sample of n observations are then given by the Mahalanobis squared distances in the array above which 5% and 1% of the trials occur. If the outlier is not included in the calculation for the mean and covariance, a simple transformation on the inclusive threshold suffices to convert it to an exclusive measure.

The data for the novelty indices here consists of a number of 50-point vectors from the various transmissibility functions. If a novelty index for a given member 'fires' i.e. goes above threshold, then there is considered to be damage somewhere in the structure. Note that there is an implicit assumption in the use of the Mahalanobis distance that the underlying statistics of the normal condition are Gaussian. This will be true to a greater or lesser extent in each situation. However, in the case here, the noise is generated synthetically from a Gaussian distribution, so the outlier statistic is valid.

LOCALISATION OF DAMAGE

The first exercise in considering the damage data is to make sure that all damage cases cause at least one novelty index to fire. This is important, because if it is true the neural network localiser only needs to consider damaged data, the assumption being that firing of a novelty index automatically passes the data to the neural network. In fact, each damage case caused the majority of indices to fire, even for the 10% reduction. This was due to the fact that the Finite Element simulation used very little damping so that all resonant peaks were very sharp. This meant that the movement of the peaks when damage occurred caused a marked change in the patterns selected. The clarity of the damage indicators is shown in Figure 3. Because the object of this exercise is to localise a 10% reduction in stiffness, the sensitivity of the indices is useful. However, if an attempt had been made to judge severity of damage also, it would have likely failed. This is due to the fact that the novelty index corresponding to the lowest and highest damage in Figure 3 would have been very similar as neither of the peaks overlap to any great extent with the undamaged peak.

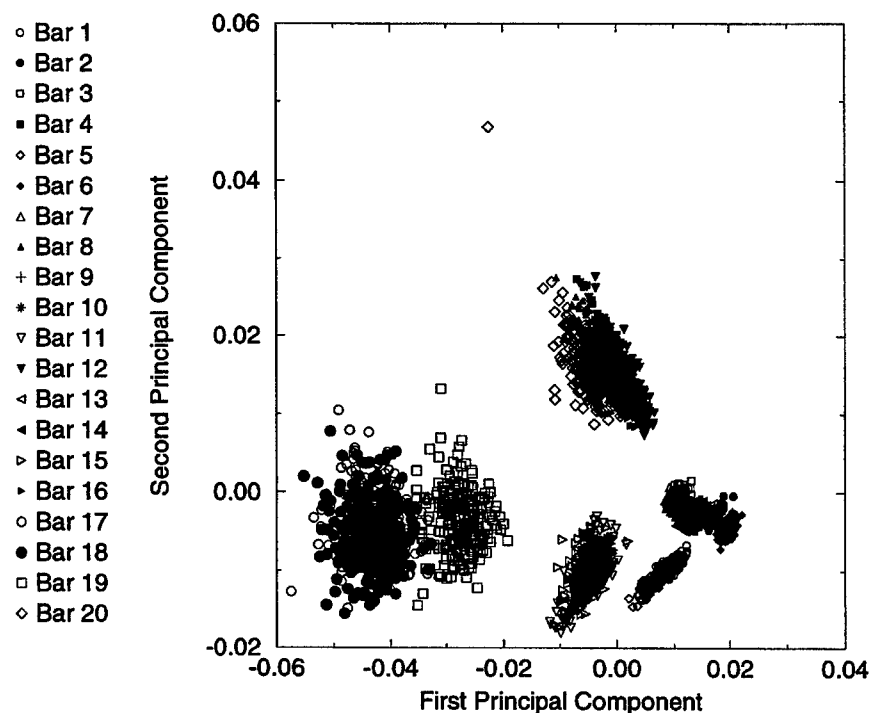


Figure 4. Projection of damage data onto first two principal components.

As at least one index fired for each damaged member, the analysis can pass on to the localisation problem. This is basically one of classification. If the data for each damage state are separated from each other in the pattern space than a neural network will be able to classify data unambiguously and thus localise the damage. In order to gain a little understanding of the distribution of the patterns, it is possible to project the data from the 50-dimensional space into a two-dimensional space and thus visualise it. There are numerous techniques for this including projections, principal component analysis and Sammon mapping [13]. The method used here is principal component analysis.

In order to train the novelty detectors, 100 points of normal condition data were used, each corrupted by a different Gaussian noise vector. For testing on the damage data, 250 versions of each pattern were used. Each pattern for the classification problem was a 20-dimensional vector with each vector being the set of novelty index values over all 20 members (actually, the *inverses* of the indices). Altogether then the data for the neural network training data comprised *damage cases* \times *noise cases* = $20 \times 250 = 5000$ patterns. Figure 4 shows the distribution of the train-

ing points after principal component analysis and projection onto the first two principal components. Figure 5 shows a zoomed-in version detailing the rightmost clusters.

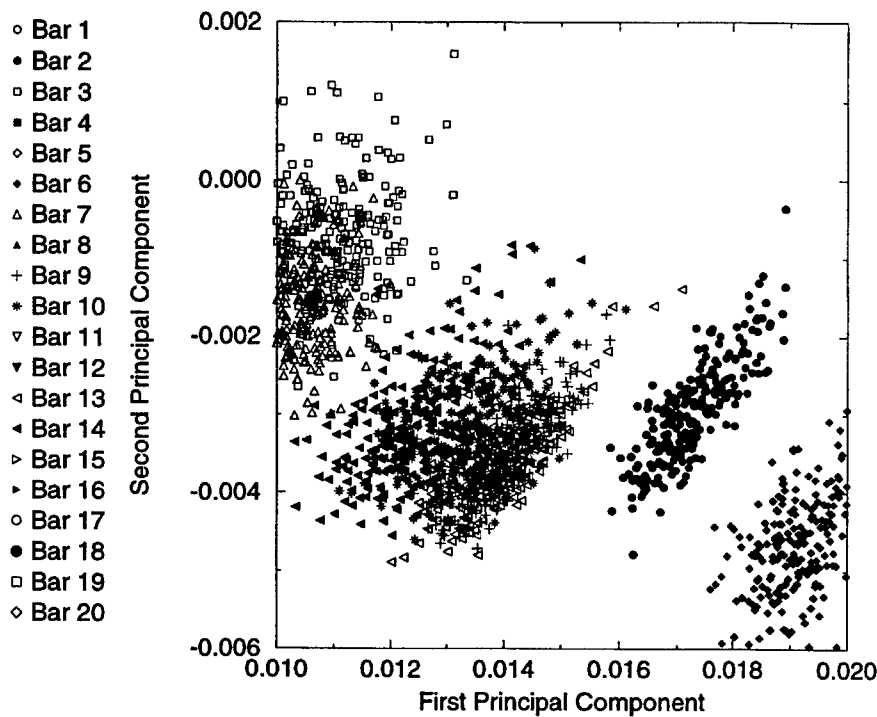


Figure 5. Projection of damage data onto first two principal components; detail.

Figures 4 and 5 show that there are significant regions of overlap in two-dimensions between the clusters corresponding to damages in different bars. There are two possible explanations. The first is that the data is separable but has a higher intrinsic dimension than two and this visualisation is too coarse to show the separations. The second explanation is that the data is intrinsically two-dimensional, but the data is not separable. What is deducible from the diagrams is that if any two clusters are separable in two dimensions then that is also true in the full 20-dimensional pattern space.

The next step is training the neural network classifier. A Multi-Layer Perceptron (MLP) was used here. In order to train a MLP in a completely rigorous manner, three different data sets are needed: one for training, one for validation and one for testing [14]. In this case, a rather unprincipled approach was taken. As the noise on the data is artificially

added Gaussian noise, it is a simple matter to generate three data sets, each with different synthetic noise.

The neural network structure needs to be set and trained before testing. The number of input nodes is set at 20 because the patterns are composed of 20 novelty indices. The number of output units is set at 20 also, and a *1 of 20* strategy is used. This means that for a fault in member 7, say, the network is trained to give a unit response at output node 7 and a zero response at all others. This strategy is effective as it is loosely equivalent to forming a Bayesian classifier [15]. During testing, the output neuron with the highest value signals the desired class.

A rigorous approach to determining the internal network structure demands that a sequence of neural networks be trained, each with different starting conditions and numbers of hidden layer neurons. Each network is trained until the generalisation error on the validation set becomes a minimum. The validation set should therefore be used to set the initial conditions, number of hidden units and stopping time. In order to obtain preliminary results quickly, the number of hidden units was set at 20. The final structure was then 20:20:20. The number of connections in the network is 840 and the number of training patterns is 5000, so no real problems with generalisation were anticipated. Trials with numbers of iterations ranging between 50000 and 500000 showed that the solutions had stabilised at 200000 iterations so this was taken as fixed.

Damage Case	Classified as					
	2	3	9	10	13	14
Bar 2	250	0	0	0	0	0
Bar 3	0	249	0	1	0	0
Bar 9	0	0	250	0	0	0
Bar 10	0	0	0	246	0	4
Bar 13	0	3	92	0	135	20
Bar 14	0	0	0	1	0	249

Table 1: Confusion matrix for classifier network on training set.

In order to investigate the effect of initial conditions, 500 networks were trained (this took approximately 6 hours on a 333 MHz Laptop running Linux). The five lowest classification errors on the training set were 0.4%, 1.34%, 2.18%, 2.42% and 2.46%. These five networks were evaluated on the validation set and the fourth gave the lowest error of 2.4%. This network was chosen for evaluation on the testing set and gave a classification error of 2.74%. Tables 1, 2 and 3 give the confusion matrices for the

three data sets.

Damage Case	Classified as											
	1	3	5	7	9	10	11	12	13	14	15	20
Bar 1	249	0	1	0	0	0	0	0	0	0	0	0
Bar 3	0	249	0	0	0	0	0	0	0	1	0	0
Bar 5	0	0	250	0	0	0	0	0	0	0	0	0
Bar 7	0	0	0	250	0	0	0	0	0	0	0	0
Bar 9	0	0	0	0	246	0	0	0	4	0	0	0
Bar 10	0	0	0	0	0	244	0	0	0	6	0	0
Bar 11	0	0	0	0	0	0	248	0	0	0	2	0
Bar 12	0	0	0	1	0	0	0	249	0	0	2	0
Bar 13	0	0	0	0	64	0	0	0	151	35	0	0
Bar 14	0	0	0	0	0	0	0	0	0	250	0	0
Bar 15	0	0	0	0	0	0	2	0	0	0	248	0
Bar 20	0	0	0	0	0	0	4	0	0	0	0	246

Table 2: Confusion matrix for classifier network on validation set.

Damage Case	Classified as						
	9	10	11	13	14	15	20
Bar 9	248	0	0	2	0	0	0
Bar 10	0	247	0	0	3	0	0
Bar 11	0	0	249	0	0	1	0
Bar 13	22	0	0	124	104	0	0
Bar 14	0	0	0	0	250	0	0
Bar 15	0	0	4	0	0	246	0
Bar 20	0	0	1	0	0	0	249

Table 3: Confusion matrix for classifier network on testing set.

In the cases of the training set and the validation set, the main sources of confusion are between pairs of diagonal members common to a bay, i.e. 9 and 13, 10 and 14 etc. This raises the possibility of only attempting to locate the diagonal members to within one of the four bays. With this interpretation of the results, the training and validation errors fall to 0.4% and 0.8% respectively. In the case of the testing set, the major source of confusion is between members 13 and 14, which are in

neighbouring bays but otherwise unrelated. This is a little puzzling as the clusters corresponding to these members are separated in the principal component plot (Figure 5). However, the MLP minimises the error by drawing the best *set* of decision boundaries which separate the training data and it may be that the network has difficulty in generalising. In this case the strategy of locating to within a bay only reduces the error to 2.15%. These results are still rather impressive as random selection would give an error of 95%.

CONCLUSIONS

This paper has demonstrated a method of locating damage on a structure by using a network of novelty indices. On a simple framework, the results are rather impressive and show a marked improvement on a previous study of the same structure. However, the paper raises a number of important questions. Foremost among these is the question of how to design an optimum set of features. Here, the problem is largely ignored and a transmissibility from each bar is used. There is certainly some possibility for data reduction as the principal component analysis which served to visualise the data in two dimensions actually showed that 95% of the variance of the original data was summarised by the first eight principal components. This shows that there is a high degree of redundancy in the set of twenty indices and more careful choice of features may result in a significant saving on measurements. This is of course vital for any practical system.

Another point raised by this study concerns the use of networks of this type for sizing the damage. In this case, it proved impossible due to the fact the indices showed little variation over the damage severities considered here. This is partly due to the fact that the negligible damping in the Finite Element model caused the undamaged and damaged resonance peaks to separate completely even at low levels of damage. A more realistic simulation may well result in more useful indices for severity assessment.

Further work is underway aimed at addressing these issues.

References

- [1] Surace, C., Worden, K. & Tonlinson, G.R., A novelty detection approach to diagnose damage in a cracked beam, *Proceedings of the 15th International Modal Analysis Conference, Florida*, 947-953, 1997,
- [2] Bishop, C.M., Novelty detection and neural network validation, *IEE Proceedings - Vision and Image Signal Processing*, 141, 217-222, 1994.

-
- [3] Tarassenko, L., Hayton, P., Cerneaz, Z. & Brady, M., Novelty detection for the identification of masses in mammograms, *In Proceedings of 4th IEE International Conference on Artificial Neural Networks, Cambridge, UK, IEE Conference Publication No.409*, 442-447, 1995.
- [4] Nairac, A., Corbett-Clark, T.A., Ripley, R., Townsend, N.W. & Tarassenko, L., Choosing an appropriate model for novelty detection, *In Proceedings of the 5th International Conference on Artificial Neural Networks, Cambridge, UK* 117-222, 1997.
- [5] Roberts, S. & Tarassenko, L., A probabilistic resource allocating network for novelty detection, *Neural Computation*, **6**, 270-284, 1994.
- [6] Pomerleau, D.A., Input reconstruction reliability estimation, *In Advances in Neural Information Processing Systems 5 ed. S.J.Hanson, J.D.Cowan & C.L.Giles, Morgan Kaufman Publishers*, 1995.
- [7] Worden, K., Structural fault detection using a novelty measure, *Journal of Sound and Vibration*, **201**(1), 85-101, 1997.
- [8] Worden, K., Manson, G., Fieller, N.R.J. & Curtis, S., Damage detection using multivariate statistics. Part I: Outlier analysis, *In Proceedings of ISMA 23, Noise and Vibration Engineering Conference, Leuven*, pp.73-79, 1998.
- [9] Worden, K., Manson, G. & Fieller, N.R.J., Damage detection using outlier analysis, *To appear: Journal of Sound and Vibration*, 2000.
- [10] Surace, C. & Worden K., A novelty detection approach to diagnose damage in structures: an application to an offshore platform, *Proceedings of the 7th ISOPE, Canada*, 1997.
- [11] Worden, K., Ball, A.D. & Tomlinson, G.R., Fault location in a framework structure using neural networks, *Smart Materials and Structures*, **2**, pp.189-200, 1993.
- [12] Barnett, V. & Lewis, T., *Outliers in Statistical data*, 3^d ed., John Wiley and Sons, Chichester, 1994.
- [13] Worden, K. & Manson, G., Visualisation and dimension reduction of high-dimensional data for damage detection, *Proceedings of the 17th International Modal Analysis Conference, Florida*, 1999 .
- [14] Tarassenko, L., *A Guide to Neural Computing Applications*, Arnold, 1998.

-
- [15] Bishop, C.M., *Neural Networks for Pattern Recognition*, Oxford University Press, 1995.

DAMAGE DIAGNOSIS USING STATISTICAL PROCESS CONTROL

Hoon Sohn[†], Michael L. Fugate[‡], and Charles R. Farrar[†]

Los Alamos National Laboratory
Los Alamos, NM 87545

ABSTRACT

Structural health monitoring is described in the context of a statistical process control paradigm. This paper demonstrates the application of various statistical process control techniques such as the Shewhart, the exponentially weighted moving average, and the cumulative sum control charts to vibration-based damage diagnosis. The control limits are first constructed based on the measurements obtained from the initial intact structure. Then, new data are monitored against the control limits. A statistically significant number of outliers outside the control limits indicate a system transition from a healthy state to a damage state. Environmental and operation conditions, such as temperature change and the magnitude variation of the input forces, are also incorporated into the monitoring process. Blind tests of various damage cases are conducted without prior knowledge of the actual damage scenarios to evaluate the performance of the presented control chart techniques.

1. INTRODUCTION

Many aerospace, civil, and mechanical engineering systems continue to be used despite aging and the associated potential for damage accumulation. Therefore, the ability to monitor the structural health of these systems is becoming increasingly important from both economic and life-safety viewpoints.

This paper attempts to state in a quantifiable manner if the system of interest has experienced structural deterioration or degradation by analyzing changes in the vibration response of the system in the presence of operational, and/or environmental variability. In particular, this paper casts the structural monitoring problem in the context of a control chart analysis paradigm, which is

[†] Engineering Sciences & Application Division, Engineering Analysis Group, MS C926.

[‡] Computing, Information, & Communications Division, Computer Research & Applications Group, MS B265.

one of the most popular methods of statistical process control. The control chart approach is very efficient and suitable for on-line continuous monitoring. The final diagnosis results are presented to end users in three categories: safe (green light), questionable (yellow light), and danger (red light) making the interpretation of the final diagnosis simple.

2. THEORETICAL FORMULATION

An auto-regressive (AR) model is first fitted to the measured acceleration-time histories from an undamaged structure. Residual errors, which quantify the difference between the prediction from the AR model and the actual measured time history at each time interval, are used as the damage-sensitive features. Next, the Shewhart, cumulative sum (CUSUM), and exponentially weighted moving average (EWMA) control charts are employed to monitor the mean and variance of the selected features. Control limits for the control charts are constructed based on the features obtained from the initial intact structure. The residual errors computed from the new data and the prediction of these data with the initial AR model are then monitored against the control limits. A statistically significant number of residual error terms outside the control limits indicate a system anomaly. In this section, the AR modeling, and the construction of the various control charts are briefly explained.

2.1. Modeling of a Auto-Regressive Process

One of the main assumptions in the use of control charts is the independence of the extracted features. Conventional control charts provide false-positive indications of damage too frequently if the selected features exhibit a high level of correlation over time. Therefore, the correlation in the raw time history data needs to be removed prior to the application of the control charts. As a feature extraction process, an AR model is fitted to the time history data in order to remove the correlation. An AR model with p auto-regressive terms can be written:

$$u(k) = a + \sum_{j=1}^p \phi_j u(k-j) + bT + e(k) \quad (1)$$

This model is referred to as an AR(p) model. $u(k)$ is the observed time history at time $k\Delta t$, and Δt is a sampling interval. ϕ_j is an unknown auto-regression coefficient, and $e(k)$ is an unobservable random error

with zero mean and constant variance. T is some form of a current temperature measure for the system and b is the associated coefficient. The ϕ_j 's and b are estimated by fitting the AR model to the data obtained from the undamaged structure. The mean of $u(k)$ for all k is μ and $a \equiv (1 - \sum \phi_j)\mu$.

Denoting $\hat{u}(k)$ as the predicted time history from the AR model at time index k , the residual error, $e(k) = u(k) - \hat{u}(k)$, is defined as the damage sensitive feature to be used in this study. When new data become available, the response at the current time point is predicted using p past time points, current temperature T , and the previously fitted AR(p) model. Then, the residual errors are computed for $k = p + 1, p + 2, \dots$

When the system varies from the initial condition and the AR model derived from the undamaged structure is applied to the new data, the AR model will show greater residual errors. However, the variation of the residual errors does not necessarily indicate that the structure is damaged. For example, variations of environmental or operational conditions such as ambient temperature, wind speed, or traffic intensity of *in-situ* bridges could also cause shifts of the residual error distribution. Therefore, the effects of these environmental or operational conditions on residual errors should be first discriminated from the effects of damage.

The measurement of the system's current temperature parameter, T , is incorporated directly in Equation (1) to take into account the effect of temperature variance on the measure response. The response time series are also normalized by the estimated standard deviation of the time series to remove the influence of the input amplitude change. Consequently, the residual error changes caused by damage are separated from the variations caused by the ambient temperature and input force intensity. The following various control charts provide statistical frameworks to detect the changes in the mean and variance of the residuals.

2.2. Shewhart Control Chart

In this section, two most commonly used Shewhart control charts, X-bar and S control charts, are presented. The X-bar control chart provides a framework for monitoring the changes of the selected feature means and for identifying observation points that are inconsistent with the past data sets. The S control chart monitors the process variance in a similar way as the X-bar control chart. We first introduce the X-bar control chart and then address the S chart.

To monitor the mean variation of the features, the features are first arranged in m subgroups of size n :

$$\begin{array}{cccc} x_{11} & x_{12} & \cdots & x_{1n} \\ x_{21} & x_{22} & \cdots & x_{2n} \\ \vdots & \vdots & & \vdots \\ \vdots & \vdots & & \vdots \\ x_{m1} & x_{m2} & \cdots & x_{mn} \end{array} \quad (2)$$

where x_{ij} is the extracted feature from previous section, *i.e.*, the residual in this study. The subgroup size n is often taken to be 4 or 5. If n is chosen too large, a drift that may be present in individual subgroup mean may be obscured, or averaged-out. An additional motivation for using the rational subgrouping, as opposed to employing individual observations, is that the distribution of the subgroup means can often be reasonably approximated by a normal distribution as a result of the central limit theorem.

Next, the sample mean \bar{X}_i and standard deviation S_i of the features are computed for each subgroup ($i = 1, \dots, m$):

$$\bar{X}_i = \text{mean}(x_{ij}) \text{ and } S_i = \text{std}(x_{ij}) \quad (3)$$

Here, the calculation of the mean and standard deviation is with respect to the n observations in each subgroup. Finally, a control chart is constructed by drawing a centerline (CL) at the mean of the subgroup means and two additional horizontal lines corresponding to the upper and lower control limits (UCL & LCL) versus subgroup numbers (or with respect to time). The centerline and two control limits are defined as follows:

$$\begin{aligned} \text{UCL} &= \text{CL} + Z_{\alpha/2} \frac{S}{\sqrt{n}}, \text{ LCL} = \text{CL} - Z_{\alpha/2} \frac{S}{\sqrt{n}} \\ \text{and CL} &= \text{mean}(\bar{X}_i) \end{aligned} \quad (4)$$

where the calculation of mean is with respect to all subgroups ($i = 1, \dots, m$). $Z_{\alpha/2}$ represents the $\alpha/2$ quantile of the standard normal distribution. The variance S^2 is estimated by averaging the variance S_i of all subgroups:

$$S^2 = \text{mean}(S_i^2) \quad (5)$$

As mentioned before, regardless of the distribution of x_{ij} , \bar{X}_i can be approximated by a normal distribution as a result of the central limit

theorem. Therefore, the control limits in Equation (4) correspond to a $100(1-\alpha)\%$ confidence interval. In many practical situations, the distribution of features may not be exactly normal. However, it has been shown that the control limits based on the normality assumption can often be successfully used unless the population is extremely non-normal [6]. The observation of the residual errors obtained from the undamaged structure reveals that the normality assumption is an appropriate approximation for this study.

If the system experiences damage, this will likely be indicated by an unusual number of subgroup means outside the control limits (a charted value outside the control limits is referred to as an *outlier* in this paper). Finally, damage monitoring is performed by plotting the \bar{X}_i values obtained from the new data set along with the previously constructed control limits.

Similar to the X-bar control chart, the variance of the individual subgroups, S_i , can be monitored by the S control chart. To construct the S control chart, UCL, LCL, and CL are defined as follows:

$$UCL = S \sqrt{\frac{\chi^2_{1-\alpha/2, n-1}}{n-1}}, \quad LCL = S \sqrt{\frac{\chi^2_{\alpha/2, n-1}}{n-1}} \quad \text{and} \quad CL = \text{mean}(S_i) \quad (6)$$

where $\chi^2_{1-\alpha/2, n-1}$ and $\chi^2_{\alpha/2, n-1}$ denote the upper and lower percentage points of the chi-square distribution with $n-1$ degrees of freedom.

2.3. Cumulative Sum Chart

The X-bar and S control charts use only the information contained in the current point and ignore any information given by the entire sequence of points. This feature makes the X-bar and S control charts relatively insensitive to small shifts in the process. Alternatives to monitor more subtle changes are the CUSUM and EWMA control charts. First, the CUSUM control chart is presented here.

The CUSUM chart incorporates all the previous information up to the current point by accumulating the deviations of the feature values from the centerline. However, the CUSUM chart for the process mean is formed by computing the following cumulative sum:

$$C_i = \sum_{j=1}^i (\bar{X}_j - CL) \quad (7)$$

Note that if the sample mean \bar{X}_i remains in control around the CL value, the cumulative sum C_i defined in Equation (7) should be a

random process with zero mean. For example, if the process mean shifts upward to a new mean value, say $CL^+ > CL$, then a positive drift in the cumulative sum C_i will be accumulated. Similarly, the downward shift of the process mean will develop a negative drift in C_i . Therefore, a trend developed among observations is utilized as an indication of the process mean shift. Since the CUSUM includes all the information up to and including the i th point, the CUSUM is more effective than the Shewhart charts for detecting small shifts. Particularly, the CUSUM are effective with subgroup size one ($n = 1$).

The actual CUSUM chart is implemented by accumulating upward and downward derivation from the CL separately:

$$\begin{aligned} C_i^+ &= \max[0, \bar{X}_i - (CL + K) + C_{i-1}^+] \\ C_i^- &= \max[0, (CL - K) - \bar{X}_i + C_{i-1}^-] \end{aligned} \quad (8)$$

where C_0^+ is the upper cumulative sum of derivations that are above $CL + K$, and C_0^- is the lower cumulative sum of derivations that are below $CL - K$. Note that the starting values are $C_0^+ = C_0^- = 0$ and both C_0^+ and C_0^- are reset to zero upon becoming negative. The reference value (or allowance value) K in Equation (8) is often set about one half of the deviation that one is interested in detecting. For example, if we intend to detect one standard deviation shift from the target value, K is chosen to be one-half of the standard deviation, $K = \sigma/2$. When either C_0^+ or C_0^- exceed the decision interval H , the process is out of control. H is often defined to be five times the standard deviation σ , $H = 5\sigma$ [6].

Similarly, a CUSUM chart for monitoring process variance can be formulated. Denoting $Y_i = (\bar{X}_i - CL)/\sigma$ and a standardized quantity V_i as follows

$$V_i = \frac{\sqrt{|Y_i|} - 0.822}{0.349} \quad (9)$$

Hawkins (1981) [3] shows that the in-control distribution of V_i is approximately a normal distribution with zero mean and unit standard deviation. Then, two one-sided CUSUMs for process variance can be defined as follows:

$$\begin{aligned} S_i^+ &= \max[0, V_i - K + S_{i-1}^+] \\ S_i^- &= \max[0, -K - V_i + S_{i-1}^-] \end{aligned} \quad (10)$$

where $S_0^+ = S_0^- = 0$, and the values for K and H are selected as in the case of the process mean monitoring.

2.4. Exponentially Weighted Moving-Average Control Chart

The EWMA chart is also a good alternative to the Shewhart charts for detecting small shifts [4,7]. The performance of the EWMA is often equivalent to that of the CUSUM chart. When a subgroup size is one ($n = 1$), the EWMA chart is defined as:

$$z_i = \lambda x_i + (1 - \lambda) z_{i-1} \quad (11)$$

where λ is a constant with $0 < \lambda \leq 1$, and the starting value z_0 is the target mean, $z_0 = CL$. Recursively substituting $\lambda x_{i-j} + (1 - \lambda) z_{i-j-1}$ for z_{i-j} , $j = 1, 2, \dots, i-1$, in Equation (11), it can be shown that z_i is a weighted average of all past and current observations:

$$z_i = \lambda \sum_{j=0}^{i-1} (1 - \lambda)^j x_{i-j} + (1 - \lambda)^i z_0 \quad (12)$$

If the observations x_i are independent random variables with variance σ^2 , the variance of z_i becomes:

$$\sigma_{z_i}^2 = \sigma^2 \left(\frac{\lambda}{2 - \lambda} \right) [1 - (1 - \lambda)^{2i}] \quad (13)$$

Finally, the control limits and center line for the EWMA are defined as

$$UCL, LCL = CL \pm L\sigma \sqrt{\frac{\lambda}{(2 - \lambda)} [1 - (1 - \lambda)^{2i}]} \quad (14)$$

and $CL = \text{mean}(x_i)$. Note that, since z_i is a weighted sum of all past and current observations, the distribution of z_i can be reasonably approximated by a normal distribution as a result of the central limit theorem. Therefore, the EWMA chart is insensitive to the normality assumption of individual observations x_i .

In Equation (14), L and λ are the design parameters of the EWMA chart. In this study, the values of L and λ are chosen $L=2.7$ and $\lambda=0.1$ to give approximately the same confidence interval as that of the CUSUM chart with $K = \sigma/2$ and $H=5\sigma$ [6].

MacGregor and Harris (1993) extended the use of EWMA-based statistics for monitoring the process variance [5]. The exponentially weighted moving variance (EWMV) is defined as:

$$s_i^2 = \lambda (x_i - z_i)^2 + (1 - \lambda) s_{i-1}^2 \quad (15)$$

It can be shown that $E[s_i^2] = \sigma^2$, and z_i is an estimate of the true population mean at the i th point in time. If individual observations are independent, the s_i^2 approximately has chi-square distribution with $\nu = (2 - \lambda) / \lambda$ degrees of freedom. Finally, the control limits for $\sqrt{s_i^2}$ statistic become:

$$UCL = \sigma \sqrt{\frac{\chi_{1-\alpha/2, \nu}^2}{\nu}} \text{ and } LCL = \sigma \sqrt{\frac{\chi_{\alpha/2, \nu}^2}{\nu}} \quad (16)$$

All the control charts are constructed such that the control limits approximately correspond to a 99% confidence interval of the given distribution.

3. APPLICATIONS

The applicability of the aforementioned control charts to damage diagnosis problems is demonstrated using the vibration test data simulated from the spring-mass system shown in Figure 1. The springs act in the axial direction and have nominal values of $k_o = 1 \times 10^7$ N/m. The masses have a nominal value of $m_o = 1.0$ N-S²/m and nominal damping of the dashpots is $c_o = 5\%$. In Figure 1, the spring, dashpot, and mass elements are numbered from left to right, k1-k11, c1-c11, m1-m10, respectively.

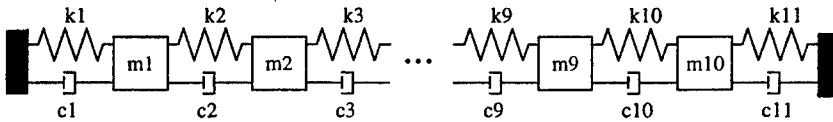


Figure 1: A spring-mass system

Excitation time series is generated such that it has a flat spectrum up to a cutoff frequency of 512 Hz. For all cases, the input force is applied at m9. One of the requirements of this study is the ability to input environmental variability into the system. The spring constant is designed to be a nonlinear function of temperature as shown in Figure 2. In this figure, the spring stiffness had a nominal value of 1×10^7 N/m at a temperature of 15° C. Then, a maximum variance of $\pm 2.5\%$ over a temperature range of -10° to 40° C is assigned.

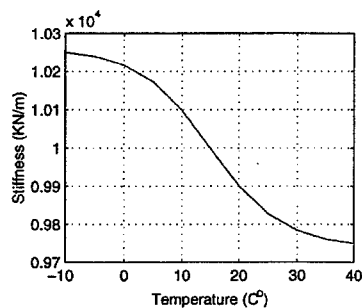


Figure 2: Temperature-stiffness relationship

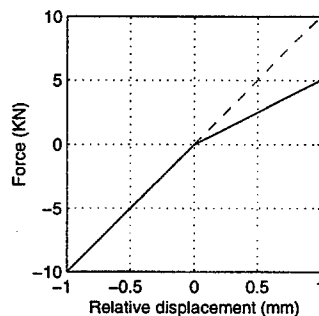


Figure 3: Damage simulation using a bilinear stiffness model

Nonlinear damage is introduced to the structure by reducing the stiffness of a spring in tension side. Therefore, after damage occurrence, the spring will have a bilinear force-displacement relationship as shown in Figure 3. In subsequent examples, the amount of damage is denoted by the percentage decrease of the tensional stiffness. For example, the stiffness in compression is 1×10^7 N/m and in tension it is 5×10^6 N/m for Figure 3 denoting 50% stiffness decrease.

Table 1 shows all the training data sets used in this study. The training data sets are divided into three categories. Data Set 1 is used to study the effect of temperature changes, and Data Set 2 is intended to investigate the influence of the amplitude variation of the input force. The control limits of the control charts are first constructed using all the data in Data Sets 1 and 2. Then, the preliminary damage diagnosis is conducted for 9 different damage cases shown in Data Set 3. Finally, diagnosis tests using 40 addition test sets are carried out to assess the performance of the proposed process monitoring technique. The condition of the 40 test sets was unknown to the analysts until the completion of the diagnosis analysis. It should be noted that the presented damage diagnosis is performed in an *unsupervised learning* mode implying that data from a damaged system is not available for training purpose [1]. This feature of the proposed study is very attractive for monitoring full-scale civil infrastructures because the collection of training data sets representing various damage states of such complex structures is typically not feasible.

For each run in Table 1, the response acceleration time series are recorded at all mass points for approximately 16 second. A sample rate of 1024 per second resulted in a Nyquist frequency 512 Hz. The measured 16385 point time series are first sampled at every 46 points yielding the frequency range of 0–11 Hz. Using the order identification

techniques described in Reference [2], AR(36) is shown to remove most of correlation between the residuals over time. This AR(36) is then fitted to individual time series resulting in 322 ($\approx 16385/46 - 35$) residual errors. For the X-bar and S control charts, subgroups of size $n=4$ are employed, and for the rest of the control charts, individual residuals are plotted ($n=1$).

Table 1: A list of training data sets

Data Set 1: Temperature variation (total 33 sets)												
(All excitation have the same amplitude, Amplitude=100)												
Random input	Temperature (C°)											
	-10	-5	0	5	10	15	20	25	30	35	40	
	1	Run1	Run2	Run3	Run4	Run5	6	7	8	9	10	11
	2	12	13	14	15	16	17	18	19	20	21	22
3	23	24	25	26	27	28	29	30	31	32	33	
Data Set 2: Input excitation variation (total 9 sets)												
Constant Temperature (C°)	Random Excitation											
	Amplitude =50					Amplitude =100		Amplitude =300				
15	Run34					35		36				
15	37					38		39				
15	40					41		42				
Data Set 3: Testing damage cases (total 9 sets)												
(All cases have the same temperature 15 C° and the same amplitude excitation)												
Stiffness Reduction	Damage Location											
	k2					k6		k2 and k6				
20%	Run43					744		58				
50%	45					46		59				
70%	47					48		60				

Figure 4 illustrates typical control charts. The time series associated with measurement point 5 (m5) of Run 59 are used for this figure. Note that all the control charts are designed such that approximately 99% of the observation points fall within the control limits when the system is in control. When Run 59 has 50% damage both on k2 and k6, all the control charts display statistically significant number of outliers (more than 1% of the entire points) in Figure 4. This damage diagnosis is repeated for all run cases, from Run1 to Run 100. The diagnosis results of m5 are summarized in Table 2 for selected damage cases of the blind test data. The entries in columns 2-7 show the number of outliers obtained from each control chart.

It is the authors' belief that most end users of the health monitoring system simply want to know if the system is safe or not. To deduce the system integrity from the presented outlier numbers, a decision table based on the number of outliers are established and presented in Table 3. According to this decision table, the system

status is assigned to one of three groups: safe (green light), questionable (yellow light), and danger (red light). When the green light is on, the end users have a confidence that the system is in-control. If a yellow light is on, the system will be still functional but a further detailed diagnosis or visual inspection is strongly recommended. Finally, a red light indicates that the system should be shut down immediately, and the operation of the system should not be resumed until assignable causes are found and regulated.

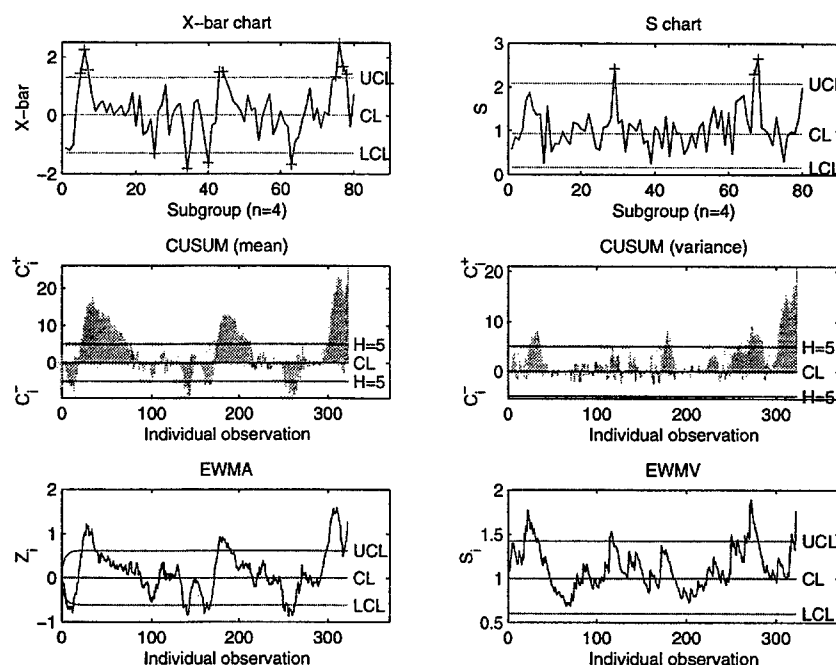


Figure 4: An example of control chart analyses

Table 2: Number of outliers and diagnosis results obtained from m5

Run #	Xchart	Schart	CUSUM (mean)	CUSUM (variance)	EWMA	EWMV	Result
63	9	14	62	298	19	189	3
72	6	11	9	236	1	116	3
76	28	23	328	318	167	261	3
79	1	8	4	176	0	68	2
80	10	5	14	17	3	20	2
84	2	5	0	12	2	13	2
87	18	9	313	289	160	106	3
90	2	8	19	139	3	80	2
93	9	4	31	19	2	15	2

For example, if 10, 5, 14, 17, 3, 20, and 2 number of outliers are observed for the X-bar, S, ..., EWMV control charts of Run 80, then red (3), yellow (2), red (3), yellow (2), green (1), red (3) lights are assigned to the X-bar, S, ..., EWMV control charts, respectively, based on the decision criteria in Table 3. That is, based on the number of outliers (n_o), the diagnosis result of each control chart is assigned to one of the following three lights: green (1), yellow (2), and red (3) lights. If we define n_l as the sum of all the numerical values of lights from each control chart, the total number of lights for this example becomes $n_l = 3 + 2 + 3 + 2 + 1 + 3 = 14$. Because $9 < n_l < 14$, a yellow light is assigned to this measurement point based on the criteria shown in the last column of Table 3. Note that the specific values of the decision criteria are assigned in a rather heuristic manner by observing the numbers of outlier from the training data sets. A further study is needed to establish a systematic way of constructing such a decision table.

Table 3: Decision table for individual control chart

Light	Xchart (m=80)	Schart (m=80)	CUSUMX (m=322)	CUSUMS (m=322)	EWMA (m=322)	EWMV (m=322)	Results
Red=3	$n_o > 5$	$n_o > 5$	$n_o > 10$	$n_o > 20$	$n_o > 7$	$n_o > 10$	$n_l > 14$
Yellow =2	$n_o > 2$	$n_o > 2$	$n_o > 4$	$n_o > 7$	$n_o > 4$	$n_o > 5$	$n_l > 9$
Green=1	else	else	else	else	Else	else	else

Although all the results are not presented in this paper, the aforementioned procedure is repeated for all ten measurement points. Only the final diagnosis of each measurement point is summarized for selected damage cases in Table 4. The last column of Table 4 shows the final decision regarding the system states combining all the diagnosis results from the ten measurement points. A red light is assigned to the system when there are more than one red light or five yellow lights from the ten measurement points. If there are less than three yellow lights for the run case of interest, a green light is assigned to the final diagnosis results. A yellow light is assigned to all the other cases.

Table 5 compares the diagnosis results analyzed by the proposed approach with the actual damage scenarios. As mentioned earlier, the actual damage status of these blind test data was not revealed to the analysts until the diagnosis analysis is completed. The 40 runs of the blind test data consist of 16 damage cases and 24 undamaged cases with various temperatures and excitation force amplitudes. Several conclusions are made based on the observation of Table 5: (1) No false-positive warning of damage is indicated out of 24 undamaged cases in spite of varying temperatures and different excitation amplitudes, and (2) out of 16 damage cases, 13 cases are

successfully assigned either to red (9) or yellow (4) lights. The remaining undetected 3 damage cases have relatively small amount of damage with 10%-20% stiffness reductions. Note that because the primary objective of this study is to identify the existence of damage, the final decision regarding the system integrity is presented in terms of only three categories: green, yellow, and red lights. The localization and quantification of damage is beyond the scope of this study.

Table 4: Final diagnosis results

Run	M1	m2	m3	m4	m5	m6	m7	m8	m9	m10	Final
61	2	2	2	1	1	1	1	1	1	2	2
63	3	3	3	3	3	3	3	3	1	3	3
66	3	3	2	1	1	1	1	1	1	1	3
68	3	2	1	1	1	2	1	1	2	1	2
72	2	2	2	2	3	3	3	2	1	1	3
76	2	2	2	3	3	3	2	3	1	2	3
79	2	2	2	2	2	2	2	2	1	1	3
80	1	1	1	1	2	2	3	1	1	1	2
84	2	3	3	3	2	2	1	1	1	1	3
87	2	2	2	3	3	2	2	1	1	1	3
90	3	3	2	2	2	3	3	1	1	1	3
93	3	3	3	3	2	3	3	3	1	2	3
99	2	2	2	1	1	1	1	1	1	1	2

Table 5: Comparison of diagnosis results and actual damage status for the blind test data

Run	61	62	63	64	65	66	67	68	69	70
T (C°)	4	39	28	23	12	28	23	4	31	27
Input	95	190	220	75	190	95	280	220	190	190
Diagnosis	2	1	3	1	1	3	1	2	1	1
Actual Damage	k4 20%	No	k3,9 70%	No	No	k2 45%	No	k1,7 15%	No	No
Run	71	72	73	74	75	76	77	78	79	80
T (C°)	23	28	-8	4	23	28	27	23	4	28
Input	75	95	190	95	280	220	190	125	95	95
Diagnosis	1	3	1	1	1	3	1	1	3	2
Actual Damage	No	k8 80%	No	k10 20%	No	k6 70%	No	No	k10 60%	k8 45%
Run	81	82	83	84	85	86	87	88	89	90
T (C°)	4	39	28	23	12	28	23	4	31	27
Input	190	280	190	95	190	190	220	125	190	220
Diagnosis	1	1	1	3	1	1	3	1	1	3
Actual Damage	No	No	No	k4 60%	No	No	k5 70%	No	No	k1,7 50%
Run	91	92	93	94	95	96	97	98	99	100
T (C°)	23	31	28	39	23	-8	4	12	28	28
Input	75	190	95	190	125	190	220	190	220	220
Diagnosis	1	1	3	1	1	1	1	1	2	1
Actual Damage	No	No	k2 80%	No	No	No	k5 15%	No	k3,9 10%	k6 10%

4. SUMMARY AND DISCUSSIONS

The structural health monitoring is described in the context of a statistical process control paradigm. First, an auto-regressive prediction model is fitted to the time series obtained from the intact structure so as to estimate coefficients of the prediction model. The residual errors between the measured time series and the predictions from the auto-regressive model are computed for each damage case. These residual errors are defined as features for the subsequent control chart analysis. Next, the control charts are constructed using the features corresponding to the initial structure in control. After the construction of the control limits, the number of outliers, which are charted points outside the control limits, is counted for each control chart. Finally, the system status is assigned into one of three lights, green (safe), yellow (questionable), and red (danger), based on the number of outliers. Damage diagnosis with the 40 blind test data demonstrated that the statistical control chart successfully identified most of stiffness reduction (13 cases out of 16 damage cases) without any false-positive indication of damage for all the examined 24 undamaged cases.

The presented control chart analysis has several advantages over most of existing damage diagnosis techniques in that (1) the presented approach does not require the construction of any complicated analytical model nor extensive computation power, (2) the environmental and operational conditions are explicitly considered so that the effect of damage on the vibration response could be discriminated from these effects, and (3) the construction of the control charts solely relies on the vibration data obtained from the undamaged structure without requiring data collection from various damage status. These features make the proposed approach very attractive for the development of an automated monitoring system for *in-situ* complex structures operating in adverse environments. However, the presented approach only indicates the existence of damage and does not locate the damage.

ACKNOWLEDGEMENT

The funding for this work has come from the Department of Energy's Enhanced Surveillance Program and a cooperative research and development agreement (CRADA) with Kinemetrics Corporation, Pasadena, California. The Department of Energy has funded the authors' participation in this CRADA. The authors also would like to thank Dr. Phillip J. Cornwell of Rose-Hulman Institute of Technology

and Jason S. McIlhaney of California Institute of Technology for generating the numerical test data.

REFERENCES

- [1] Bishop, C. M., *Neural Networks for Pattern Recognition* Oxford University Press, 1995.
- [2] Box, G. E. P., Jenkins, G. M., and Reinsel, G. C., *Time Series Analysis: Forecasting and Control*, 3 ed. Prentice Hall, 1994.
- [3] Hawkins, D. M., "A CUSUM for a scale parameter," *Journal of Quality Technology*, vol. 13, 1981.
- [4] Lucas, J. M. and Saccucci, M. S., "Exponentially weighted moving average control schemes: properties and enhancements," *Technometrics*, vol. 32, 1990.
- [5] MacGregor, J. F. and Harris, T. J., "The exponentially weighted moving variance," *Journal of Quality Control Technology*, vol. 25, 1999.
- [6] Montgomery, D. C., *Introduction to Statistical Quality Control* John Wiley and Sons Inc., 1997.
- [7] Roberts, S. W., "Control chart tests based on geometric moving averages," *Technometrics*, vol. 1, 1959.

MRI GRADIENT COIL CYLINDER SOUND FIELD SIMULATION AND MEASUREMENT

Chris K. Mechefske¹, Yuhua Wu² and Brian K Rutt³

Dept. of Mechanical and Materials Engineering

The University of Western Ontario

London, Ontario, Canada N6G 5B9

¹ c.mechefske@uwo.ca, ² ywu@irus.rri.on.ca

³ The John P Robarts Research Center

100 Perth Drive

London, Ontario, N6A 5K8

brutt@irus.rri.on.ca

ABSTRACT

High-field, high-speed Magnetic Resonance Imaging (MRI) can generate high levels of sound. The process that produces the gradient magnetic field is the primary source of this noise. This noise can cause difficulties in verbal communication in and around the scanner, heightened patient anxiety, temporary hearing loss and possible permanent hearing impairment for health care workers. In order to effectively suppress the sound radiation from the gradient coil cylinder, the sound field needs to be characterized. The characterization can be made either through simulation prediction or measurement analysis. This paper presents both the simulation and measurement results of a study of the sound radiation from a gradient coil cylinder within a 4 Tesla MRI scanner. The measurement results for the sound pressure level distribution, and the acoustic frequency response function are presented. The sound pressure distributions predicted from Finite Element Analysis of the gradient coil are also presented. Details of the prediction method and the results of the modeling will be given in the paper. A comparison of the measured results and the predicted results shows close agreement.

1. INTRODUCTION

High-field, high-speed magnetic resonance imaging (MRI) scanners are used to generate images of the internal structure of biological subjects. These machines are used extensively for medical diagnostic and research work. The way that the magnetic field must be manipulated during the scanning process causes significant vibrations of the gradient coil (a cylindrical electro-magnet which produces a spatially varying magnetic field) and therefore acoustic noise levels to be generated within and nearby the scanners.

The acoustic noise generated by the gradient coil presents problems to patients and health care workers that range from simple annoyance to difficulties in verbal communication, heightened anxiety, temporary hearing loss and possible permanent hearing impairment. Because the antenna that collects the signal which eventually forms the image is integral to the gradient coil, the vibrations that are generated also affect the degree of resolution that is achievable. It is important to find ways to reduce the acoustic noise and vibration levels of MRI scanners in order to improve both the resolution of MRI and the working and patient environment in and around the scanners.

The acoustic problems of MRI scanners have received very little research attention in the past ten years. Acoustic noise associated with MRI was first evaluated by Hurwitz et al in 1989 [1]. Further work during the 1990s included papers published, which outlined acoustic noise measurement, characterization and reduction for MRI scanners [2,3,4,5]. There has not been, however, any simulation method and/or results published which can be compared with measurement results. To fully understand the mechanism of the acoustic noise production in real MRI gradient coils and then exploit this understanding to reduce the acoustic noise generated it is important to set up the sound simulation method. The simulated results can then be compared with the measured results to test the validity of simulation method. In this paper both the simulation method and measurement method will be described. The measurement and analysis results will also be presented.

2. SOUND PRESSURE LEVEL SIMULATION

The interaction between the pulsed gradient magnetic coil and the main (static) magnetic field is the dominant source of the acoustic noise in MRI scanner. For the purposes of this work we assume that only the gradient coil radiates sound. Besides this, we also make the following assumptions while we are calculating the sound pressure for MRI scanner.

- 1) The geometry of the scanner can be modeled as being axisymmetric.
- 2) The gradient coil cylinder is vibrating due to the Lorentz forces which are acting on the cylinder. These forces are caused by the current flowing in the coils that are themselves located within a strong magnetic field. The vibrating surface produces the acoustic energy, which is the main source of the noise.
- 3) The gradient coil cylinder can be modeled as a baffled finite duct with vibrating walls.
- 4) Nonlinear acoustic noise can be ignored.

Figure 1 is a schematic representing a baffled finite duct with vibrating wall and showing sound radiation. The boundary surface illustrated in Figure 1 is modeled as being divided into three parts, *S1*, *S2* and *S3*. *S1* is the vibrating wall of the cylinder. The vibration velocity normal to the surface of the

cylinder is considered as being equal to the normal fluid velocity on the surface. At the aperture areas, $S2$ and $S3$, the acoustic noise is assumed to radiate into infinite domains.

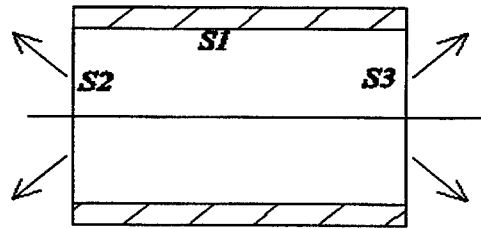


Figure 1: A baffled finite duct model of the gradient coil cylinder with vibrating walls and showing sound radiation

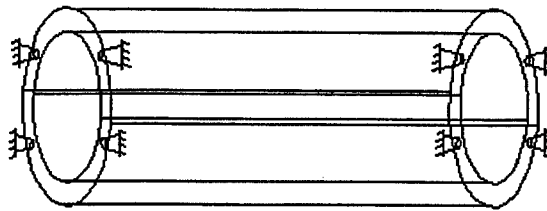


Figure 2: The model of the gradient coil cylinder with constraints

According to the above assumptions, we can calculate the acoustic noise field within the cylinder using the following steps.

- 1) Compute the Lorentz force distribution acting on the cylinder.

The Lorentz force, F , acting on a conductor of length l carrying a current I and which resides in a magnetic field B is given by equation (1) [4].

$$F = I l \times B = \beta I l B \sin\theta \quad (1)$$

In equation (1), $B = Bk$, $l = l\alpha$ and $F = F\beta$ in which k , α , and β are unit rectors and θ is the angle between k and α .

Knowing the gradient coil conductor pattern, main (uniform) magnetic field and the current through the coil conductor, we can compute the Lorentz force distribution acting on the gradient coil cylinder using equation (1).

- 2) Set up the finite element model for the gradient coil cylinder.

The finite element model includes a geometric model, the relative material parameters, and the boundary conditions (constraints and loads) [9,10]. Figure 2 shows a schematic of the model and the type of constraints for the gradient coil cylinder. The only load is the Lorentz force distribution.

- 3) Calculate the normal vibration velocity distribution on the cylinder surface.

Using the finite element modeling software available the normal vibration velocity distribution on the cylinder surface is calculated by combining the Lorentz force distribution and the FE model. Normally this step can be conducted using common commercial FEM software, such as SDRC IDEAS, Ansys, Nastran etc.

- 4) Calculate the acoustic noise distribution within the interior field of the gradient coil.

This step can be implemented according to the Kirchhoff-Helmholtz integral equation, which is a mathematical description of the acoustic radiation from structures with vibrating surfaces. This approach is widely used as a basic theoretical formulation for acoustic radiation calculation through boundary element modeling [6,7,8].

By applying the 4-step procedure just described, a model of the sound pressure level distribution of a prototype head and neck sized gradient coil intended for novel high-resolution MRI studies in humans was conducted. Figure 3 shows the duct model (the gradient coil cylinder in a magnetic resonance imager).

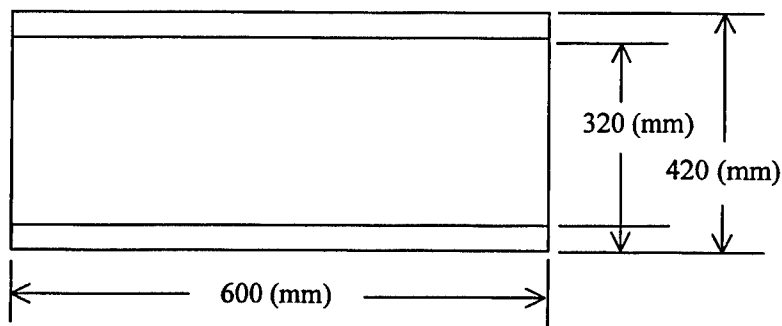


Figure 3: Duct model of the head/neck gradient coil cylinder

3. SOUND PRESSURE LEVEL MEASUREMENTS

To check the validity of the simulation and sound field distribution inside the gradient coil cylinder was measured along the centerline of the gradient coil. The experiment was conducted during operation of a 4T Varian/Siemens whole-body MRI system. The gradient coils were excited with continuous sawtooth excitation waveforms of amplitude 25Amps and

sound pressures were obtained by using a microphone that could be moved along the axis of the cylinder to determine sound pressure level (SPL) as a function of position. A G.R.A.S type 40AF prepolarized microphone and a G.R.A.S type 21SB pre-amplifier was used. This unit was connected to a tape recorder and digital analyzer in another room using a 10-meter shielded cable.

In order to further investigate the character of the sound field inside the gradient coil cylinder further measurements were taken to obtain the acoustic frequency response functions on the 4T Varian/Siemens whole-body MRI system. The body gradient coil was excited with single-lobe gradient impulses. The SPL was measured immediately following the gradient impulse, at a sampling rate of 20 kHz and at one fixed point inside the gradient coil cylinder. The frequency response function was then derived from these measurements.

4. RESULTS AND DISCUSSION

Both the acoustic sound pressure simulation and measurement tests were conducted on a 600 mm long by 420 mm diameter gradient coil. The coil wall thickness was 50 mm. The gradient coil used is made of several layers of epoxy resin with the current carrying copper coils embedded inside. The coil windings are made up of three layers of conductors (referred to as X, Y, and Z windings) wrapped in differing configurations in order to achieve a linear magnetic gradient of appropriate slope within the coil working space. The current that passes through these coils may vary in amplitude, wave shape and frequency.

Figure 4 shows the calculated acoustic noise distribution along the centerline for the head/neck gradient coil cylinder. A continuous wave sinusoidal waveform excitation was assumed, applied to the vertical gradient axis (Y winding) with parameters of, sinusoid frequency = 1000 Hz, current amplitude = 25 Amps, and main magnetic field strength = 4 Tesla. The plot shows the sound pressure level (in dB) along the centerline of the coil. The plot shows sound pressure level maximums in the mid 90 dB range at the ends of the gradient coil cylinder and plus or minus 100 mm from the center point of the cylinder. Minimum sound pressure levels in the range of 70 dB are shown at the center point and plus or minus about 200 mm from the center point

Figure 5 shows the measured sound pressure level distribution along the centerline for the head/neck gradient coil cylinder. The excitation parameters are identical to those used for the simulation.

Figure 5 is similar in general shape to Figure 4. The maximum sound pressure levels again occur at the ends of the gradient coil and approximately plus or minus 100 mm from the center point of the cylinder. The minimum sound pressure levels also appear at the center point as in the simulation and relatively close to plus or minus 200 mm from the center point of the cylinder.

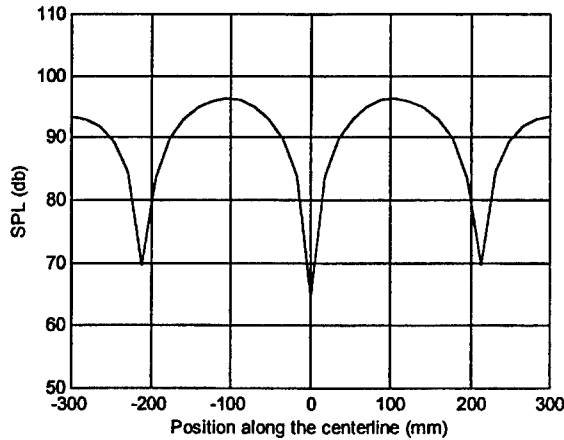


Figure 4: Calculated sound pressure level distribution along the centerline for the head/neck gradient coil cylinder.

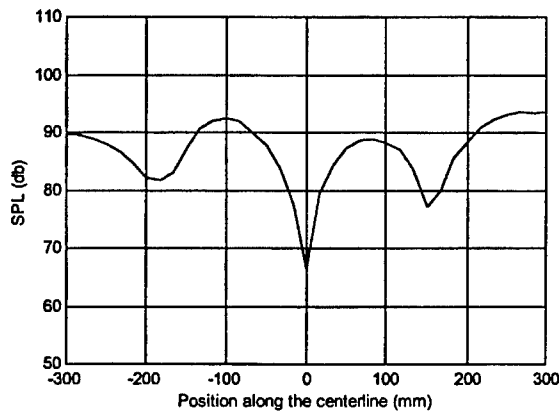


Figure 5: Measured sound pressure level distribution along the centerline for the head/neck gradient coil cylinder

A comparison of Figures 4 and 5 suggests that there is a good match between the measured and calculated sound pressure level distribution shapes. However, detailed inspection of these distributions indicates some notable differences in sound pressure level at some locations along the centerline of the gradient coil cylinder. These differences are likely the result of the MR imager structure, room space, model simplification and boundary condition approximation.

These results suggest several things. First, the simulation and measurement results correlate well. This indicates that future fine-tuning of the modeling procedure and/or improvement of the measurement technique

could bring these two techniques into very close agreement. The ability to accurately model the dynamic behavior of MRI scanners under a variety of operating conditions could lead to improved designs that significantly reduce the sound pressure levels generated during use. Changes in the operating procedures and excitation parameters could also be explored using the model in order to predict settings that would reduce the acoustic noise. Secondly, there is a clear and predictable variation of the sound pressure level along the centerline of the gradient coil cylinder. This suggests that there is a potential to adjust the magnetic gradient produced and/or the position of the patient to minimize the sound pressure levels at the patient's ear. While any individual change may result in only relatively small reductions in the overall acoustic noise in MRI scanners the combined effect could result in marked improvements in patient care and health care working environments.

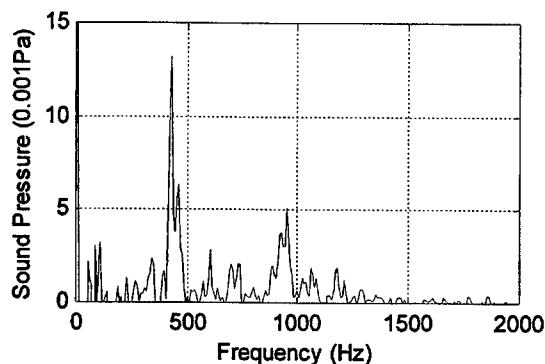


Figure 6: Acoustic frequency function under the excitation of one single-lobe gradient impulse when only the X gradient coil was turned on and the maximum gradient strength was 20mT/m.

Figure 6 is an acoustic frequency response function when only the X gradient coil was turned on and maximum gradient strength was 20mT/m. Figure 6 shows two main peaks in the acoustic frequency response function which occur at around 430Hz and 950Hz for the Siemens AS25 body gradient coil. This figure represents the natural response of the system to an impulse type input signal. Clearly the response shows that there are two main frequencies that are excited by the input signal. Further modeling of the gradient coil cylinder and/or acoustic measurements will reveal how movement of these frequencies could affect the performance of the MRI scanner and the character of the acoustic field within the gradient coil cylinder.

5. CONCLUDING COMMENTS

While high-field, high-speed magnetic resonance imaging (MRI) scanners are extremely useful tools in medical research and diagnostics, they

also produce high levels of acoustic noise within and nearby the working space. The acoustic noise generated results in associated problems for patients and health care workers. It is important to find ways to reduce the acoustic noise and vibration levels of MRI scanners in order to improve both the resolution of MRI and the working and patient environment in and around the scanners.

The comparison of the sound pressure distributions along the centerline of the gradient coil cylinder obtained by both simulation and measurement shows close agreement. This agreement indicates that the FE model developed can be used to perform acoustic simulation and analysis of cylindrical MRI gradient coil cylinders. Further work needs to be done to improve the accuracy of the model and validate the simulated results. With a fully validated FE based simulation method, the next step in our research will be to calculate the acoustic frequency response functions. This type of simulation tool will extend the acoustic analysis procedures at hand allow for improvements in the gradient coil electrical and/or structural design without the need for multiple prototypes and testing. Ultimately this research work is directed toward reducing the acoustic noise and vibration levels of high-field MRI scanning system.

6. REFERENCES

1. R.Hurwitz, S.R.Lane, R.A.Bell, M.N.Brant-Zawadski, Acoustic analysis of gradient coil noise in MR imagine. Radiology 173, 545-548 (1989)
2. Frank G. Shellock, Stacy M. Morisoli, Mokhtar Ziarati, Measurement of acoustic noise during MR imaging: evaluation of six "worst-case" pulse sequences. Radiology 191, 91-93 (1994)
3. Robert A. Hedeem, William A. Edelstein, Characterization and prediction of gradient acoustic noise in MR imagers, Magn. Reson. Med. 37, 7-10 (1997)
4. Peter Mansfield, Barry L.W.Chapman, Richard Bowtell, Paul Glover, Ron Coxon, Paul R. Harvey, Active acoustic screening: reduction of noise in gradient coils by Lorentz force balancing, Magn. Reson. Med. 33, 276-281 (1995)
5. Yuhua Wu, Chris K. Mechefske, Blaine Chronik, Brian K. Rutt, Acoustic distribution within gradient coils in MR imagers, CMBEC 25, 1999
6. Pierce, A.D., 1994, Acoustics -- An Introduction to Its Physical Principles and Applications Acoustical Society of America, Woodbury, New York
7. Gary H.Koopmann, John B. Fahnlne, Designing quiet structures -- A sound power minimization approach. Academic Press, 1997
8. R.D.Ciskowski, C.A.Brebbia, Boundary element methods in acoustics. Computational Mechanics Publications, 1991
9. Seybert, A.F., 1990, The solution of coupled interior/exterior acoustic problems using the boundary element method, J. Acoust. Soc. Am. 88(3), pp. 1612 - 1618
10. Petyt, M., 1990, Introduction to finite element vibration analysis. Cambridge University Press,

APPLICATION OF THE PRONY METHOD IN MACHINE CONDITION MONITORING

Zhidong Chen¹ and Chris K. Mechefske²

Dept. of Mechanical and Materials Engineering
The University of Western Ontario
London, Ontario, Canada N6G 5B9

¹ chenz@engga.uwo.ca, ² mechefske@uwo.ca

ABSTRACT

Transient vibration signals have not been as widely studied as stationary signals, but may well contain significant amounts of useful information. This paper investigates a method for the analysis of transient vibration signals and the application of this method in Machine Condition Monitoring (MCM).

The Prony method is a modeling technique that fits a linear combination of a series of exponential functions to sampled data such that the model describes the underlying process of the sampled data. Because of its exponential basis functions, this method is inherently suitable for analyzing transient signals. The intention of this paper is to explore the application of the Prony method to the study of transient vibration signals and the potential of this method in Machine Condition Monitoring.

This paper describes the work done to investigate this procedure as the basis of a useful machine condition monitoring and diagnostic technique. Also presented are preliminary numerical results of Prony model based frequency analysis of computer generated simulated vibration signals as well as experimentally derived vibration signals.

1. INTRODUCTION

Recent decades have seen a significant amount of research activities being devoted to Machine Signature Analysis (MSA) [1,2,3]. The major tool used for MSA has been, and remains, spectral analysis. Classical spectral estimation techniques include Periodogram, Averaged Periodogram and Blackman-Tukey spectral estimation. Newer approaches to spectral analysis include a variety of Parametric modeling techniques. Within this category are the Rational Transfer Function Modeling Method, Autoregressive (AR) Power Spectral Density (PSD) Estimation, Moving Average (MA) PSD Estimation, Autoregressive Moving Average (ARMA) PSD Estimation, Prony Spectral Density Estimation and Maximum Likelihood Method (MLM) [2,3].

The majority of the research and development work carried out to date in regard to signal processing strategies for machine condition monitoring and diagnostics applications has focused on signals generated from stationary processes. Non-stationary processes have been left relatively unstudied.

Examples of methods that are applicable to non-stationary processes are Wavelet and Short Time Fast Fourier Transform [1,4]. The Prony method, originated by French scientist Baron de Prony in 1795 [5], is also capable of analyzing non-stationary processes [5,6] and is inherently suitable for the study of exponentially decaying dynamic signals, such as those that develop as a result of many different types of machinery condition deterioration. This paper explores the use of the Prony method to study such transient signals [6,7,8,9].

The Prony method was originally used for interpolation between available data points. The method and its modified versions are techniques used for modeling data of equally spaced data samples. Similar to the well-known system identification techniques such as AR and ARMA models, the Prony model seeks to fit an exponential model, which is a linear combination of a series of exponential functions, to sampled data. The Prony method first determines the linear prediction parameters that fit the sampled data. Such linear prediction parameters are then used as coefficients to form a polynomial. The roots of this polynomial are finally employed to estimate the damping coefficients, the sinusoidal frequencies, the exponential amplitude and sinusoidal initial phase of each of the exponential terms.

2. THE PRONY METHOD

If one has N complex data samples $x[1] \dots, x[N]$, the Prony method estimate, $x[n]$, with a p -term complex exponential model is;

$$\hat{x}[n] = \sum_{k=1}^p A_k \exp[(\alpha_k + j2\pi f_k)(n-1)T + j\theta_k] \quad 1 < n < N \quad (1)$$

where A_k is the amplitude, α_k is the damping coefficient, f_k is frequency, T is the sample interval, and θ_k is the initial phase.

Equation (1) can be rewritten as

$$\hat{x}[n] = \sum_{k=1}^p h_k Z_k^{n-1} \quad (2)$$

where

$$\begin{aligned} h_k &= A_k \exp(j\theta_k) \\ Z_k &= \exp[(\alpha_k + j2\pi f_k)T] \end{aligned} \quad (3)$$

or expressed in matrix form as,

$$\begin{bmatrix} z_1^0 & z_2^0 & \dots & z_p^0 \\ z_1^1 & z_2^1 & \dots & z_p^1 \\ \vdots & \vdots & \vdots & \vdots \\ z_1^{p-1} & \dots & z_p^{p-1} \end{bmatrix} \begin{bmatrix} h_1 \\ h_2 \\ \vdots \\ h_p \end{bmatrix} = \begin{bmatrix} x[1] \\ x[2] \\ \vdots \\ x[p] \end{bmatrix} \quad (4)$$

The matrix Z has a Vandermonde structure. Baron de Prony discovered a method to separately determine the z elements and h elements so that the matrix expression represents a set of linear simultaneous equations, which can be solved yielding the unknown vector of complex amplitudes.

First define the polynomial $\phi(z)$ that has the z_k exponentials as its roots,

$$\phi(z) = \prod_{k=1}^p (z - z_k) \quad (5)$$

Then expand equation (5) to arrive at,

$$\phi(z) = \sum_{m=0}^p a[m] z^{p-m} \quad \text{where } a(0) = 1.0 \quad (6)$$

and shift the index on equation (2) from n to $n-m$ and multiplying both sides by $a[m]$ yields,

$$a[m]x[n-m] = a[m] \sum_{k=1}^p h_k z_k^{n-m-1} \quad (7)$$

The same procedures are followed to form similar products $a[0]x[n]$, ... $a[m-1]x[n-m+1]$ and then summed to give,

$$\sum_{m=0}^p a[m]x[n-m] = \sum_{i=0}^p h_i \sum_{m=0}^p a[m] z_i^{n-m-1} \quad (8)$$

which is valid for $p+1 \leq n \leq 2p$.

Making the substitution $z_i^{n-m-1} = z_i^{n-p} z_i^{p-m-1}$ then,

$$\sum_{m=0}^p a[m]x[n-m] = \sum_{i=0}^p h_i z_i^{n-p} \sum_{m=0}^p a[m] z_i^{p-m-1} = 0 \quad (9)$$

The right hand side of equation (9) may be recognized as the polynomial defined by equation (5), evaluated at each of its roots z_i , yielding the zero result indicated.

The linear difference equation (9) has a homogeneous solution given by equation (2) and polynomial (5) is its characteristic equation. The Prony method first determines the polynomial coefficients $a[n]$. A $p \times p$ matrix equation, which satisfies equation (9), is used to evaluate the coefficient.

$$\begin{bmatrix} x(p) & x(p-1) & \cdots & x(1) \\ x(p+1) & x(p) & \cdots & x(2) \\ \vdots & \vdots & \ddots & \vdots \\ x(2p-1) & x(2p-2) & \cdots & x(p) \end{bmatrix} \begin{bmatrix} a[1] \\ a[2] \\ \vdots \\ a[p] \end{bmatrix} = - \begin{bmatrix} x[p+1] \\ x[p+2] \\ \vdots \\ x[2p] \end{bmatrix} \quad (10)$$

Once $a[n]$ are available, roots of polynomial (6), z_i , can be found and h_k by using equation (4). Based on these roots, the damping coefficient, frequencies, amplitude and initial phase are determined.

In engineering applications, the number of available data points usually exceeds $2p$, and the Least Squares Prony Method (LSPM), which minimizes the total squares error, is applied to find the coefficients.

3. THE SPECTRUM COMPUTATION

The spectrum here is defined in terms of the exponential approximation $\hat{x}[n]$ rather than $x[n]$. That is, it is the spectrum of the Prony model. One starts with a one sided discrete-time exponential sum

$$\hat{x}[n+1] = \begin{cases} \sum_{k=1}^p h_k z_k^n & n \geq 0 \\ 0 & n < 0 \end{cases} \quad (11)$$

which is defined over the interval $-\infty < n < \infty$. By taking the z-transform, Prony spectral density is found as

$$\hat{S}(f) = \left| T \sum_{k=1}^p \frac{h_k}{1 - \left(\frac{z_k}{\exp(j2\pi f T)} \right)} \right|^2 \quad -1/2T \leq f \leq 1/2T. \quad (12)$$

which is to be used to compute the frequency content after H and Z are found.

4. NUMERICAL EVALUATION

4.1. NUMERICAL IMPLEMENTATION

The Prony modeling and spectrum procedures are coded in a FORTRAN 77 program with double precision. As mentioned in the last section, data points numbering more than $2p$ are usually expected in engineering practice. Therefore, the scheme incorporated in the program for the computation of the polynomial coefficients, $a[n]$, is the Least Square Prony method. In the program, some of the subroutines were borrowed from reference [5] with modifications and from reference [10]. The critical root finding algorithm is the 'Three stage variable shifting iteration' by Jenkins and Traub [11]. In this algorithm variable-shifting was introduced to remedy the problem of polynomials with many nearly equimodular zeros, which existed in its previous version, the two stage algorithm [12]. When the order of the Prony model increases, which is inevitable in some situations, it becomes critical to find accurate polynomial coefficients and the root finding algorithm 'Three stage variable shifting iteration' serves this purpose well.

4.2. PROGRAM CALIBRATION

In this section, examples are presented for calibration of the computer program. Three deterministic functions were adopted to generate data sets, which in turn were used as input to the program for computation. All data generated according to the deterministic functions consist of 64 points. Computation results collected include parameters recaptured and spectral figures.

The first function was,

$$x(t) = 10 \exp(-0.5t) \cos(2\pi 25t + \pi) \quad (13)$$

and calculated results are presented in Table 1 and Figure 1. The order of the model was 2.

Table 1. Parameters Recaptured

Amplitude	Damping	Frequency (Hz)	Phase (rad)
10.0000000000	-0.5000000000	25.0000000000	3.1415926536

The second equation used to generated data was,

$$x(t) = 10 \exp(-0.5t) \cos(2\pi 25t + \pi) + 5 \exp(-0.8t) \cos(2\pi 10t + \pi / 2) + 3 \exp(-0.3t) \cos(2\pi 40t + 3\pi / 2) \quad (14)$$

and the recaptured parameters are listed in Table 2. Frequency content is presented in Figure 2. The order of the Prony models used were 6.

Table 2. Parameters Recaptured

Amplitude	Damping	Frequency (Hz)	Phase (rad)
5.0000000000	-0.8000000000	10.0000000000	1.5707963268
3.0000000000	-0.3000000000	40.0000000000	-1.5707963268
10.0000000000	-0.5000000000	25.0000000000	3.1415926536

The third set of data was generated by using equation (15),

$$x(t) = 10 \exp(-0.5t) \cos(2\pi 25t + \pi) + 10 \exp(-0.5t) \cos(2\pi 26t + \pi / 4) + 5 \exp(-0.8t) \cos(2\pi 10t + \pi / 2) + 3 \exp(-0.3t) \cos(2\pi 40t + 3\pi / 2) \quad (15)$$

Table 3 shows the recaptured parameters and the frequency presentation is in Figure 3. The model order was 8 for this example.

Table 3. Parameters Recaptured

Amplitude	Damping Constant	Frequency (Hz)	Phase (rad)
5.0000000000	-0.8000000000	10.0000000000	1.5707963268
3.0000000000	-0.3000000000	40.0000000000	-1.5707963268
10.0000000000	-0.5000000000	25.0000000000	-3.1415926536
10.0000000000	-0.5000000000	26.0000000000	0.7853981634

Examples with higher damping coefficients were also tested and the results were all accurate provided the vibration lasted no less than one period before it dies down. Note that the parameters presented in the tables are with 10 decimal points due to limited paper space while they were actually accurate up to 16 decimal points. From the three examples, one can see that the program runs well and the results are accurate.

4.3. SIMULATION TEST

The simulated data were generated according to the following function, which is constituted by four exponential components and a stationary Gaussian white noise process. The data generated consists of 256 points.

$$\begin{aligned}
 x(t) = & 10\exp(-0.5t)\cos(2\pi 25t + \pi) + 10\exp(-0.5t)\cos(2\pi 26t + \pi/4) \\
 & + 5\exp(-0.8t)\cos(2\pi 10t + \pi/2) \\
 & + 3\exp(-0.3t)\cos(2\pi 40t + 3\pi/2) + W(t)
 \end{aligned}
 \tag{16}$$

where $W(t)$ is a Gaussian white noise process with zero mean and rms of 1.0. The spectral plot computed by using the program with order 32 is presented in Figure 4.

Because it is expected that very limited (short) vibration signals will be collected for analysis, all transient components are assumed to start simultaneously. If a time lag between the components exists, it should be depicted in terms of initial phase.

5. LABORATORY TEST

An experiment was conducted to illustrate the application of the Prony model based method to the analysis of transient vibration signals. The structure tested was a metal frame, which was made of angle shaped mild steel with bolt-nut secured joints. The dimensions of the frame are 67.5cm by 54 cm by 54 cm. The experiment set-up is shown in Figure 5.

Vibrations were generated by impact testing the frame. Two accelerometers were mounted on an upper horizontal piece of the frame. Vibration signals were collected through a Dynamic Signal Analyzer. Unlike a beam type structure [13], the theoretical calculation of the natural frequencies of the frame was not employed due to the fact that the joints may not be rigidly secured. Rather, for the purpose of comparison, the analyzer

was also used to analyze the same signals. The signals and computed results are presented in Figure 6 through Figure 9, where Figure 6 is the vibration signal and Figure 7 is the result calculated by the Prony program. Figure 8 presents the analyzed frequency contents synthesized by the Dynamic Signal Analyzer with one trial whereas Figure 9 outlines the spectrum by the same analyzer with ten averages.

It is worth mentioning that while the Dynamic Signal Analyzer is capable of analyzing frequency content of impact (transient) signals, it generally needs at least several averages to give a clear frequency spectral plot. As one observes from Figure 8, the figure resulting from one trial of signal processing on the DSA is rather unclear and barely reveals any useful information. The plot that was the result of ten averages arrives at a much clearer picture. The portion in the low frequency region is still not as sharp as the one generated by the Prony program. For the Prony method, one trail (trace) is enough for the program to come out with a clear spectral figure. Such an advantage would be extremely valuable in situations where repeated signals are difficult or even impossible to collect.

For the sake of testing the program, one of the joints was slightly loosened purposely and impact vibration testing was again conducted. The signal and its frequency spectral content are presented in figures 10 and 11. From Figure 11, one clearly sees that the pattern of the frequency presentation has changed. The dominant frequency has shifted down by almost 30 Hz and higher frequency content has also increased. This reveals the potential application of the Prony method in Machine Condition Monitoring. Note that all laboratory test data collected are 2048 points. The order of Prony model varies from 80 to 128. The order selection rule is that the richer the frequency content, the higher the model order. Computations of these data by the program took less than one second CUP run time on a dual Pentium II 266 MHz machine, which implies that there is a possibility for the program to be used for real time machine condition monitoring.

6. CONCLUDING REMARKS

Preliminary work has been carried out in exploring the application of the Prony method to the analysis of transient vibration signals, which has been left relatively unstudied. Numerical calibration, computer simulation and laboratory testing have been conducted to examine the Fortran 77 program that implements the Prony modeling procedures. From the preliminary results presented in this paper a few concluding remarks can be made.

- It was proven that the Prony method can be effectively employed for transient vibration signal analysis.

- The test results show that the program runs well and the computations are accurate and efficient.
- It is revealed that the program has potential to be adopted in Machine Condition Monitoring and real time applications.
- The immediate step to follow is to test the program on lab MCM tests and industrial problems.

7. ACKNOWLEDGEMENTS

Sincere thanks are due to professor S.M. Dickinson for his help and support during the course of this study and NSERC for financial support.

8. REFERENCES

1. Braun, S., *Mechanical Signature Analysis -- Theory and Applications*, Academic Press Inc., 1986.
2. Kay, S.M. and Marple, S. L., Spectrum Analysis--A Modern Perspective, *Proceedings of the IEEE*, Vol. 69, No. 11, Nov. 1981, pp.1380-1419.
3. Kay, S. M., *Modern Spectral Estimation: Theory And Application*, Prentice Hall Inc., 1988.
4. Gade,S. and Gram-Hansen, K., "The analysis of nonstationary signals", *Sound and vibration*, Jan. 1997, pp. 40-46.
5. Marple Jr, S. L., *Digital Spectral Analysis With Applications*, Prentice Hall, 1987.
6. Innes, A. G., The use of Prony Method for Modeling Induction Motor Current Waveforms Under Fault Conditions, Dept. of Electrical and Electronic Engineering, Univ. of Tasmania, Hobart, Australia.
7. Mechefske, C. K., Correlating power transformer tank vibration characteristics to winding looseness, *Insight*, Vol. 37, No. 8, 1996, pp. 599-604.
8. Sun, T., Zhang, Z. Y., Grattan, K. T. V. and Palmer, A. W., Analysis of Double Exponential Fluorescence Decay Behavior for Optical Temperature Sensing, *Rev. Sci. Instrum.*, Vol. 68(1), Jan., 1997, pp. 58-63.
9. Dowling, E. M., DeGroat, R. D. and Linebarger, D. A., Exponential parameter Estimation in the presence of known components and noise, *IEEE Transactions on Antennas and propagation*, Vol. 42, No. 5, May 1994, pp. 590—599.
10. Vetterling, W.T., et al., *Numerical Recipes in Fortran 77*, Cambridge Press, 1992.
11. Jerkins, M. A. and Traub, J. F., Zeros of a Complex Polynomial, *Communication of ACM*, Vol. 15, Feb. 1972, pp. 97-99.
12. Jerkins, M. A. and Traub, J. F., A Three-Stage Variable-Shift Iteration for Polynomial Zeros and Its Relation to Generalized Rayleigh Iteration, *Numeriske Mathematik*, Vol. 14, 1970, pp. 252—263.

13. Chen, Z. and Mechefske, C. K., Machine Condition Monitoring Based on Transient Vibration Signal Analysis, *Proceedings of the Sixth International Congress on Sound and Vibration*, Copenhagen, Denmark, 5-8 July 1999, pp2951-2958.

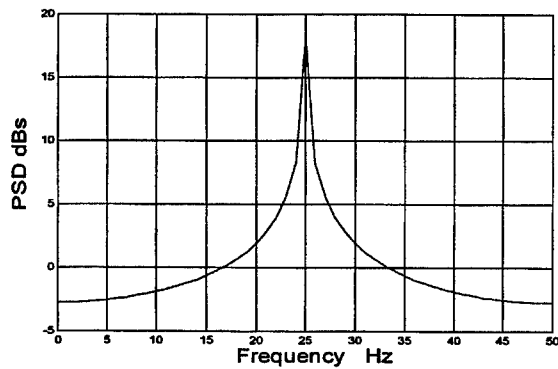


Figure 1: Spectral presentation of data by Equation 13.
The peak in the figure is at frequency 25.0 Hz.

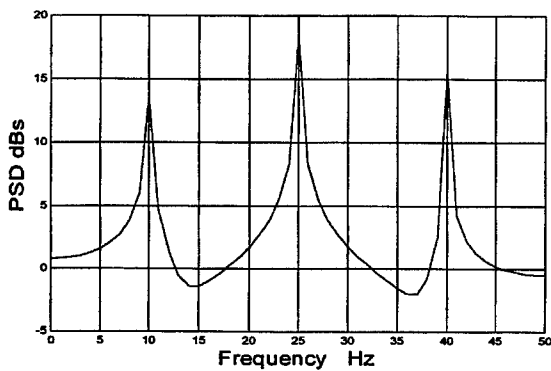


Figure 2: Spectral presentation of data by Equation 14.
The peaks in the figure are at the frequencies of 10.0 Hz, 25.0 Hz and 40.0 Hz.

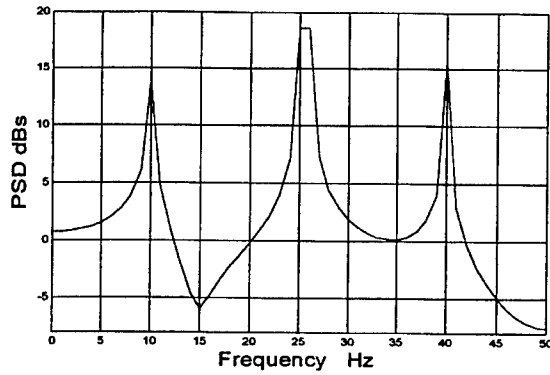


Figure 3: Spectral presentation of data by Equation 15.
The peaks in the figure appear at 10.0 Hz, 25.0 Hz, 26.0 Hz and 40.0 Hz.

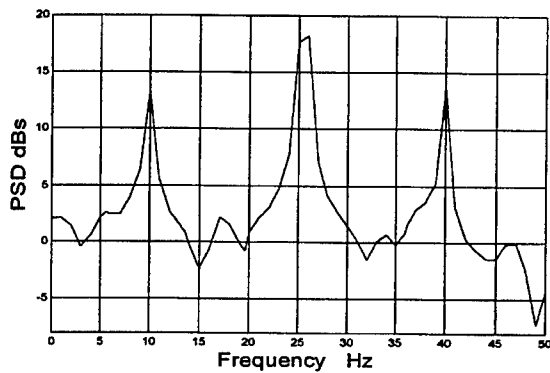


Figure 4: Spectral presentation of simulated data.
The peaks in the figures land at frequencies 10.0, 25.0, 26.0 and 40.0 Hz.

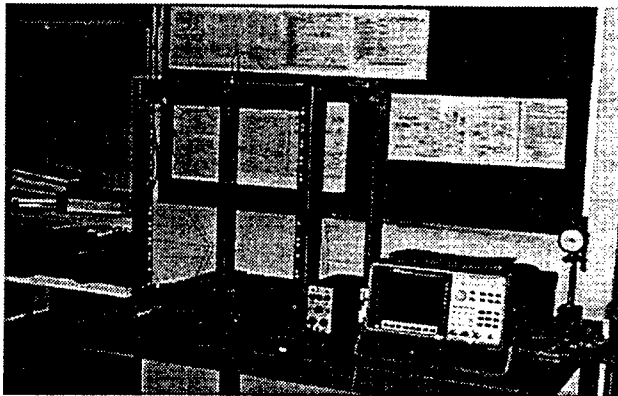


Figure 5: Experiment set-up of the metal frame.

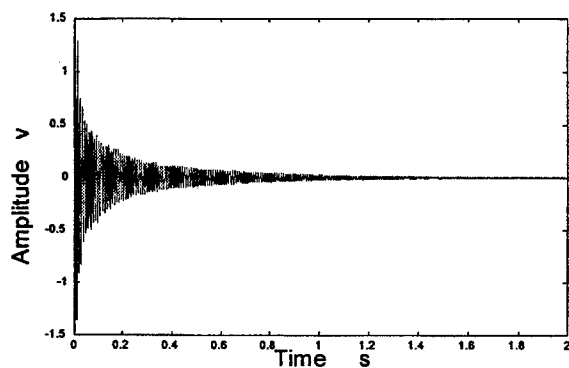


Figure 6: Sample impact test vibration signal.

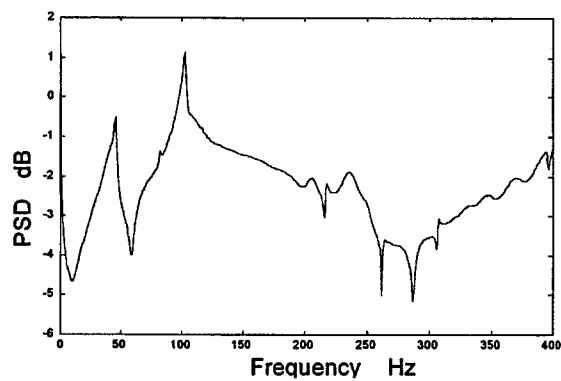


Figure 7: Sample spectrum of an impact test computed using the Prony method.

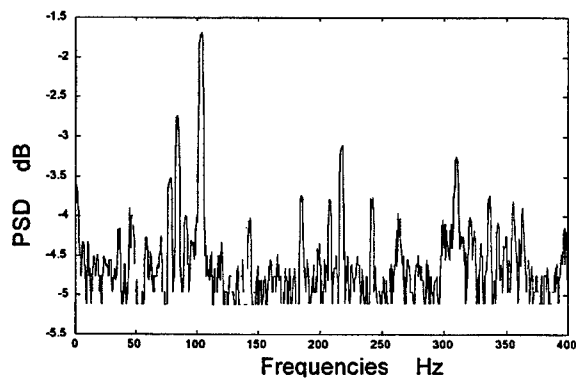


Figure 8: Spectrum of the vibration signal (one trial) from the DSA.

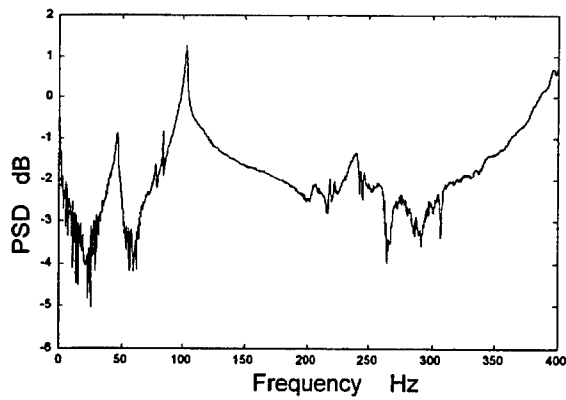


Figure 9: Spectrum of vibration signals (ten averages) from the DSA.

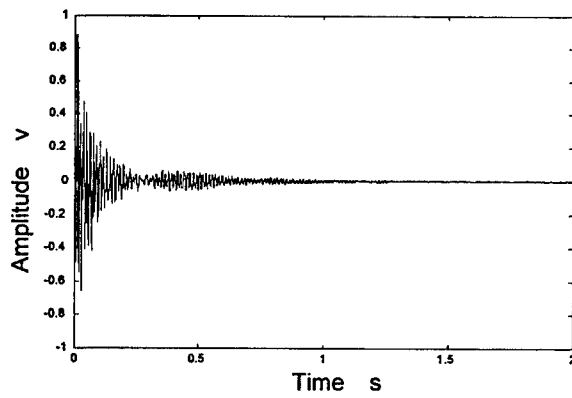


Figure 10: Sample impact test vibration signal (loosened bolt).

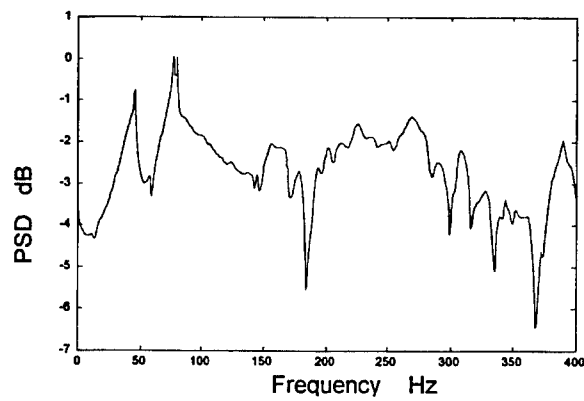


Figure 11: Spectrum of the vibration signal with the loosened bolt using the Prony method.

FINITE ELEMENT ANALYSIS OF RUBBER MOUNTS UNDER SHOCK LOADING

K. T. Feroz, S. O. Oyadiji, J. R. Wright and A. Y. T Leung
Dynamics and Aeroelasticity Research Group
Division of Mechanical Engineering
Manchester School of Engineering
University of Manchester
Manchester M13 9PL

ABSTRACT

The responses of two rubber mounts subjected to shock loading were studied using the finite element method. The mounts consist of steel plates which are bonded to blocks of polyisoprene and silicone rubber. The mounts were subjected to two half-sine wave acceleration pulses of maximum amplitudes of 500g and 1000g, applied to the bottom plates of the mounts. A procedure for transforming the complex modulus of the rubber from the frequency domain to the time domain relaxation modulus using the Fourier transform analysis and Prony series is presented. The predicted non-dimensionalised responses, which are presented in the time and frequency domains, show that the silicone rubber mount had better damping characteristics in terms of reducing the amplitude of the high frequency content of the input shock spectra.

INTRODUCTION

Viscoelastic materials, such as vulcanised, natural or synthetic rubber, are widely used as shock and vibration isolators in the mechanical, civil, marine and aerospace industries. For example, they are used as shock and vibration isolators in submarines and surface vessels, as bumpers, bushings, mounts and for suspensions in automotive vehicles. They are also used as foundation bearings for buildings located above underground train tunnels and areas prone to earthquakes.

The use of viscoelastic material in anti-vibration mount for the passive isolation and control of structural vibration and noise is well established experimentally and theoretically. Vibration isolation properties can be predicted accurately using analytical and numerical methods, with the finite element method being the principal numerical technique. On the other hand, theoretical work on the use of viscoelastic materials for shock loading condition is relatively less developed. This might be due to the nonlinear behaviour of viscoelastic materials under a fast transient shock loading. Also, the theoretical analysis of the shock isolation properties of a viscoelastic element requires the use of time domain relaxation modulus. The dynamic properties of viscoelastic materials are commonly obtained in the frequency

domain. It is, therefore, necessary to transform the data into the time domain to enable its use in a short duration fast transient shock analysis.

Nashif et al [1] and Tschoegl [2] show that the viscoelastic properties represented in one domain can be transformed to the other domain using mathematical models. Chan [3] concluded that Prony series implemented in ABAQUS for the time domain analysis to predict the transient response of a viscoelastically-damped system provided good agreement between measured and predicted responses. Kazakoff et al [4] studied the non-linear behaviour of a viscoelastic system due to shock loading and concluded that geometrical non-linearity has a significant effect on the transmissibility of a viscoelastic system. Recent work by Tomlinson et al [5] investigated a finite element modelling of viscoelastic elements subjected to shock loading. The viscoelastic element was modelled using HYPERELASTIC option within the ABAQUS code and the displacement response show good agreement with the experimental measurements.

In this work, the responses of two rubber mounts subjected to shock loading were studied using the finite element method. Each mount consists of two steel plates which are bonded to a block of polyisoprene rubber of shore hardness 55 or to a block of silicone rubber. The input shock loading was in the form of a half-sine wave acceleration pulse of amplitude ranging from 500 g to 1000 g where g is 9.81 ms^{-2} . The successful prediction of the vibration and shock response of the rubber mount depends on the choice of appropriate element types for both the rubber and metal plates, and also on the accurate representation of the viscoelastic material property in the time domain using Prony series. The procedure for transforming the frequency domain complex Young's modulus properties of the rubber to the time domain relaxation modulus using Fourier transform and Prony series is presented. The predicted acceleration responses, which are presented in the time and frequency domains, show that the silicone rubber mount had better damping characteristics in terms of reducing the amplitude of the high frequency content of the input shock spectra.

DERIVATION OF PRONY SERIES CONSTANTS

For the time domain FE analyses, the most important parameters needed were the Prony series coefficients which describe the relaxation modulus $E(t)$ in the time domain. To derive these coefficients, the magnitude of the complex Young's modulus $E(\omega)$ and loss factor $\eta(\omega)$, available from the master curve [6,7], are read manually for a limited range of frequency. From these, the storage modulus $E'(\omega)$ and loss modulus $E''(\omega)$ are obtained using the following expressions:

$$E(\omega) = E'(\omega)\sqrt{1+\eta(\omega)^2} \quad ; \quad E'(\omega) = E''(\omega)\eta(\omega) \quad (1)$$

The time domain relaxation modulus $E^*(t)$ is related to the real and imaginary parts of $E(\omega)$ by the Fourier transform as [8]

$$E^*(t) = \int_{-\infty}^{\infty} \left(\frac{E'(\omega) + jE''(\omega)}{j\omega} \right) e^{i\omega t} d\omega \quad (2)$$

The derived $E'(\omega)$ and $E''(\omega)$ values from Eq.(1) are used in the integration indicated in Eq.(2) to obtain the relaxation Young's modulus in the time domain. This is carried out numerically by means of the inverse Fourier transform procedures of the MATLAB [9] software. The resulting time domain master curves of relaxation Young's modulus for polyisoprene and silicone rubber are shown by the solid lines in Figure 1 (a) and (b).

The time domain Young's modulus was read at equal intervals on a logarithmic scale in order to find the Prony series constants consisting of the modulus ratio e_k , and the relaxation time constant τ_k . These constants were determined using,

$$e_k = \frac{E_k}{E_g} \quad ; \quad k = 0, 1, 2, \dots, N \quad (3)$$

$$\tau_k = a * 10^{(m+jp)} \quad ; \quad j = 1, 2, 3, \dots, k \quad (4)$$

where E_k 's are the relative relaxation moduli, E_g is the glassy or instantaneous modulus, 'a' is a proportionality constant, which must be determined in a suitable way, 'm' is the beginning of the time scale and 'p' is the time interval at which the Young's moduli were chosen. The method adopted in the present work is the collocation method [6]. These Prony series constants are used in the Wiechert-Kelvin model of viscoelasticity to curve-fit the relaxation modulus data using,

$$E_j = E_g \left(1 - \sum_k e_k [1 - \exp(-t/\tau_k)] \right) \quad (5)$$

The derived Prony series constants are shown in Table 1. Figures 1(a) and (b) show the comparison between the relaxation modulus obtained from the original frequency domain data, represented by solid lines, and from Eq.(5), represented by the dashed lines, using the derived Prony series constants. These figures also show that five terms of the Prony series are enough to obtain a good comparison between the measured data and fitted curve.

FINITE ELEMENT MODELLING

The rubber mounts used consisted of two metal plates of dimensions 280x200x10 mm which were bonded to the top and bottom of polyisoprene and silicone rubber blocks of dimensions 200x190x150 mm. The finite element modelling was performed using 3D solid elements of types C3D20 to model the mild steel metal plates and C3D20H to model the polyisoprene and silicone rubber blocks. The FE mesh is shown in Figure 2. The element types

C3D20 and C3D20H were 20 node quadratic brick element. In addition, elements C3D20H were hybrid elements intended for use with incompressible and almost incompressible material behaviour. The model had free boundary conditions. The FE mesh generation, analysis and extraction of results were carried out using the ABAQUS [10] and PATRAN [11] FE codes. Non-linear time domain dynamic analyses of the viscoelastic mounts were performed by means of the *DYNAMIC option in the ABAQUS.

The input shock loading, in the form of half-sine wave acceleration, was applied at the nodes of the bottom metal plate as a base excitation. The maximum amplitudes of the half-sine wave were 500 g and 1000 g. The time domain extensional relaxation modulus data of the viscoelastic material was supplied to the finite element model as a Prony series defined by the parameters e_k and τ_k . Using a time step of 1 microsecond, the acceleration responses at the middle of the bottom and top plates were predicted.

DISCUSSION OF RESULTS

The input acceleration–time history obtained at the middle of the bottom plate for a maximum pulse amplitude of 500 g and its frequency spectrum, computed by means of fast Fourier transform (FFT), are shown in Figure 3. In this figure, plot (a) is the time history, while plots (b) and (c) are frequency spectra, in linear and log scales respectively, obtained by performing FFT using MATLAB [8] on the data shown in plot (a). The predicted output responses are presented in non-dimensional form. Thus, in Figures 4 to 7, the y-axis of plot (a) is the ratio of the output acceleration to the maximum input acceleration while the x-axis is the ratio of the total time, t , to the duration of the input acceleration, T . Plots (b) and (c) are obtained by performing FFT on the data shown in plot (a); plot (b) is in linear scale, while plot (c) is in logarithmic scale.

Figure 4 shows the output response for an input acceleration pulse of 500 g amplitude for the polyisoprene rubber. The time domain response shows that a maximum acceleration amplitude ratio of 0.65 is obtained at the middle of the top steel plate after an elapsed time ratio of about 2.3. The amplitude ratio decreases as the time ratio increases and remains at an amplitude ratio of less than 0.2 after a time ratio of 70. The frequency domain responses show a high peak in amplitude at a frequency ratio of 0.6. After a frequency ratio of 2.5 the amplitude becomes negligibly small. For the input acceleration pulse of 1000g amplitude, Figure 5(a) shows that a maximum acceleration amplitude ratio of 0.65 was obtained at the middle of the top steel plate after an elapsed time ratio of about 8.3. Figure 5(a) also shows that after a time ratio of 40, the amplitude ratio reduces to less than 0.3. The frequency spectra shown in Figures 5(b) and (c) indicate a high peak in amplitude at a frequency ratio of 0.6. Also, the amplitude becomes negligibly small after a frequency ratio of 5 (plot (c)).

For an input half-sine shock of 500 g amplitude, Figure 6 shows the response of the silicone rubber mount. A maximum output to input acceleration ratio of 0.25 was obtained at the middle of the top plate after an elapsed time ratio of 10 as can be seen from Figure 6(a). Similarly, Figure 6(b) and (c) show peak amplitudes at frequency ratios between of 0.1 and 0.5, but the amplitude ratio becomes negligibly small after a frequency ratio of 1. When the input half-sine shock was of 1000 g amplitude, Figure 7 shows that the output response remains the same as in the previous case. A maximum output to input acceleration ratio of amplitude 0.25 was obtained after an elapsed time of 10. Also, the frequency domain response shows peak amplitude ratios at frequency ratios of between 0.1 and 0.5. Beyond the frequency ratio of 1.0, the amplitude ratio becomes negligibly small.

Comparing Figure 4 with Figure 5, it is seen that the shock response amplitudes of the rubber polyisoprene mount increase as the input acceleration increases. In the case of the silicone rubber mount, Figures 6 and 7 show that the responses are almost the same as the input acceleration increases. This suggests that the behaviour of the polyisoprene mount is non-linear, while the behaviour of silicone the rubber mount is approximately linear. Furthermore, comparing Figures 4 and 5 with Figures 6 and 7 shows that the silicone rubber mount provided greater shock isolation than the polyisoprene rubber mount. For example, for an input half-sine shock of 500 g amplitude, the maximum shock response amplitude ratios were 0.65 and 0.25 for the polyisoprene and silicone rubber mounts respectively. Also, the figures show that the high frequency content of the shock spectrum is isolated completely above a frequency ratio of 1.0 by the silicone rubber mount, whereas complete isolation is obtained only above a frequency ratio of 6 by the polyisoprene rubber mount.

CONCLUSIONS

Procedures for transforming frequency- and temperature-dependent complex Young's modulus properties of viscoelastic materials to relaxation moduli using Fourier transform and Prony series have been demonstrated. The shock response characteristics of two rubber mounts were predicted for input half-sine acceleration pulses of 500 g and 1000 g amplitudes. In all cases, the maximum amplitude of the output shock response was less than the maximum amplitude of the input shock excitation. Also, the maximum amplitude of the shock response increased as the input shock excitation amplitude was increased for the polyisoprene rubber mount, whereas it remained the same for the silicone rubber mount. Overall, the silicone rubber mount provided greater shock isolation than the polyisoprene rubber mount.

ACKNOWLEDGEMENTS

This work is supported by the Engineering and Physical Science Research Council.

REFERENCES

1. Nashif, A. D, Jones. D. I. G and Hendersom, J. P, vibration damping, John Wiley and Sons, New York, 1985.
2. Tschoegl, N. W, The phenomenological theory of linear viscoelastic behaviour, Springer-Verlag, 1989.
3. Chan, Y. W, Characterisation and prediction of the dynamic response of viscoelastic elements, PhD thesis, University of Manchester, UK.
4. Kazakoff, A. B, Rongong, J. A, and Tomlinson, G. R , Identification of the influence of shock impact on the non-linear dynamic behaviour of double mass viscoelastic system.
5. Tomlinson, G. R, Kazakoff, A. B, and Thompson, P. R, Finite element modelling of Viscoelastic elements subjected to large static and dynamic deformations.
6. Feroz, K. T, Oyadiji, S.O and Tomlinson, G. R, Analysis of mechanical filters, Technical report, TR95/DRA/ No.3 (for DRA Dunfermline), Manchester school of engineering, 1995.
7. Oyadiji, S. O, Feroz, K. T and Tomlinson, G. R, Design of polymer-based mechanical filters for shock measurement accelerometers, in smart structures and material 1996: passive damping and isolation, Johnson, C.D, Editor, Proc. SPIE2720, 1996, pp305-316.
8. Bracewell, R. N, The Fourier transform and its applications, 2nd edition, McGraw-Hill book company, New York, 1978.
9. MATLAB users manual, The Math Works Inc. 1991.
10. ABAQUS users and theory manuals, Hibbit, Karlson & Sorensen, 1996.
11. PATRAN manual, PDA Engineering software products divisions, 1996.

Table 1: Prony series parameters

No	Polyisoprene ϵ_k	Silicone rubber ϵ_k	τ_k
1	0.13366	0.3977	0.1443E-04
2	0.17159	0.18143	0.1443E-03
3	0.5153E-01	0.1091	0.1443E-02
4	0.354613E-01	0.3822E-01	0.1443E-01
5	0.12322E-01	0.4847E-01	0.1443

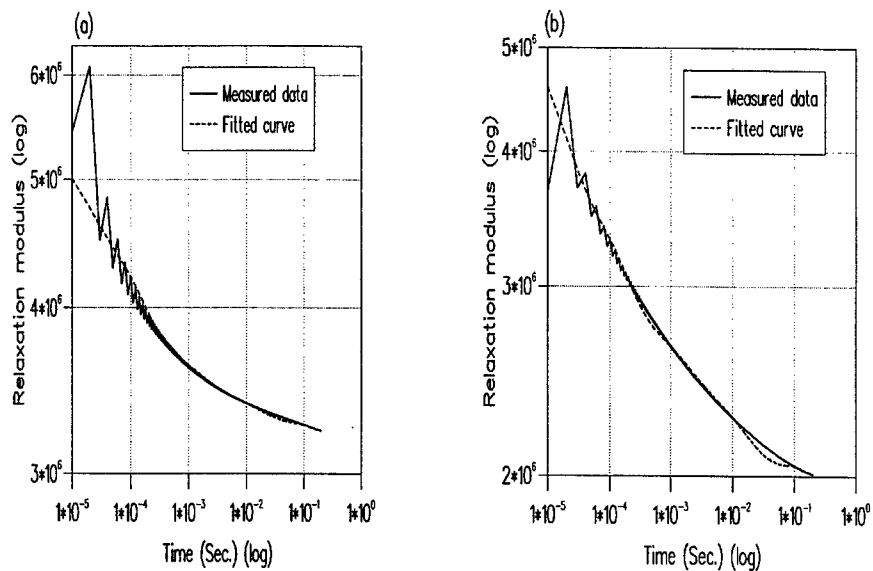


Figure 1: Relaxation modulus of viscoelastic materials:
(a) polyisoprene rubber, (b) silicone rubber.

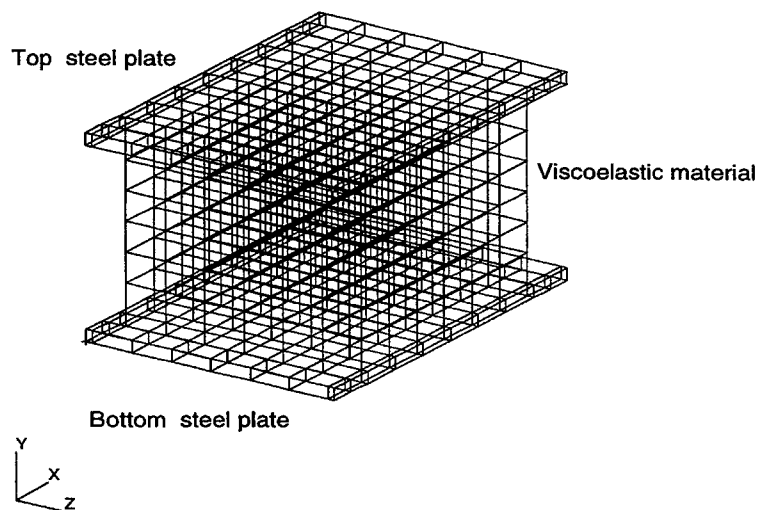


Figure 2: Finite element mesh for the rubber mount.

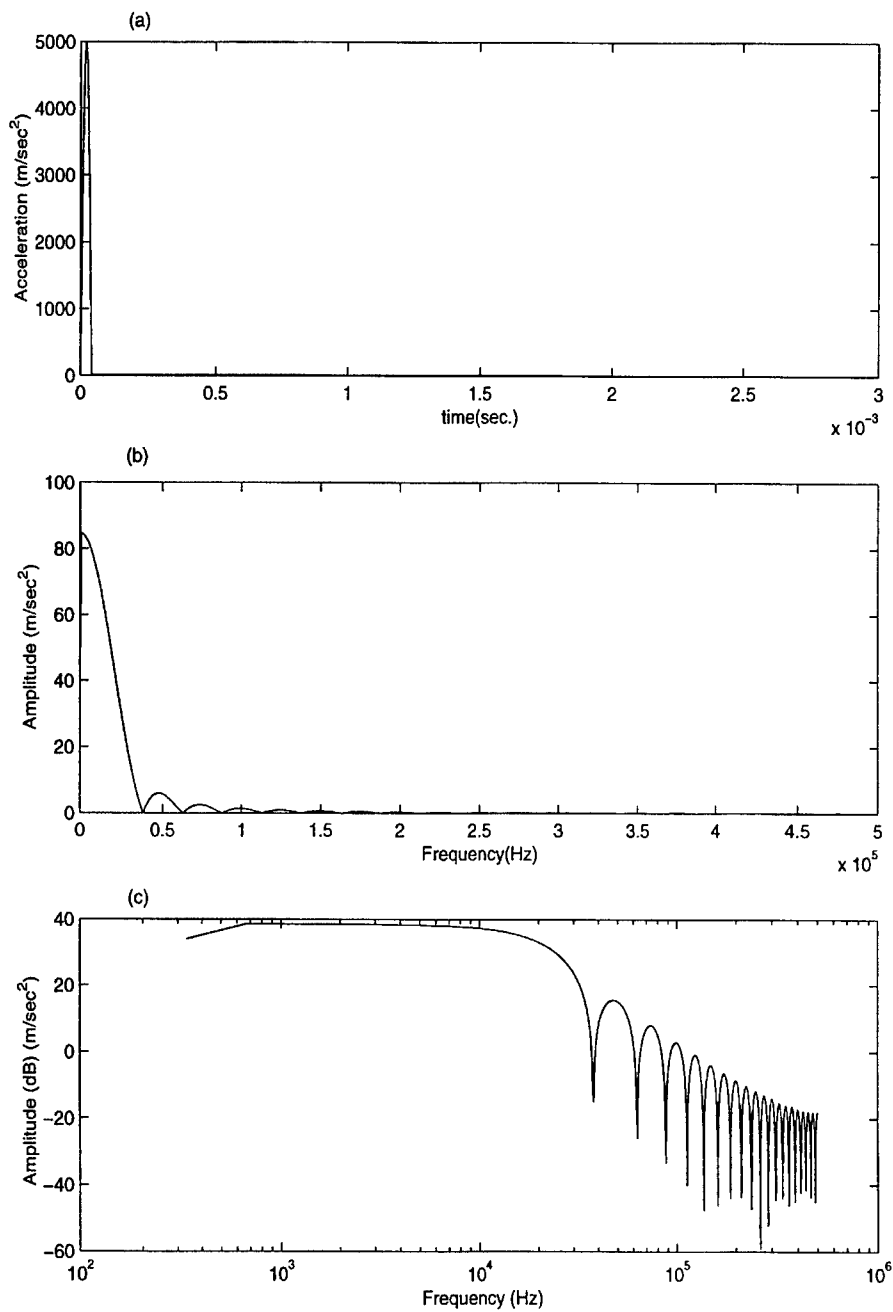


Figure 3: The input force history and spectra at the bottom plates of the rubber mounts for a maximum acceleration of 500 g (a) in time domain (b) in frequency domain, linear scale, and (c) in log scale.

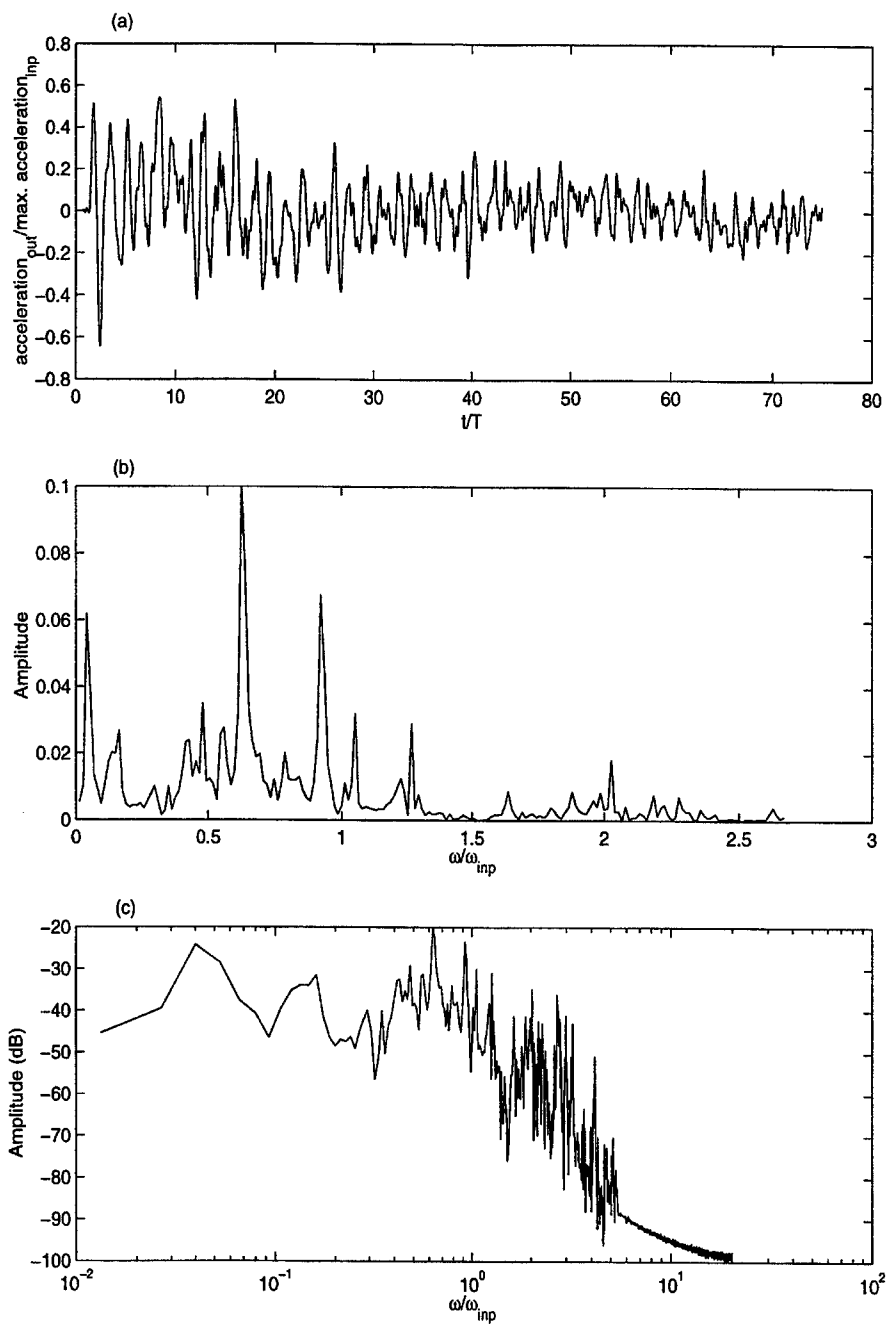


Figure 4: Output response at the top of the polyisoprene rubber mount for a maximum amplitude of input acceleration of 500 g : (a) time domain response (b) frequency domain response in linear scale and (c) in log scale.

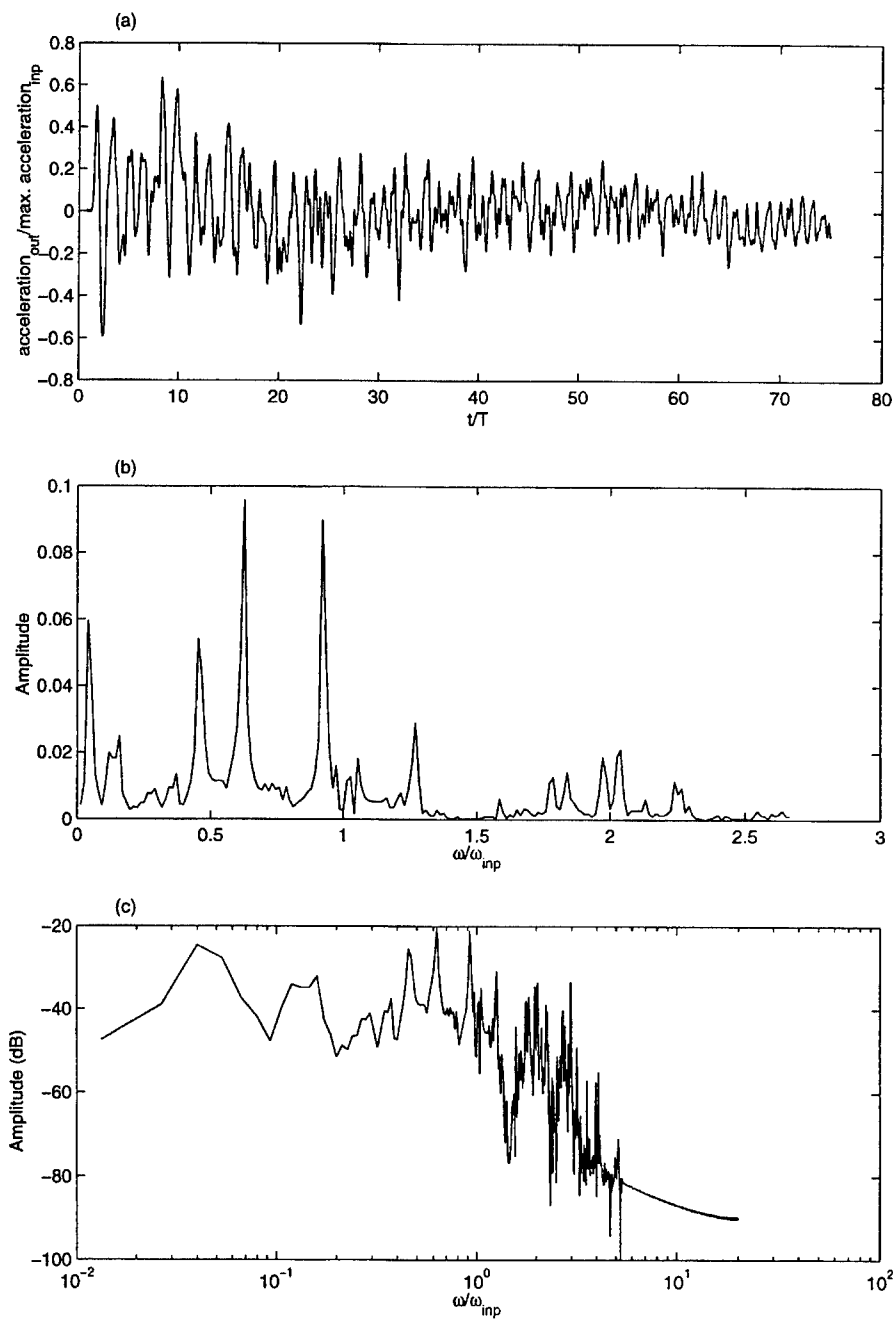


Figure 5: Output response at the top of the polyisoprene rubber mount for a maximum amplitude of input acceleration of 1000 g : (a) time domain response, (b) frequency domain response in linear scale and (c) in log scale.

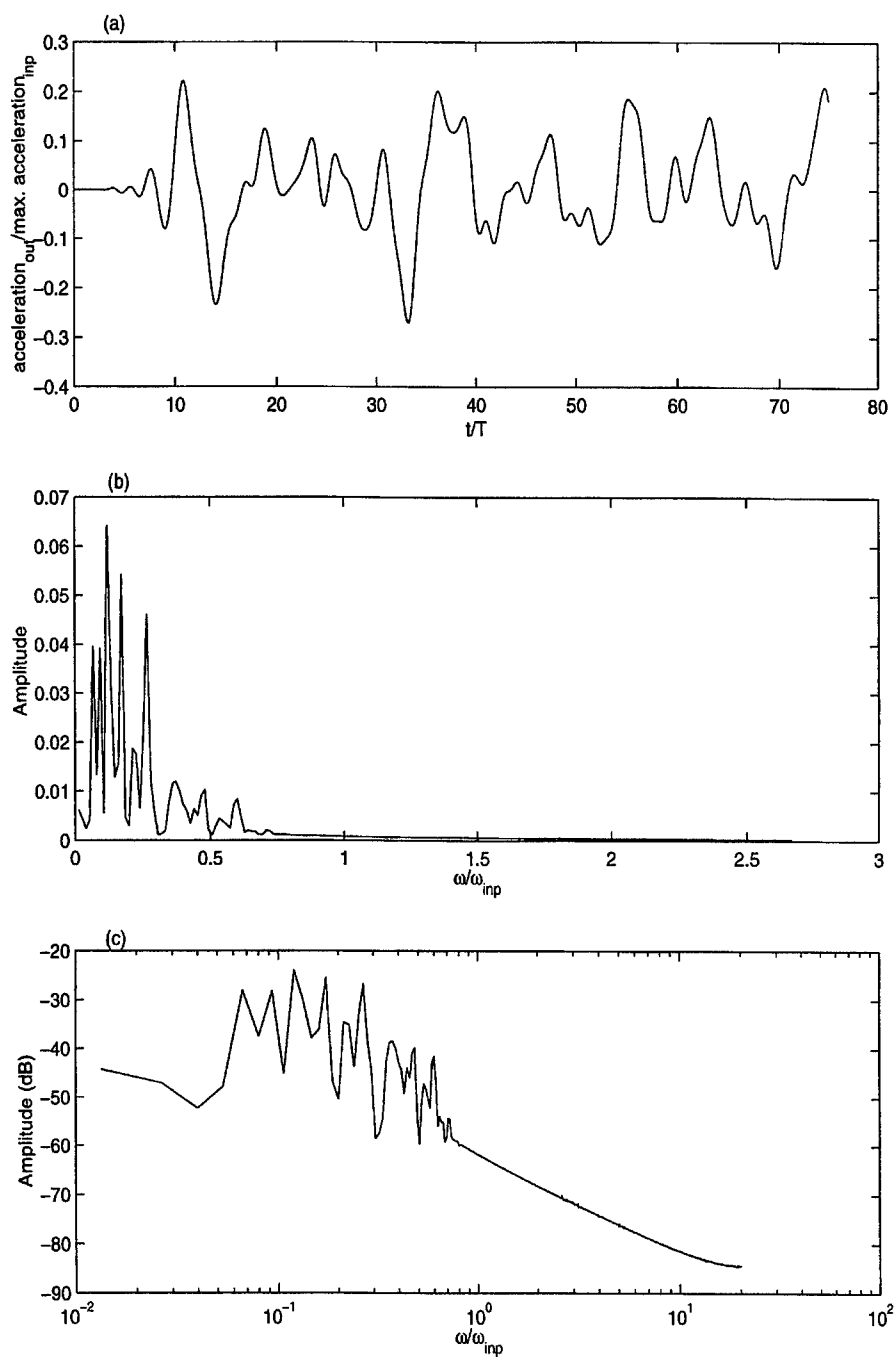


Figure 6: Output response at the top of the silicone rubber mount consist for a maximum amplitude of input acceleration of 500 g : (a) time domain response, (b) frequency domain response in linear scale and (c) in log scale.

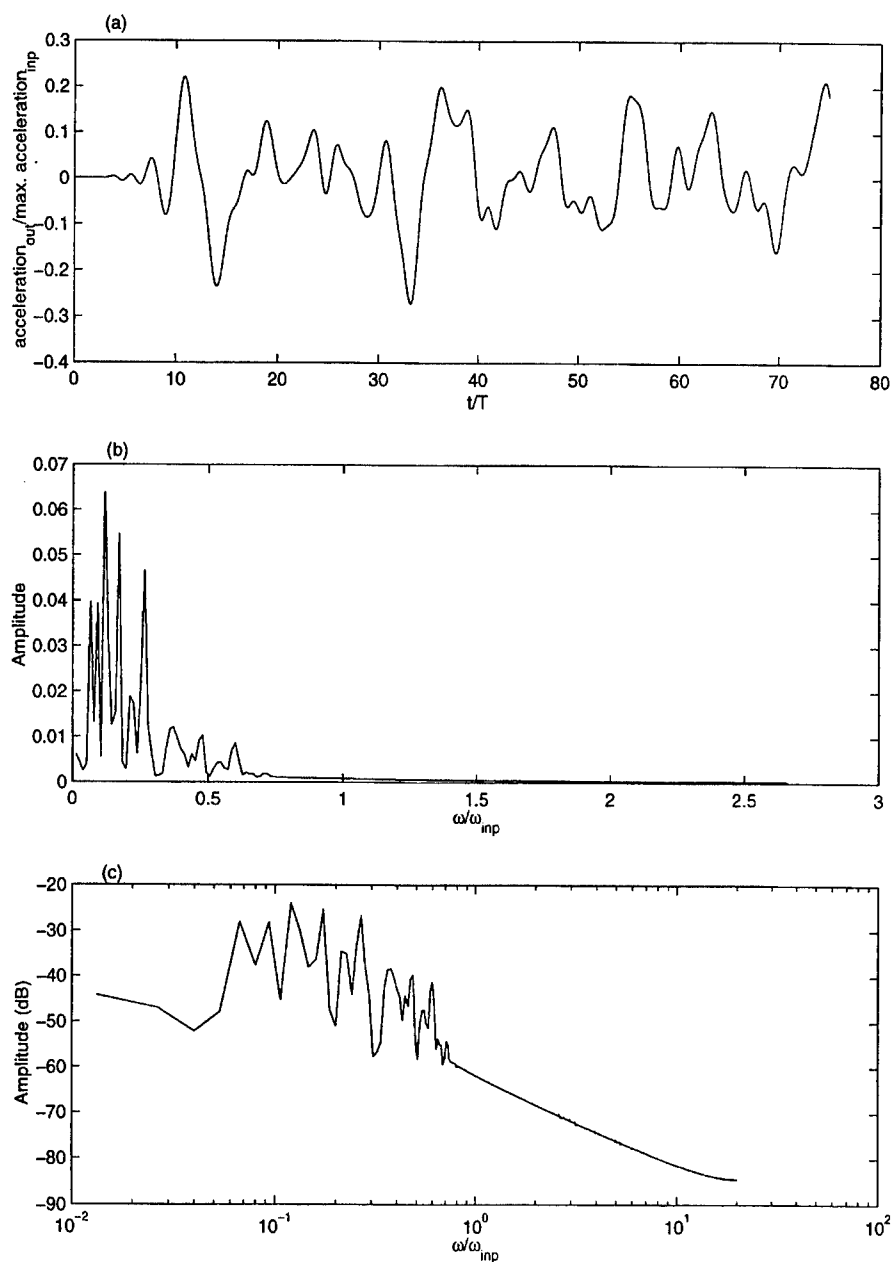


Figure 7: Output response at the top of the silicone rubber mount for a maximum amplitude of input acceleration of 1000 g : (a) time domain response, (b) frequency domain response in linear scale and (c) in log scale.

A DYNAMIC CALCULATION MODEL OF SHANGHAI SATURATED SOFT SOIL

Huang Yu, Tang Yiqun, Ye Weimin, Chen Zhuchang

Department of Geotechnical Engineering, Tongji University, Shanghai
200092, China.

SUMMARY

In this paper, the saturated soil is modeled as a two-phase porous media system consisting of solid and fluid phases. On the basis of resonant column test and dynamic triaxial test data of Shanghai saturated soft soil, the dynamic calculation model including a set of relationships of stress, strain, pore water pressure and earthquake subsidence is developed to compute the seismic response of soil. The procedure to identify soil constants for the dynamic calculation model is also reported in detail. Subsequently, a dynamic effective stress analysis with the finite element method has been recommended to predict the seismic response of soil. Finally, the developed dynamic calculation model together with the dynamic effective stress analysis is utilized to predict the seismic response of Shanghai soil strata through the finite element method.

KEY WORDS: Shanghai; saturated soft soil; dynamic calculation model; seismic response; finite element method

INTRODUCTION

Shanghai is located on the East Coast of China at the mouth of the Yangtze River at the Donghai Sea. The alluvial soil deposit of Shanghai is 150-400m deep with an about 100m thick saturated soft soil, which has a large water content and a high compressibility. Although Shanghai is not a seismic area, there are several seismic sources within a range of 200-300 km. The earthquake influencing Shanghai was firstly recorded in 288. Several moderate earthquakes have affected Shanghai in the past twenty years, such as Liyang Earthquake in 1979 ($M = 6.0$), South Huanghai Sea Earthquake in 1984 ($M = 6.2$), Changshu-Taicang

earthquake in 1990 ($M = 5.1$) and South Huanghai Sea Earthquake in 1996 ($M = 6.1$). It has a great meaning to predict the earthquake response of Shanghai saturated soft soil.

The equivalent linear approach has been widely used to compute the approximate nonlinear response of soil approximately. The equivalent linear method and the nonlinear methods were reviewed by Martin and Seed [1]. From the study of an extensive experimental data, a dynamic computation model is proposed in this paper, which is an equivalent viscoelastic model including a set of relationships of stress, strain, pore water pressure and earthquake subsidence. Compared with elastoplastic models, the model simulates the soil dynamic behavior in a cycle of loading as a whole, not in detail.

Biot [2-3] established the basic dynamic equations for porous media. Later, Zienkiewicz et al. [4-5] introduced the numerical solution of these equations. Based on these theories the dynamic effective analysis method is conducted with the dynamic calculation model in this paper.

CALCULATION MODEL

Shear modulus

The proposed expression of the secant shear modulus G at a strain amplitude γ is

$$\frac{G}{G_{\max}} = 1 - H(\gamma) \quad (1)$$

In the model, the function $H(\gamma)$ is

$$H(\gamma) = \left[\frac{(\gamma/\gamma_r)^{2B}}{1 + (\gamma/\gamma_r)^{2B}} \right]^A \quad (2)$$

where γ_r = a reference or yield strain; and A and B = two dimensionless parameters.

It is suggested that values of γ_r for Shanghai saturated soft soil could be determined by the empirical relationship

$$\gamma_r = C \cdot \sqrt[3]{\sigma'_0} \quad (3)$$

where σ'_0 = the effective mean principal stress in kPa, and C = an empirical parameter. Table 1 shows a summary of the experimental numerical values for the three parameters A , B , and C obtained for

Shanghai saturated soft soil.

Table 1. Reference value of parameters: A , B , and C

Soil type	A	B	C
Clay	1.62	0.42	0.00013
Silt	1.12	0.44	0.00017
Sand	1.10	0.48	0.00022

The following relationship between G_{max} , the void ratio e , the over consolidation ratio OCR, and the confining pressure σ'_0 has been widely used:

$$G_{max} = D \frac{OCR^k}{0.3 + 0.7e^2} P_a \left(\frac{\sigma'_0}{P_a} \right)^{0.5} \quad (4)$$

where P_a = atmospheric pressure, and k = a coefficient which relates to plasticity index of soil. Shanghai saturated soft soil may be treated as normally consolidated soil except surface crust and dark green stiff clay of about 3m thickness in the depth of 25m. Based on the above relationship and experimental data, an acceptable fit for Shanghai saturated soft soil is obtained, as follows: $D = 353$ for clay, $D = 451$ for silt, and $D = 485$ for sand.

The curve of shear modulus ratio G/G_{max} of Shanghai clay with γ is compared with the experimental data in Figure 1.

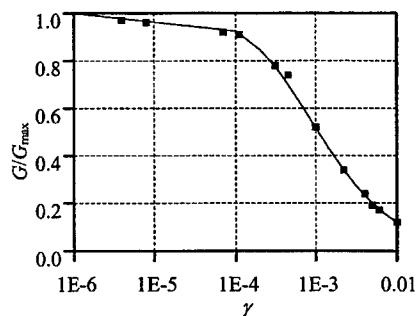


Figure 1. The relationship between shear modulus ratio and shear strain of Shanghai clay

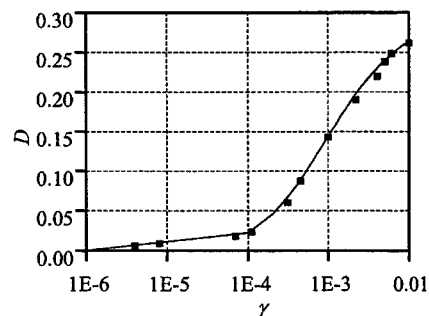


Figure 2. The relationship between damping ratio and shear strain of Shanghai clay

Damping

For Shanghai saturated soft soil, the variation of the damping ratio, D , with strain level is

$$\frac{D}{D_{\max}} = \left(1 - \frac{G}{G_{\max}}\right)^{\beta} \quad (5)$$

where $D_{\max} = 0.30$ for clay, $D_{\max} = 0.25$ for silt and sand; and $\beta = 1.0$. A comparison between the proposed model and experimental data is shown in Figure 2.

Pore water pressure generation

On the basis of the results from undrained cyclic triaxial test data, the pore water pressure buildup of Shanghai clay and silt may be expressed as

$$\frac{p}{\sigma'_0} = aN^b \quad (6)$$

where p = the pore water pressure; N = the number of uniform stress cycles; and a and b = two experimental parameters which are determined by the ratio of the dynamic shear stress to the effective confining pressure. Table 2 shows the reference value of a and b for Shanghai clay and silt. The curve of pore water pressure ratio p/σ'_0 and N of Shanghai mucky clay is compared with the experimental data in Figure 3.

Table 2. Reference value of a and b for Shanghai clay

Soil type	a	b
Clay	$0.274 r_{\tau}^{0.767}$	$0.375 r_{\tau}^{0.431}$
Silt	$0.273 r_{\tau}^{0.711}$	$0.348 r_{\tau}^{0.394}$

$r_{\tau} = \tau_d / \sigma'_0$; τ_d = dynamic shear stress.

For Shanghai sand, the development of pore water pressure in laboratory cyclic loading tests is of the form

$$\frac{p}{\sigma'_0} = (1 - ms_l) \frac{2}{\pi} \arcsin \left(\frac{N}{N_f} \right)^{\frac{1}{2\theta}} \quad (7)$$

where s_l = static stress level; m and θ = experimental parameters, for Shanghai sand $m = 1.1$ and $\theta = 0.7$; and N_f = the accumulative number of

cycles at the same stress level required to produce a peak cyclic pore water pressure ratio of 100% under undrained conditions.

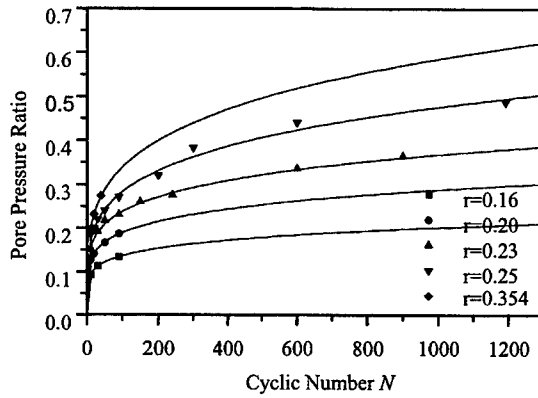


Figure 3. Variation of pore water pressure ratio and N of Shanghai

Earthquake subsidence

The earthquake subsidence can be divided into the volumetric and deviatoric components, ε^p and γ^p . The volume change, ε^p , comes from dissipation of seismic pore water pressure and can be calculated through consolidation equation. For Shanghai saturated soft soil, γ^p is formulated according to the undrained cyclic triaxial tests as follow

$$\gamma^p = \frac{r^*}{d - (d - 20)r^*} \quad (8)$$

where d = an experimental parameter, $d = 8$ for Shanghai sand, $d = 3$ for Shanghai clay. r^* is

$$r^* = \frac{r - r_s}{r_f - r_s} \quad (9)$$

where r_s = initial dynamic stress ratio; r_f = failure dynamic stress ratio.

DYNAMIC ANALYSIS METHOD

If the pore water acceleration has been neglected, the formulation of Biot governing equations is represented as the following

$$\begin{aligned} \sigma_{ij,j} + \rho g_i &= \rho \ddot{u}_i \\ (k_{ij} p_{,j})_{,i} - \dot{\varepsilon}_{ii} - (k_{ij} \rho_f g_j)_{,i} &= 0 \end{aligned} \quad (10)$$

where σ_{ij} = the total Cauchy stress in the combined solid and fluid mix at any instant, u_i = the displacement, p = the pore water pressure, ρ and

ρ_f are the density of the mixed soil and fluid itself respectively. The equations can be solved numerically under given boundary and initial conditions by the finite element method. In this the displacements \mathbf{u} are described in terms of the nodal values $\bar{\mathbf{u}}$ as

$$\mathbf{u} = \mathbf{N}\bar{\mathbf{u}} \quad (11)$$

with a similar discretization for the pressures,

$$\mathbf{p} = \bar{\mathbf{N}}\bar{\mathbf{p}} \quad (12)$$

where $\bar{\mathbf{p}}$ is the vector of nodal pressure values. In the above \mathbf{N} and $\bar{\mathbf{N}}$ are appropriate shape functions. Performing spatial discretization, the finite element formulation are derived as

$$\begin{aligned} \int_{\Omega} \mathbf{B}^T \boldsymbol{\sigma}' d\Omega + \mathbf{M}\ddot{\bar{\mathbf{u}}} - \mathbf{Q}\bar{\mathbf{p}} &= \mathbf{f} \\ \mathbf{H}\bar{\mathbf{p}} + \mathbf{Q}^T \dot{\bar{\mathbf{u}}} &= \bar{\mathbf{f}} \end{aligned} \quad (13)$$

where \mathbf{M} = mass matrix, \mathbf{Q} = couple matrix, \mathbf{H} = permeability matrix, \mathbf{f} = nodal earthquake load vector, $\bar{\mathbf{f}}$ = nodal seepage discharge vector.

The main analysis procedures are as follows:

1. Calculate initial static state of soil.
2. Determine parameters of the dynamic calculation model.
3. Calculate dynamic state of soil.
4. Calculate seismic pore water pressure increment and undrained residual strain.
5. Repeat step 2-4 until the earthquake motion ends.
6. Continue post-earthquake static analysis until the dissipation of pore water pressure completes.

APPLICATION

The formulation presented allows any problem of earthquake response to be studied quantitatively. In the example the Shanghai horizontal soil layer of depth 280m, which is subjected to a base motion of the first 10s N-S component of the El Centro Earthquake (May, 1940) with the maximum acceleration scaled to 0.1g, is studied in terms of the dynamic calculation model. The base motion input for analysis is shown in Figure 4.

The ground acceleration history and the distribution of maximum accelerations are shown in Figs. 5 and 6 respectively. It is interesting that the surface maximum acceleration is only 0.92 m/s^2 . Why is the surface maximum acceleration less than the base? The main reason is probably that the buildup of pore water pressures causes a decrease in stiffness of Shanghai soil. The ground and bedrock response spectra with 5 percent damping ratio are shown in Figure 7. The spectral values of the ground acceleration are less than those of the bedrock accelerations between the period of 0.1 and 1.2 seconds. The soil deposit acts as a filter when the bedrock earthquake acceleration is transmitted through it. The soil deposit filters out a significant portion of the high frequency content of the bedrock acceleration.

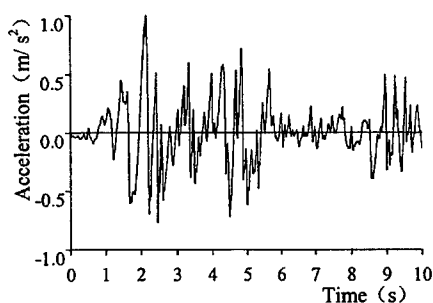


Figure 4. Input earthquake wave

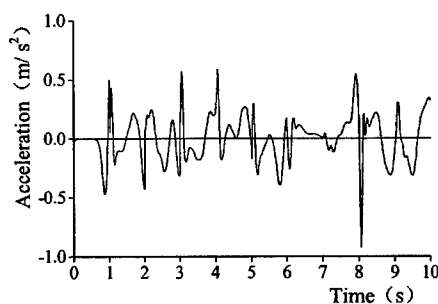


Figure 5. Predicted acceleration time history of ground

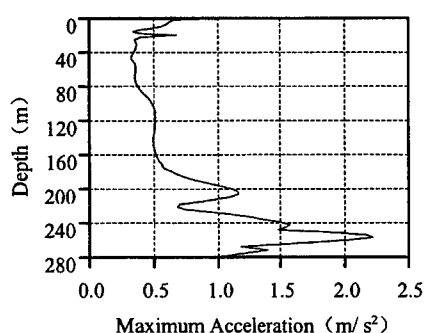


Figure 6. Predicted variation of the maximum acceleration with depth

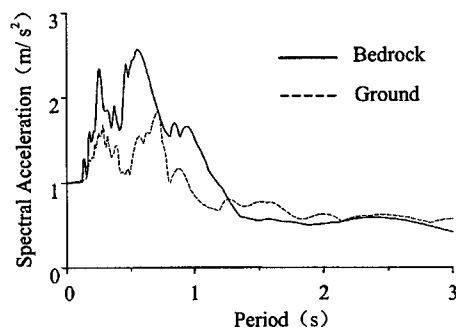


Figure 7. Predicted response spectra of ground and bedrock

During the earthquake, the pore water pressure of deep soil is very small. But the pore water pressures from the depth less than 20m to the

ground is gradually increasing. The maximum pore water pressure ratio equals 0.35 in the depth of 9m. The calculated maximum earthquake subsidence is about 15mm until the dissipation of pore water pressure completes.

CONCLUSION

An equivalent viscoelastic dynamic model for Shanghai soil is presented. It contains four formulas for calculating the shear modulus, the damping ratio, pore water pressure and earthquake subsidence.

An approach of dynamic effective stress analysis in the fluid-saturated porous solid is summarized in terms of Biot governing equations and finite element formulation. The seismic response of Shanghai soil strata of 280m depth is also investigated by FEM with the Biot dynamic consolidation formulation and presented model. Some valuable conclusions are obtained from the results.

REFERENCES

1. Martin, P. P. and Seed, H. B., One-dimensional dynamic ground response analyses. *Journal of the Geotechnical Engineering Division, ASCE*, 1982, **108**, 935-52.
2. Biot, M. A., Theory of elasticity and consolidation for a porous anisotropic solid. *Journal of applied physics*, 1955, **26**, 182-5.
3. Biot, M. A., Mechanics of deformation and acoustic propagation in porous media. *Journal of applied physics*, 1962, **33**, 1483-98.
4. Zienkiewicz, O. C. and Bettess, P., Soils and other saturated media under transient, dynamic conditions; general formulation and the validity of various simplifying assumptions. In *Soil Mechanics-Transient and Cyclic Loads*, ed. G. N.Pande and O. C. Zienkiewicz, Wiley, 1982, pp. 1-16.
5. Zienkiewicz, O. C. and Shiomi, T., Dynamic behaviour of saturated porous media; the generalized Biot formulation and its numerical solution. *International Journal for numerical and analytical methods in geomechanics*. 1984, **8**, 71-96.
6. Li, X. S., Shen, C. K. and Wang, Z. L., Fully coupled inelastic site response analysis for 1986 Lotung earthquake. *Journal of Geotechnical and Geoenvironmental Engineering, ASCE*, 1998, **124**, 560-

73.

7. Zhou, J., Yasuhara, K., Hyodo, M. and Hirai, M., Prediction of earthquake induced settlement. *Proceedings of International Conference on Computational Methods in Structural and Geotechnical Engineering*, Hong Kong, 1994, 907-11.

THE DYNAMIC STIFFNESS OF THE BALLAST LAYER IN RAILWAY TRACK.

CJC Jones, DJ Thompson and MGR Toward

Institute of Sound and Vibration Research
University of Southampton, Highfield, Southampton SO17 1BJ, UK
tel: +44 1703 593224, fax +44 1703 593190, email: cjcj@isvr.soton.ac.uk

ABSTRACT

The ballast layer has an important influence on the dynamics of a railway track. It affects both the radiated noise and the vibration transmitted to supporting structures. Little information exists to characterise the behaviour of ballast at frequencies for audible noise. Two types of measurements of the stiffness of the ballast layer have been made on a test track with specially constructed force transducers installed under the ballast. These cover the frequency range up to 2000 Hz. The variation of the stiffness of the ballast under a range of preloads is studied and a simple theoretical model for the frequency dependent stiffness of the ballast is developed.

1. INTRODUCTION

Rolling noise from a railway arises from the vibrations excited in the wheel, the rail and the sleeper due to the combined roughness of the wheel and rail surfaces at their contact. In order to study the generation of rolling noise from railways, accurate theoretical models of the track are required. The properties for the ballast layer are the least well defined parameters in a model for the structural dynamics of a railway track.

When rail vehicles traverse structures such as bridges, the noise level is often raised because of the transmission of vibration to the bridge structure, which thereby becomes a large radiator of low frequency noise [1]. A number of different railway track structure types are used on bridges including direct fasteners. However, ballasted track is often preferred, since track maintenance machines can then be run over a stretch of normal track without having to introduce specialised maintenance for the length of the bridge. Some studies have identified that the mass loading and damping introduced by the ballast to the bridge structure is beneficial in reducing the rolling noise [2]. A knowledge of the vibration characteristics of a ballast layer is therefore important in the modelling of noise on bridges as well as for the effect of the support stiffness of the sleepers on normal track.

In order to develop and validate a suitable model for the point and transfer, high-frequency, dynamic stiffness of the ballast layer measurements

have been made on a test track. The estimation of the frequency dependent direct stiffness at the sleepers is made using an indirect technique that is based on the shift in the resonance frequencies of a sleeper when laid in the track compared to freely supported conditions. The transfer stiffness of the ballast layer is also measured by locating the internal resonance frequency of the ballast using specially constructed force transducers that were installed under the ballast layer during construction of the track.

2. THE TEST TRACK AND BURIED FORCE TRANSDUCERS

In order to facilitate a number of detailed measurements of the properties of railway track and the validation of theoretical models for high frequency track dynamics, a 36 m length of railway track has been constructed at the University of Southampton. The track design is that of a typical main line. The top soil was removed, the ground was levelled and it was compacted to mainline railway specification. A layer of granite ballast (to the Railtrack specification [3], from the Glensander quarry) was laid to a depth of 30 cm and compacted with a vibro-tamper in a manner similar to the preparation of mainline track. The concrete sleepers were laid on the ballast, the rails fixed and welded and ballast poured to fill the spaces between sleepers and to form the ballast shoulder. The track was levelled to mainline standard at the end of the process.

As no rolling stock has run on the line, the ballast layer should be regarded as being in the new condition and, although compacted as if ready to open for traffic, is not expected accurately to reflect the compaction of a trafficked main line. With this inevitable limitation, the ballast layer was designed to be as close as possible to a realistic railway ballast layer.

Prior to the laying of the ballast, a concrete block, occupying the area covered by three sleepers and approximately 30 cm deep was laid under part of the track. Five specially constructed force transducers were installed on the upper surface of the concrete block. The construction of these is shown diagrammatically in Figure 1. Each transducer is 20 cm by 20 cm has 4 pairs of piezo-electric ceramic tiles (25 mm diameter). The top and bottom plates are 6 mm thick aluminium. To protect against moisture, the transducers were filled with an electronic potting compound. The outer top and bottom plates of the transducer form the ground connection which also forms the electrical screening. Coaxial (microdot) cables from each of the four piezo-ceramic stacks were laid to the side of the track in steel conduit.

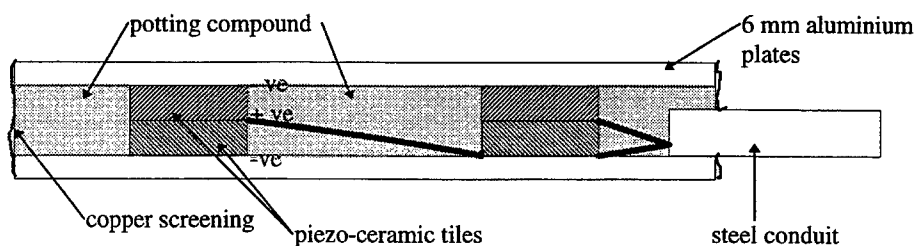


Figure 1. Cross-section of a force transducer.

Prior to installation, the force transducers were calibrated in the laboratory using a mass accelerated using an electrodynamic shaker. However, due to the static loading by the ballast layer and an interval of two years between installation of the track and execution of this measurement programme, the calibration of the force transducers is not expected to be trustworthy.

The arrangement of the force transducers under the track is shown in Figure 2. In this paper, only measurements from force transducer T_2 are presented. This is on the middle sleeper below the rail position.

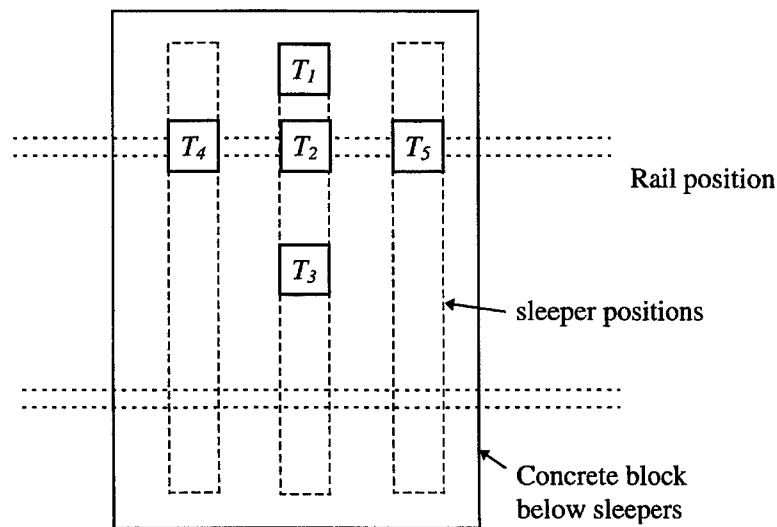


Figure 2. Positions of the force transducers below the sleepers.

3. LOADING THE TRACK

The ballast is highly non-linear and it is important therefore to study the effect of static loading in determining its dynamic stiffness. Rail vehicles typically apply a wheel load of between 5 tonnes, for a passenger vehicle and

12.5 tonnes for a heavy freight vehicle or locomotive. Because of the bending stiffness of the rail about half of this load would be expected to be transmitted to a single sleeper as the axle passes over it.

Here a static pre-load has been applied to a single end of the sleeper using the arrangement shown in Figure 3. The pre-load is isolated from the dynamic excitation of the sleeper at a very low frequency using a rubber block. The masses (β) consisted of palettes of concrete blocks. With this arrangement it was practicable to apply pre-loads of up to 3.5 tonnes via the isolation mount (v). The load was measured by the deflection of the mount which was calibrated for this purpose using a materials testing machine. Six loading steps were used in the measurements.

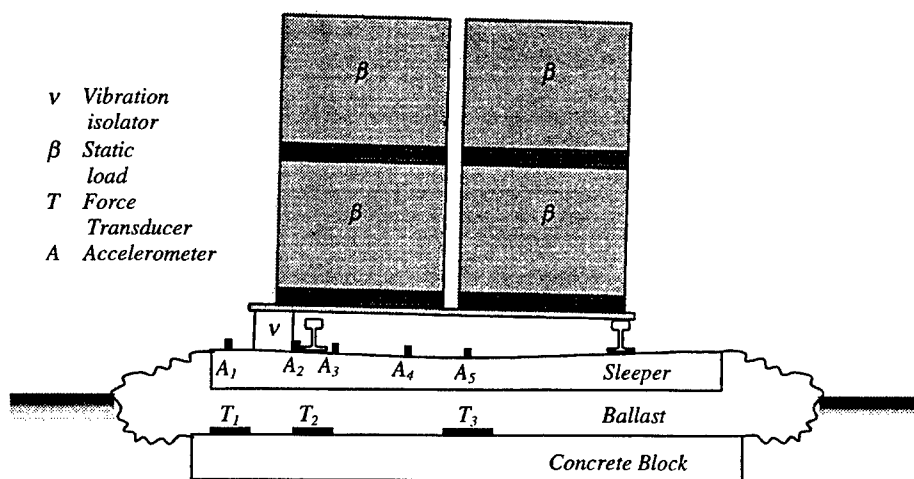


Figure 3. Arrangement for applying static pre-load to a single sleeper end.

4. AN INDIRECT METHOD FOR THE ESTIMATION OF THE SUPPORT STIFFNESS OF A SLEEPER

An indirect method has been used to measure the support stiffness that the ballast applies under the sleeper. This uses the modification of the sleeper's modal frequencies caused by the foundation stiffness that it experiences. The modal frequencies of a freely suspended sleeper were identified in the laboratory before it was laid in the track. A finite element model was then set up for the sleeper. A model using 18 tapered cross-section, Timoshenko beam elements, was found to reproduce the first 4 modal frequencies of the sleeper to within about 1%. The measured and calculated modal frequencies are given in Table 1.

Table 1. Modal frequencies of a freely supported sleeper.

Mode	Measured frequency (Hz)	Calculated frequency (Hz)
1	120	120.0
2	352	357.6
3	682	678.9
4	1036	1032.3

The measured modal frequencies of the sleeper *in situ* in the ballast are shown for the different loading values in Table 2. These were compared with the frequencies calculated using the FE model with spring support elements added under the sleeper. The stiffness of the spring support elements was then adjusted to give the same modal frequency of the sleeper with support as the measurement. In this process the difference between the FE model and the measured frequencies for the freely supported sleeper were also taken into account.

Table 2. Measured modal frequencies of the sleeper in situ.

Static load above isolator (kg)	Measured modal frequencies (Hz)			
	1	2	3	4
300	188	436	737	1119
930	194	478	730	1134
1690	205	502	734	1148
2440	222	509	746	1157
3200	231	522	753	1178
3570	236	535	762	1193

The point stiffnesses under the whole sleeper evaluated, indirectly, using this technique are given in Table 3.

Table 3. Indirectly measured stiffnesses under the sleeper.

Static load above isolator (kg)	Stiffness at each mode (10^8 N/m)			
	1	2	3	4
300	2.7	7.5	12.0	25.8
930	3.0	12.6	10.4	30.6
1690	3.6	15.4	11.3	34.8
2440	4.5	16.4	13.7	38.2
3200	5	18.2	15.1	44.2
3570	5.3	20.0	17.0	48.8

5. MEASUREMENTS OF THE INTERNAL RESONANCE FREQUENCY OF THE BALLAST LAYER

The transfer function between each of a number of accelerometers placed along the upper surface of the middle sleeper and the three force transducers placed under it have been measured. The positions of the accelerometers are shown on Figure 3. An instrumented hammer was used as the source of vertical excitation of the sleeper, striking 50 mm from the end near the isolation mount. For convenience, the measurement was carried out in terms of the frequency response function of each of the four leads of the buried force transducer to the hammer excitation and also, separately, of the response of each accelerometer to the hammer excitation (accelerance) at the same position.

The signals from the force transducers were scaled according to the laboratory calibrations and averaged. This response function was then divided by the displacement response at the accelerometer (calculated from the accelerance) to give the transfer function between the accelerometer and the force transducer.

Both the force measurement and the accelerometer measurement contained peaks and dips representing the resonant behaviour of the sleeper. On inspection of the transfer functions from the accelerometers to the force transducer, difficulty was found in identifying the location of the peaks corresponding to the resonance of the ballast layer amongst the residue of the sleeper modal response which did not cancel well for most of the force transducer/accelerometer pairs. Here, only the data for the transfer function between accelerometer A_3 and force transducer T_2 is presented and used in the calculation as this was comparatively free from this problem and well damped peaks due to the internal resonance of the ballast layer can be identified. The amplitude of this transfer function is presented in Figure 4 for each of the 6 loading steps in terms of the force at T_2 due to the displacement at A_3 . The frequency response functions have the units of stiffness but do not represent the stiffness of the ballast layer since the force transducer only measures the force over a small area (0.2 m by 0.2 m) rather than over the total area to which the force from the sleeper may spread through the ballast. It should also be remembered that the laboratory calibration of the force transducer is not expected to be reliable.

In the results presented in Figure 4, the coherence function of the force response measurement was used to determine where the excitation was insufficient to make reliable measurements. This resulted in the rejection of some data between 1600 Hz and 2000 Hz which is omitted from the graph.

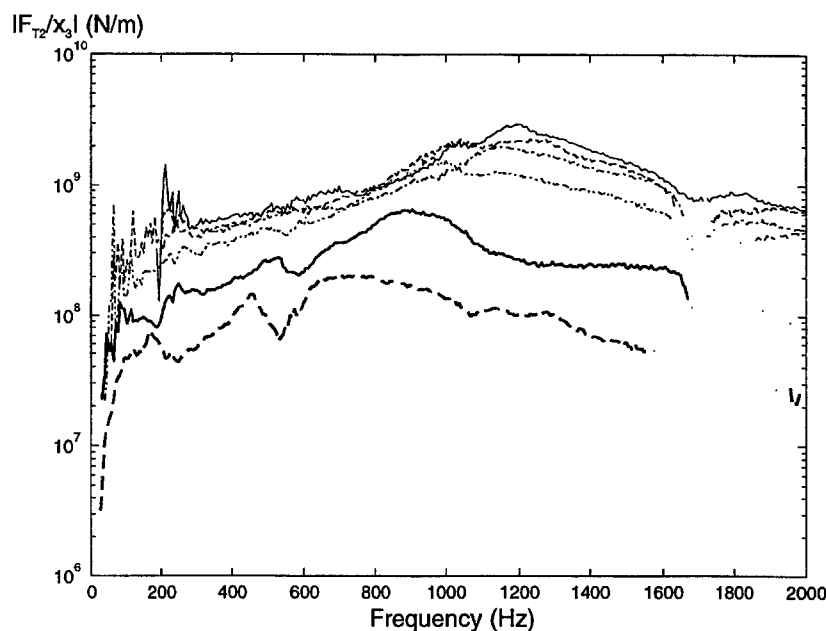


Figure 4. The amplitude of the transfer function from force transducer T_2 to displacement at A_3 on the sleeper;
 --- load step 1, — load step 2, load step 3,
 - . - . load step 4, - - - - load step 5, — load step 6.

In order to identify stiffness parameters from the measurements it is necessary to compare them to results from a model for the ballast layer and to use the phase information to locate the frequencies of the ballast resonances.

6. A MODEL OF THE VERTICAL STIFFNESS OF A FRUSTUM

In order to interpret the behaviour of the ballast a model of the vertical stiffness of a solid frustum of material (Figure 5) has been used.

The axial displacement of a rod of variable cross-section is represented by the wave equation

$$\frac{\partial^2 u}{\partial x^2} + \frac{1}{A(x)} \frac{\partial A(x)}{\partial x} \frac{\partial u}{\partial x} + k^2 u = 0$$

where u is the displacement in the x direction and $A(x)$ is the variation of the cross-sectional area with x along the rod. $A(0) = a_2$, $A(L) = a_1$. k is the wave number for longitudinal waves and is given by

$$k = \omega \sqrt{\frac{\rho}{E}}$$

where ω is the circular frequency, ρ is the mass density and E is the Young's modulus of the material. The hysteretic model is used for damping, i.e. E is complex and given by $E_R(1 + j\eta)$ where E_R is a real value of Young's modulus and η is the material loss factor.

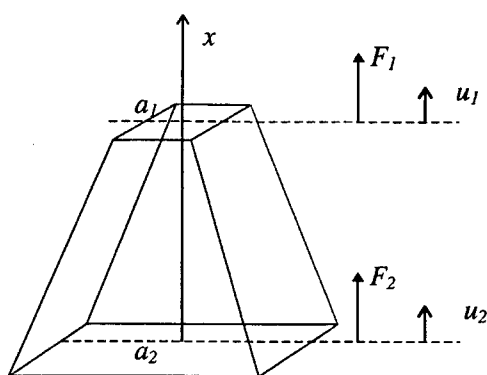


Figure 5. The frustum model.

The cross-sectional dimension ('diameter') is allowed to vary linearly along the rod. This leads to the solution for displacement [4], assuming $u_2 = u(0) = 0$.

$$u(x) = \frac{1}{(x - \beta L)} [C \sin(kx)] e^{j\omega x}$$

where C is a constant of integration, L is the height of the frustum and β is $\frac{1}{1 - d_1/d_2}$ where d_1 and d_2 are the diameter at the top and bottom of the frustum.

Evaluating the force at the top and bottom of the frustum as

$$F_1 = -A(x)E \left. \frac{\partial u}{\partial x} \right|_{x=L}, \quad F_2 = -A(x)E \left. \frac{\partial u}{\partial x} \right|_{x=0}$$

yields the point and transfer stiffnesses, K_{11} and K_{12} of the model as

$$K_{11} = \frac{F_1}{u_1} = -a_1 E \frac{[k(1 - \beta)L \cos(kL) - \sin(kL)]}{(1 - \beta)L \sin(kL)}$$

and

$$K_{12} = \frac{F_2}{u_1} = a_2 E \frac{k}{(\beta L)^2 \sin(kL)}$$

The values of E for the ballast at the various loadings have been evaluated by comparison with results from the model in terms of the phase of the transfer function shown in Figure 6. The frequency of the first internal resonance of the ballast layer is indicated by the phase curve crossing the value of $-\pi/2$ radians. A loss factor of 0.3 has been found to produce a reasonable correspondence with the measurements at all loadings. Although the top and bottom areas used in the frustum model do not influence the values of E found by this method, the top area of the frustum has been assumed to be the base area of the sleeper and it has been assumed that the ballast spreads the load downwards at an angle of 60° .

The amplitudes of the transfer stiffness, K_{12} calculated from the model with the fitted E values are presented in Figure 7. These are factored to make them equivalent to the measured transfer functions in which the force transducers only measure a proportion of the base area of the frustum. Comparison with Figure 4 shows that the shape of the curves and the positions of the resonance peaks are reproduced well but that the levels are not. With the uncertainty in the calibrations of the force transducers, this is not unexpected. Differences between the stiffnesses at different preloads may also occur due to differences in top and bottom areas.

The values of E found from the comparison of the phase of the transfer function have been used to calculate the point stiffness K_{11} also. These are plotted in Figure 8 and compared with the values found by the indirect measurement method. It can be seen that comparable levels for this stiffness are obtained with the two methods.

In order to examine the behaviour of the Young's modulus with the pre-load, the values gained from the model/measurement comparison are plotted versus the load (taking into account the mass of the sleeper) in Figure 9. The line drawn on this graph indicates that the relationship of E to the pre-load follows approximately a $1/2$ power law. The theory of Hertzian contact of spheres suggests a $1/3$ power law. The higher power found here may result from an increase in the effective number of contacts between grains of ballast and the sleeper as the pre-load increases.

Phase of K_{12} (radians)

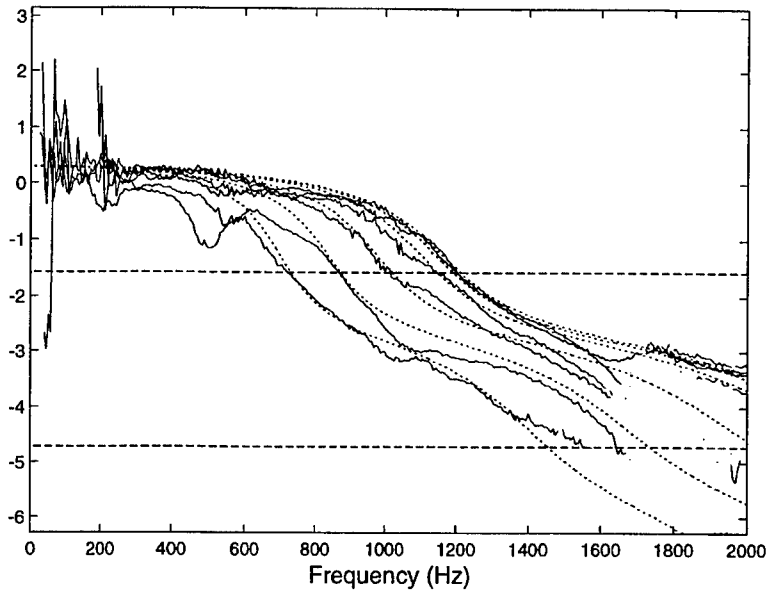


Figure 6. The phase of the transfer function from force transducer T_2 to displacement at A_3 (for clarity lines for the various loadings are not distinguished on this graph).

K_{12} (N/m)

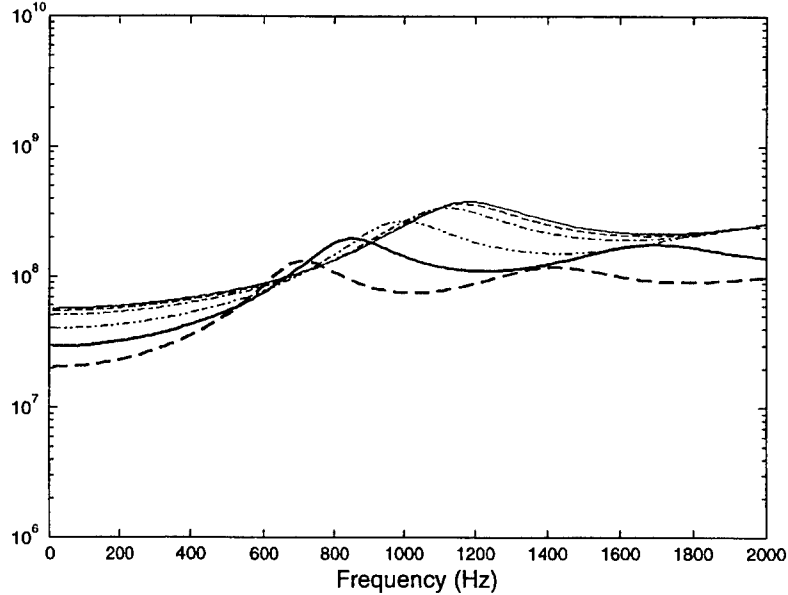


Figure 7. The amplitude of K_{12} calculated from the model
 - - - load step 1, — load step 2, load step 3,
 - · - · load step 4, - - - - load step 5, — — — load step 6.

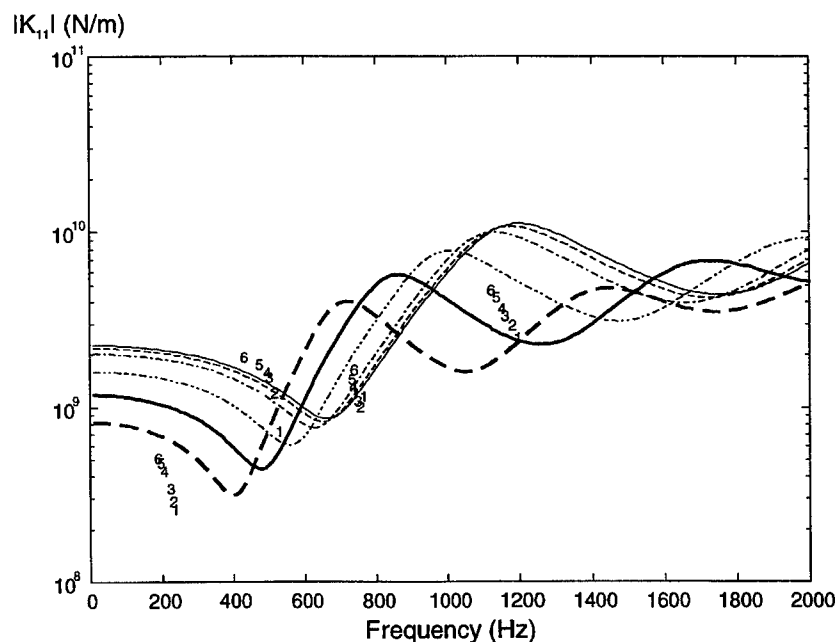


Figure 8. The amplitude of K_{11} calculated from the model compared with the total stiffness under the sleeper from the indirect measurement method

--- load step 1, — load step 2, load step 3,
 - - - - - load step 4, — load step 5, load step 6,
 (measurement points plotted using load step numbers).

7. CONCLUSIONS

The stiffness of a layer of ballast has been measured by two independent techniques. The first method is indirect and relies on the shift in modal frequencies of a sleeper when embedded in the track. The second relies on the identification of the internal resonance frequencies of the ballast layer by measurements of blocked force under the ballast. The stiffness of the ballast layer is estimated by comparison of the measured transfer functions to a model of a frustum of material under axial compression. The two methods produce similar estimates of the point stiffness of ballast. The effective Young's modulus of the ballast is found to increase according to the square root of the pre-load rather than the one-third power that may be expected from Hertzian contact theory.

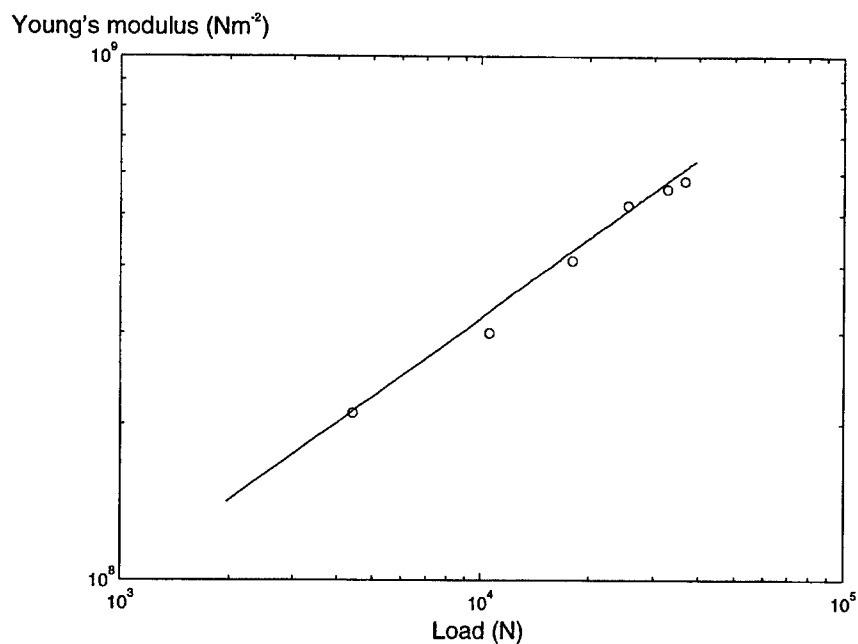


Figure 9. Derived values of Young's modulus versus load indicating a 1/2 power law.

8. REFERENCES

- 1 Janssens, M.H.A. and Thompson, D.J., A calculation model for the noise from steel railway bridges, *J. Sound Vib.*, 1996, **193**(1), 295 - 305.
- 2 Hardy, A.E.J., Noise from railway bridges, *Proc. Inst. Mech. Eng.*, 213, Part F, 1999, 161 - 172.
- 3 Railtrack line specification - Track Ballast, Reference RT/CE/S/006, Issue 2, Railtrack PLC, February 1998.
- 4 Snowdon, J.C., Vibration and shock in damped mechanical systems, John Wiley and Sons Inc., New York, 1963.

ISBN 0 85432 7215

Cover designed by Roger Pinnington
ISVR University of Southampton